Building Tools for the Modelling of Epoch of Reionisation Galaxies in the Era of JWST

Ciaran Fairhurst

University of Sussex

A thesis submitted for the degree of

PhD Astrophysics

2020

"Let’s go."

"We can’t."

"Why not?"

"We’re waiting for Godot."

Acknowledgements

The author would like to provide specific thanks to his supervisor Stephen Wilkins, without whom none of this work would have been possible. He has truly gone above and beyond as a supervisor and his support through both the science portion of my work, and the later writing portion while we have both been under immense personal strain due to 2020 will always be appreciated, and was far more than I deserved. The author would also like to thank his mother and sisters, who have been a bedrock of support throughout.

Throughout the course of my studies I have met some of the most brilliant, inspiring people I could have ever hoped for, and I wish to thank them for pushing me to be better in every sense of the word. Their contributions to my growth as a person are – like make things in astronomy – nigh on impossible to measure in a satisfactory manner, but undeniably vast. Therefore I simply list them here sorted roughly by how we crossed paths, and then alphabetically. To try and state what each has done for me individually would only do them a disservice, so I won't – they know what they have done.

Ridwan Barbhuiyan
Darren Baskill
Sunayana Bhargava
Charlotte Clarke
Scott Clay
Pippa Cole
Benoît Fournier
Jess Hislop
Chris Lovell
Mark Sargent
Lizi Swann
Michaela Bagley
Andreia Carrillo
Jackie Champagne
Steve Finkelstein
Taylor Hutchison
Briana Indahl
Intae Jung
Danny Krolikowski
Rebecca Larson
Sophía Rojas
Justin Spilker
Matt Stevans
Sam Hetherington
Madeline Kinkel
Camilla Pacifici

Abstract

One of the Holy Grails of modern astronomy is to observe the first generations of stars and how they assembled into galaxies. While recent years have made incredible progress in this endeavour, we have reached somewhat of a cul-de-sac in terms of the sensitivity and wavelength coverage necessary to push further back into reionisation. We also struggle to make substantive statements about the physical properties of the galaxies we do detect at $z > 6$. The *James Webb Space Telescope (JWST)* promises to revolutionise our view of this epoch, however modelling must keep up in order to satisfactorily interpret these new observations.

In this thesis I chart the development of a Bayesian SED fitting code INTERROGATOR. This code is optimised for maximum flexibility in model choices, so as to test between the suite of existing stellar, nebular and dust models, and also to modularly add new models as they are developed.

I use this code on a sample of low redshift Extreme Emission Line Sources (EELS), selected from the GAMA survey as analogues to high redshift galaxies. Specifically I use INTERROGATOR to show how the various assumptions implicit in modern SED fitting affect the inferred physical properties of these objects, biasing results on even the most basic properties such as stellar mass and star formation rates.

Finally, using the BLUETIDES simulation, I propose a novel technique for modelling the stellar spectra of galaxies in the Epoch of Reionisation (EoR). By relaxing the single metallicity approximation commonly used in SED fitting, I show that improvements can be made to the recovery of these properties at the cost of adding additional parameters to the model.

Preface

I declare that no part of this work has been submitted for any other award of the University of Sussex, or any other awarding body.

Chapter 2 contains entirely my own work, with supervision from my supervisor Dr Stephen Wilkins, and technical assistance from Dr Peter Hurley.

The galaxy selection process in Chapter 3 (section 3.2) is loosely based on previous unpublished work by Dr Scott Clay, but the exact final procedure was designed by me. In addition, the spectra obtained later in the same chapter from VLT/XSHOOTER (section 3.5) were obtained in an observing proposal designed by Dr Joseph Caruana (U. Malta), Dr Stephen Wilkins (U. Sussex) and Dr Scott Clay (U. Sussex). The data reduction process, and subsequent re-reduction were performed by Dr Joseph Caruana.

In chapter 4, the pre-processing of the BLUETIDES simulation snapshots was performed by Dr Stephen Wilkins to divide the particle data in to galaxies. The rest of the analysis was performed by me.

CIARAN FAIRHURST

Contents

List of Figures

Chapter 1

Introduction

In this thesis, I chronicle the development of a variety of tools which are targeting the analysis of high redshift galaxies and their low redshift analogues. This work is performed with an eye to predicting the revolutionary impact of the *James Webb Space Telescope* (JWST, Webb) upon its launch in late 2021. Webb promises to find large numbers of Epoch of Reionisation (EoR) galaxies, pushing well into the first billion years of the Universe, and it is important to understand what we expect to see there both to design survey strategies, and to interpret the galaxies that are detected. The thesis is structured as follows:

The rest of chapter one is dedicated to setting the necessary background, briefly describing the giant's shoulders upon which modern observational astronomy stands. Chapter two introduces INTERROGATOR, a Bayesian SED fitting code developed with the modelling of high redshift observations specifically in mind. The code is designed to be as modular as possible to allow for the users choice of models and model parameters, or more importantly, to allow the characterisation of model uncertainties by comparing between them. How the code works is discussed, followed by a brief demonstration of the recovery of model parameters of various model galaxies.

Chapter three will demonstrate an application of INTERROGATOR, selecting a sample of Extreme Emission Line Sources (EELS) from the GAMA survey with an equivalent width cut of EW(Hα)>200. It has been claimed in the literature that galaxies such as these are analogues of high redshift galaxies, and we find that although they closely match in stellar

mass and specific star formation rate, they are of a higher metallicity than typical EoR star-forming galaxies, at least based on simulation predictions. We also carry out model comparison using INTERROGATOR, and find that these galaxies have rising exponential SFHs, which the standard GAMA pipeline does not account for. As these galaxies have such a high amount of young stars, they are very sensitive to model assumptions, seeing a scatter on the median of the sample of ~ 0.4dex in both SFR and M_* depending on model choices.

Finally, chapter 4 will explore the star formation and metal enrichment histories, and stellar spectra, of galaxies using the BLUETIDES simulation. Galaxies at very high redshift do not have enough time to sufficiently mix their metals throughout the galaxy. By creating an analytic model of the joint age-metallicity distribution of simulation galaxies at redshifts above 8, we identify whether modelling of this type provides additional insight into the buildup of stellar material through the epoch of reionisation.

Throughout this thesis I assume the following ΛCDM parameters $\Omega_M = 0.30$, $\Omega_\Lambda = 0.69$, $\Omega_b = 0.048$ and $H_0 = 68 \mathrm{kms}^{-1}\mathrm{MPc}^{-1}$, where Ω_M, Ω_Λ, and Ω_b are the total (baryon plus dark) matter fraction, dark energy fraction, baryonic matter fraction respectively, and H_0 is the present day Hubble constant. These parameters were measured in Planck Collaboration *et al.* [2016a].

1.1 The Contents of the Universe

While the Universe is home to incredible complexity, in the broadest strokes it can be considered to have relatively few ingredients. This section will simply outline the properties of each of these, including common observational strategies for characterising them. In the following chapter (section 2.3) the precise details of how to model them will be outlined.

1.1.1 Dark Matter and Dark Energy

Dark Matter has been theorised without any real evidence since antiquity, with the idea of matter that could not be seen (either completely or due to insufficient observational power) being brought up by many thinkers throughout history as an explanation for physical phenomena.

In Zwicky [1933], a study of the Coma cluster found that the observed velocity dispersion was some 10 times larger than the dispersion that could be supported by the system according to the Virial Theorem. They mass of the cluster was thus estimated to be some 10^3 larger than the sum of the masses of the galaxies within – this strongly implied the presence of additional material which could not be detected via the light it gives out.

This observation was supported by galaxies rotation curves – how the circular velocity of material in a galaxy varies with radius. Under simplifying assumptions, one can calculate the mass distribution of a galaxy as a function of radius by considering all mass inside the radius being considered to act as a point source in the centre, and all mass outside of the radius to not act at all via the Shell Theorem. At large radius one would expect to approximately recover the Keplerian solution ($v \propto r^{-1/2}$), however observations of stars, and HI regions on the galaxies' outskirts suggest that they orbit at speeds independent of distance. This "flattening" of the rotation curve provided strong evidence that additional mass was lurking in the outskirts of galaxies that direct observations were incapable of finding. Figure 1.1 shows that the agreement at low radii is actually fairly convincing, however as radius increases, especially into the HI observations, there is significant deviation.

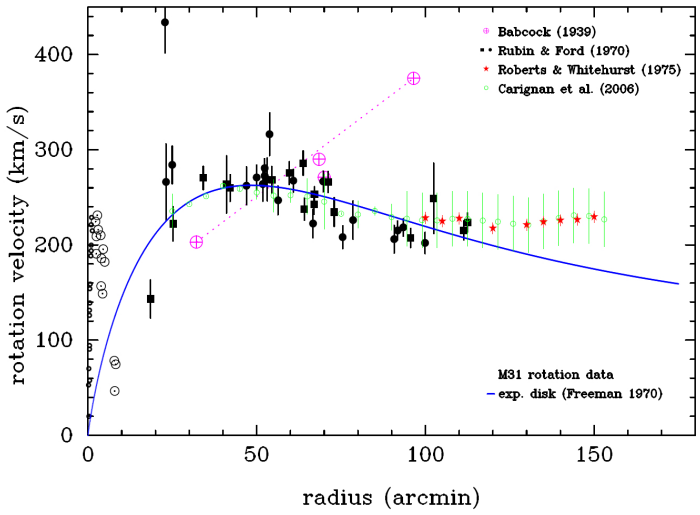

Figure 1.1: Rotation curve of the galaxy M31 (Andromeda) with data from a variety of sources. Purple points are from Babcock [1939], one of the first detailed studies of this effect. The black points are from Rubin and Ford [1970], observing stellar motion via spectroscopy. Red and green points are from Roberts and Whitehurst [1975] and Carignan *et al.* [2006] respectively, both employing radio telescopes to measure the HI 21cm signal. Solid line represents a scaled model of an exponential disc mass profile, which would well describe the mass distribution of the stars in M31 [Freeman, 1970].

The precise nature of Dark Matter is not well understood. Theories of dark matter fall into two main camps. Firstly, Massive Compact Halo Objects (MACHOs); effectively astronomical objects ranging in size from sub micrometer sized to multiple solar masses, which if there is enough of them add mass to a galaxy without being visible [Alcock *et al.*, 2000]. A subclass of dark matter MACHOs are primordial black holes – black holes which formed in the very early Universe and are not astrophysical in nature [Carr *et al.*, 2016]. Secondly is the Weakly Interacting Massive Particle (WIMP) model of dark matter – dark matter is a class of sub-atomic particle which does not interact with EM radiation. WIMPs are the currently the favoured candidate, as CMB measurements which provide strong evidence for non-baryonic Dark Matter [Aprile *et al.*, 2018]. At its core however, evidence of Dark Matter other than its gravitational presence remains elusive.

Dark energy is much less well understood than even Dark Matter, despite making up the majority of the Universe's energy budget. The expanding Universe had been largely

accepted for the better part of a century since Hubble's seminal 1929 paper [Hubble, 1929]. However the rate of change of this expansion was unconstrained, with three possible scenarios: gravitation eventually overcomes the expansion, bringing everything back to a singularity; gravitation and expansion are in balance; the Universe expands at a constant velocity; or expansion which accelerates, perpetually increasing in velocity.

Observations of type Ia supernovae [e.g. Perlmutter *et al.*, 1999; Riess *et al.*, 1998] allowed for discrimination between these models. By finding supernovae in galaxies out to $z \sim 1$, when the Universe was half the age it is now, slight deviations could be detected from the constant rate of expansion measured previously.

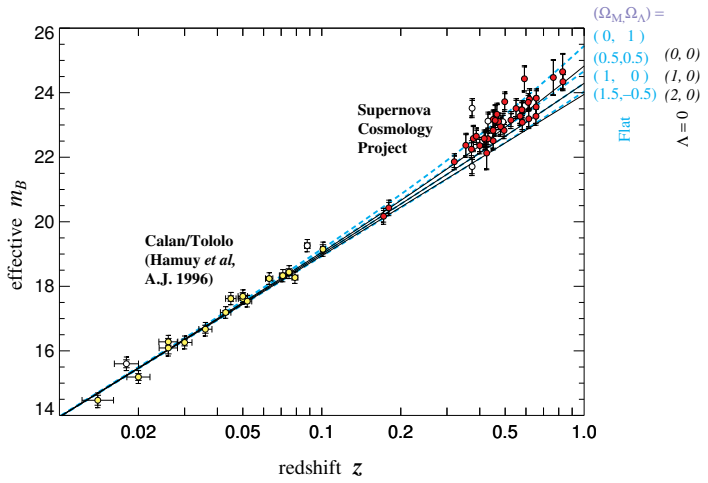

Figure 1.2: Hubble Diagram from S. Perlmutter's 1999 paper [Perlmutter *et al.*, 1999] on the use of 42 high redshift supernovae extending to $z \sim 1$ to constrain the cosmological parameters. Black solid lines represent cosmological models with constant expansion $\Lambda = 0$, with $\Omega_M = (0, 1, 2)$ being the (top,middle,bottom) lines respectively. Similarly the blue dashed lines represent cosmological models with $[\Omega_M, \Omega_\Lambda] = ([0, 1], [0.5, 0.5], [1, 0], 1.5, -0.5])$ from top to bottom respectively.

Figure 1.2 shows some of the motivating evidence for dark energy. Supernovae in galaxies with $z > 0.2$ are more faint than they would be in a Universe without an accelerating expansion. In the last 20 years this evidence and other similar studies have coalesced into a heavy favouring of a cosmological model with a positive Ω_Λ [Betoule *et al.*, 2014]. Other evidence for dark energy can be found within lensing of the CMB [Planck Collaboration *et*

al., 2016a, e.g.] and the large scale structure through large galaxy surveys [e.g. Abbott *et al.*, 2018].

1.1.2 Baryons

By energy density, the baryonic content of the Universe is only around 4%, however it is where the majority of the complicated physics takes place because of its readiness to interact with electromagnetic radiation. The majority of this baryonic content is in the form of hydrogen and helium gas, which was formed primordially, with traces of the other elements. For our purposes, gas in the Universe can largely be divided into two categories: the Intergalactic Medium (IGM) and the Interstellar Medium (ISM).

1.1.2.1 The Intergalactic Medium

The IGM in the present day is a web of ionised gas that forms a filamentary structure between galaxies. This gas is typically of temperature $10^5 - 10^7 K$, with a low density – around $n \sim 1 - 10m^{-3}$. Due to its highly ionized state the IGM has little effect on observations at low redshift, however this is not true for galaxies that are seen prior to the completion of reionisation (see section 1.2.3). At early times, the IGM was neutral, and any starlight passing through it with short $\lambda < 1216$Å wavelengths would be scattered of absorbed. This is both the cause of reionisation, but also a source of attenuation that must be accounted for. This is addressed in more detail in section 2.2.1.2.

1.1.2.2 The Interstellar Medium

The other major gaseous component of the Universe is the The Interstellar Medium (ISM). As the name suggests, this is an umbrella term for all of the content within a galaxy between the stars. The ISM has a few different phases, with the differentiating factors mostly being the temperature and density.

Molecular Gas The coldest ($T \sim 10-20K$) parts of the ISM are molecular clouds. These are clouds of hydrogen that are dense and cold enough to support molecule formation, specifically H_2 and other very simple molecules such as CO (an important observational tracer) [Bolatto *et al.*, 2013]. They can have particle densities of $10^2 - 10^3 cm^{-3}$, and the densest parts – called molecular cores – can have densities exceeding $10^6 cm^{-3}$ [Bergin and Tafalla, 2007]. Molecular clouds are the birth sites for new stars, and are thus inherently unstable – any cloud which is this cold and dense will collapse further and form a population of stars. Molecular gas is detected most commonly through the CO molecule transitions – it is thought that L_{CO} is directly proportional to the H_2 content, so it is an effective tracer for the spatial distribution of molecular hydrogen.

Atomic Gas HI regions are clouds of mostly neutral atomic Hydrogen. They typically have temperatures of either $T < 10^2 K$ (cold HI) or $T \sim 10^4 K$ (warm HI) [Cox, 2005] – gas with temperatures lying between these ranges has access to efficient heating and cooling mechanisms causing it to quickly settle into one of these two temperature regimes. These phases have particle number densities of around $10 cm^{-3}$ (cold) and $0.1 - 1 cm^{-3}$ (warm). HI is commonly traced by the 21cm signal – light spontaneously produced by the hydrogen gas due to the hyperfine structure of the Hydrogen atoms energy levels.

Ionised Gas Finally, it is worth noting the presence of HII regions. When a molecular cloud begins to form stars, the hot, young stars have powerful radiation fields which are easily capable of ionising the surround medium. This results in strongly ionised bubbles within the ISM. Because of their formation mechanism, these regions are short lived ($<$ 10 million years) as the radiation pressure of the living stars – and the extreme pressure produced by supernovae when they die off – drives the gas away leaving behind a star cluster. HII regions powered by stars are the primary source of nebular line emission, but also the bulk motions of particles in the gas mean that HII regions also produce a significant amount of continuum emission too, which can bias the overall normalisation of a spectra. Emission

lines serve as an important observational diagnostic of galaxies, providing accurate redshifts, compositions (metallicities), and the physical conditions (temperature, density) of the HII regions themselves.

1.1.2.3 Dust

Dust can best be described as particulate matter which exists within the ISM, with particles ranging in size from just a few molecules across to $\sim 1\mu m$. These particles are chiefly made up of organic, carbon based molecules which can be produced in a variety of circumstances. In the high redshift Universe, it is thought that dust is mostly produced three scenarios: Asymptotic Giant Branch (AGB) stars throwing off enriched material during the final stages of their lives, supernovae casting out the metals they have created into the ISM, some of which eventually cools and accretes into dust grains [Leśniewska and Michałowski, 2019], and finally HII regions, which are often enriched even at these early times [Vijayan *et al.*, 2019].

In terms of the light that a galaxy emits, dust in the ISM has two major effects. It absorbs light in the UV-NIR portion of the spectra , and thermally re-emits this light in the far infra-red $10^2 - 10^4 \mu m$. The absorption effect preferentially affects the UV light, much more severely reducing its brightness when compared to redder wavelengths.

This absorption process has two mechanisms associated with it: extinction and attenuation. Extinction is the absorption of photons emitted from a source by the dust grains, and the scattering of photons out of the line of sight of the observer. The amount of overall extinction, and the shape of the extinction curve as a function of wavelength can vary due to a variety of effects: the geometry of the dust between source and observer, the column dust mass, and the distribution of the dust grain size can all play non-trivial roles in the extinction effect.

Attenuation refers to the more general impact of dust on a spectrum, specifically when the object is made up of many sources (e.g. a galaxy made up of many stars). Attenuation takes into account that each individual star in a galaxy has a different amount of extinction

associated with it, and these individual extinctions will have an aggregate effect on the galaxy spectrum. Secondly, the scattering of photons into the observers line of sight is considered to be a small effect when only considering a single source, but this is no longer true for the composite objects attenuation serves to model, so this is included also. The sum total of all of these effects is described by an attenuation curve. For highly star forming galaxies as will be discussed in much of this work, a common choice for this attenuation curve is Calzetti [2001], but a variety of different parametrisations for this curve exist. Discussion of their exact nature will be deferred to section 2.2.1.3.

Absorption of UV and optical light causes the dust to heat up. Each individual grain re-emits as a black body according to its temperature. The secondary effects the dust population having a range of temperatures due to its non-uniform geometry, and scattering of the re-emitted photons by subsequent interactions with other dust grains mean that the overall IR spectra differs slightly from this slightly – for that reason it is known as a grey-body [Casey, 2012]. Mathematically, a grey body is expressed as:

$$S(\nu|T) \propto (1 - e^{-\tau(\nu)})B_\nu(T) \tag{1.1}$$

where $S(\nu|T)$ is the grey-body expressed in units of erg s^{-1} cm^{-2} Hz^{-1}, or Jy. $\tau(/nu)$ is the optical depth – defined as $\log(I/P)$ with I and P being the incident and transmitted power respectively, and $B_\nu(T)$ is the traditional Planck blackbody curve, with parameter T denoting the ambient dust temperature.

1.1.2.4 The Stars

When molecular Hydrogen gas clouds exceed a certain temperature dependant density they become unstable and collapse gravitationally. Specifically, for a cloud with number density of molecular hydrogen n and sound speed c_s, when the cloud exceeds mass M_J – known as the Jeans Mass for physicist Sir James Jeans – it will begin to collapse. The equation for M_J, presented here without derivation is:

$$\mathrm{M_J} \approx 2\mathrm{M}_\odot \cdot \left(\frac{\mathrm{c_s}}{0.2\mathrm{km/s}}\right)^3 \cdot \left(\frac{\mathrm{n}}{10^3\mathrm{cm}^{-3}}\right)^{-0.5} \tag{1.2}$$

Stars do not typically form in isolation – if a large cloud of gas is sufficiently dense to collapse, it typically undergoes a process called fragmentation: as the cloud collapses it become easier and easier for sub-sections to exceed the Jeans limit independently, and thus they will begin to collapse on their own. This process leads to many smaller collapses rather than the entire cloud becoming a singular, giant collapsed object. This process is known as fragmentation and is the dominant theory for star formation on the gas cloud scale [Shu *et al.*, 1987].

The mass distribution of the stars that form via fragmentation is known as the Initial Mass Function (IMF). The IMF describes the distribution of initial stellar masses of a population of stars once they join the main sequence. The IMF is very important in the study of galaxies as even small deviations can have large effects on the overall SED due to the face that young stars contribute so much to an overall galaxies' SED. As the IMF cannot be measured directly, only inferred from evolved star clusters, the precise form of the IMF (or for that matter, whether it even has a single, universal form) remains somewhat uncertain and an critical assumption to be made when modelling the light from stellar populations [Lee *et al.*, 2020].

The simplest parametric form of the IMF is a single power-law,

$$\xi(M) = \frac{\mathrm{dn}}{\mathrm{dM}} \propto \mathrm{M}^\alpha \tag{1.3}$$

where n is the relative number density of stars as a function of their mass M, and $\alpha \approx -2.35$ is the power law slope parameter [e.g. Massey *et al.*, 1995]. This is known as the Salpeter IMF Salpeter [1955], and for the stars that were measured in that work ($M_* > 1\ M_\odot$) this has remained largely unchanged.

This simple parameterisation presents an obvious problem however, that at small, sub-stellar ($M <\sim 0.018 M_\odot$) masses the number of objects becomes incredibly large, requiring

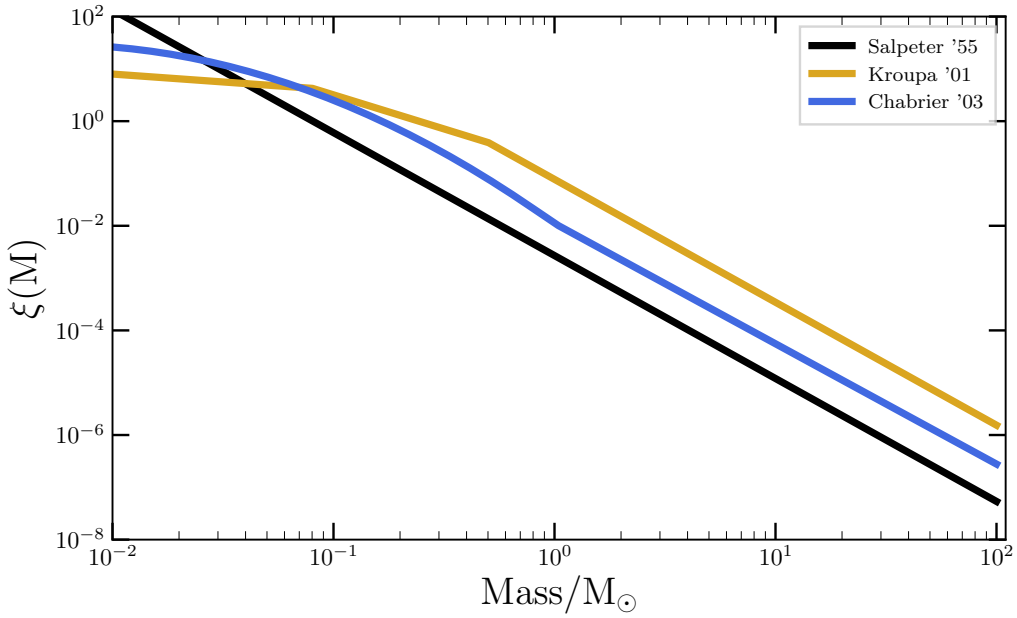

Figure 1.3: Examples of Initial mass functions. Black solid line is a simple power law – often known as the Salpeter IMF [Salpeter, 1955] . Yellow solid line is a broken power law at 0.1 and $0.4M_\odot$ to account for the number density of sub-stellar objects. Blue solid line is the Chabrier IMF – a smoothing of this broken power law into a turnover beginning at $1M_\odot$ [Chabrier, 2003].

some arbitrary cutoff. Even with a well placed cutoff, the numbers of low mass objects is over-predicted compared to measurements of the low mass end of the luminosity functions of local star clusters [e.g. Blaha and Humphreys, 1989].

Common low-mass corrections include broken, shallower power laws or smooth turnovers at low mass [Kroupa, 2001; Chabrier, 2003]. It is natural for IMFs of all forms to be cutoff at $\sim 0.018M_\odot$ as below this mass, pressure in the protostellar core is insufficient to initiate fusion, which can be taken as a definition of a star. These sub-fusion masses are known as Brown dwarfs, and while it follows that they dominate in terms of numbers, their low masses and luminosities mean they do not meaningfully contribute to the galaxies luminous output.

While galactic measurements suggest that within the galaxy the IMF is likely spatially universal [Hopkins, 2018] there are suggestive measurements of the wider Universe that

the IMF can vary from galaxy to galaxy. This variation could be proportional to the star formation rate [Gunawardhana *et al.*, 2011; Zhang *et al.*, 2018], although any statements made about the IMF are naturally tentative as it is very difficult to isolate from other physical properties of galaxies.

Stellar Life Cycle After a population of stars have formed from a dense molecular cloud they join the stellar main sequence, where they are relatively stable – the force of gravity trying to collapse the material pushing against the radiation pressure emanating from the Hydrogen fusion in the core.

The defining features of a star on the main sequence can be largely inferred from just their mass and the metallicity of the gas they have formed from. As mass increases, the pressure in the core, and thus its temperature increases. The nuclear reactions that drive a star are very sensitive to temperature, so even a small mass (and thus temperature) increase leads to much faster reaction rates, and therefore plenty more radiation being produced. This relation is commonly quoted as

$$\left(\frac{L}{L_\odot}\right) \approx \left(\frac{M}{M_\odot}\right)^\alpha \tag{1.4}$$

where α can vary between 1 and 6. For example – for main sequence stars between $0.43\mathrm{M}_\odot$ and $2\mathrm{M}_\odot$, $\alpha \approx 4$ and more massive stars between $2\mathrm{M}_\odot$ and $55\mathrm{M}_\odot$ have $\alpha \approx 3.5$. Similarly, one can also observe a tight relation between the luminosity of a star, and its colour. As the core temperature increases due to the pressure, the surface temperature also increases, meaning that the black body emission from the surface becomes bluer and bluer. This relation is known as the Hertzprung-Russel relation and is well documented in the literature.

While going into the details of the stellar physics is beyond the scope of this thesis, it is crucial for the modelling of galaxies to understand that for fixed metallicity, stars of higher mass are rare, but they dominate in terms of the light produced. These high mass stars also burn through their Hydrogen much faster, so even though they start with more fuel, they

have much shorter lifetimes, approximately:

$$t_{\text{lifetime}} \sim \left(\frac{M}{M_{\odot}}\right)^{2.5} \cdot 10\text{Gyrs}. \tag{1.5}$$

In summary, simple stellar populations on the main sequence are dominated in number and mass by low-mass stars, but by luminosity the rare high-mass stars are the dominant force. As these populations age, the stars die off effectively in order of decreasing mass, leaving behind a much less luminous, redder population. This knowledge is a vital part of galaxy evolution, as the presence or absence of young, blue, high-mass stars can tell us much about the recent star formation activity of a galaxy. This will be explored in exhaustive detail in later sections 1.5.1.1, 2.2.1.1, and 4.6.

Remnants Stars eventually use up their available hydrogen. When they do a variety of things can happen depending on their mass. Lower mass stars $M <\sim 10M_{\odot}$ will ultimately form white dwarfs. These are effectively the exposed stellar core of a star, largely composed matter which has become electron degenerate – the electrons are forced to occupy all of the available energy levels, and the Pauli exclusion principle prevents them from being compressed any more. This degeneracy pressure prevents the star from collapsing further, but also means that no thermal energy can be extracted from the material. White dwarfs have a theoretical upper mass limit, beyond which electron degeneracy will be overcome by the self gravitation. This mass limit is $\sim 1.4M_{\odot}$ and is known as the Chandrasekhar limit. Sub-Chandrasekhar white dwarfs can accrete matter from a companion star and exceed this limit, causing a type Ia supernovae.

Neutron stars are similar objects – remnants of stars which are no longer powered by fusion, they are a balance of gravitation and neutron degeneracy pressure. However, their progenitor stars are of higher mass, $10M_{\odot} < M <\sim 30M_{\odot}$. The extra mass means that the remnant left behind as the star dies will exceed the Chandrasekhar limit, and will overcome electron degeneracy pressure. This causes the protons to undergo inverse beta decay with the degenerate electrons, the result being effectively an object made entirely of neutrons. As

they are composed entirely of nuclear material, neutron stars are incredibly dense – a $1M_{\odot}$ neutron star would have a radius of around $10km$. They also have extremely large magnetic field strengths and rotation speeds, owing to the angular momentum conservation between the large progenitor star and the small radius remnant. Analogously to white dwarfs, neutron stars have an upper limit of $\sim 2.3M_{\odot}$, above which neutron degeneracy pressure cannot support them, in fact, nothing can – they will collapse to a singularity: a black hole [Iben and Renzini, 1983].

For the purposes of this thesis, we must consider that remnants contribute mass to older stellar populations – in the case of the more common white dwarf, this can actually be a significant fraction of the mass. However they contribute very little in terms of light, white dwarfs emit thermally, but it is not particularly significant all but the oldest stellar populations [Eldridge *et al.*, 2017a]. To neglect the contribution of remnants would cause systematic underestimations of the stellar masses of galaxies.

1.1.2.5 Black Holes

Black holes can be defined in a variety of ways, however for our purposes we will define them as an astrophysical object so dense that nothing (including EM radiation) can escape from its surface.

Black holes can largely be divided into two types – Astrophysical black holes, which form throughout the Universe's history during the death of massive stars; and Supermassive black holes (SMBHs), which form at the center of galaxies, whose formation mechanisms remains unclear.

Stellar Mass Black Holes When a star of sufficient mass goes supernovae and leaves behind a remnant with , that remnant is either supported by electron degeneracy pressure or neutron degeneracy pressure. If the mass of the original star is large enough, the remnant left behind will be too massive ($M_{rem} > 2.3M_{\odot}$) to be supported by either of these forces, and with nothing else to support the material, it will collapse freely to a

singularity. Astrophysical black holes are formed relatively rarely – only around 0.004% of stars are above $15M_{\odot}$ i.e. large enough to form remnants that will collapse into black holes. Astrophysical black holes typically range in mass from the lower limit at around $2-3M_{\odot}$, potentially up to as much as $45M_{\odot}$, for stars with extremely low metallicities and high masses ($130-250M_{\odot}$) [Farmer *et al.*, 2019].

Super Massive Black Holes Super-massive black holes on the other hand, although are similar in terms of their structure, are entirely different in both scale formation mechanism. Super-massive black holes are thought to have either formed via the rapid hierarchical merger of astrophysical black holes after the formation of the first stars, or from direct collapse of HI clouds around the end of the dark ages/beginning of the EoR via processes that prevent the fragmentation of said clouds into a population of stars.

In addition to growing through mergers super-massive black holes can grow by accreting surrounding material – if this rate of accretion is high enough, the black hole is known as an active galactic nucleus (AGN). This is often enough to heat the surrounding gas stopping it from stars, effectively quenching the galaxy. Super-massive black holes then play an important part in regulating the growth of galaxies, particularly those that are very massive. Active super-massive black holes regularly outshine their host galaxies' stellar content and are amongst the most luminous objects in the Universe, easily observable to the highest redshifts.

1.1.3 Galaxies

Galaxies can be thought of effectively as a summation of all of these parts. Working from the outside in, we will briefly outline the general structure of a galaxy.

The outermost part is the dark matter halo. In an isolated galaxy these are approximately spherically symmetric mass distributions, which is commonly parametrised as the so-called NFW profile [Navarro *et al.*, 1996]. These halos are typically $\sim$ 1000 times the mass of the galaxy they host. The dark matter halo serves to funnel baryonic matter into the centre,

where it will take the various forms HI, molecular clouds, dust etc. and will also form stars, producing HII regions.

Finally at the galaxies core, lies a super-massive black hole (SMBH), which typically has mass $M_{BH} \sim 10^{-3} M_{gal}$ where M_{gal} is the mass of the host galaxy [Magorrian *et al.*, 1998].

1.1.4 The Radiation

In addition to baryonic and dark matter components, the Universe contains radiation from a wide variety of sources. Radiation of all types permeates intergalactic space in varying energy densities, and is sourced from both baryonic processes over the lifetime of the Universe, and primordial photons.

The dominant component of the intergalctic radiation is the Cosmic Microwave Background (CMB). This is relic radiation from the big bang, emerging from recombination and the decoupling of photons from baryonic matter. Since its discovery in the 1960's [Penzias and Wilson, 1965] it has been found that the CMB encodes a wealth of information [Tegmark *et al.*, 2004; Planck Collaboration *et al.*, 2014, e.g.], spurring on one of the most fertile grounds for observational cosmology of the past 50 years.

In addition, baryonic processes at any point in the Universes history produce more radiation. For example the cosmic UV, optical and IR backgrounds are mostly produced by starlight, with contributions from AGN and dust/gas re-emission [Martin *et al.*, 1991; Lauer *et al.*, 2020; Hauser, 2001]. Higher energy background radiation is produced by the hot gas found in within galaxy clusters between the galaxies, and through material falling into black holes (both regular and super-massive) via accretion, however the background levels of these are extremely low, punctuated by higher flux sources throughout the sky.

1.2 Cosmology: From the Big Bang to the Formation of the First Stars

While section 1.1 addressed the structure of the Universe in terms of its contents, this section will describe how these constituents evolved chronologically. The favoured model of how the Universe evolves in time is Lambda Cold Dark Matter (ΛCDM) [Peebles, 1984]. This is a model of the Universe which contains Baryonic matter in its various forms, Cold Dark Matter – i.e. dark matter which allows formation of structure hierarchically, and a positive cosmological constant – the Universe is expanding, and that expansion is accelerating. ΛCDM parameters are constrained by measurements of the large scale structure in the local Universe, and measurements of the CMB at redshift $z \sim 1100$ [Tegmark *et al.*, 2004; Planck Collaboration *et al.*, 2016a] and other probes.

1.2.1 The Early Universe

At some small time after the Big Bang, the Universe can be simply described as incredibly hot, dense, and almost uniform. This uniformity is not however, perfect: it contains fluctuations of size around 1 part in 10^{-5} due to the quantum vacuum energy. At around 10^{-36} seconds after the Big Bang, these fluctuations are blown apart by inflation, with the Universe expanding by a factor of around 10^{26} almost instantaneously. Inflation pushed these fluctuations out of each others causation horizons, freezing them in place [Guth, 1981; Liddle and Lyth, 2000].

As time goes on, these fluctuations became more and more extreme: under-densities expand faster, becoming more and more under-dense; over-densities expand more slowly due to the additional material present, eventually "turning around" and collapsing into halos which will eventually go on to be the sites of star formation and galaxies.

At these early times, the energy budget of the infant Universe was almost entirely photons. After 10 seconds have passed, electrons, protons, and neutrons have formed and begin to form nuclei, but were unable to form into atoms due to the intense pressure and

heat. As the Universe expanded and cooled more, the nucleons could combine into ions, fixing the initial conditions for the Universes chemistry [Coc and Vangioni, 2017].

It then took some 370000 years for the Universe to be sufficiently cooled for these ions to hold on to electrons. This process is known as recombination, and marks two major changes. Firstly the Universe became populated by neutral atoms, rather than ionised gas. Secondly, the photons now decouple from the baryonic matter, freely streaming throughout the now almost transparent Universe. Cosmic expansion has redshifted these photons, from the high energies of the early Universe ($z \sim 1100$, $T \sim 3000K$) down to today, where they make up a blackbody with $T = 2.73K$: the Cosmic Microwave Background (CMB) [Penzias and Wilson, 1965; Dicke *et al.*, 1965].

The CMB is important because it is the furthest back in time it is possible to directly observe – anything that happened prior to this can only be inferred by its imprint on the CMB. This phase transition from an opaque Universe to a transparent one marked a huge change in the composition of the Universe.

1.2.2 The Dark Ages

Post recombination the Universe largely contains neutral Hydrogen, photons which are now not energetic enough to ionise said Hydrogen, dark matter, and dark energy. This period is known as the dark ages, as the only photons streaming through the Universe are largely low energy, rapidly redshifting through the infrared. The gravitational instabilities continue to grow, forming more and more dark matter structures. So goes the dark matter, so goes the Baryonic material: the Baryons are able to cool down via electromagnetic processes, enabling them to lose energy and fall to the center of the budding dark matter halos, rather than being distributed throughout.

Our options for observing the dark ages are very limited, however nature fortunately provides us with an option. In a neutral Hydrogen atom, the electrons and the protons dipole moments can be oriented in two possible ways: aligned ($F = 1$, excited state), or anti-aligned ($F = -1$, ground state). The energy difference between these two states is

small, but vitally it is non-zero, corresponding to a frequency of 1420MHz, or wavelength of 21cm. This signal was observationally discovered in 1951, and was quickly used to map the Milky Way's spiral structure [Muller and Oort, 1951].

This transition is highly forbidden – the mean lifetime of the excited state is around 10^7 years, which means that only immense amounts of neutral Hydrogen can produce a detectable signal. It is to our benefit that these are precisely the conditions found in the dark aged Universe. In more recent years, powerful radio telescopes such as LOFAR have begun the task of mapping the presence of neutral hydrogen during the dark ages [e.g Patil *et al.*, 2017]. After around 500 million years, the baryonic matter at the center of clouds has had enough time to congeal enough to form the first stars: a new source of short wavelength photons. Thus ends the dark ages of the Universe, and the beginning of the Epoch of Reionisation.

1.2.3 First Light and The Epoch of Reionisation

The dark ages are brought to an end with with the ignition of the first stars. At this time, the Universes baryonic stockpile is almost entirely neutral. Ionizing radiation emanating from these primordial star clusters begins to ionise the gas in their immediate surroundings.

At the time the first star formed, the entire Universe was filled with neutral, virtually metal-free gas containing only the products of Big Bang Neucleosynthesis (Hydrogen, Helium, and traces of Lithium-7) [Kawasaki *et al.*, 2005]. Those initial stars which formed from this primordial Hydrogen were thus similarly metal free – known as Population III stars.

This thesis will focus on galaxies within the Epoch of Reionisation (EoR). The EoR is bracketed by two important events: the collapsing of pristine hydrogen clouds into stars and galaxies, and the phase transition of the Intergalactic Medium from neutral Hydrogen - opaque to UV photons, to ionized gas which allowed these photons to stream freely throughout the Universe.

The beginning of reionisation is not well constrained. The beginning of the EoR

corresponds to the ignition of the first stars, which have not been directly observed as of the present. Constraints exist based on the cosmic star formation relations [e.g. Madau and Dickinson, 2014], but as data simply doesn't exist at early enough times, the process of initial star formation – and therefore reionisation – is unknown.

Two scenarios (along with a sliding scale between them) exist for the beginning. Firstly, young massive stars contribute most ionizing photons, which means the EoR must have started much sooner, and more slowly built up.

Alternatively, large rare objects such as quasars can also produce ionizing photos, and if they are the dominant source of said photons, the EoR can start much later - more like z $\sim$ 10 [Madau and Haardt, 2015].

On the other hand how reionisation progresses from the halfway point is fairly well understood. The Planck Collaboration's constraints on electron optical depth place the midpoint (50% of the IGM being ionized) of the EoR being at around $z = 8$ [Planck Collaboration *et al.*, 2016b].

The end of reionisation on the other hand is also difficult to measure, as the process is quasi-asymptotic towards the end. Clouds of neutral Hydrogen which are the most distant from ionising sources (i.e. galaxies) can persist potentially up to as late as $z \sim 4$ [Finkelstein, 2012], but their low 21cm flux at this stage means they are very hard to detect. One could argue that the end of the EoR being defined as when the last cloud in the IGM becomes ionised is largely academic, but it nevertheless remains a useful constraint for cosmological simulations at intermediate redshift [e.g. Feng *et al.*, 2016b].

Study of this period is a vital part of the universal star formation picture because even small changes in the initial conditions of star formation can have large consequences for how the Universe's constituents subsequently evolved to the present day.

In addition, other than the trace amounts of Lithium created during nucleosynthesis, the EoR is the beginning of the elemental enrichment of the Universe, as just like "standard" core collapse supernovae, the deaths of the first stars produced all the chemical elements in varying quantities. These very first stars – population III stars – are thought to be metal free,

and potentially extremely massive and therefore short lived [Tominaga *et al.*, 2007, e.g]. With the destruction of these stars through supernovae, we also see the first (non-primordial) black hole formation, which seed the production of the super-massive black holes we see evidence of in even the earliest observed galaxies.

1.2.4 The Ionised Universe

After $z \sim 6$, once the IGM is fully reionised, star formation continues to increase until around redshift 2. Figure 1.4, charts the history of the rate of star formation over cosmic time. As mentioned previously: in the EoR while there is plentiful material to construct stars, it has not had time to properly coalesce into the dark matter halos that host galaxies, and therefore while star formation in individual galaxies is very high, they are relatively rare and thus the overall density is low. As time goes on this increases more and more, as both the number density of galaxies and their star formation both get higher and higher.

Around $z \sim 2$, so-called cosmic noon, star formation is at its most intense, however it begins to decline as cold dense gas becomes less plentiful.

As can be seen in figure 1.4, from $0 < z < 4$ the cosmic star formation rate density is is well constrained by a variety of observations, with a combination of rest frame Optical, UV and far infrared observations. However at high redshift, the rest frame optical has been largely inaccessible, as has the FIR. This lessens the strength of constraints there as only unobscured star formation can be properly characterised (stellar mass and dust-obscured star formation being highly model dependant and degenerate with other parameters without that data). Additionally, due to the distances involved, UV selected samples of galaxies at high redshift likely select against dusty objects, as their UV will be pushed below detection limits. Similarly it is thought (e.g. Finkelstein *et al.* [2012], Dunlop *et al.* [2013]) that a significant amount of star formation at these early times takes place in sub L^* galaxies, the number density of which is extremely hard to constrain – the slope of the luminosity function beyond the knee can have a huge impact on the overall cosmic star formation density . One of the largest motivations for ever more powerful telescopes in EoR science is to construct

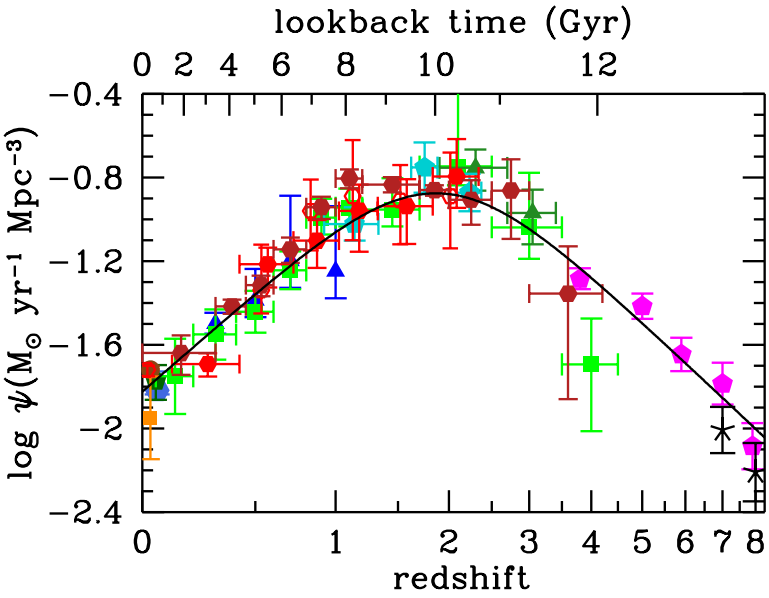

Figure 1.4: The cosmic star formation density (CSFd) as a function of redshift, as presented in Madau and Dickinson [2014]. Purple, green and blue points are star formation rates derived from rest frame UV luminosities. Red and orange points are from FIR luminosities. Both use a Salpeter IMF. Solid line represents a best fit double power law.

a more complete luminosity function [McLure *et al.*, 2013; Coe *et al.*, 2013; Ellis *et al.*, 2013], which would offer a much less biased picture of stars in the early Universe.

It should however be noted that although these $z > 4$ measurements possess a myriad of challenges, and still have large statistical and systematic uncertainties, they have relatively little impact on the global total star formation of the Universe. Only 1% of the stellar content of the Universe present in the modern day was formed at $z > 6$. These measurements will have a vital impact on the reionisation history of the Universe, but not so much on the budget of stars.

1.3 Observing the Distant Universe

Galaxies in the distant Universe are challenging to observe for a myriad of reasons, however if these challenges can be overcome, there is ample opportunity to push at the frontiers of our knowledge. These galaxies are difficult to observe because not only are they at very large distances from the Earth, but also – relative to present day galaxies – they have not had the time to build up a large reservoir of stars, so while they might be bright objects in the rest-UV thanks to their massive stars, the population are fainter in the rest optical & near IR.

Cosmological redshift also serves to increase the degree of difficulty. Their rest frame UV and optical emission is shifted into the near-IR. While some of the near-IR is observable from the ground ($< 2\mu m$), much of the longer wavelength emission is absorbed by the atmosphere. In addition, as the atmosphere is so problematic in this regime, the capability of instrumentation is much less mature. For galaxies $z \sim 7$ and above, the rest frame optical and near-IR are entirely inaccessible from ground based observatories, limiting the information we can glean from these objects. The alternative of course, is space based observatories. While this is an ideal solution, they are notoriously expensive both in terms of time and money, and thus their observing time is at a premium.

1.3.1 The Astronomer's Arsenal

As noted previously, the EoR and the galaxies which exist within are one of the frontiers of our understand of how the Universe has evolved. Observations of this period rely on many of the most advanced astronomical facilities ever built. This section will present a brief overview of the telescopes most commonly used for this purpose, and the vital service they provide to understanding the EoR.

The instruments can largely be divided into three categories, with individual telescopes often containing cameras covering two or even all three categories. Those categories are photometry or imaging, spectroscopy, and Integrated Field Units (IFUs). Photometry is the most simple – light incident on the telescope is focused onto a CCD, which can be thought of as a grid of collectors. Each photon generates charge which allows it to be recorded, producing an image. Usually instruments have one or more filters, allowing the observer to restrict the wavelength range of photons which are recorded. By taking multiple images in this way, a rough approximation of the shape of the SED can be built up, and physical parameters extracted by modelling the underlying SED. Photometry offers the advantage of being able to probe the faintest objects by collecting together light over a wide range of wavelengths. For the same reason, it is also very efficient in terms of observation time – it will always offer the shortest exposure times of the three methods.

Traditional spectroscopy in some ways offers the opposite approach – rather than retrieving spatial information but little wavelength resolution, traditional spectroscopy involves dispersing the integrated light of an object (either by laying a long slit over the object, or using an optical fibre to collect the light). This results in high wavelength resolution (often measured by $R = \lambda/\Delta\lambda$) but the light is averaged either over an aperture or the axis of the long slit. In extragalactic astronomy, spectroscopy is the gold standard for data on an object, as it can offer insight into the starlight via continuum emission, but more subtle aspects of the SED than its general shape such as line emission. Prime examples of this would be dust content (which can be measured much more accurately using relative emission line heights)

or metallicity. Section 3.3 explores the measurement of physical parameters in this way, and would be impossible without spectroscopy.

Early spectrographs could be used to observe only a single galaxy, or even, only part of a galaxy, using a single slit. In doing so they often "threw away" much of the light actually falling on the telescope making spectroscopic observations much more time intensive than imaging. This significant reduction in aperture size combined with the narrow wavelength binning both contribute to the time intensiveness.

Two evolutions of single-slit spectrographs exist. The simplest is multi-slit spectrographs. These take the principles of single slit spectroscopy, and lay down multiple long slits over different objects in a single field of view. While this can be effective, one must be very careful with the geometry of the objects and the orientation of the slits – as they are physically dispersing the light on the focal plane they dispersal patterns can easily overlap. The second evolution, which takes care of this problem is fibre fed instruments. Essentially, fibres are placed (either manually or robotically) at positions across the focal plane corresponding to objects of interest. These fibres are then fed to separate dispersal mechanisms, sidestepping the overlap issue entirely. Multi-object spectrographs (MOSs) are able to observe 10-1000s of galaxies simultaneously, dramatically improving their survey efficiency. For example, the 2 degree Field (2dF) facility on the Anglo-Australian Telescope (AAT) was able to observe 400 galaxies simultaneously over a two degree field. The Dark Energy Spectroscopic Instrument (DESI) which recently (2019) had first light is able to observe up to 5000 galaxies simultaneously.

The ultimate evolution of MOS systems are Integral Field Units (IFUs). These can be thought of as a combination of imaging and spectroscopy. These devices take an image of the object, but each pixel of the image is attached by optical fibre to a spectrograph. This offers all the advantages of both imaging and traditional spectroscopy, and enables new science to be done involving the spatial distribution of emission line flux in a galaxy. For example, IFUs have enable the detailed study of galactic rotation curves by mapping the redshift of emission lines across the galaxies disk. One example of a modern IFU is the

multi-unit spectroscopic explorer (MUSE) on the Very Large Telescope. In its wide-field mode MUSE is able to observe a 1 arcmin^2 field with 90,000 individual spectral elements. It is however worth noting that modern IFUs are not yet a replacement for fibre-fed MOS systems due to their small field of views. Examples include MaNGA, responsible for IFU data in the Sloan Digital Sky Survey [Bundy *et al.*, 2015] and CALIFA, a project focusing on using an IFU to map the the state and evolution of 600 nearby galaxies Sánchez *et al.* [2012].

A final variation worth mentioning, which is particularly important for *Hubble* and *Webb*, is slit-less spectroscopy, often referred to as Wide Field Slitless Spectroscopy (WFSS), which combines elements of imaging and spectroscopy. WFSS works by adding a grism to a traditional imaging camera. The grism diffracts the light producing a spectrum of each object on detector. The chief advantage is that WFSS can easily be added to existing cameras by either adding a second filter wheel containing the grisms or simply replacing a filter by a grism+filter combination. This is particularly important where space is at a premium, such in the space observatories like *Hubble* and *Webb* where a long arm of a spectrograph would have logistical challenges. A second advantage is that WFSS systems yield spectra of all objects in the field providing excellent completeness. The downside is that the resulting spectra from objects often overlap both leading to confusion and a significantly higher background limiting the sensitivity.

1.3.1.1 Hubble Space Telescope

For the past 30 years, the *Hubble Space Telescope (HST)* has been the flagship UV, optical and near-IR ($< 1.7\mu m$) space based observatory. HST is effectively a 2.4m reflector telescope optimised for imaging, grisms and spectroscopy. The main instruments for EoR science are the Advanced Camera for Surveys, and Wide Field Camera 3 (WFC3). WFC3 has a wide variety of filters and grisms for observations in the optical and near-IR. It has a field of view of 164" $\times$ 164", with 40mas pixels. ACS offers similar capabilities: a 202" $\times$ 202" field of view with 50mas pixels.

HST has produced a series of deep imaging campaigns which have revolutionised our understanding of how the Universe has evolved. The Hubble Deep Field (HDF), Hubble Ultra Deep Field (HUDF) and Hubble eXtreme Deep Field (XDF), and CANDELS, each have the same philosophy or observing an area around 2 arc-minutes square for as long as possible, in 9 bands, with the aim of finding the faintest objects. [Williams *et al.*, 1996; Beckwith *et al.*, 2006; Illingworth *et al.*, 2013; Grogin *et al.*, 2011, respectively]

A novel approach used in the Hubble Frontier Fields (HFF) [Lotz *et al.*, 2017] has been to point HST at six low redshift galaxy clusters, using them to lens background objects. This has the advantage of finding even fainter objects due to them being magnified, however at the cost of vital morphological information, as the lensing models are quite uncertain.

1.3.1.2 Spitzer Space Telescope

The Spitzer Space telescope had a 16 year career stretching from 2003 to 2020. It is a near to mid-infrared space telescope. At just 0.8m in diameter Spitzer lacked sensitivity and angular resolution, but for its lifespan was unique in its above-the-atmosphere wavelength coverage. The initial mission was slated to last 2.5 years, and after 6 years, Spitzer ran out of liquid helium coolant. This left the longer wavelength channels unusable because the thermal noise from the telescope itself overwhelmed any observations. Most of the high redshift science carried out by Spitzer is thus based on the two shortest wavelength channels: IRAC 1 ($\sim 3.6\mu m$) and IRAC 2 ($\sim 4.5\mu m$). These channels served as a perfect complement to HST, providing access to the rest frame optical of bright high-redshift objects.

However, after the cryogen ran out, Spitzer also was producing valuable data taking long exposures in its shortest wavelength $3.4\mu m$ and $4.5\mu m$ channels. For example deep imaging of the CANDELS/GOODS-N field has revealed candidates potentially at $z \sim 11$ [Oesch *et al.*, 2016]. Spitzer detections of objects even just in the two IRAC channels available are important because at at these extreme redshifts the rest frame optical is being probed, allowing estimates of stellar masses.

1.3.1.3 VISTA

The Visible and Infrared Survey Telescope for Astronomy (VISTA) is a 4.1m telescope at the Paranal Observatory. The VISTA telescope has just one instrument – VIRCAM, which is entirely focused on carrying out large area surveys of the sky in the near infrared. VIRCAM is sensitive between 0.85 and $2.3\mu m$, and has a large field of view ($\sim 3deg^2$).

In the context of EoR science, VISTA is well placed to find rare, bright high redshift candidates as it probes a huge cosmological volume with each pointing [e.g. Findlay *et al.*, 2012].

1.3.1.4 VLT, Keck and Subaru

The Very Large Telescope is an array of four 8m optical telescopes, which can be used both separately – achieving an angular resolution of 50mas, or together as an interferometer, giving unprecedented angular resolution: around 2mas [Le Fèvre *et al.*, 2005]. The VLT is one of the workhorses of modern astronomy, conducting imaging, spectroscopy, single object, multi object and integral field spectroscopy. VLT lacks the sensitivity to directly observe most EoR galaxies, however it has managed to detect Ly-α emission lines in some of the brightest sources at high redshift ($z > 6$) [Wisotzki *et al.*, 2016].VLT is also ideally placed to study analogues – galaxies with similar properties to the typical EoR galaxy, but residing at much lower redshift. In section 3.5, the X-Shooter single object spectrograph is used to analyse a sample of these galaxies. It is well placed to do this as it is a very wide band spectrograph (from $\sim$ 4000Å – 17000Å) which is designed with unusual objects such as these in mind.

The W. M. Keck observatory (Keck) is another 8m class telescope array, which has a pair of telescopes operating across the optical and near infrared sporting a variety of instruments for imaging, single/multi object spectroscopy and integral field units. Keck is one of the most sensitive instruments in the world, and one of the few ground based telescopes capable of detecting high redshift galaxies. It is primarily used to provide

spectroscopy of these objects at $\lambda < 2\mu m$, which at the redshifts of EoR galaxies provides access to Lyman-α [Larson *et al.*, 2020], along with a select few metal lines such as [CIII] and [CIV]. These observations are extremely useful for confirming the redshfits of objects found via photometry, photometric observations are always vulnerable to artefacts and low redshift interlopers. [CIII] detections – for example as found in Stark *et al.* [2017] – also provide information about the gas: both its metallicity and the strength of the radiation field it is exposed to.

Subaru is a very similar observatory to Keck, an 8.2m telescope which operates in the optical and infrared. It is an instrument that – like Keck – is optimized for followup of high redshift candidates, taking spectroscopy of Lyman-α and the rest frame UV metal lines.

1.3.1.5 ALMA

The Atacama Large Millimeter/submillimeter Array is a radio interferometer which came online in 2004. It operates in the wavelength range $320\mu m$ to $3600\mu m$. It offers unparalleled sensitivity and angular resolution in this wavelength range, however this is at the cost of having a small field of view.

ALMA is used to characterise the dust content of EoR galaxies. The peak of dust emission at temperatures consistent with modelling (10-60 K) [Casey *et al.*, 2014] are redshifted into the ALMA bands. Ideally one would conduct observations in as many bands as possible to get data on either side of the peak, constraining the temperature, however ALMA is notoriously competitive to get time on, so many observations are in 1 or 2 bands, with dust temperatures fixed at some assumed value. Combining ALMA observations with rest frame UV observations from telescopes such as Hubble or Keck can give more unbiased estimates of their star formation rates, and thus the stellar assembly of the Universe.

1.3.1.6 Future Observatories: Euclid, Roman, Rubin, and the ELTs

The core of this work is to focus on making predictions of what future observatories are going to see, and using these predictions to optimise tools to accompany the observations.

Euclid Euclid is a space telescope with a mirror diameter of 1.2m which is set to launch in 2022. It will focus on observations in the near IR ($0.6\mu m - 2/mum$). Euclid will provide both photometry and spectroscopy, focusing on objects above $z = 2$. Euclid's stated science goal is to survey many ($/sim10^6 M_\odot$) galaxies, for research into dark energy, Baryon Acoustic Oscillations and gravitational lensing. However more fundamentally, Euclid will provide huge samples of galaxies to characterise the luminosity function at mid to high redshift ($z \sim 2 - 8$). As discussed earlier, understanding the evolution of the luminosity function is vital to understanding the overall construction of stellar populations in the Universe.

Roman The Nancy Grace Roman Space Telescope (Roman), formerly the Wide Field InfraRed Survey Telescope (WFIRST), has similar operational statistics to HST, with a 2.8m mirror and operating across the optical and near-IR. It is set to launch in 2025. Roman will however have updated instruments compared to Hubble, the main confirmed one being a wide-field instrument with resolution comparable to Hubble but with a $0.28 deg^2$ field of view. This telescope is ideally outfitted to carry out surveys deep into the Universes past, finding more of the relatively rare super-$L^\star$ objects at high redshift, whose number counts are vital to characterising the bright end of the EoR luminosity function.

Extremely Large Telescopes The European Southern Observatory's Extremely Large Telescope (ELT) is a ground based observatory under construction in Chile, close to the Paranal observatory and the VLT. The ELT has a 39m primary mirror, supported by adaptive optics and laser guide stars in order crate an unprecedented level of flux sensitivity and angular and spectral resolution. Instruments will operate from the optical into the mid-infrared, and will provide imagine, object and integral field spectroscopy with incredible – although weather dependant – angular resolution, up to 5mas in ideal conditions. The ELTs extremely small field of view (10 arc-minutes across) but exquisite sensitivity and resolution make the ideal complement for Euclid, Roman, and other wide field survey telescopes [Gilmozzi and Spyromilio, 2007]. In addition to the ELT two other ELT-class telescopes

are under development: the Thirty Metre Telescope and Giant Magellan Telescope offering similar, capabilities.

1.3.1.7 Future Observatory: James Webb Space Telescope

The James Webb Space Telescope (JWST, Webb) is a next generation flagship space telescope, set to launch in December 2021. It will have many varied science goals, but one of the major ones is characterising the assembly of galaxies in the first billion years. Webb will carry out similar observations in scope to the Hubble Space telescope – it has a comparably sized ($2.2' \times 4.4'$ in the case of NIRCam) field of view, with significantly improved angular resolution at fixed wavelength. In addition, thanks to a 6.5m diameter mirror it will offer improved sensitivity by a factor of 10.

Webb has four instruments, NIRCam, NIRSpec, NIRISS, and MIRI, all of which will make a contribution to EoR science. NIRCam is a wide field near infrared camera, operating from $0.6\mu m$ to $5\mu m$, and will be the primary imaging camera aboard the telescope. It offers significant optimisations to maximise observation time, for example a splitter prism separates light at $2.5\mu m$, which can then pass through two separate filters to detectors, effectively doubling imaging efficiency. NIRCam also a WFSS capability allowing it to obtain low-resolution near-IR spectra of sources, albeit with lower sensitivity. NIRISS is similar to NIRCam but with a focus on the shortest wavelengths $< 2.5\mu$m and a stronger emphasis on WFSS. NIRSpec has the same spectral coverage as NIRCam, but offers medium to high resolution (R $\sim$ 100 - 2700) multi object spectroscopy. To do this NIRSpec employs an array of microshutters, which can be independently opened and closed depending on target positioning. In addition, NIRSpec sports an IFU 3" $\times$ 3" in area with 900 spatial elements, each 100mas in size. Finally MIRI offers longer wavelength ($5\mu m$ to $28\mu m$) imaging and integral field spectroscopy with R $\sim$ 3000. While providing significantly lower sensitivity than the other instruments MIRI provides the opportunity for rest-frame optical imaging of $z > 8$ galaxies for the first time.

Webb will offer improvements over existing observatories in almost very aspect of

observing EoR galaxies. The improved sensitivity at longer wavelengths over e.g. Spitzer will allow both detections of bright galaxies with redshifts of greater than 10, and also at lower redshifts, allow progress down the faint end slope of the luminosity function, exploring the contribution to from these fainter, lower mass galaxies to the timeline of reionisation.

For EoR galaxies, Webb will offer improved sensitivity, allowing detections of even higher redshift galaxies than currently known. Pushing further back into the EoR will go further to completing the picture of early star formation in the Universe. Another angle of attack provided by Webb will be a push into the rest frame optical of EoR galaxies. Previously, the most powerful observatory offering photometry in the micron range was Spitzers IRAC channels. Often a galaxy detected in Hubble's J and H bands ($z > 7$) would not be supported by these rest frame optical observations (which are redshifted beyond Hubble's IR wavelength coverage), only giving us data on the rest-UV – we can tell how many stars are currently forming, but have very little information on the reservoir of stars already built up.

1.3.2 Measuring the Physical Properties of Distant Galaxies

Observing high redshift galaxies is challenging for three reasons, all of which compound each other. Firstly, these galaxies are often intrinsically faint in the optical as they have not had the time to build up the large amounts of stellar mass we see in galaxies in the contemporary Universe. Secondly, these galaxies are found at extreme distances, further reducing their apparent brightness via the inverse square law. Finally the surface brightness of objects drops off rapidly with redshift - $\propto (1 + z)^{-}4$ - due to the Universe's expansion, a result which is almost independent of chosen cosmology [Hogg, 1999].

Further frustrating efforts, the redshift moves most of the stellar emission from the UV and optical into the near infrared. This radiation is much less able to penetrate the Earth's atmosphere, even further reducing the brightness, and severely limited the number of telescopes able to detect them from the ground. The obvious alternative is space

telescopes, but coverage of the near IR from space is patchy (awaiting the launch of Webb) so assembling large samples is extremely difficult. Fortunately, there are various techniques we can exploit in order to find high-z galaxies, confirm they are in fact at high redshift, and say something about their properties.

1.3.2.1 Detections and Redshifts

As discussed earlier in section 1.1.2, even the present day Universe is awash with Hydrogen gas clouds, both inside (the ISM) and in between galaxies (the IGM).

Neutral Hydrogen atoms can be fully ionised by any photon with $\lambda < 912$Å, which are produced in plentiful supply by high mass stars. This ionisation process has a very high cross section, so even small amounts of neutral material will severely attenuate short wavelength photons. In addition, the stellar atmospheres also provide significant absorption of these short wavelength photons, resulting in this break being visible even in the spectra of individual stars.

It can be seen in the spectra of individual O/B/A class stars that their stellar atmospheres attenuate this radiation significantly, and any neutral ISM can further suppress these photons. Due to these effects when one constructs photometry of a galaxy at low redshift in the UV, a significant break is visible, known as the Lyman break. At 912angstrom a galaxy suddenly increases in brightness by several orders of magnitude, and stays at that approximate brightness throughout the UV and optical.

This can be exploited to pin down the redshift of a galaxy – if we increase the distance between observer and galaxy, all of the light gets redder by a factor $(1 + z)$, therefore the Lyman break moves by this same factor – the break is now located at $(1 + z) \cdot 912$Å. These galaxies are thus known as Lyman drop-outs [Steidel *et al.*, 1996]. While other techniques are viable for the location of high redshift galaxies (e.g. radio observations [Shao *et al.*, 2019]), Lyman drop-out searches are very effective at finding galaxies via blind surveys – one can point a powerful optical/near IR telescope at any quiet part of the sky and expect to find high redshift galaxies as long as the detection limit is low enough.

Additional details must be considered before applying this technique. At intermediate redshifts ($0.5 < z < 6$), strong absorption lines appear in the wavelength range $912\text{Å} < \lambda < 1216\text{Å}$. These lines arise from clouds of neutral hydrogen in the IGM at intermediate redshifts between the source galaxy and the observer, as yet not reionised by reionisation. Each cloud encountered extracts photons in some small wavelength range around to $\sim 1216\text{Å}/(1+z_{cloud})$. If the object is at high enough redshift, there are so many of these clouds that effectively the entire wavelength range is eaten away, completely moving the Lyman Break from 912Å to 1216Å in the rest frame. This is known as a Gunn-Peterson trough, first predicted in the 1960s [Gunn and Peterson, 1965], and observationally confirmed by quasar detections in the Sloan Digital Sky Survey [Becker *et al.*, 2001]. This doesn't present a huge problem however, in fact it can be thought of as advantageous for our purposes, because it simply provides a single sharp break at (rest frame) 1216Å at high redshifts.

We can thus use the Lyman break to estimate the redshift of galaxies. If one wishes to search specifically for high-z galaxies, one would typically wish to run a photometric survey, focusing on wide filters that continuously cover a spectral range around $(1 + z) \cdot 1216\text{Å}$, where z is the approximate redshift to be focused on. The strategy is generally to not only capture the objects in red/NIR bands, but also non-detections in bands bluewards of the break help to minimize the number of low-z interlopers, which can include intrinsically red galaxies, and even M-class or brown dwarf stars in our own galaxy [Wilkins *et al.*, 2014].

Figure 1.5 shows an example of a how a low redshift interloper can appear to be a high redshift galaxy. In the top panel is a BPASS [Eldridge *et al.*, 2017b] Simple Stellar Population (see section 1.1.2.4) with an age of 10^7 years and metallicity $\log_{10} Z = -2.4$. It has then been artificially redshifted to $z = 8.0$. The bottom panel is another BPASS SSP, but is significantly older with an age of $10^{8.5}$ years and the same metallicity, this SSP has been redshifted to $z = 1.74$. The dashed lines correspond to the theoretical locations of the Lyman break (red) and Balmer break (green) respectively in the observational frame.

If one were to observe this pair of galaxies to a depth where one could acquire detections

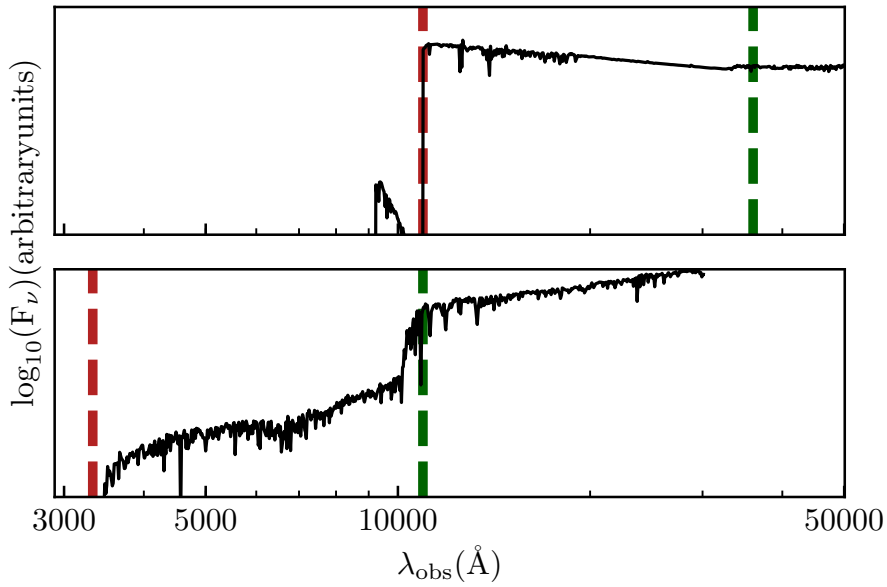

Figure 1.5: Example spectras: a $t = 10^7$years, $z = 8$, and $\log_{10} Z = -2.4$ SSP (top panel); and a $z = 1.74$, $t = 10^{8.5}$years, and $\log_{10} Z = -2.4$ SSP (bottom panel). In this example the Lyman break of one galaxy coincides with the Balmer break of the older, lower redshift galaxy. If the shorter wavelength observations (grey bands) are not deep enough, and signal is only acquired in the bands redwards of the break (yellow bands) then differentiating between these two cases can be challenging.

redward of the break (yellow bands), but did not have sufficient depth to make detections blueward of the break (grey bands), one would struggle to distinguish between these two cases – has one made an observation of a $z = 1.74$, low star formation galaxy, or a highly star-forming $z = 8.0$ galaxy?

One angle of attack is to examine the colour of the detection bands. In this example the colour $y_1 - y_2$ – where y_x are the yellow bands as numbered from short to long wavelength – is red in the low redshift solution, and blue in the high redshift solution. However, this can be muddied if significant amounts of dust are present, which will redden the high redshift spectra, making the two solutions completely degenerate if spectral coverage only extends to the rest-frame UV at the higher redshift.

This technique is commonly formalised by the use of colour-colour diagrams. The principle behind these diagrams is to use three filters with pivot wavelengths $\lambda_1 < \lambda_2 < \lambda_3$,

and construct a plot of $m_1 - m_2$ vs. $m_2 - m_3$, where m_1, m_2, m_3 are the apparently magnitudes in each of the three filters. Approximately speaking, galaxies with their Lyman break lying somewhere between filters 1 and 2 to have extremely red $m_1 - m_2$ colour, and blue or neutral $m_2 - m_3$, due to the reasoning above.

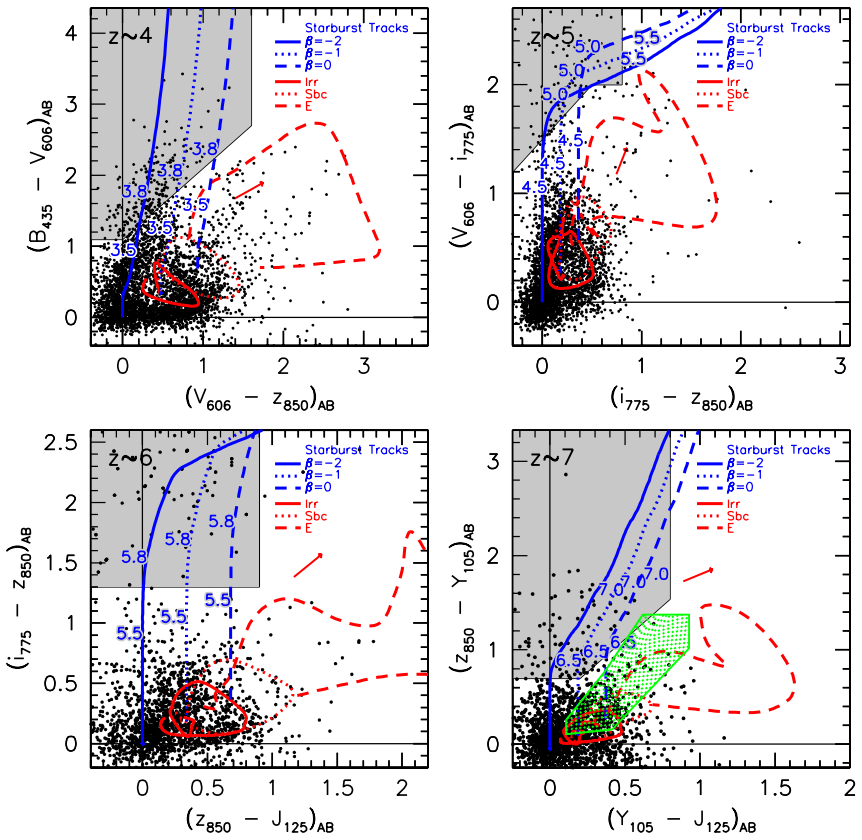

Figure 1.6: Example of high redshift galaxy selection using a colour-colour criteria. Blue tracks represent the expected paths in colour space which star-forming galaxy spectras (with varying UV continuum slopes β = fracd $\log_{10} \mathrm{F}_\nu \mathrm{d}\lambda$, a common proxy for dust content) take as their redshifts are increased. Red tracks represent the same concept, but for various types of low-redshift interloper. Green hatched region in the bottom right panel represents the possible location of low-mass stars . Black data points are measured in the HUDF field, with those lying in the grey shaded area being selected for high-redshift galaxy candidacy. Figure reproduced from Bouwens *et al.* [2012a].

One can be more careful about this by using SED modelling. By constructing synthetic spectra of star-forming galaxies, and galaxies likely to be interlopers from lower redshifts,

one can repeatedly apply the following transformation for many different redshifts –

$$\lambda \rightarrow \lambda_0(1+z) \tag{1.6}$$

$$F_\nu(\lambda) \rightarrow F_\nu(\lambda_0(1+z)) \tag{1.7}$$

where λ_0 is the rest frame wavelength, and F_ν is the flux density at a given λ. By remeasuring the photometry at each step, one can track how the galaxy moves in the two-colour space that has been constructed. By finding areas of the space traversed by the star-forming spectra, but not by the interloper spectra, one can build an efficient selection criteria for EoR galaxies.

Figure 1.6 [Bouwens *et al.*, 2012a] shows an example of this in action.

1.4 Simulating the Distant Universe

While observations are important to understanding the Universe, they are merely descriptive unless they can be tied to physics. Development of theoretical modelling is just as important to understanding the Universe as observation.

When we talk about theoretical modelling in the context of galaxies, it can largely be split into two types: Cosmological simulations model how the Universe as a whole evolves, and what the distribution of its contents would look like at a given time. The rest of the section will be dedicated to briefly outlining their workings. The other major type of theoretical modelling we will be concerned with is SED modelling, which is concerned with modelling what the SED from a galaxy with known physical properties would look like. SED modelling will be addressed in the following section 1.5.

1.4.1 Analytical Cosmology Models

What can be considered the progenitor of all modern simulations are analytic models which take a volume expanding according to the Friedmann Equations, with an ideal gas of self gravitating mass particles within [Press and Schechter, 1974]. They show that although the

Universe on large scales is governed by the rules of General Relativity, it is effective to treat particle-particle interactions as Newtonian. One such example is the PressSchechter formalism which finds that the distribution of masses under these conditions are self-similar, a function of the from [Press and Schechter, 1974]:

$$n_R(M) \propto M^{-1-\alpha} \cdot \exp\left[-const. \times \left(\frac{M^{1-\alpha}}{R}\right)^2\right] \tag{1.8}$$

where $n_R(M)$ is the number density of objects of mass M at some expansion factor R, and α is an adjustable parameter that depending on the amount of variance in initial particle positions, ranges between $\frac{1}{2}$ and $\frac{1}{3}$. This form of distribution is now commonly known as a Schechter function, and is commonly used for the distribution of dark matter halos, galaxy masses, and even galaxy luminosities.

1.4.2 Dark Matter Simulations

Unfortunately, analytical models like the PressSchechter formalism don't capture the full complexity of even dark matter structure formation, let alone the interactions of baryons. A first step in the road to fully self-consistent galaxy formation simulations are then dark-matter only (DMO) simulations. In virtually all DMO simulations the dark matter is assumed to interact solely via gravity, dramatically reducing the computational complexity on simulations.

In brief, a box is created with some initial conditions at a very early time: an initial mass distribution; divided equally into particles, typically of constant mass, periodic boundary conditions, and some box size. Depending on the science question being addressed the size of box can vary from a few Mpc to many Gpc, i.e. from the scale of the local group to that of the entire observable Universe, and even beyond. Similarly particle masses range from as low as a few hundreds or even tens of solar masses to billions of solar masses for the largest simulations.

The collection of particles in the box is then evolved in time, expanding according to

Friedmanns Equations [Friedmann, 1922]. Although General Relativity (GR) is required to obtain these equations for the boxes evolution, the particles are typically only considered to interact according to Newtonian gravity, as GR corrections on the force between them are small.

Evolving the set of particles in time requires calculating the net force on each particle due to every other particle, and then updating the velocity and position in a finite time step. The choice of time step impact of the accuracy/precision of calculation and computational cost - a large time step would result in a loss of precision/accuracy while a small time step will add significantly to the computation cost, resulting in lower-resolution and/or box size for the same computational effort.

In the simplest implementation the net force on each particle is obtained by calculating the force due to every other particle in the simulation. However, such a process is computationally inefficient, scaling as $O(N^2)$. It is however possible to reduce this to $\sim O(n \log(n))$ using one of two, or a combination, methodologies: hierarchical algorithms, and particle meshes.

Hierarchical algorithms functionally take the particle for which the force is being calculated for, and form a set of cells around it - small cells at small distances, and increasing in size with the distance we move away. Forces are then calculated for the cells as a whole, thus only needing single calculations for large groups of particles at long distance, while still maintaining individual force pairs of particles at short range.

Particle meshes work by dividing the space into discrete small cells, and calculating the gravitational potential on the grid by sampling the particle density in Fourier space, and using the resulting potential to calculate the force on each particle.

Modern Simulations Modern simulation codes (e.g. Springel [2005]; Schaye *et al.* [2015]) often adopt a hybrid approach, using a hierarchical approach at short range, and particle meshes for long distance forces and the periodic boundary conditions, which are handily handled for free due to the mathematical properties of the Fourier transformation

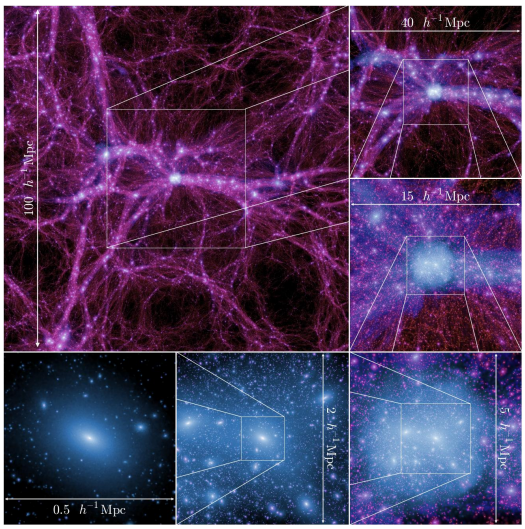

Figure 1.7: A slice through the DMO Millennium simulation [Boylan-Kolchin *et al.*, 2009] showing the distribution of dark matter particles.

for periodic functions.

Figure 1.7 shows an example of a slice from the Millennium simulation **??**, a famous DMO simulation. This shows that dark matter accumulates in a complicated (cosmic) web or foam like structure with the highest densities lying at the intersections or nodes of filaments and sheets. The filaments and sheets surround areas of relative emptiness called voids.

Dark Matter Structures In the highest density regions dark matter particles form collapsed virialised clumps, or halos – virialised meaning that the halo as a whole satisfies the virial theorem $2T = -U$ where T is the total kinetic energy of the particles within the halo, and U is the total gravitational potential energy of the same particles.

These halos join together over time, forming larger and larger main halos with sub-halos inside. These collapsed halos contain the majority of the mass of the Universe, while being the minority by volume. Figure 1.8 shows a simplified sketch of how these structures are assembled.

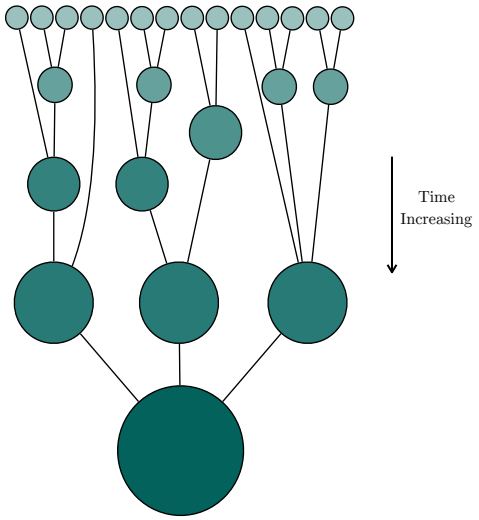

Figure 1.8: Sketch of hierarchical dark matter structure formation.

Structure Finding These halos must be detected within the simulation before they can be used for analysis, and a variety of techniques exist for doing this, for example Friends-of-Friends (FOF) algorithms [Efstathiou *et al.*, 1985]. Broadly speaking, this class of halo finder works by linking all particles together such that for any particle in the set, all of the other particles lie within some distance l – often called the linking length. One can adjust the linking length in order to find structures of different sizes, and form these structures into hierarchies by examination of which smaller scale structures link together to form larger ones (for example, which individual virialised DM halos belong to a larger DM halo, indicative of a galaxy cluster). Several alternatives for identifying collapsed structures also exist, for example making use of the full 6D phase space (position and velocity) information to separate spatially coincident, but dynamically independent, halos.

1.4.3 Semi-analytical Models

Because they do not simulate the baryons (stars, gas, super-massive black holes) dark matter only simulations do not produce galaxies. This means that they cannot (in most cases) provide enough information to directly compare with observations, the exception being the results of weak lensing surveys which can probe the distribution of matter in three

dimensions.

To produce galaxies from a dark matter simulation it must be combined with additional modelling. These models are called Semi-Analytical Models (SAMs) and were the first true galaxy formation models. SAMs work by analytically associating dark matter halos with baryonic content, which can be subjected to processes such as cooling, star formation etc. This allows the possibility of assignment of stars, gas and even black holes to the underlying DM halos, creating a population of galaxies allowing comparisons with observation

Like all models involving baryonic physics much of the physics is still not fully understood, and the parameters are poorly constrained. For example, a key assumption in many models is the amount of thermal and mechanical energy injected into the ISM by supernovae explosions. With the right choice of parameters SAMs have been demonstrated to match many observations, however a physical motivation for these choices isn't always trivial to extract [e.g. Henriques *et al.*, 2020].

While SAMs are being increasingly replaced by cosmological hydrodynamical simulations (see below) they still benefit from being much less computationally expensive. This allows a much wider range parameters and changes to the physics to be explored. For this reason SAMs are currently better able to match some key observations such as the galaxy stellar mass function.

1.4.4 Hydrodynamical Simulations

A more direct technique than that found in semi-analytical models is to spatially track components of the Universe and to let them evolve naturally with time. Hydrodynamical simulations begin with some physically motivated distribution of baryons and dark matter, and self-consistently follow the evolution of this in time. Gravitational forces bring the material together, forming dark matter halos, stars and galaxies in as realistic of a way as possible. The major advantages of hydrodynamical simulations over simpler models such as semi-analytics is that they can include processes which affect the baryons other than gravity. Examples include gas cooling and heating via radiative transfer, metal enrichment from

supernovae (which affects rates of cooling), the formation of stars driving off surrounding gas via strong radiation fields from young stars and supernovae, the formation of supermassive black holes, and their effects on their host galaxies (for example their feedback quenching star formation). Finally, higher order effects such as the mergers of galaxies can be modelled self-consistently, which can offer insight into the buildup of large galaxies at any point in the Universe's history.

Hydrodynamical simulations are much more computationally expensive because they are producing all of this from "first principles" – a distribution of baryons and dark matter is given some physical rules to follow (such as gravity, and fluid dynamical equations) and then everything falls out of that, unlike SAMs which commonly use observed distributions to approximate conditions. Because of how computationally intensive this can be, hydrodynamical simulations must trade off between resolution (the mass of an individiaul "particle" of dark matter or baryons"), volume (the size of the simulation volume initially, this will expand according to general relativity as the simulation evolves), and timescale (both the redshift of the initial conditions and stopping redshift).

With increases in computational power and code efficiency however it became possible to simulate cosmologically useful ($> (25\ \mathrm{Mpc})^3$) volumes with sufficient resolution to simulate galaxies. Two of the first projects to achieve this milestone were the EAGLE [Schaye *et al.*, 2015] and Illustris [Vogelsberger *et al.*, 2014] projects, each of which simulated $\sim (100\ \mathrm{Mpc})^3$ resolving galaxies $M_* \simeq 10^8\ \mathrm{M}_\odot$.

Unlike DMO simulations combined with SAMs, fully-hydrodynamical simulations predict the full distribution of dark-matter, gas, stars, and super-massive black holes, alongside all of their properties. Figure 1.9 shows a slice through the EAGLE simulation showing both the distribution of gas and stars.

Since these projects simulations have increased in resolution and/or volume and explored a wider range of physics.

In addition, the self-consistent modelling of radiation fields including their coupling to baryons has been folded into these simulations in recent years. This is particularly

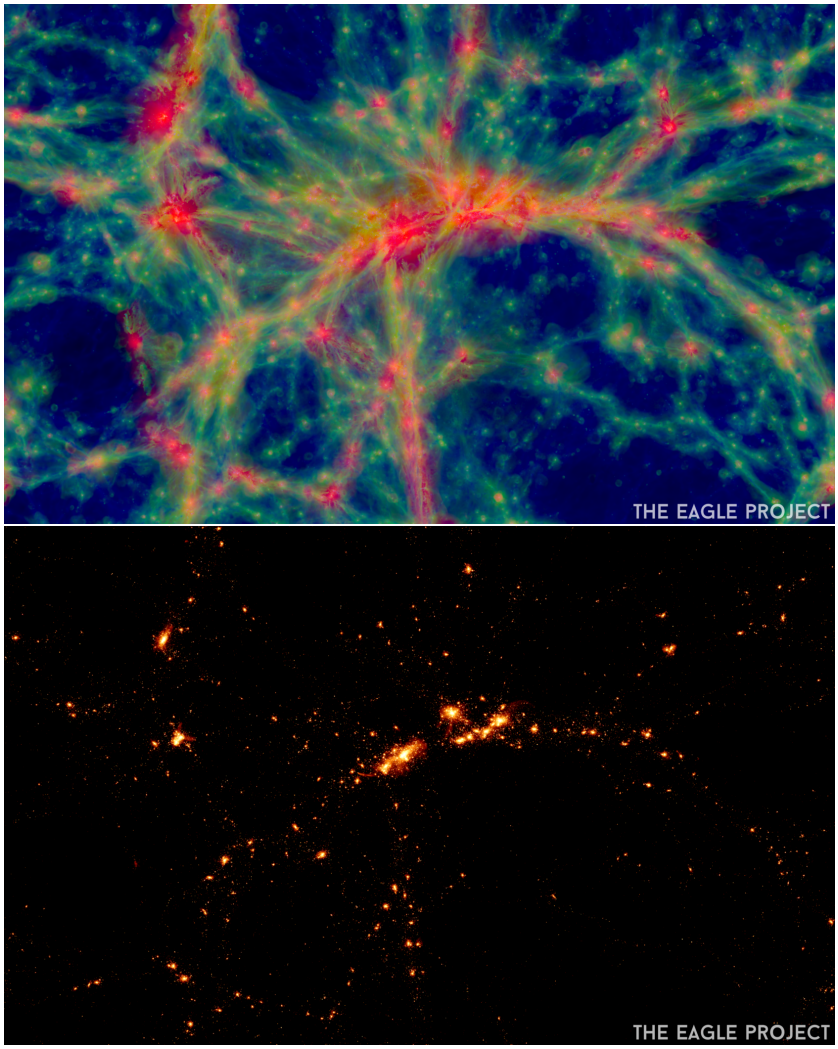

Figure 1.9: Slices through the EAGLE simulation showing the distribution of gas (colour coded by temperature) and the distribution of stars.

important in the low-mass high-redshift Universe where external photons can photo-ionise a halos baryons suppressing star formation. The addition of radiative transfer in this way is vital for the modelling of the epoch of reionisation, as it is largely driven by the interaction of strong radiation fields with neutral hydrogen [e.g. Feng *et al.*, 2016a].

1.5 Marrying Simulations and Observations with SED modelling

Simulations are intrinsically tied to modelling, as the simulation only tracks galaxies at relatively low resolution, often in $\sim 10^6 M_\odot$ "particles". To convert these into a luminosity or a flux to predict what observations would look like, one must model the light that these particles would give out. Notably, this is the reverse of the process of SED fitting – we observe the light that a galaxy gives out, and must infer the physical properties that produced said light. Simulating the light from galaxies and SED fitting therefore, can be thought of as the reverse processes of each other

In this section we will discuss two important aspects of SED fitting. Firstly model generation: what effects do each ingredient of a galaxy outlined in section 1.1 have on the overall SED? and for a given set of models of these components and parameters, how does one generate an SED in practice? Secondly, we will discuss model fitting techniques: What is the best algorithmic approach to comparing a generated model to the observations? How do we make progress better than change at converging to the best set(s) of parameters? and What is a sensible metric to use to compare between the two?

This section will be dedicated to discussing the general techniques involved, and later chapters will go into the specifics of the models used therein.

1.5.1 Generating Model Galaxies

Model generation is very much the starting point of any attempt to put Astronomical observations into context. At its core, model generation takes as an input a set of models

for dust, starlight, and gas, and a list of parameters for each, and outputs an SED of a synthetic galaxy with those properties. This SED is then degraded to the same state as the observations – either the resolution of the spectra is reduced, or it is convolved with filter transmission curves to generate photometry – in order to be compared to them by some metric.

1.5.1.1 Starlight

In order to generate starlight, it is most common to use a technique called Stellar Population Synthesis (SPS). The construction of one of these models involves building it up from building blocks called Simple Stellar Populations (SSPs), which assume a single metallicity and age, which are in turn built from individual stellar spectra (for various reasons discussed below these stellar spectra can be empirical or synthetic, each offering various advantages and pitfalls).

An SSP at its core is a model describing a population of stars that are born according to some initial mass distribution called the Initial Mass Function (IMF) as described in section 1.5.1.1. These stars will have a fixed set of chemical abundances and all have the same (fixed) metallicity. The SSP then describes how the SED of these stars evolves with time.

SSPs require significant input from stellar theory and observation, which is beyond the scope of this thesis, however it should be noted that each of these components brings with it uncertainties of varying size. Discussion of this can be found in paper such as Bruzual *et al.* [2019] and Eldridge and Stanway [2012] .

An SSP contains three essential ingredients - an IMF to provide the initial distribution of masses, denoted ($\Phi(M)$), a library of stellar spectra (f_{stell}), and finally a numerical description of the evolution of stars in time in the form of an isochrone library (determining the relationship between the effective temperature T_{eff}, surface gravity g, and mass M of a star at a some fixed metallicity Z and age t.

Initial Mass function The initial mass function (IMF) is the mass distribution of the stars in an SSP at the time of formation ($t = 0$). It is vitally important because even small changes in the distribution of the stars can have large changes in the resulting SED, especially at young ages. However, the IMF is very hard to isolate observationally. An SSP is an approximation of how stars form in the real world, and finding populations that are truly at age zero to census their population is not really possible. This leaves a myriad of unknowns about the IMF – its precise form is uncertain, and whether that form is even universal in time [Wilkins *et al.*, 2008] or across different galaxies environments is something that is uncertain [Jeřábková *et al.*, 2018]. Specific formulations of the IMF are discussed earlier in section 1.1.2.4.

Isochrones Isochrones describe contours of fixed age and metallicity that stars of varying mass occupy in Temperature-Luminosity space (known as a Hertzsprung-Russell diagram). They are fairly simply constructed from stellar evolutionary theory (which again, will not be discussed here except for how it pertains to SSPs as a whole).

Many tables of these isochrones exist in the literature, which all roughly work in the same way - by specifying an age and metallicity of a population, the track in effective temperature and bolometric luminosity space is defined.

A common problem here is that there are many isochrone tables to choose from, each derived in different ways, producing slightly different results. This is compounded by the fact that not all of the various libraries cover the entire age/metallicity space, so for the purposes of galaxy SED construction, different libraries must be “stitched" together. This can be difficult because assumptions about the stars themselves (such as their rotation and interior physics) cause the stars to turn off the main sequence at different times, resulting in potential inconsistencies in the isochrones at the boundary [Conroy and van Dokkum, 2012; Paxton *et al.*, 2011].

Canonically, most SSPs are constructed using the Padova Isochrone library, which is supported by the Geneva models at particularly young ages for their specific handling of

high mass stars.

Stellar Spectra Once the IMF and isochrone sets have been used to determine the proper mass, temperature and luminosities of a set of stars at a fixed age, a library of stellar spectra can be used to convert these properties into a set of SEDs. Similarly to stellar isochrones, the biggest challenge here is the stitching together of various existing libraries. These libraries fall into two large families - theoretical libraries created from numerical simulations of single stars, and empirical libraries obtained by spectroscopy of nearby stars.

Theoretical libraries have the advantage of being able to arbitrarily sample the space – even rare and exotic species such as the largest O stars or Wolf-Rayett stars can be modelled with relative ease. These spectra are not vulnerable to observational effects such as atmospheric absorption and don't require flux calibration. Spectra can also be produced to almost arbitrary spectral resolution, so effects that arise from under-sampling are minimised.

There are however two major issues with the use of theoretical spectra. Firstly, solar models such as Kurucz (2011) are still unable to reproduce all of the spectral lines found in very high resolution solar spectra.Missing these spectral lines can result in severe discrepancies to the point where these model spectra cannot be used to recreate broadband SEDs . Often these libraries are corrected manually for the cumulative effect of these extra lines on broad band photometry [Coelho *et al.*, 2007].

$$f_{SSP}(t,Z) = \int_{m0}^{m1(t)} f_{stell}(T_{eff}(M), g(M)|t,Z)\Phi(M)dM \tag{1.9}$$

where M is the initial mass of a star at t=0, $\Phi(M)$ is the IMF as outlined above, f_{stell} is a stellar spectra of star with mass M at time t and metallicity Z. The use of the isochrones is wrapped up in the stellar spectra, defining the effective temperature T_{eff} and surface gravity g for a given M, t and Z.

Example SSP Spectra These SSPs are typically provided as black boxes to users, and there are a large variety on the market with various choices and assumptions in the ingredients already built in. Commonly used modern examples include Bruzual and Charlot [2003] (bc03), Maraston [2005] (M05), and Eldridge *et al.* [2017b] (BPASS).

One must be careful when choosing which SPS models to use for this reason, as some assumptions (such as rotation of stars and binary systems) can turn out to be important for the starlight of a galaxy as a whole under certain conditions.

In Fig. 1.10 and Fig. 1.11 we show examples of the spectra of single stellar populations with various ages and metallicities. Fig. 1.10 shows the evolution of the SSP SED with age for both $Z = 0.01$ and $Z = 0.001$. As a simple stellar population ages the most massive, and thus most luminous and hottest (at least on the main-sequence) stars progressively move off the main-sequence. This leaves the SED progressively fainter and redder: in the UV the luminosity drops by a factor of $\sim \times 10,000,000$ as the population ages from $t = 1$Myr to $t = 10$Gyr. In the optical/NIR the decline is less steep by still sees a decrease of $\sim \times 10,000$. Fig. 1.11 shows the effect of metallicity $Z = 10^{-5} \rightarrow 0.04$ ($\times 4000$ change) for 3 different ages ($t = 10,\ 100,\ 1000$ Myr). The effect of metallicity is much less important than age, but does have a significant effect on the UV, and specifically the Lyman Continuum (hydrogen ionising) emission. This in turn will have a significant impact on the strength of nebular line emission.

Composite Stellar Populations Once a set of SSPs has been (carefully!) chosen, they can be used to build up Composite stellar Populations (CSPs) which are considered to be a reasonable approximation of real galaxy populations. The main task is then to decide how each of these SSPs should be weighted according to their age and metallicity.

From section 2.2.1.1, it is natural to weight these SSPs by the SFH of the galaxy [Behroozi *et al.*, 2013], but it is unclear how best to properly treat the metallicity distribution of the stars. Chapter 4 will address a variety of choices that can be made both for the SFH ($SFR(t)$) and $P(Z,t)$, the metallicity distribution.

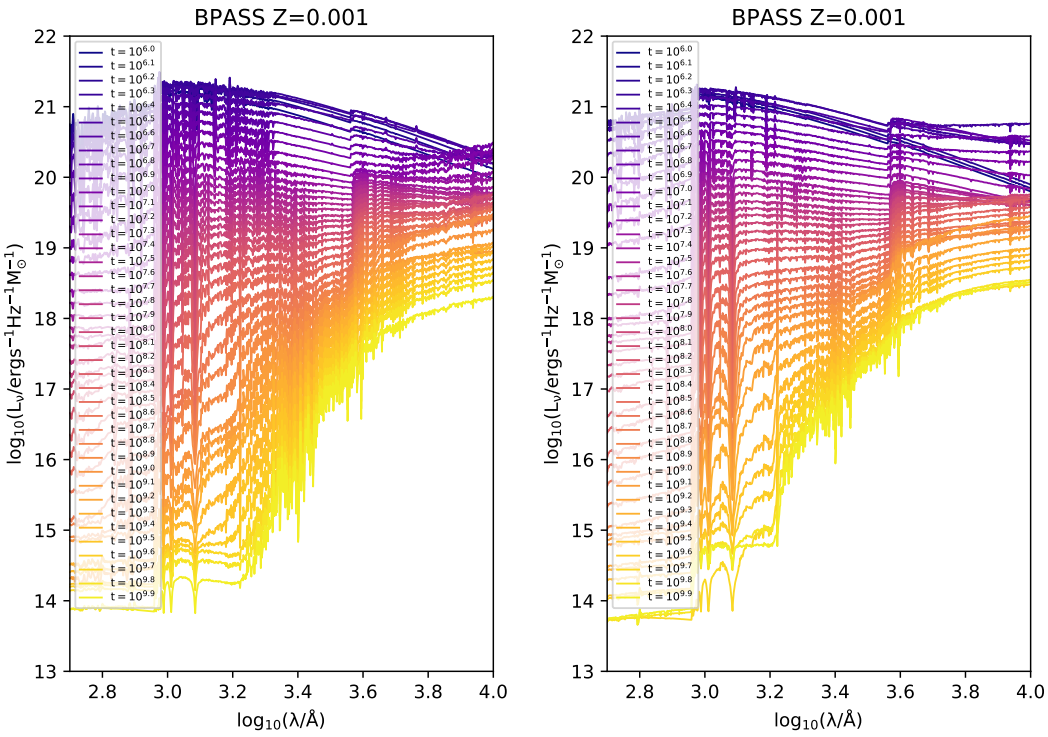

Figure 1.10: Luminosity of BPASS simple stellar populations with metallicity $Z = 0.01$ (left) and $Z = 0.001$ (right). Populations range in age from 1Myr (top, purple) to 10Gyr (bottom, yellow). As SSPs age, the young stars die off, causing them to become overall redder and reduce in bolometric luminosity.

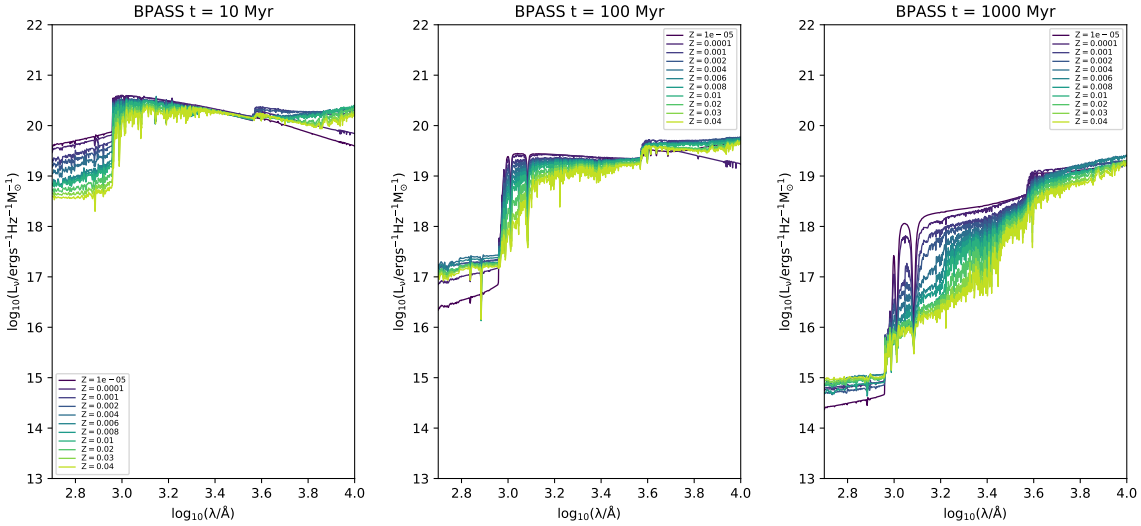

Figure 1.11: Luminosity of BPASS simple stellar populations with fixed ages 10Myr (left), 100Myr (center) and 1Gyr (right), and varying metallicity from $Z = 10^{-5}$ (top, purple) to $Z = 0.04$ (bottom, green). The presence of metals causes reddening of the SSPs, and a slight reduction in luminosity. At young ages the reddening can boost continuum emission at$\lambda > 4000$ as the spectra are so extremely blue at low metallicity.

These elements are combined together thus:

$$f_{CSP}(t) = \int_0^t \int_0^\infty SFR(t-t') \cdot P(Z, t-t') \cdot f_{SSP}(t', Z) \cdot D dt' dZ \tag{1.10}$$

where f_{SSP} is the spectra of the SSP as defined in equation 1.9, $SFR(t)$ is the star formation history, $P(Z,t)$ is the distribution of metallicities and f_{CSP} represents the spectra of the resulting composite stellar population, that is - the emission from a galaxy purely from the stars. The integration variables and limits are t - the age of the Universe at time of observation (i.e. a proxy for the redshift of the galaxy), t' the infinitesimal age interval of the stellar population, and Z, the metallicity.

While there is much debate on the proper treatment of star formation histories, the treatment of metallicity is often reduced to simply the use of a single value across all ages - a δ-function. More advanced techniques of fitting an age dependant metallicity do exist [Tojeiro *et al.*, 2007, e.g.], but a thorough exploration of this will be deferred to the bulk of chapter 4.

1.5.1.2 Dust

As discussed in section 1.1.2.3 interstellar dust is made up of grains of organic material. Dust has two major effects on the emission from galaxies. Firstly the dust suppresses light in the UV-NIR portion of the spectra, absorbing some wavelength dependant fraction of the stellar photons in this range. The second effect is a large amount of thermal emission in the far IR due to the reprocessing and remission of this energy.

Modelling attenuation (especially photon scattering) is an extremely difficult process, but typically produces a transmission curve $T(\lambda, \Theta)$ as a function of wavelength, and contains some set of parameters Θ which encode a variety of other factors. These models are generated both theoretically [Charlot and Fall, 2000] under certain sets of simplifying assumptions, or empirically for a certain class of galaxy, for example Calzetti [2001] is derived from the observations of local starburst galaxies.

These attenuation curves are most simply presented as a transmission fraction – a simple multiplicative factor at each wavelength which states the fraction of light which is not removed by the dust that is, dust models are added into stellar populations thusly:

$$f_{\nu,obs}(\lambda) = f_{\nu,CSP}(\lambda) \cdot T(\lambda, \Theta) \tag{1.11}$$

At wavelengths longer than $10\mu m$ or so, a galaxies dominant component in terms of emission is the dust grains. The overall emission of these grains results from their exposure to the overall light emitted from the other components.

1.5.2 Fitting Techniques

Generating models is only part of the process – the other aspect of SED fitting is inferring the physical properties of the observed galaxies must be based on generating models which produce similar mock observations. This can similarly be divided up into two parts – what metric can be used to make quantitative statements about the quality of a model reproduction of observations? and what algorithm(s) can be used to efficiently find areas of parameter

space that produce these high(er) quality reproductions, as opposed to searching the space systematically or at random?

The former question is much more simply answered than the latter. By exploitation of the central limit theorem, the difference between a data point generated by the model model and the same point in the observations is χ^2 distributed:

$$\chi^2 = \sum_i^N \frac{(o_i - m_i)^2}{\sigma_i} \tag{1.12}$$

where N is the number of data points, o_i represents the observations with index i and error σ_i, and similarly m_i represents that same observable but as generated by the model. χ^2 for a model which reproduces the data well are $\approx N$, as this represents an average 1 error-bar deviation from the observations. Significantly higher χ^2s suggests a model which does not appropriately fit the data, whereas significantly lower χ^2s can mean the model is *over-fitted*: there are too many free parameters to be justified by the type and quality of data available, and the model is (at least partially) fitting the noise.

The probability of a given χ^2 value being produced by chance, P_{χ^2}, is:

$$P_{\chi^2} = \left[2^{(d/2)}\Gamma\left(\frac{d}{2}\right)\right]^{-1} \int_{\chi^2}^{\infty} t^{(d/2-1)} \exp[-t/2]dt \tag{1.13}$$

where d represents the number of degrees of freedom, Γ is the gamma function – the extension of the factorials to non-integers, and t is simply a dummy integration variable. This implementation of χ^2 also assumes no prior knowledge, which is the most common situation when considering SED fitting – throughout this work we assume flat priors on all χ^2 fits.

The other problem, concerning the efficient traversal of parameter space, is more complicated to answer. If one was to naively to approach this problem, one could take each

parameter, and step through some reasonable range of values, carrying out a systematic grid search over an N-dimensional box. However this is extremely inefficient – fitting N parameters with ranges divided into s steps results in an algorithm with efficiency $O(s^N)$. For anything more than a few parameters this quickly becomes infeasible, and most of the runtime of the algorithm is used computing models which are highly unlikely to be even close to the solution. This problem can be mitigated in one of two ways – by reducing the dimensionality of the parameter space via the use of template galaxies, or by intelligently moving through the space.

1.5.2.1 Template based fitting

Template fitting is a commonly used technique for SED fitting, which rather than traversing parameter space, uses a set of pre-generated models, some linear combination of which are used as the overall model. The overall parameters of the model can then be computed from the known template parameters and the weights. Template fitting is often deployed in SED fitting codes optimized for speed, and can allow establishment of the basic facts about a galaxy (i.e. its redshift and order of magnitude stellar mass) in a matter of seconds. This technique is typically used on photometry only, as emission lines require many more parameters, and thus many more templates in order to get a good model.

We begin with a vector of the photometric observations with components $F_{\lambda,i}$, where i is an index running over the filters which the observations were made. The set of template spectra $T_i(\lambda)$ are then convolved with the same filters, resulting in a matrix $\mathbf{T_{ij}}$ where i runs over the filters as before, and index j runs over the different templates.

The choice of galaxy templates is not an easy choice. The set that is chosen needs to cover the parameter space sufficiently such that it is possible to represent the observed colours with some linear combination of templates. For example if every template has a red $g-r$ colour, but the observations are blue in these filters, then it is impossible to model this galaxy with this set: no non-negative linear combination of red colours will ever produce a blue colour. The choice of templates is therefore vitally important.

Once we have chosen a set of templates, the following algorithm is applied in order to find the probability distribution of redshifts, and the best fit stellar mass at this redshift. Other parameters such as dust content can be derived from the properties of the templates and their weights, however this is not advisable because degeneracies and co-variances in these parameters are not taken into account.

1. start at $z_0 = 0$, and define some finely spaced redshift up to $z = z_{max}$ grid to step over, and a vector of the observations $\mathbf{F}_\lambda, \mathbf{i}$, where index i runs over the filters observations were performed in.

2. redshift the all the model spectra by factor z, and convolve with the filters, to obtain matrix $\mathbf{T_{z,ij}}$, with each entry representing the normalised flux in filter index i for model spectra index j.

3. invert the matrix equation $\mathbf{F}_\lambda = \mathbf{w} \cdot \mathbf{T_z}$, solving for a set of weights $\mathbf{w}$ using an implementation of the non-linear least squares algorithm - it physically does not make sense to have negative weights for these templates as they represent

4. calculate χ^2 (equation 1.12) between the model and the observations, a measure of the goodness-of-fit of the model.

5. store chi^2 and the calculated vector of weights $\mathbf{w}$.

6. If $z < z_{max}$, increment z, and go to (2.) Else, if $z = z_{max}$ proceed to (7.).

7. All post-processing, e.g. calculation of most likely redshift, stellar mass can be performed on this list of χ^2 values. Terminate algorithm here.

Once the χ^2 as a function of z has been calculated, equation 1.13 can convert this into a probability distribution $P(z)$.From this probability distribution, we define the following "best fit" parameters:

$$z_\mu \quad = \int_0^\infty zP(z)dz \tag{1.14}$$

$$z_m \quad : \int_0^{z_m} P(z)dz = \tfrac{1}{2} \tag{1.15}$$

$$z_p \quad : \text{value of z where P(z) is maximised} \tag{1.16}$$

where $z_\mu, z_m and z_p$ are the mean, median, and mode (maximum likelihood) redshifts respectively. Galaxies which both have plenty of good quality data, and are well represented within the template space, typically have one, roughly Gaussian solution, and $z_\mu \approx z_m \approx z_p$. However, especially in the context of EoR galaxies, this is rarely the case. Commonly, high redshift galaxies only really have one defining feature – the break. As was discussed earlier – and as demonstrated in figure 1.5 – it is common unless the signal to noise in detected bands is very high to end up with a bi-model PDF: a high redshift star-forming solution and a low redshift, more quiescent solution.

In this situation these definitions can become less useful – if the solutions are comparable in probability, the mean and median will pick a compromise redshift, applicable to neither. The maximum likelihood on the other hand, will only take into consideration the larger of the two modes, completely ignoring the less probable – but still potentially very significant – smaller mode. Extreme care must therefore be taken when data is of poor quality.

Other parameters are calculated in a very simplistic way, for example if the mass of each model template is known, we can define a vector of those masses $\mathbf{M_{*j}}$, and calculate total stellar mass in the following way:

$$M^*_{fit} = \sum_j^{N_{template}} \mathbf{w_j M^*_j} \tag{1.17}$$

where $\mathbf{w_j}$ is the vector of best fit weights as calculated in step 3 of the algorithm above. Other parameters such as the star formation rate can be calculated in a similar way if the information is known about the templates.

1.5.2.2 Monte Carlo-Markov Chain

Monte Carlo-Markov Chain (MCMC) is a technique by which parameter space with many dimensions can be efficiently sampled. Specifically for our purposes, we have a set of observations, and many parameters controlling what a model spectra will look like. We wish to find the optimal parameters (or locus of parameters) which will recreate the observations as closely as possible.

Rather than pre-computing some well chosen models and using a combination, Monte-Carlo methods involve the random sampling of a parameter space, and in principle can be used to solve any problem with a probabilistic interpretation. Monte-Carlo analysis usually proceeds in the following way.

1. Choose a set of input parameters Θ randomly from a probability distribution, and generate a model with those parameters.

2. Perform some computation on the inputs - for example a χ^2 calculation or an accept/reject criteria

3. Aggregate the results in some way - which parameter set is the best fit? What is the ratio of acceptances/total trials.

Monte-Carlo methods effectively involved trial and error, and is largely inefficient – if the sampling finds a good model by chance, it simply moves on, picking another random location in parameter space. Monte Carlo methods are therefore rarely used in isolation. They are commonly combined with Markov Chains – a chain of trials where each step is probabilistically dependant on the previous step. This combination, known as MCMC, is extremely powerful, able to sample parameter space efficiently to find solutions.

Most common MCMC algorithms are variants of the Metropolis-Hastings algorithm, which proceeds as follows:

1. Generate an initial guess of parameters $\boldsymbol{\Theta}$

2. Calculate the probability that this set of parameters matches the vector of observations $\mathbf{F}_\lambda$. In our case we do this by evaluating the χ^2 probability distribution $P(\chi^2|N_{obs})$ where N_{obs} is the number of filters we have observations for.

3. We now generate a new guess $\mathbf{\Theta_{test}}$ according to some compact probability distribution $Q(\Theta_{test};\Theta)$ around $\mathbf{\Theta}$ - for example, a multidimensional Gaussian - and calculate the probability $P(\chi^2_{test}||N_{obs})$.

4. a) If $P(\chi^2_{test}|N_{obs}) > P(\chi^2|N_{obs})$, we "accept" the new set of parameters. We set $\mathbf{\Theta}$ to $\mathbf{\Theta_{test}}$.

   b) If $P(\chi^2_{test}|N_{obs}) < P(\chi^2|N_{obs})$, we reject the guess, leaving $\mathbf{\Theta}$ as it is. However, with some probability we accept this guess anyway. This is so that even if we have found a good solution, we will continue exploring the space. This probability in principle can be anything (with a probability of 1 simplifying the algorithm to a Monte Carlo approach). However what is most commonly used is $\min\left(1, \frac{p(Y|D)}{p(X(t)|D)}\frac{Q(X(t);Y)}{Q(Y;X(t)}\right)$

5. We store $\mathbf{\Theta}$, and repeat steps 3 & 4 many times, storing each $\mathbf{\Theta}$. The better a guess $\mathbf{\Theta}$ is, the more likely the algorithm is to store it multiple times.

6. The samples generated by this algorithm are distributed according to the true posterior of the parameter space, thus the posterior can be approximated based on these samples. For a large number of samples this will approach the true probability distribution of the parameters.

It is uncommon to use the original Metropolis-Hastings algorithm as listed here. If the posterior PDF is not well behaved (for example bi-modal), then the algorithm is vulnerable to settling local minima if the size of the distribution governing the new choice of Θ in step 3 is too narrow. As it is impossible to know if this is the case *a priori*, modified versions of this algorithm are used for most practical applications, usually making many draws in parallel which then interact with each other so that a global picture of the posterior is built

up. A full discussion of the algorithm used in this work – the affine invariant ensemble sampler Goodman and Weare [2010] – is deferred to section 2.3.1.

Chapter 2

Interrogator

This chapter introduces the INTERROGATOR spectral energy distribution fitting code. We begin in Section 2.1 by describing the motivation for INTERROGATOR's development. In Section 2.2 we describe the INTERROGATOR code, including its SED generation model (§2.2.1) and inference engine (§2.3). In Section 2.4 we document INTERROGATOR's testing before, in Section 2.5, providing a summary and outlining potential future development.

2.1 Motivation

In the context of early galaxies, the quality of data has rapidly improved in recent years, especially in the near infrared and is only set to leap forward again with the advent of the Webb telescope. Alongside this, there must be a similar improvement in modelling techniques, in order to fully take advantage of the data being produced.

As outlined in section 1.5, this conversion between photometric fluxes or spectral data into physical properties of a galaxy is achieved using SED fitting. Historically, this has been accomplished using template techniques – create known stellar mass/dust content templates using local observations or simulations, then taking non-negative linear combinations of the templates to fit the data [Brammer *et al.*, 2008; da Cunha *et al.*, 2008], and allowing estimation of the redshift, stellar mass and dust content. As discussed, this method is computationally fast, and can produce impressive results, especially for the redshifts of galaxies which have their Lyman/Balmer breaks represented in the data. However the

information this type of analysis can supply is limited – parameter spaces outside of this are highly non-linear, and many parameters are degenerate. For example one of the most well known degeneracies is that between redshift, stellar age, dust and metallicity. These four parameters can have very similar effects on the rest frame UV-NIR, and depending on the templates used in such an SED fitter, the result can fall down very certainly in some area of the parameter space simply because others are not properly spanned by said templates.

Another limiting factor of modelling is the stellar physics models which go into making templates & SPS models. These have also improved vastly with time, taking into account more and more stellar atmospheric effects, and the effects of a star being in a binary on its overall spectra [Eldridge *et al.*, 2017b]. We thus get a process where stellar observations get better, which provide more information with which to improve stellar population models, and these improved models are used to improve SED fitting as the models now more closely match reality.

In order to make progress combating these myriad issues, a new generation of SED fitters have emerged, which aim to take a much higher dimensional parameter space, and traverse it in an efficient manner using MCMC or similar algorithms – see section 1.5.2.2 for more details. This chapter will chart the development of INTERROGATOR, an MCMC based SED fitting code designed to maximise flexibility in model choice as much as possible.

INTERROGATOR is unique in the SED fitting space, filling a few important niches: firstly, the code is designed out of the box to be optimised for the fitting of EoR galaxies, using the most current versions of the BPASS SPS model, which takes into account many effects which are of vital importance in young stellar populations. Secondly, the code offers flexibility to switch out models arbitrarily as they are updated and/or as needed. This is important for the exploration of modelling assumptions by carrying out fits to the same data with different models, and for comparison with literature by re-creating the conditions which other work was carried out. Finally, INTERROGATOR also uniquely supports distributions in age-metallicity space, generalising the traditional star formation history plus uniform metallicity used in other SED fitters. Chapter 4 explores this implementation in detail and

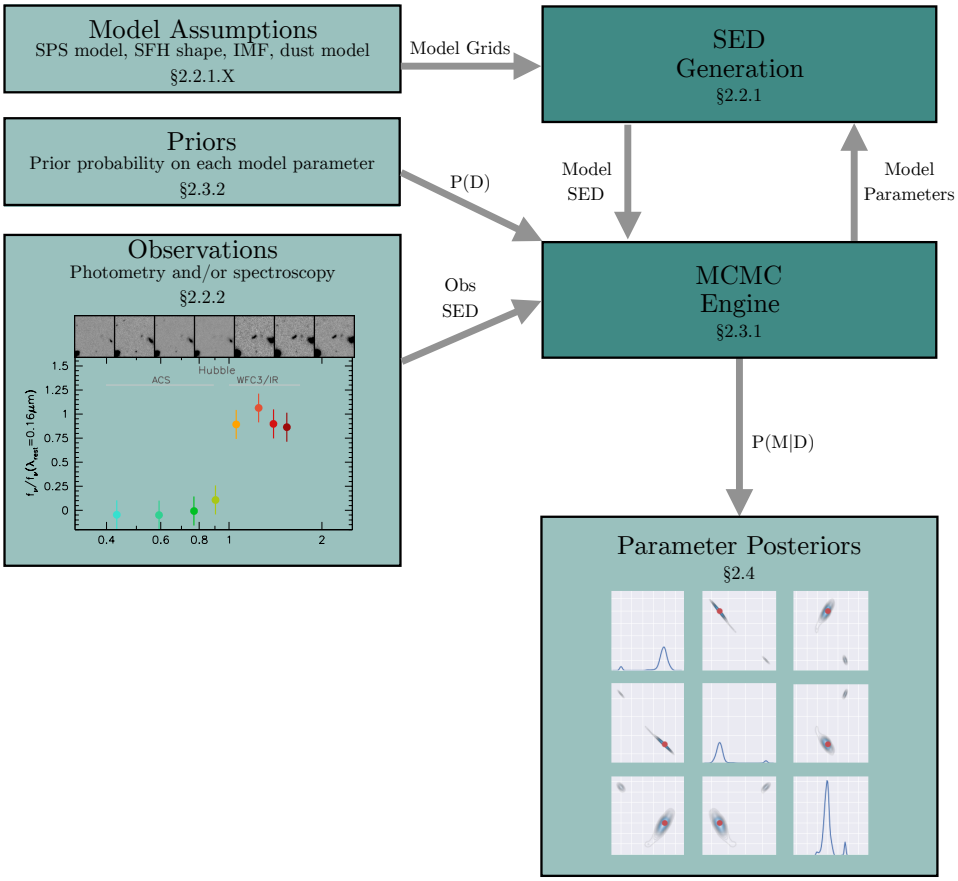

Figure 2.1: Flowchart of the structure of the INTERROGATOR code. The code is largely split into two major modules: An SED generator, which takes model assumptions such as an SPS library, an IMF, a dust model shape, and a SFH shape, along with relevant parameters and turns them into a spectra. And an inference engine, which is used to find the optimal parameters to match a set of observations. Section numbers discussing each part of the code are found below their labels in the figure.

what effects it has on SED fits to simulated galaxies.

This chapter will therefore break down INTERROGATOR into its constituent parts, and discuss how each is specifically handled within the code. Figure 2.1 is a flowchart showing the overall flow of the code, with appropriate section references added for where they are found in the main body.

2.2 The Interrogator Code

In section 1.5.1, we discussed how to generate an SED from a set of model parameters in general. In this section we will outline how INTERROGATOR accepts a set of parameters, and outputs a spectra and/or photometry set. We then will detail how INTERROGATOR uses it's inference engine to fit these models to data, and solve for probability distributions in parameter space.

2.2.1 SED Model Generation

In order to fit data with models, we first must be able to generate convincing model galaxies from a set of physical parameters. Precisely which parameters go into this set depends on the models being used – while some such as some description of the star formation history are common across all choices, some others are not always present, for example the star formation history can feature almost an arbitrary number of parameters if one has enough data to support them.

2.2.1.1 Stellar Emission

The generation of stellar emission is arguably the most important aspect of SED modelling – it is the base on which the other effects are applied. It is also a component which is subject to significant modelling uncertainty, because it is reliant on underlying stellar models.

In Section 2.2.1.1 we briefly described how, through the procedure of stellar population synthesis, the spectra of simple stellar populations (SPSs) are assembled from the combination of isochrones, stellar spectra, and a choice of initial mass function.

There are a range of SPS models available in the literature, each of which makes different choices or assumptions for the isochrones, stellar spectra, and/or IMF. Some models. For example some include more detailed modelling of rare (but seemingly important) phases of stellar evolution [Maraston, 2005] or include the effects of binary star interactions Eldridge *et al.* [2017b].

In practice each of these models provide a grid of stellar spectra for different ages and metallicites for one or more IMFs. The specific choices of ages and metallicities for the grid vary from model to model, with some models providing relatively sparse grids and others providing a much more comprehensive library.

By default however, INTERROGATOR uses the BPASS [Eldridge *et al.*, 2017b], an SPS model which is ideally placed for the generation of model EoR galaxies for a few reasons. Firstly and most prominently for purely stellar SEDs, BPASS does not treat all of it's stars as individual entities. Stars are allowed to form binaries, which has large effects on the ionising spectra, which naturally has important consequences for reionisation. Secondly, BPASS features extremely metal poor, high mass stars which are thought to be found in early galaxies. As stellar luminosity scales so steeply with stellar mass – an effect which is even more stark in the UV, young, high mass stars are vitally important to the overall UV spectra of the galaxy.

However, it is important to stress that the core philosophy of INTERROGATOR is flexibility and the code can, and does, employ a range of models. Chapter 3 will feature a practical application of this flexibility.

Each model also presents these spectra in a different file format, though many simply provide a single ASCII file for each SSP. Further, models use a range of different wavelength resolutions with some models providing spectra at resolution varying as a function of wavelength. Finally, each model has different unit conventions for both the wavelength/frequency grid - with , nm, μm, m, and Hz all used - and the luminosity - with Jy, nJy, W, erg s^{-1}, and erg s^{-1} Hz^{-1} all utilised. Most SEDs are normalised to 1 $M_\odot$ but some assume 10^6 $M_\odot$.

Our first task is to integrate these models into the INTERROGATOR code is to harmonise the unit choices and collect each grid of spectra into a single machine readable (Python pickle file) for efficiency. We use wavelength in units of and describe the spectra using the spectral luminosity density (L_ν) with units erg s^{-1} Hz^{-1}. We normalise each SED to assume a mass of formed stars of 1 $M_\odot$. We do not however alter the resolution or age/metallicity grid; the

main code takes these into account in subsequent calculations. This grid is mathematically described by $L_{i,j}^{\mathrm{SSP}}$ where i, j are indices running over the number of age and metallicity bins respectively.

As discussed in 2.2.1.1 these grids of SED can be combined together, through a star formation and metal enrichment history (SFZH), to produce the SED of a composite stellar population.

Within Interrogator the the SFZH is implemented as a grid with the same dimensions as the SPS model age/metallicity grid. Each grid point denotes the amount of (initial) mass associated with each age and metallicity. Mathematically, $\psi_{i,j}$ denotes the amount of (initial) mass in the ith age bin and jth metallicity bin.

The composite stellar SED is then simply the sum of the product of the SSP SED $L_{i,j}^{\mathrm{SSP}}$ and the SFZH grid $\psi_{i,j}$:

$$L^{\star}(\lambda) = \sum_{i,j} L_{i,j}(\lambda)^{\mathrm{SSP}} \psi_{i,j} \tag{2.1}$$

In principle every grid point of the SFZH could be left as a free parameter to be fit by the model, and indeed, Interrogator has this capability. However, for our primary usage - the analysis of broadband photometry - this will not only result in unphysical over-fitting but will dramatically increase the computational requirements. Like many SED fitting codes Interrogator can instead adopt a simplified parametrisation of the SFZH of the users choice.

The most common simplification is to adopt a constant metallicity independent of age (i.e. $Z = Z_0$), decoupling the star formation history and the metal enrichment history. Figure 2.2 shows an example of these SFHZ grids for a variety of different star formation histories. More complicated star formation and metal enrichment histories require the provision of an analytic formula describing the amount of star formation as function of age t and metallicity Z, $\psi(t, Z)$. Armed with this it is then possible to calculate the amount of stellar mass, in each age/metallicity bin by simply integrating across the bin, in both

dimensions. In chapter 4 we formulate a more sophisticated possible model for use on high redshift galaxies, influenced by the analysis of the BLUETIDES cosmological hydrodynamical simulation.

It is important to note here however that SPS typically do not provide SED integrated across an age bin but at a specific midpoint age. Were the spacing between bins large this would lead to a systematic bias. Fortunately most SPS models are output using a relatively fine age grid mostly mitigating this issue. We therefore define the bin edges over which the SPS spectra applies as $t_i - 0.5(t_i - t_{i-1})$ and $t_i + 0.5(t_{i+1} - t_i)$ for the upper and lower limits respectively, defining the metallicity bin edges in the same way. The exceptions to this are the first and final bins: for the lower bins we define the age and metallicity limits as $t = 0$ and $Z = 0$ respectively, and for the final bins we define the maximum as $t_i + 0.5(t_i - t_{i-1})$, again defining the metallicity overall upper limit in the same way.

As noted above, with both the SPS SED grid and SFZH we can produce a composite stellar SED. Figure 2.3 shows example composite stellar SEDs assuming a constant star formation history.

An important physical property of a galaxy is the total mass in stars, $M_\star$. While naively this might be thought of as being equal to the sum of the SFZH grid this is not the case as the values in this grid are the *initial* mass. The reason for this convention is that SPS models are typically normalised by the initial mass and not the current mass. Over a stellar populations lifetime some fraction of the initial mass will be returned to the inter-stellar medium, this is dependent on both age and to a lesser extent the metallicity. Fortunately most SPS models provide this *remaining* fraction $f_{i,j}^{\rm rem}$.

The current stellar mass can then be calculated by simply summing the product of the star formation and metal enrichment history and this grid, i.e:

$$M_\star = \sum_{i,j} \psi_{i,j}\ f_{i,j}^{\rm rem}. \tag{2.2}$$

This is automatically calculated and recorded by INTERROGATOR for utilisation later.

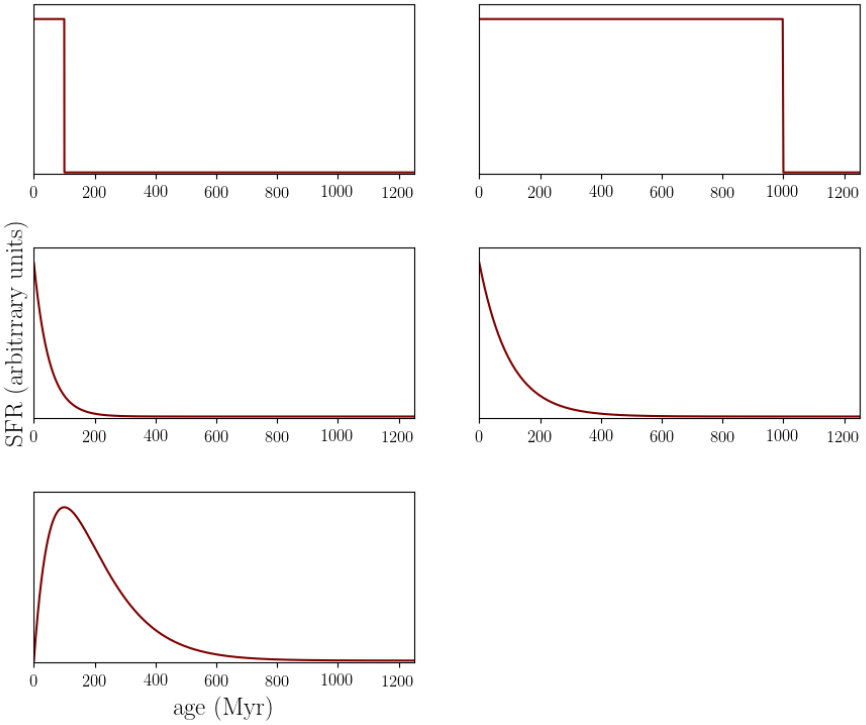

Figure 2.2: Example SFZH grids assuming the BPASS model age and metallicity bins, with constant metallicity $\log_{10} Z = -2.0$ and varying star formation histories. Top row shows constant SFHs with durations of $100Myr$ and $1Gyr$, second row shows SFHs with time constants $\tau = 10Myr$ and $\tau = 100Myr$. Final row shows a delayed tau model: $SFR \propto t \exp -t/\tau$ with $\tau = 100Myr$.

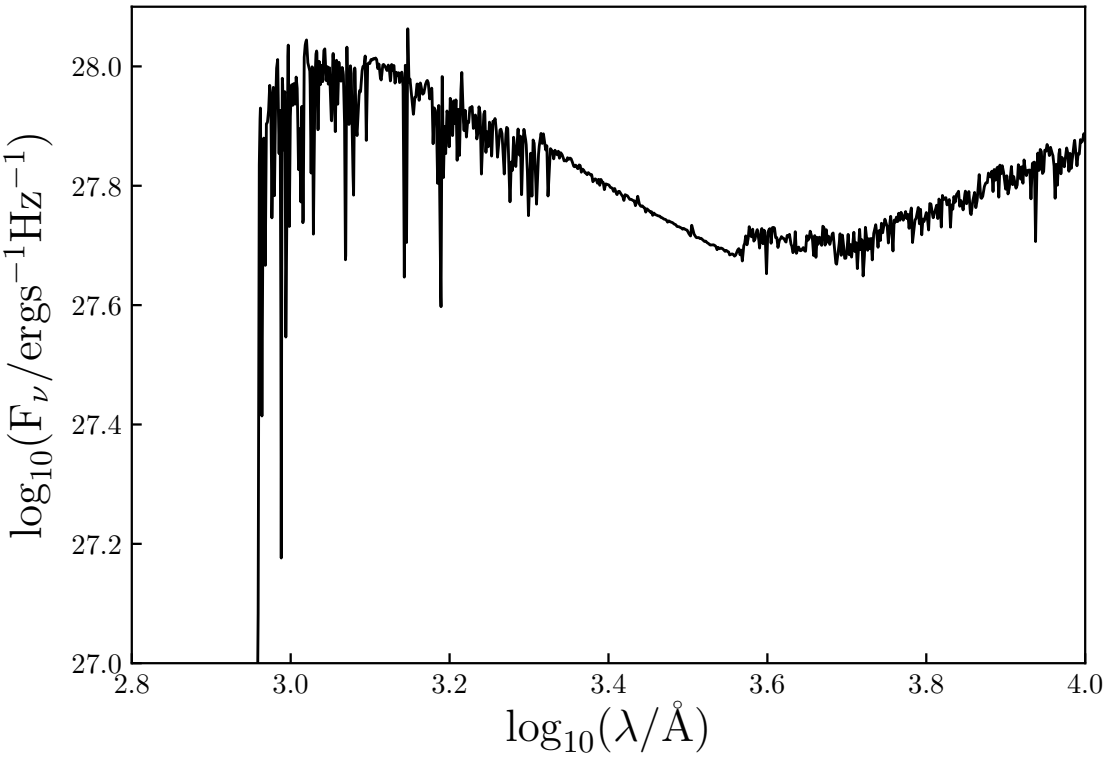

Figure 2.3: The pure-stellar spectra of a $M_\star = 10^8$ $\mathrm{M}_\odot$ that constantly formed stars over 100 Myr with $Z = 0.001$ generated by INTERROGATOR from the BPASS SPS model.

2.2.1.2 Reprocessing by Gas

Unfortunately, not all light produced by stars escapes unimpeded from galaxies, some, and in some cases most, is reprocessed by gas and/or dust in the inter-stellar medium of each galaxy. Gas excited by nearby hot/massive stars results in the creation of nebular HII regions which are dominated by strong emission lines with an underlying continuum.

To model nebular emission in INTERROGATOR we combine the SPS SEDs with the CLOUDY photon-ionisation model [Ferland *et al.*, 2013]. For each age/metallicity bin, we treat the pure stellar spectra as the incident spectra on a nebular region with some parameters encoding geometry and composition. We assume that the composition of the nebular regions mirror the stars it is being illuminated by, as the young stellar populations will have formed out of this material itself.

For the fiducial model we assume parameters of $n_H = 100$ cm^{-3} and $\log_{10} Q = -2$, and assume that there is an almost zero Lyman-continuum escape fraction, effectively calculating the maximum nebular contribution.

Using these parameters we compute a single SED grid of the output nebular emission over the same age and metallicity bins. While in principle we could compute many nebular grids, and include $n_H, \log_{10} Q$ as parameters in fits, this significantly adds to computational expense which is unnecessary for photometric observations as the effect is small. It is important to note that these parameters can be important for predicting the exact flux of emission lines however, and when comparing to spectroscopy re-computation of grids with other parameters can be a valuable exercise.

Example SSP SEDs including maximum nebular emission $f_{\rm esc} = 0$ are shown in Fig. 2.5 for a range of ages and metallicities. As nebular emission is mostly driven by the amount of Lyman-continuum photons it is only important at young ages ($t < 100$ Myr) and is enhanced at lower metallicities.

Because we know that some fraction of ionising photons must escape the ISM of high-redshift galaxies in the default implementation of INTERROGATOR we then introduce a free parameter, the Lyman-continuum escape fraction $f_{\rm esc}$, which can either be fit or fixed.

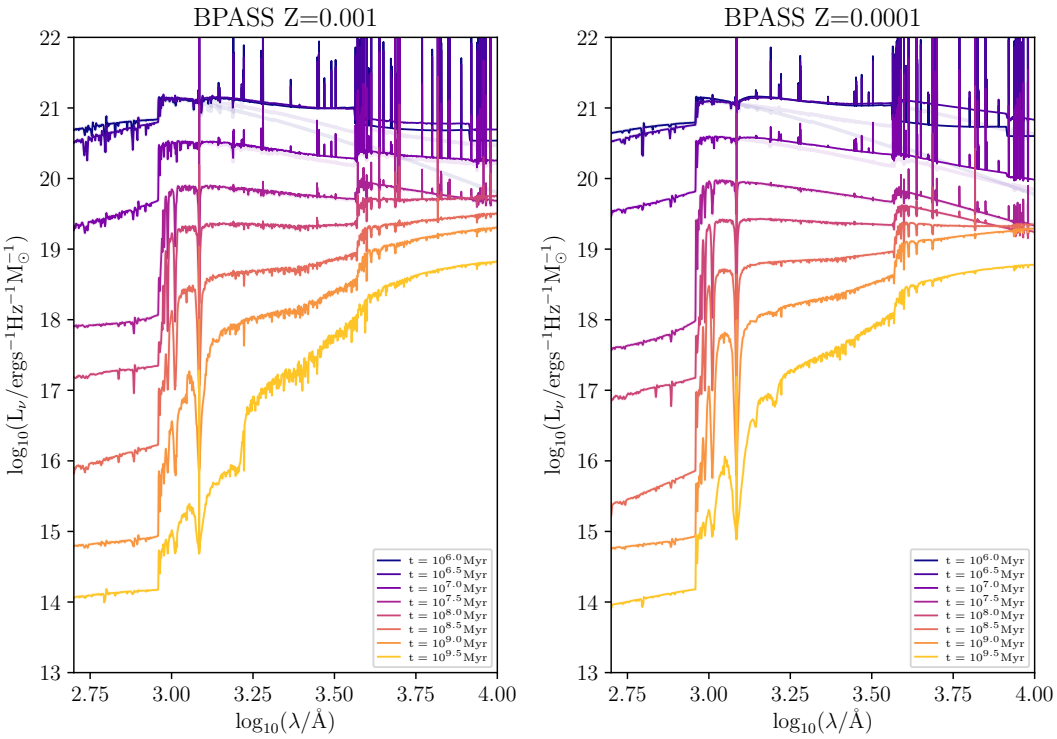

Figure 2.4: The normalised spectra of an SSP with maximum $f_{\mathrm{esc}} = 0$ nebular emission for a variety of ages and $Z = 0.001$ (left) and $Z = 0.0001$ (right). The faint lines show the pure stellar emission.

Instead of re-running CLOUDY on-the-fly (which would be computationally prohibitive – a CLOUDY call is a factor of ~ 10 slower than a single call to the rest of the model) or even building a grid for different values of $f_{\rm esc}$ we assemble our composite spectrum $L^{*\,+\,neb}$ as the addition of a pure stellar component, and a component affected by nebular attenuation. That is:

$$L^{*\,+neb}(\lambda) = f_{\rm esc} L^{*} + (1 - f_{\rm esc})(L^{*}_{T} + L^{n}eb) \tag{2.3}$$

where L^{*} is the pure-stellar emission as if there were no nebular component, L^{*}_{T} is the stellar emission transmitted through the surrounding gas predicted by CLOUDY, L^{neb} is the nebular continuum plus line emission and L^{*+neb} is the resulting composite stellar and nebular emission.

In Fig. 2.5 we show the SED of a galaxy formed assuming 100 Myr of constant star formation with $f_{\rm esc} \in \{0, 0.5, 1\}$.

In Figure 2.6 we show the same spectra as Fig. 2.5 but also show the resulting *Webb*/NIRCam fluxes at $z = 7$, demonstrating the impact of nebular emission on broadband fluxes. For this SFZH the addition of nebular emission boosts broad-band fluxes by up-to 0.2 dex. More extreme star formation and metal enrichment histories (e.g. exponentially increasing with time and/or lower metallicity) will produce an even larger effect. This clearly demonstrates that including nebular emission is crucial to accurately inferring stellar masses and other physical properties.

2.2.1.3 Reprocessing by Dust

Dust has a large effect on the overall SED, especially in the UV, and optical with attenuation, and the far infrared with re-emission. As discussed in Section 1.5.1.2, dust curves are derived in a variety of ways, but ultimately boil down to a function which acts as a multiplicative factor on the un-attenuated spectra produced by starlight & nebular emission combined. The exact form on this function depends on the amount of dust, the grain size distribution

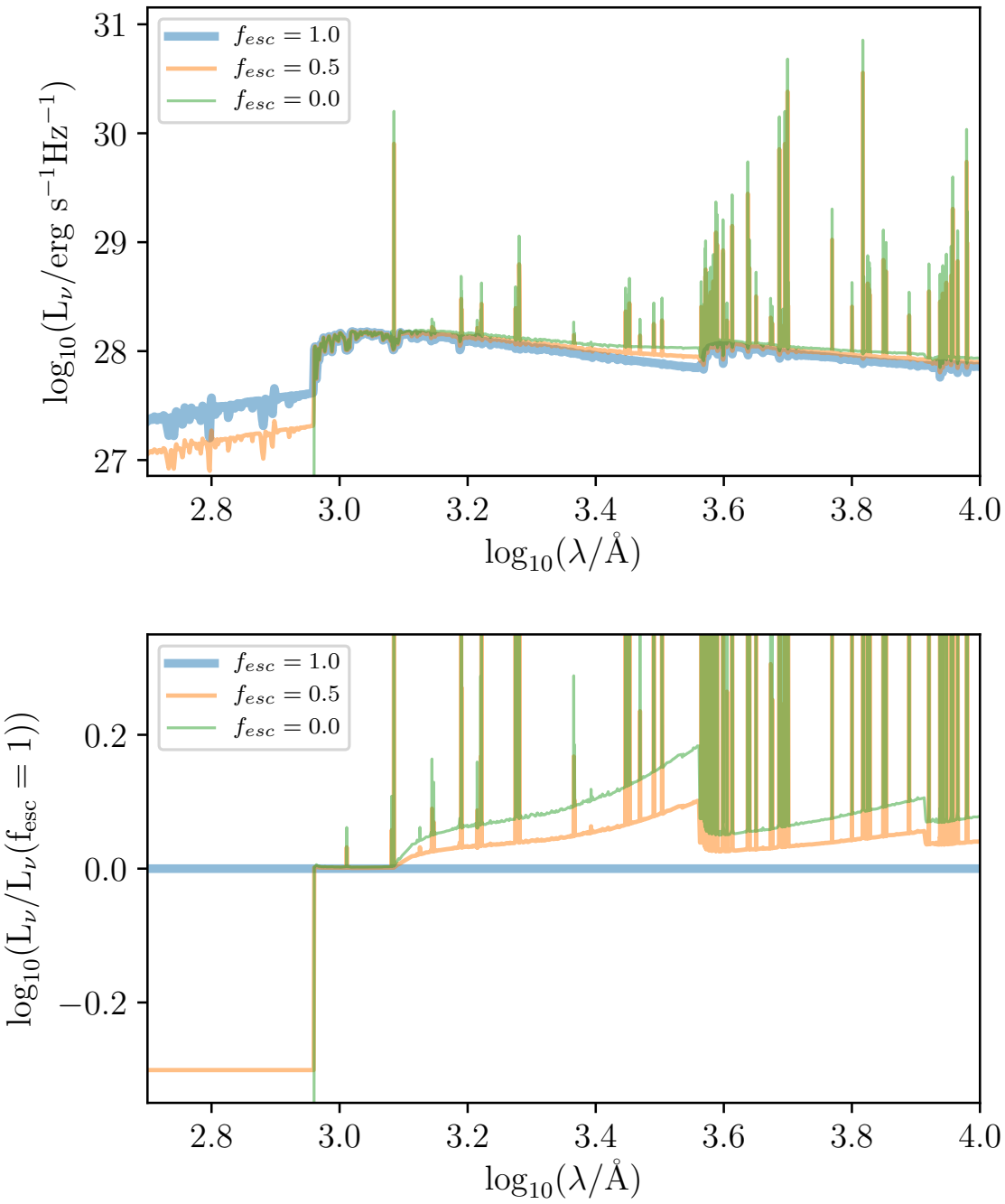

Figure 2.5: The spectra of a dust-free $M_\star = 10^8$ $M_\odot$ that constantly formed stars over 100 Myr with $Z = 0.001$ and assuming $f_{\rm esc} \in \{0, 0.5, 1\}$. The bottom panel shows the difference relative to $f_{\rm esc} = 1$.

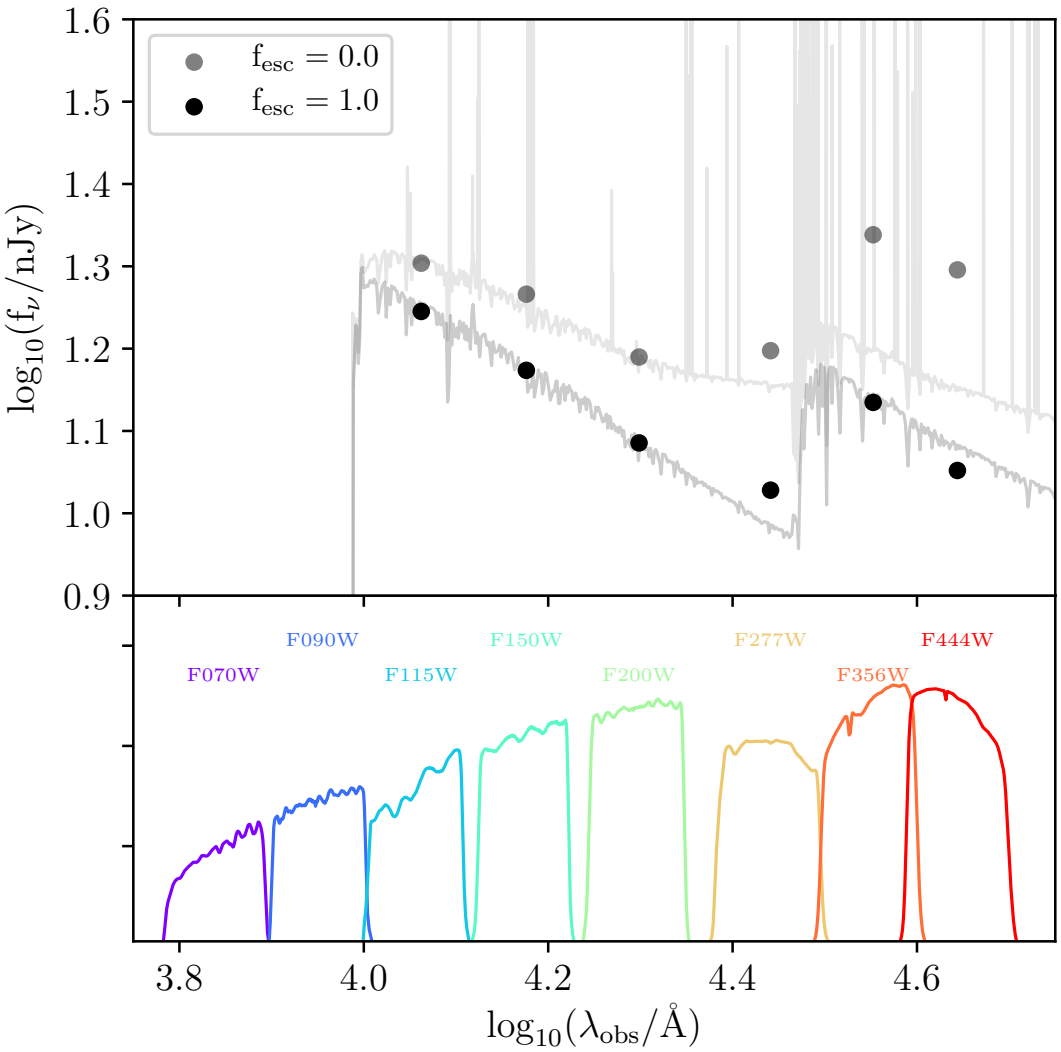

Figure 2.6: Observed NIRCam fluxes of the same model galaxy shown in Fig. 2.5 assuming $f_{esc} = 1$ (no nebular emission / gas reprocessing) and $f_{esc} = 1$ (maximum nebular emission).

of the dust, and the assumed geometry between the stars and dust.

INTERROGATOR is capable of using a range of dust models, both fixed in shape (with normalisation only) and flexible (with one or more shape parameters in addition to normalisation).

The simplest possible model here is the simple screen. This model assumes that the dust is arranged in a uniform thickness screen between stars and observer, i.e. that all stellar populations in the galaxy feel the same attenuation. In this case the total spectrum $L^{*+neb+dust}$ is simply,

$$L^{*+neb\ +\ dust}(\lambda) = L^{*+\ neb}(\lambda) \times T_d(\lambda), \tag{2.4}$$

where T_d is the dust transmission function. T_d is related to the optical depth,

$$T_d(\lambda) = exp(-\tau_\lambda). \tag{2.5}$$

τ_λ itself can have a number of forms, though one of the simplest is,

$$\tau_\lambda = -\tau_0 \left(\frac{\lambda}{\lambda_0}\right)^{-\alpha} \tag{2.6}$$

where τ_0 is the optical depth of the dust at some normalising wavelength λ_0 and α is some free parameter describing the slope of the curve. λ_0 is often chosen to correspond to the rest-frame V-band (5500). A common choice for α is 0.7 which mimics the shape of several literature attenuation curves. Alternatives for $T_d(\lambda)$ include extinction curves such as those applicable for the Milky Way (MW) or Small Magellanic Cloud (SMC). Figure 2.7 shows the wavelength dependence of dust extinction and attenuation curves built into INTERROGATOR.

In Figure 2.8 we demonstrate the effect of dust assuming our simple power-law model (assuming $\alpha = 1$) on the constant star forming SED (with $f_{\rm esc} = 1$) shown in Figure 2.5. In Figure 2.9 we show how the choice of dust-curve or slope with fixed τ_V affects the overall SED.

One popular alternative to simple model is the empirical dust attenuation law as derived in Calzetti [2001]. This law is derived from the observation of nearby starburst/blue compact

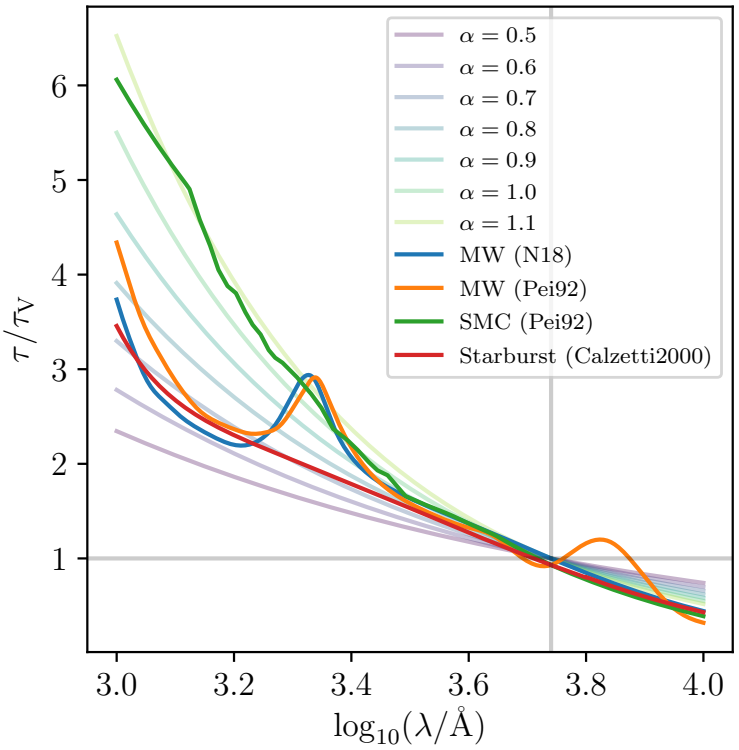

Figure 2.7: Dust extinction and attenuation curves built into INTERROGATOR. Shown are curves commonly used from the literature [Nataf, 2018; Pei, 1992; Calzetti, 2001] and a simple power-law parametrisation and varying slope α.

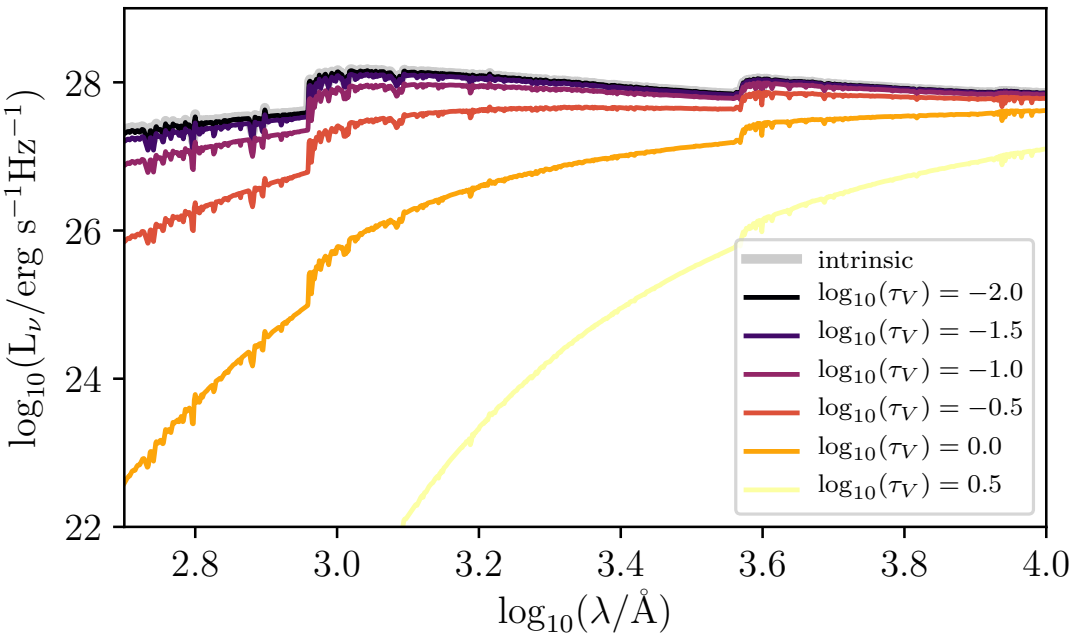

Figure 2.8: The same model galaxy as shown in Fig. 2.5 but with dust attenuation. Taking a power law dust curve with $\alpha = 1.0$ as shown in figure 2.7 at various different normalisations τ_V, and convolving it with the model galaxy show the effect of adding more and more of the same type of dust to a galaxy.

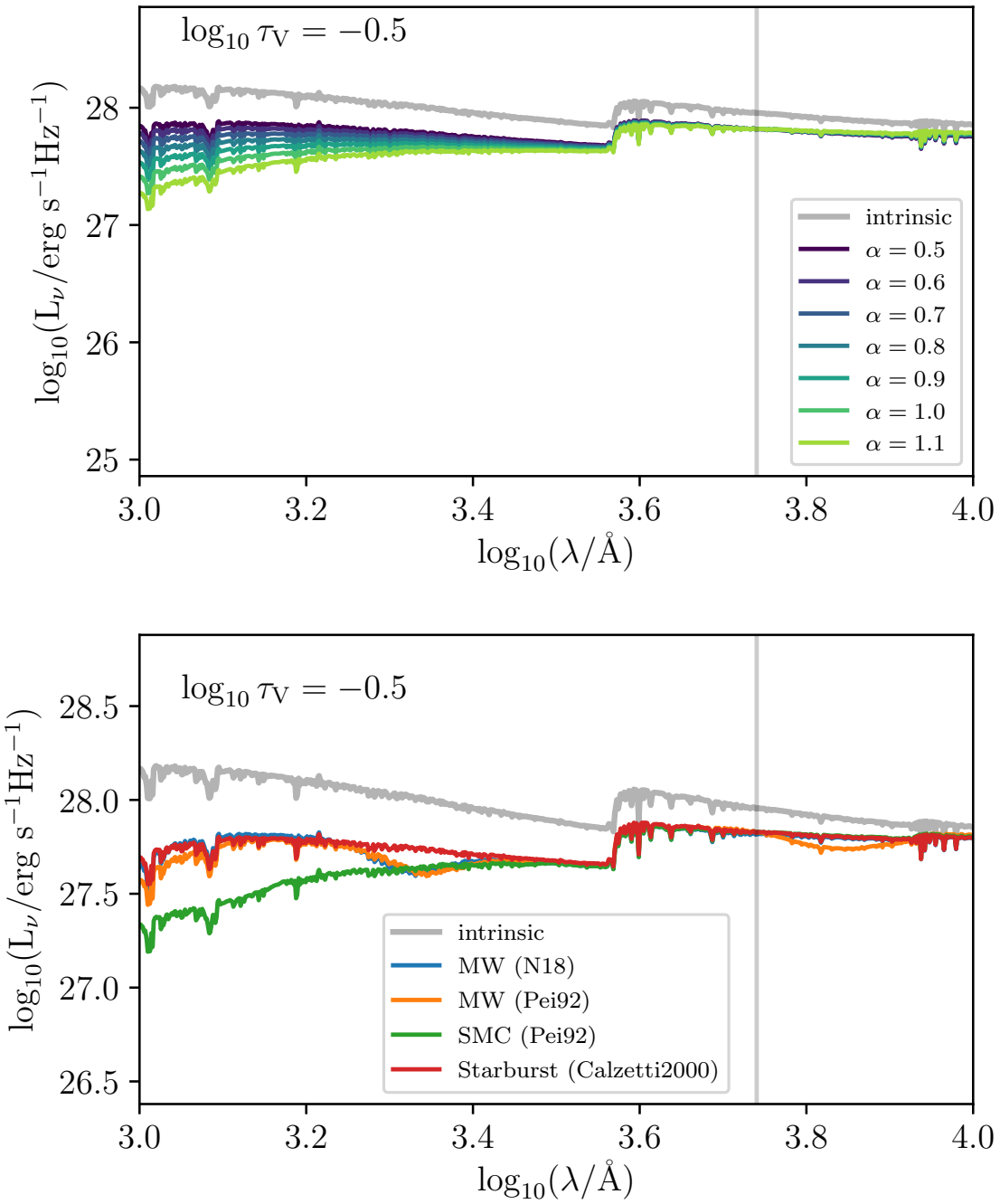

Figure 2.9: The same model galaxy shown in Fig. 2.5 but with dust attenuation assuming $\log_{10}\tau_V = -0.5$ but different dust-curve slopes (top) and literature curves (bottom).

dwarf galaxies, using their UV continuum slope and Balmer decrements to empirically fit a dust curve which takes the form:

$$k(\lambda) = A(\lambda)/E(B-V)_* = a + b\lambda^{-1} + c\lambda^{-2} + d\lambda^{-3} \tag{2.7}$$

where $a, b, c\&d$ are constants which are over piece-wise wavelength ranges.

While the Calzetti model is largely a variant of a simple screen model, it formally treats nebular emission differently from stellar emission requiring that these two components be separated inside the code.

Charlot & Fall A popular alternative model, implementing a more realistic geometry is that developed by . In this model young stars are embedded in their "birth clouds" and thus feel an additional source of attenuation compared to older stars, which are only affected by dust in the diffuse ISM.

The innovation of this model is treat young and old stellar populations differently, reflecting the observation that young stellar populations are often still embedded in their birth-cloud, and thus subject to greater attenuation.

The total transmission T_d is then written as the produce the birth-cloud and diffuse ISM transmission,

$$T_d = T_{\rm ISM} \times T_{\rm BC} \tag{2.8}$$

where crucially all stars feel the same $T_{\rm ISM}$ but only young stars feel $T_{\rm BC}$. Mathematically, this is described by,

$$T_{\rm BC} = \begin{cases} \exp(-\tau_{\rm BC}) & \text{if } t < t_{\rm BC}, \\ 1.0 & \text{if } t \geq t_{\rm BC}, \end{cases}$$

where $\tau_{\rm BC}$ are the transmissions through the ionised and neutral gas in the birth cloud respectively and $t_{\rm BC}$ is the timescale over which the birth cloud is assumed to have an effect.

In the CF01 model $\tau_{\rm BC}$ and $\tau_{\rm ISM}$ were assumed to be power laws,

$$\begin{aligned} \tau_{\rm BC} &= \widehat{\tau_{\rm BC}} \left(\tfrac{\lambda}{5500}\right)^{-\alpha_{\rm BC}} \\ \tau_{\rm ISM} &= \widehat{\tau_{\rm ISM}} \left(\tfrac{\lambda}{5500}\right)^{-\alpha_{\rm ISM}} \end{aligned},$$

In the original CF01 model $\alpha_{\rm BC} = \alpha_{\rm ISM} = 0.7$ and $\widehat{\tau_{\rm BC}} = 2 \times \widehat{\tau_{\rm ISM}}$. The separation between the young and old components was fixed to be 10^7 years. This model is implemented in Interrogator but it is disfavoured because it contradicts the use of the escape fraction parameter.

Pacman Model Interrogator can use the default implementation of the CF01 model but makes two generalisations providing additional flexibility. Firstly, $\alpha_{\rm BC}$ and $\alpha_{\rm ISM}$ can have independent values and can even be left as free parameters. Similarly, $\widehat{\tau_{\rm BC}}$ and $\widehat{\tau_{\rm ISM}}$ can be decoupled and both left as free parameters. Secondly, in the nebular section, we introduced $f_{\rm esc}$ as a free-parameter to allow some fraction of the Lyman-continuum emission to escape the galaxy. As dust and gas are coincident with each other such a model only makes sense if the dust also has a similar open channel allowing photons to escape unimpeded by both gas and dust. As such, the default dust model in Interrogator is a modified implementation of the CF01 model. A schematic of this "PACMAN" model is shown in Figure 2.10.

Implementing this dust-model in Interrogator requires that we separate both the young and old stellar population (defined potentially a free parameter, but by default fixed chosen to be 10^7 years) and the light which is able to freely escape from that which is reprocessed by dust and gas. Figure 2.11 shows the total SED and both the young and old components assuming $f_{\rm esc} = 0$ and no dust. Figure 2.12 shows the same as Figure 2.11 but shows the spectrum for a galaxy forming stars over 10^9 years.

Figure 2.13 now shows the total SED and both the young and old components assuming with dust $\log_{10}(\tau_V) = -0.5$ and $f_{\rm esc} = 0$ and $f_{\rm esc} = 0.2$. $\log_{10}(\tau_V)$ is however no longer the total actual V-band attenuation but is only the V-band attenuation felt by the old component.

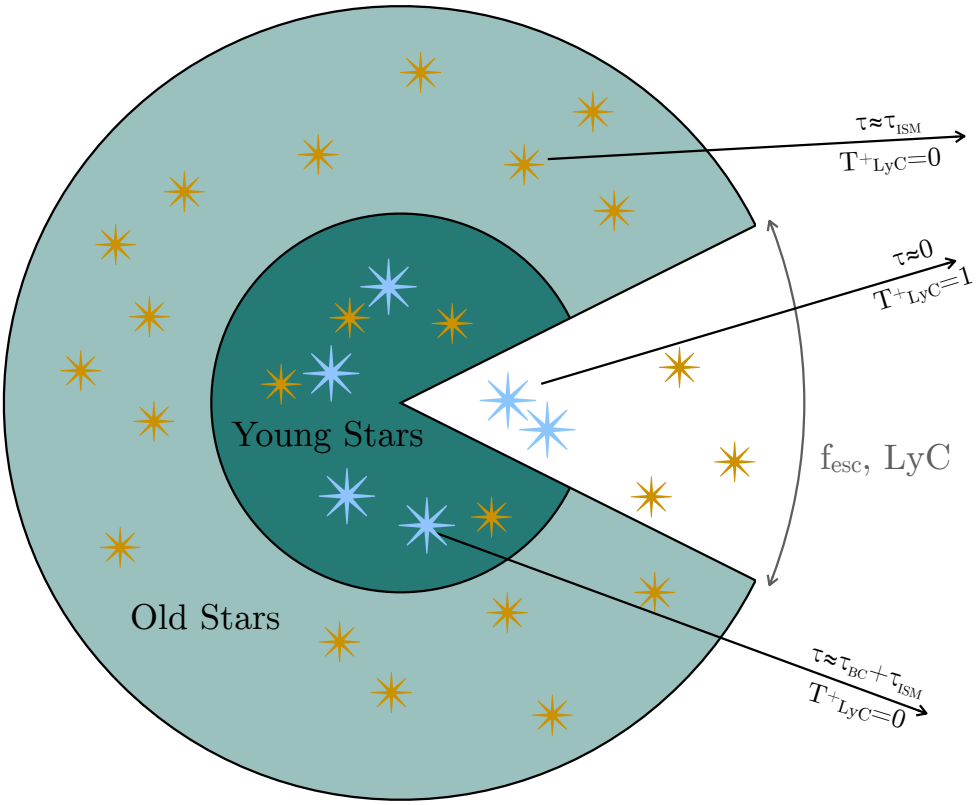

Figure 2.10: Structure of the default dust-model in INTERROGATOR a modified version of the Charlot & Fall (2001) model.

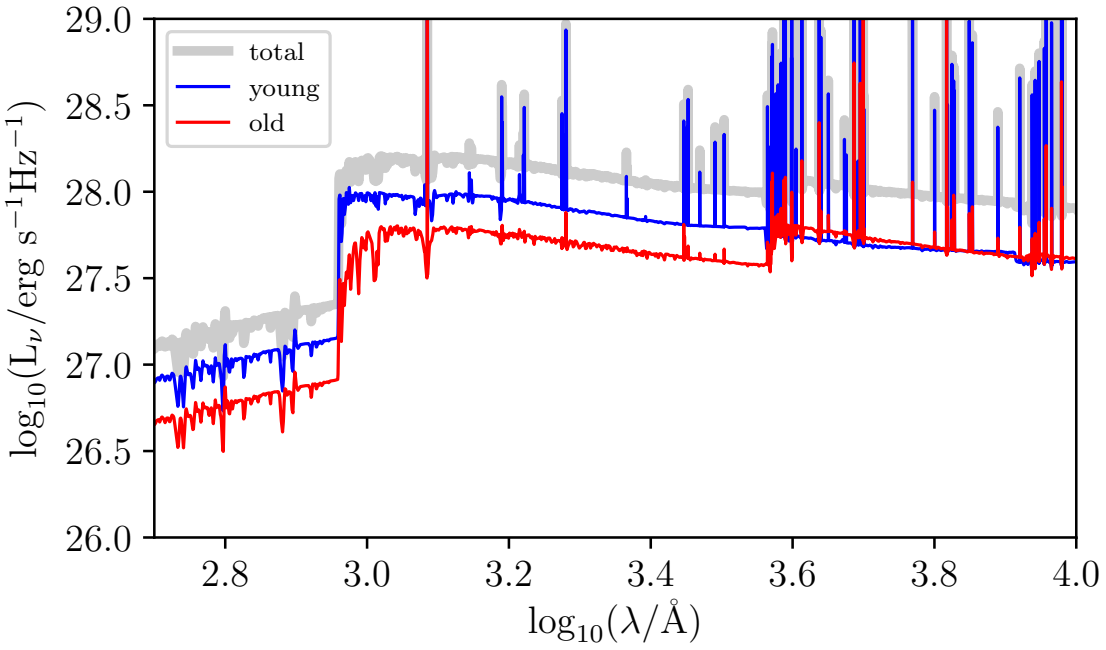

Figure 2.11: Dust attenuation of young and old stellar components assuming $f_{\rm esc} = 0$ and no dust.

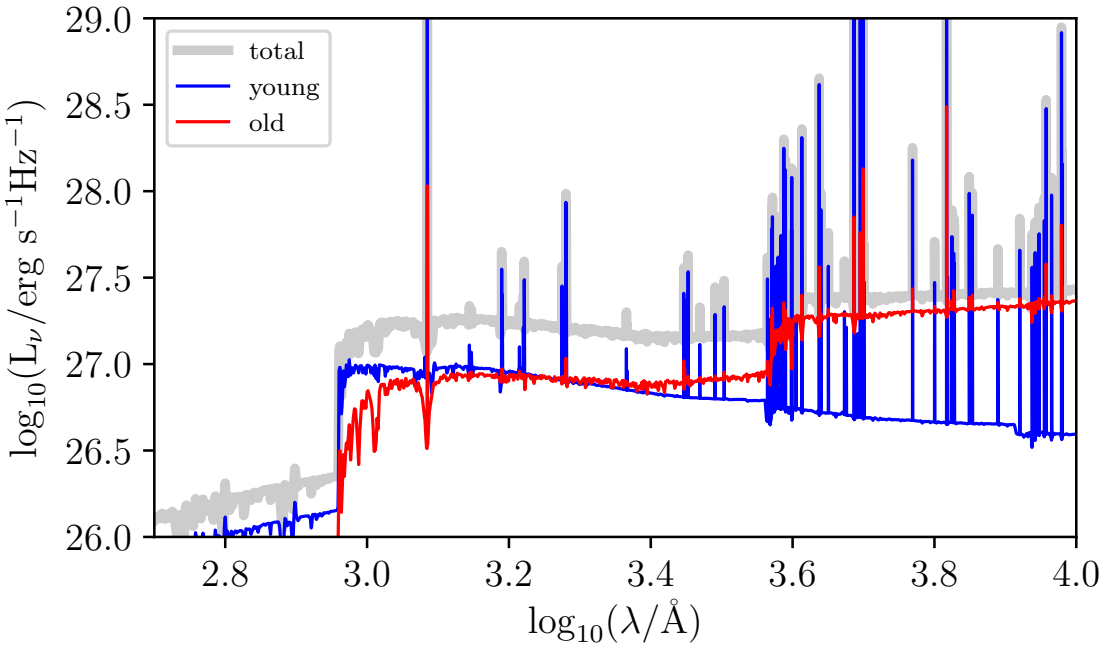

Figure 2.12: The same as Figure 2.11 but now assuming constant star formation for 10^9 years to emphasise the contribution of the young component.

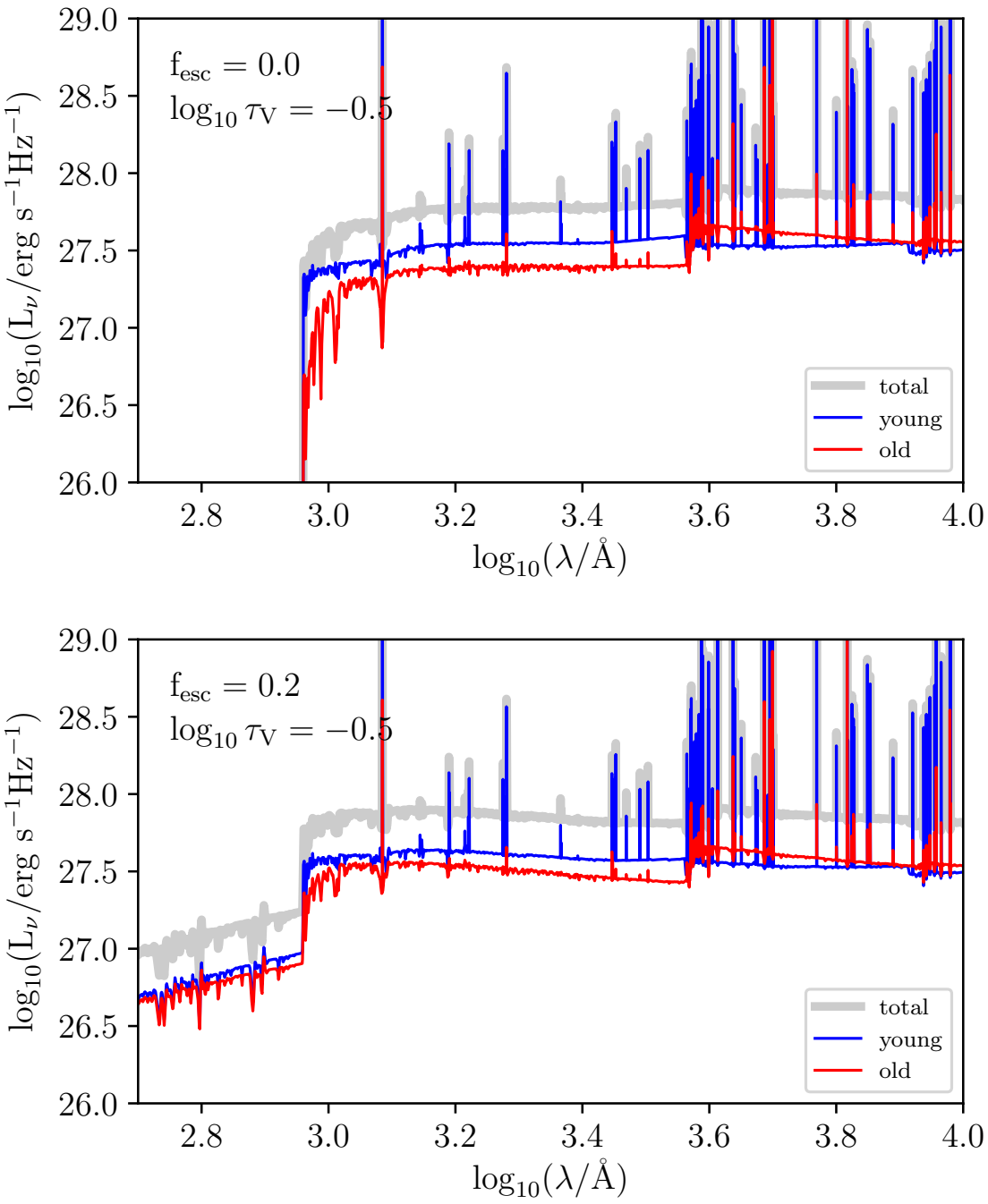

Figure 2.13: Predicted SED for the "PACMAN" dust model with the V-band attenuation of the old component $\log_{10}(\tau_V) = -0.5$ and $f_{esc} = 0$ (top) and $f_{esc} = 0.2$ bottom.

2.2.1.4 Reprocessing in the IGM

The final effect we need to account for, before calculating observables, such as broadband fluxes and spectra, is absorption by the diffuse intergalactic medium (IGM) along the line-of-sight to each galaxy. While *mostly* ionised the IGM contains some neutral gas in clouds capable of absorbing radiation from distant galaxies and quasars.

Firstly, any residual emission falling below the Lyman-limit (912Å) will be rapidly absorbed. However, by the time a a photon emitted by a galaxy at $z_{\rm gal}$ has reached the cloud at $z_{\rm cloud}$ it will have lost some energy and may no longer fall below the Lyman-continuum when it reaches the cloud. As a consequence, not all the Lyman-continuum radiation escaping a galaxy will necessarily be absorbed by intervening clouds. The effect then clearly depends on the distribution of clouds along the line-of-sight.

In addition to the absorption of Lyman-continuum photons intervening clouds can also absorb light at various electron transitions, most prominently the Lyman-series, and in particular Lyman-α. However, for the same reason as described above, the location of the line absorption in the emitted rest-frame will depend on the redshift separation of the cloud and galaxy. The result of multiple discreet clouds along the line of sight will then be the imprinting of a series of lines on the emitted rest-frame spectrum, at $\lambda_{\rm rest} < 1216$Å. Where this process is incomplete the spectrum appears dominated by multiple absorption lines giving rise to the Lyman-α forest. At high-redshift ($z > 7$) the density of absorbers and thus lines is large enough to effective remove all the photons at $\lambda_{\rm rest} < 1216$Å, becoming the Gunn-Peterson trough.

At least at $z < 7$ where the effect is incomplete, the effect will be unique to each galaxy as the line travels through a unique set of clouds. However, the effect can be statistically modelled with several implementations in the literature. For Interrogator we choose to utilise, by default, the prescription of Madau et al. (1996). However, in-line with the philosophy of Interrogator, this can be easily replaced with an alternative.

To demonstrate the extent of this effect in Figure 2.14 we show the transmission function

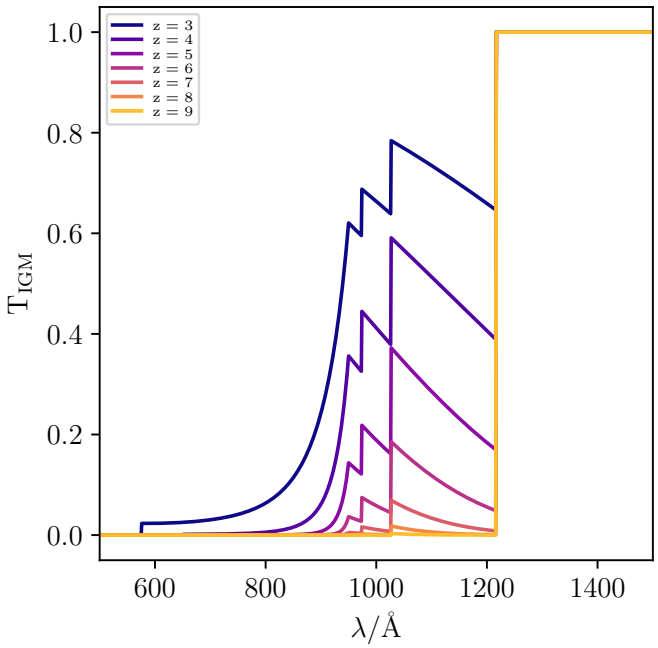

Figure 2.14: The IGM transmission predicted by Madau et al. (1996) as a function of redshift.

$T_{\rm IGM}$ as a function of rest-frame wavelength for our default implementation. As expected, due to the increasing neutral fraction at high-redshift, the transmission fraction drops precipitously, with less than 10% of the photons between the rest-frame Lyman-limit and Lyman-α transmitted.

2.2.2 Mock observations

Our final step before comparing with observations is the creation of *mock* observations. In the context of spectra, this would require degrading our SEDs to the resolution and wavelength range of the observed spectra. While the analysis of spectra from *all* of *Webb's* instrumentation will be of interest to high-redshift astronomers, high-quality spectra will only be available for the brightest galaxies at these redshift. With this in mind our focus is on interpreting broad-band photometry/imaging which can be obtained much more cheaply thus allowing us to probe to lower-luminosities and thus star formation rates and stellar masses.

Imaging, or broad-band photometry, is obtained using filters which selectively only transmit light through a relatively narrow range of wavelengths. Each filter or band is characterised by a transmission function T_λ. Many of the transmission functions of filters on existing or upcoming observatories are shown in Fig. 2.15.

To determine the flux in a particular filter $F_{\nu,i}$ we must multiply the observed spectrum f_ν by the filter transmission function T. To appropriately normalise the flux:

$$F_{\nu,i} = \frac{\int T_{\lambda,i} f_\nu \mathrm{d}\lambda}{\int T_{\lambda,i} \mathrm{d}\lambda} \tag{2.9}$$

Within INTERROGATOR this is achieved by first, at initialisation, loading all the relevant filters and mapping (interpolating) them on to an *observed* wavelength grid. Each model SED, with knowledge of the redshift, is then mapped to the same observed grid and the integration described in Equation 2.9.

An example of both the model observed spectrum and the broadband fluxes using *Webb*/NIRCam are shown in Figure 2.16.

2.3 Inference Engine

Within the context of INTERROGATOR the inference engine's purpose is to characterise the probability distribution of the parameters, based on the observations and any other prior knowledge that is present. A variety of techniques exist for doing this, with various advantages and disadvantages – the most common in this application are discussed in section 1.5.2.2. INTERROGATOR uses a specific type of Monte Carlo Markov Chain (MCMC) algorithm called affine invariant MCMC.

2.3.1 EMCEE and Affine Invariant MCMC

Affine invariant MCMC is a solution to the problem of it being unclear exactly how one should adjust various hyper-parameters for the specific problem being solved. The most

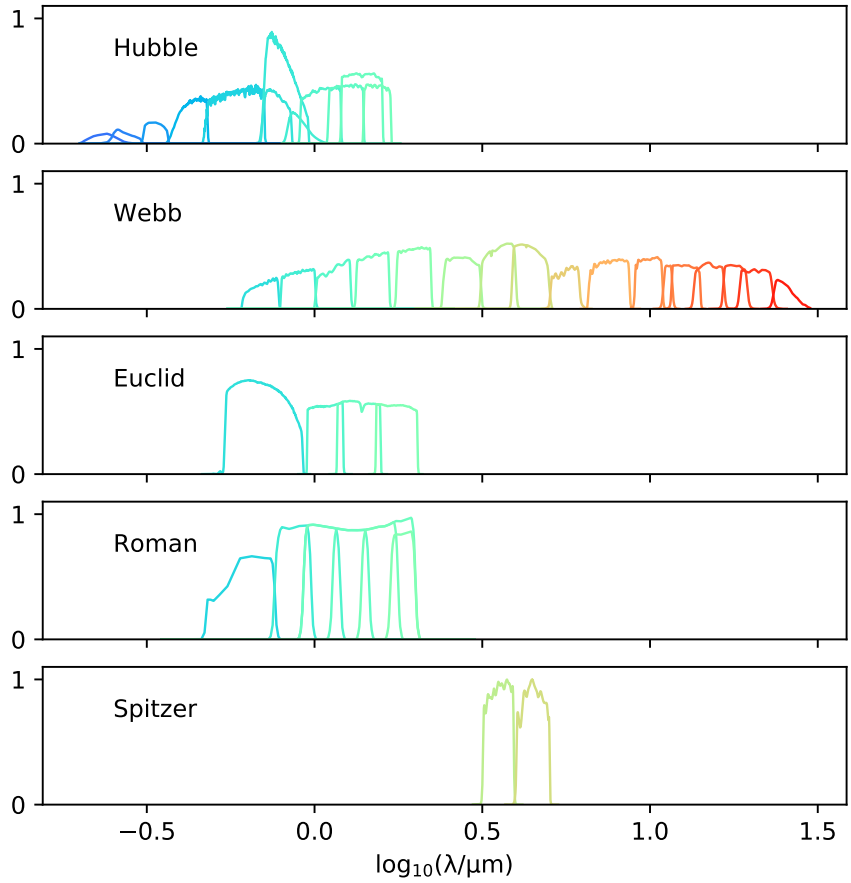

Figure 2.15: Examples of filter packages included in INTERROGATORby default as transmission fractions as a function of wavelength. HST filters shown are broad band filters from the Advanced Camera for Surveys [Sirianni *et al.*, 2005] and Wide Field Camera 3 [Windhorst *et al.*, 2011]. From Webb filters shown are broad band filters from both NIRCAM and MIRI [Tokunaga and Vacca, 2005; García Marín *et al.*, 2018, respectively]. Euclid [Maciaszek *et al.*, 2016] and Roman [Spergel *et al.*, 2015] have all broad band filters on board shown. Finally, the Spitzer space telescope's IRAC channels 1 & 2 [Fazio *et al.*, 2004] have been used in high redshift astronomy post-cryogen up until its de-orbiting in 2020, so they are included by default.

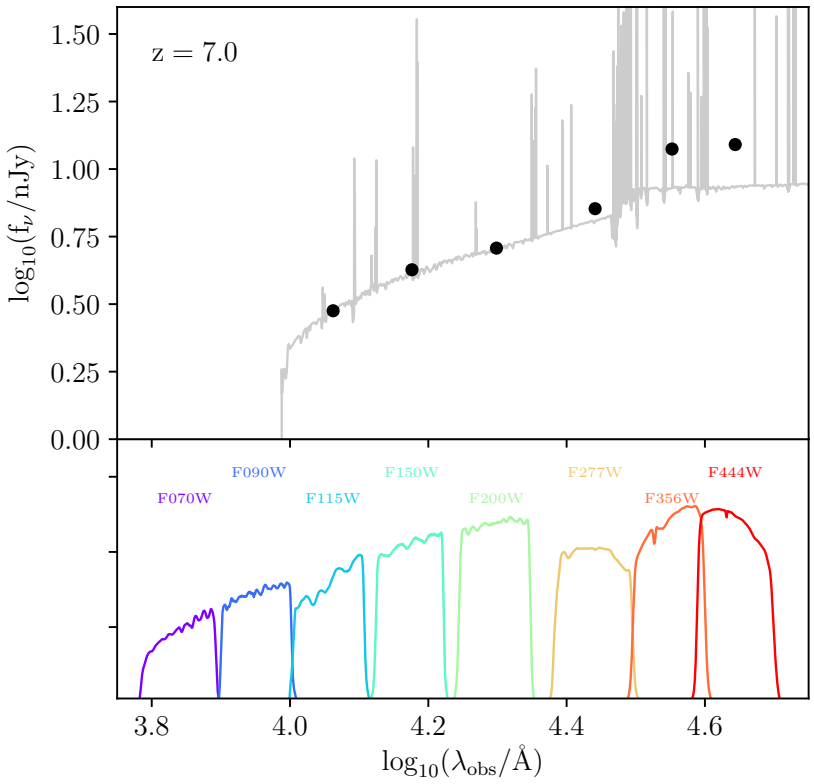

Figure 2.16: The predicted observed SED f_ν of a dusty high-redshift ($z = 7$) galaxy alongside the calculated broad-band fluxes in the *Webb*/NIRCam bands.

egregious example is that of the proposal distribution (see step 3 of the description of the Metropolis-Hastings (hereafter MH) algorithm in section 1.5.2.2. The optimal form of this distribution – both the functional form and the values of any tuning parameters governing the average "jump length" – is not something that is easily generalisable for SED fitting because often the posterior distributions are so irregular.

The solution of affine invariance is outlined in Goodman and Weare [2010], and involves the use of an ensemble of N Markov chain samplers, hereafter called "walkers". Each walker is effectively an individual MH sampler, however when it comes to the step of proposing a new set of parameters Θ_{test} instead of drawing the values in this vector from a pre-defined distribution, each walker is paired with another walker, and the proposal distribution is generated based on the position of that walker instead.

This offers significant advantages over a transitional MH style algorithm in virtually all aspects. The process can be paralellised by randomly pairing off the walkers at each step, carrying out the proposal, acceptance/rejection, and position updating steps in N/2 parallel strands, and then shuffling the walkers to repeat. In addition, for situations where hyper-parameters can't be tuned to the specific problem, it offers significant improvements in auto-correlation times, which translates to significantly cheaper computation expense.

The Markov chains can be used in the same way as traditional chains to extract posteriors, with the caveat that all of the walkers must be used together, as this pairing off process means that at a given step t, $\Theta_j(t)$ has some partner walker $\Theta_k(t+1)$ with whom it is correlated.

The specific implementation which INTERROGATOR employs is EMCEE [Foreman-Mackey *et al.*, 2013], a commonly used PYTHON implementation of the algorithm. As this inference engine is effectively the "core" of the fitting portion of INTERROGATOR it is the only module which cannot be freely swapped out. While other techniques exist such as nested MCMC or machine learning type methods, they would be beyond the scope of the code, and other codes exist (e.g. BAGPIPES, PROSPECTOR which center those inference methods.

2.3.2 Priors

An intelligent choice of prior is vital in SED fitting, as the correct choice can offer a severe reduction in the volume of parameter space needing to be explored, a reduction in degeneracies, and much better behaved posteriors. However, informative priors can offer a variety of pitfalls – an incorrect choice can offer a precise, yet biased result, and an informative prior without the observation quality to support it can lead to the posterior simply reflecting the prior.

By default then, and throughout this work, the priors used by INTERROGATOR are "flat" priors, i.e. for some parameter μ: $P(\mu) = 1/(\mu_1 - \mu_0)$ where μ_0, μ_1 are the extrema of the given parameter. These extrema are ultimately a free choice, however by default they are set so that the parameters can take any physically meaningful values.

One important consequence is that these input priors actually enforce priors on certain output parameters. A simple example would be t_0, the maximum stellar age of a galaxy. This age is intrinsically defined to the redshift of the galaxy – the maximum stellar age can't exceed the age of the Universe as that would be nonsensical, so any prior on z intrinsically applies a prior to t_0.

Less obviously, the two part work by Carnall *et al.* [2019] and Leja *et al.* [2019] constructs a compelling argument that the use of a flat prior on SFH parameters, actually imposes a strong priors on both the specific star formation rate, and the mass weighted timescale of formation (t_{MW}) (or equivalently - the mass weighted age).

Specifically, they find that applying the naive uniform prior on the exponential SFH parameter τ causes a strong preference for high sSFR, and late time t_{MW}. An effect which is only compounded at higher redshift where the very oldest stellar populations are not present. This effect is replicated in the other (delayed-τ, log-normal, double power law) SFH models they use. They find that switching to a prior which is uniform in $\gamma = \tau^{-1}$ lessens this effect, however does not completely remove it.

At least in the regime of photometry only, it is suggested that these effects introduce a

bias which is roughly consistent across all models tested, and that there is little preference between them. This potentially motivates sticking to simpler models in the interests of computation expense, and avoidance of underfitting which will result in an overestimate of the uncertainties on the parameters inferred. It should be noted however that while the median inferred parameters see little change, the shape of the whole posterior can vary significantly depending on the prior chosen, and therefore extreme care must be taken. This variation is unfortunately found to be the worst in very blue starforming galaxies. This is due to the fact that younger stellar populations are overwhelming in terms of bolometric luminous output compared to older ones, making it hard to make statements about the older stars in any highly starforming galaxy without knowledge of the dust. Additionally, a degeneracy exists between stars under 100MYr old and 100-300Myr old. One can effectively replicate the photometric properties of a 300MYr old population with a combination of a smaller < 100MYr population, and a second, older population.

In the table below, we show the recommended (and default) priors within INTERROGATOR. It should be stressed however that these are chosen to be largely as uninformative s possible, or to align with historic usages. Depending on the use case, a well chosen prior can either offer a more uninformative prior on desired physical properties (such as SFR) or a clever choice of informative prior can offer significant advantages if one has prior information to use.

2.4 Testing

While in chapter 3, we will use INTERROGATOR to analyse a sample of real galaxies as a case study, on a most basic level it is important to establish that the code will reproduce model galaxies with known model parameters.

To this end, we setup a sample of galaxies made using INTERROGATOR's fake observation tools, with a set of observations over the rest frame UV, optical and near IR based on the broad-band photometry available in the GAMA survey (see section 3.2. These galaxies all

SPS model	BPASS v2.1
IMF	Salpeter, $\alpha = -2.35$
Nebular Emission.	CLOUDY, escape frac. = 0
Dust	Modified Charlot & Fall "Pacman" model $\tau_V = 1.0$, $\mu = 0.25$, $t_{BC} = 10Myr$
Other params	$z = 0.0$, $\log_{10}(M_*) = 8.0$, $Z = Z_\odot/20$

Table 2.1: Table of synthetic galaxy parameters

use the parameters outlined in table 2.1, with varying SFHs: two constant star formations (age 1Gyr and 100Myr), and two exponentially rising SFHs (with e-folding times of 100Myr and 1Gyr). We opt for the Salpeter IMF as it is the only IMF that BPASS v2.1 supports.

We also setup the same models, but with the 3 most blue filters (GALEX-FUV, GALEX-FUV and SDSS-u) only as a test cast for galaxies which only have UV observations, such as those at high redshift. Figure 2.17 shows the model galaxy SEDs for each input model, with "UV only" models using just the first three filters (X's) and the other models using all of the shown filters (X's and circles). Figure 2.18 shows the un-normalised star formation histories of the galaxies which produced these SEDs. These SFHs are un-normalised for visualisation purposes – in reality as we have fixed the stellar mass to $10^8 M_\odot$.

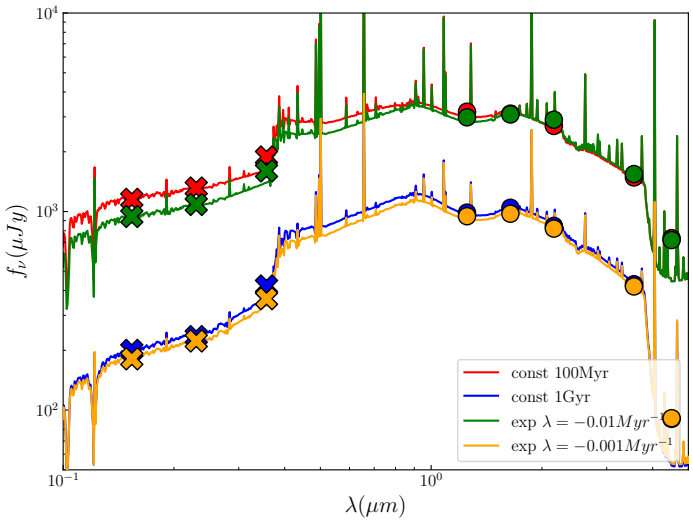

Figure 2.17: Model galaxy SEDs with parameters as laid out in table 2.1. broad band fluxes marker with X's are used in both UV only model and full GAMA model, circle marked fluxes are in full model only.

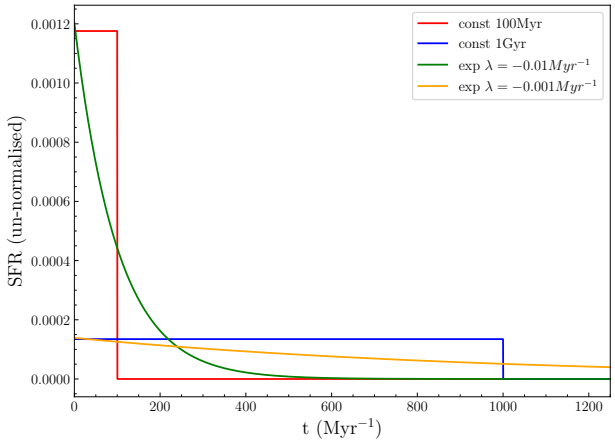

Figure 2.18: Star Formation histories of the model galaxies, with model parameters as laid out in 2.1. SFHs are un-normalised for visualisation purposes, in reality as the stellar mass is fixed, the integral under each curve is equal.

We then run these synthetic observations through INTERROGATOR, with EMCEE set to use 200 walkers, and 5000 iterations, the first 10% of which are discarded as burn-in, which results in 900,000 total samples. INTERROGATOR assumes the same model as that used to make the galaxies, and an exponential star formation history with λ allowed to vary both positive and negative and a cutoff age parameter where SF began. Note that constant star formations can be exactly reproduced in this scenario if $\lambda = 0$, however we wish for the code to not be locked into a constant SFH only, and for it to reconstruct this itself if it is appropriate.

Figures 2.19, 2.20 2.21, and 2.22 shows an example of this reconstruction for a galaxy with a constant star formation of 1Gyr. The same figures for other models are in appendix A.

Looking at the full set of observations (fig 2.19, 2.20), we first notice that the SED itself is convincingly reconstructed, with the median of each flux posterior passing within 1-σ of – the reduced χ^2 value between the model and observations for this example is 0.85. However, looking at the posteriors it is notable that a significant amount of probability resides in solutions that lie slightly further out, specifically a solution appears to exist with higher flux in the blue filters, and lower in the redder filters – likely tying into the bimodality of the μ parameter in the dust curves in figure 2.20. When we drop down to only three filters (figure 2.21), we see that the flux reconstructions are much more compact, however they do exhibit a small second mode (again likely tying into the shape of the dust posterior). This is not unexpected as a large variety of models can fit the UV only, as can be seen in the indifference of many of the parameter posteriors.

We then turn to the inferred parameters, in figures 2.20 and 2.22, each pan represents the 2-D (1-D if the row and column are the same) marginalised probability distributions. The input values are represented by vertical/horizontal grey lines, and the maximum likelihood parameters by white circles. It is important to note that the maximum likelihood overall fit may not co-incide with the maximum likelihood of that individual parameter, and in fact isn't particularly informative with such complicated parameter spaces, where parameters

are degenerate or multi-modal. We address the parameters in order of appearance:

Stellar Mass - both sets of observations recover the stellar mass to within 1-σ, with the UV-only observations reporting a slightly wider posterior. This shows some degeneracy with the metallicity, with lower metallicity solutions slightly increasing the stellar mass. Similarly solutions with more steeply decreasing star formation histories also have higher stellar masses, as older stars have higher M/L ratios.

SF Duration - the star formation duration is a parameter which is intrinsically hard to measure unless it is a very short duration. This is because of the issue plaguing mixed age galaxies – old star formation is of much lower luminosity than recent activity, and so the star formation activity of a galaxy beyond the last 1Gyr is hard to make statements about – populations of 1 and 10 Gyr are very hard to distinguish with data. However, the SF duration is reconstructed within one sigma, plus a long fail to much longer durations, as all of the older stars' luminous contributions can easily be nullified by a small change in e.g. dust content.

Metallicity - The metallicity is relatively uncertain, however the optical observations seem to rule out the highest values. There is a notable degeneracy between both metallicity and λ (and by proxy the average age) and also metallicity and the dust content. These degeneracies arise because all three broadly have the same effect – they all serve to redden the spectra but with slightly different shapes.

Escape Fraction - The escape fraction governs the amount of nebular emission added to the model. As evidenced by the posterior, the escape fraction is hard to measure through photometry because the biggest give-away of large escape fractions is emission lines, which can be absorbed into the photometry fairly easily. The posterior in both cases is fairly indifferent across all values, but a weak preference is shown for lower values (closer to the truth of $f_{esc} = 0$).

Star Formation History Shape - The star formation history shape is recovered almost exactly, with a long tail of decreasing histories also offering solutions. The posterior resoundingly rejects rising SFHs, as the young stars that would be added are so efficient in the production of UV and optical photons that they cannot reproduce the correct continuum shape. However, the addition of more old stars (via a declining SFH) does not add much light, so therefore these can present viable solutions.

Dust Parameters - τ_V and μ are heavily intertwined, as evidenced by the degeneracy between them. The normalisation τ_V is accurately reproduced, with a long tail co-inciding with its other degenerate parameter's tails (metallicity and stellar age). μ, the shape parameter, offers an almost perfectly bimodal distribution. As dust effects are strongest in the UV, it is un-surprising that the distributions of both parameters here are almost identical despite the many fewer observations in the UV only sets.

The story is largely repeated for the other star formation histories (listed in appendix A). The 100MYr constant star formation over-represents the stellar mass/offers rising star formation solutions, as the population is so extremely and uniformly young that high SFR-high dust- low Z solutions also fit the data well (especially in the UV) but add significantly more mass in older stars.

The exponential star formation histories offer similar stories. Stellar masses are recovered within 1-σ, and star formation duration is intrinsically tied to the shape of the star formation history, both of which have weak constraints placed on them based on the youngest stellar populations. Similarly we find that the dust parameters are degenerate both with each other and weakly with the SFH. Finally, the metallicity and escape fraction are very weakly, or entirely unconstrained, requiring emission line fluxes to really constrain.

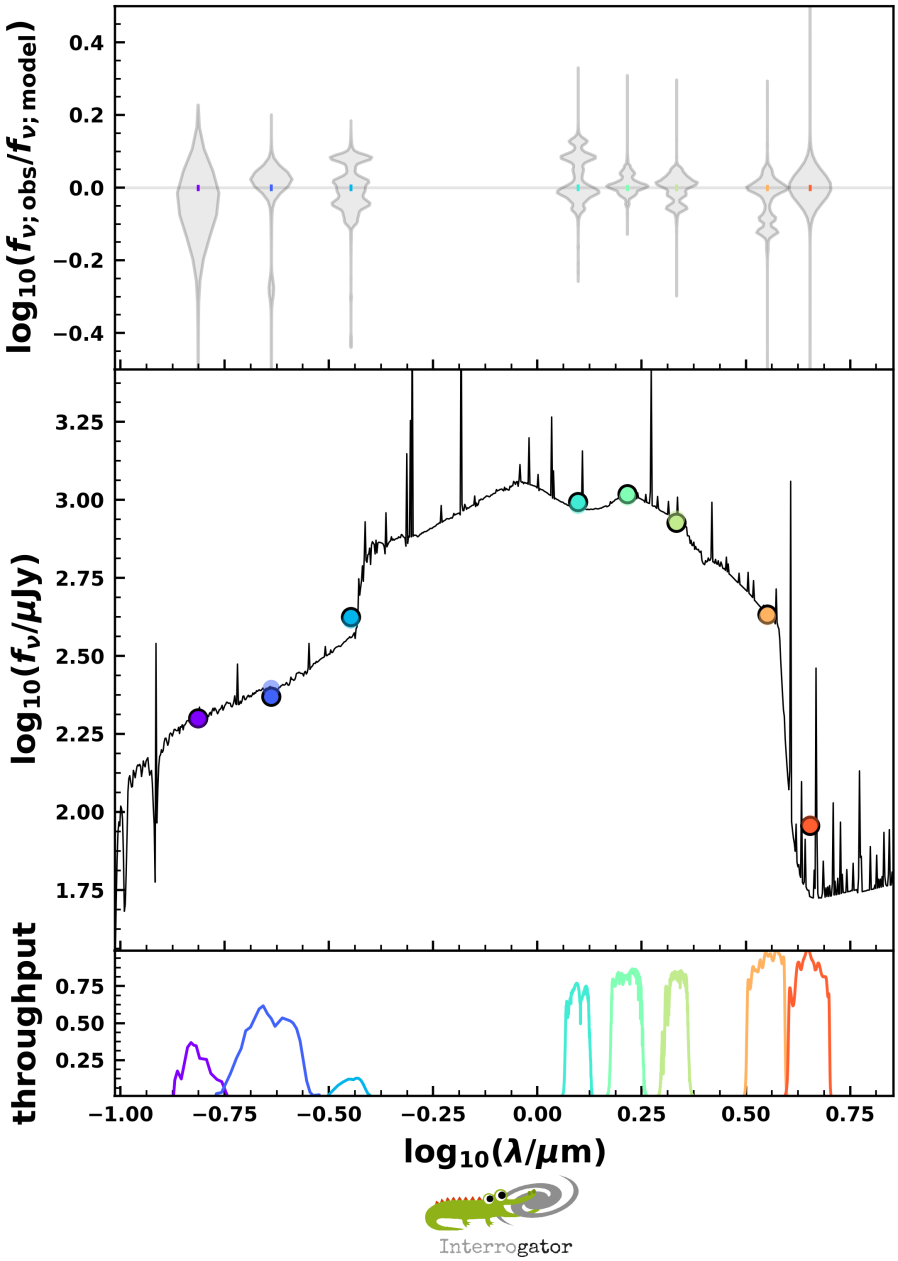

Figure 2.19: Fitted SED of input synthetic galaxy with constant SFH lasting 1Gyr and $S/N = 50$. Top panel violin plots the posteriors of the fluxes (grey violins) normalised to the true flux (0 line, coloured error bars). Middle panel shows model SED (black line), observed broad band fluxes (coloured points, faded), and median reconstructed model fluxes (coloured points, solid). Bottom panel shows filter throughput curves for each observation.

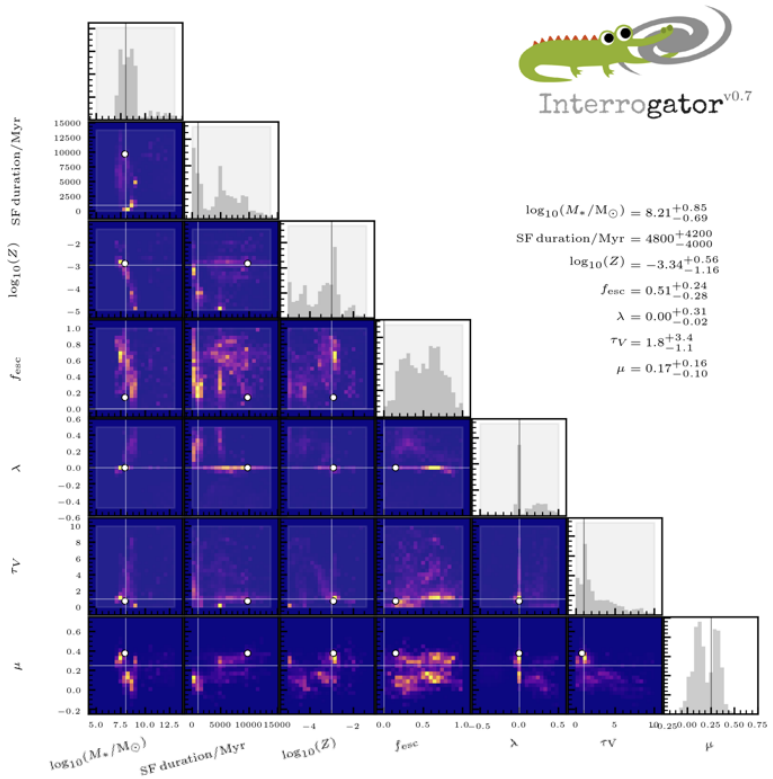

Figure 2.20: "Triangle plot" of the marginalised 1-D and 2-D probability distributions of the fitted parameters of synthetic galaxy with constant SFH lasting 1Gyr and S/N = 50. Parameters listed, in order of row/column are: stellar mass $\log_{10} M_*$, Star formation maximum age cutoff (SF Duration), metallicity Z, ionising photon escape fraction f_{esc}, exponential SFH inverse time constant λ, and dust curve shape parameters $\tau_V \& \mu$ (see section 2.2.1.3). White points on 2-D histograms show maximum likelihood of the fit, grey vertical/horizontal lines show input values.

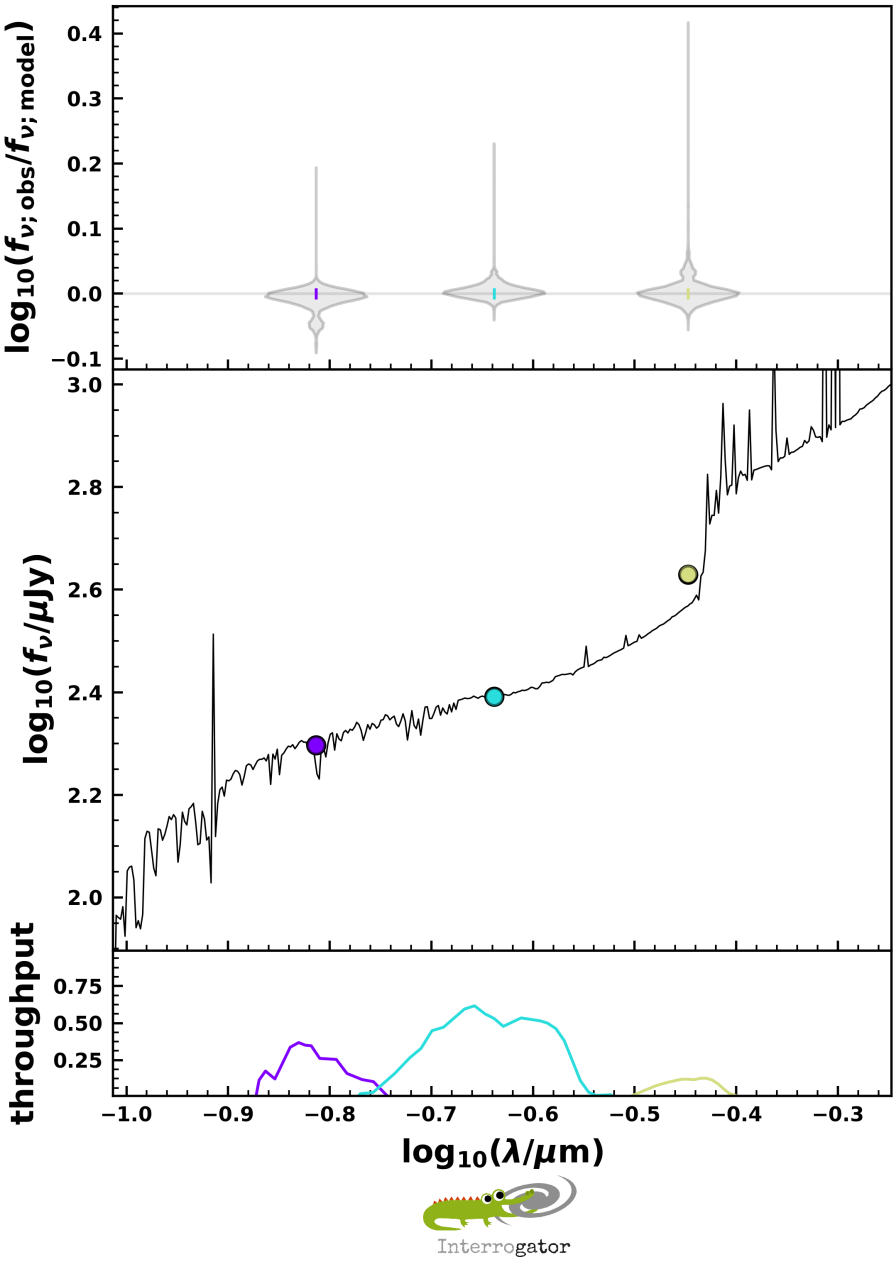

Figure 2.21: Fitted SED of the same synthetic galaxy as figure 2.19, but with only the three bluest filters. Top panel violin plots the posteriors of the fluxes (grey violins) normalised to the true flux (0 line, coloured error bars). Middle panel shows model SED (black line), observed broad band fluxes (coloured points, faded), and median reconstructed model fluxes (coloured points, solid). Bottom panel shows filter throughput curves for each observation.

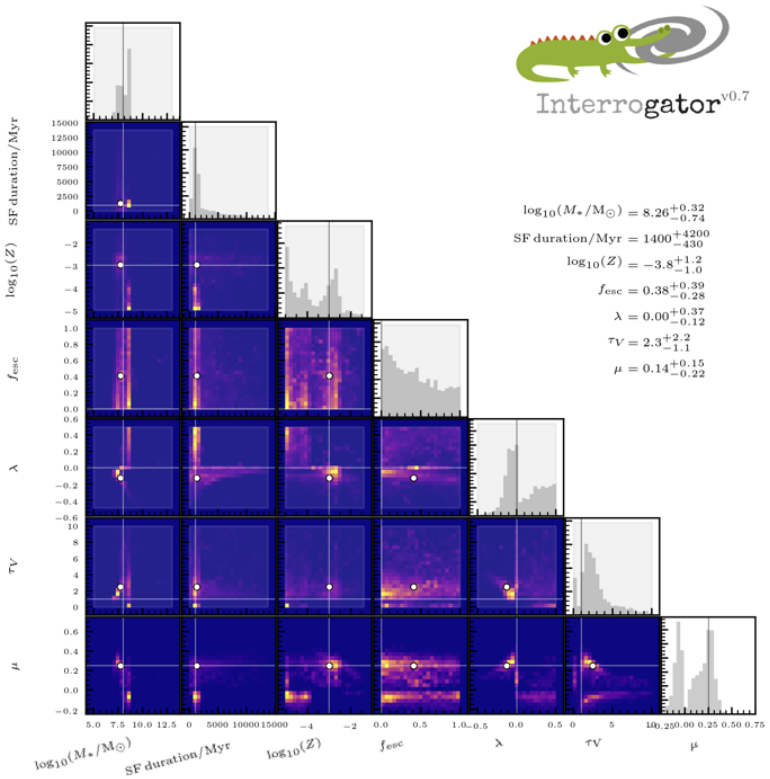

Figure 2.22: "Triangle plot" of the marginalised 1-D and 2-D probability distributions of the fitted parameters of synthetic galaxy with constant SFH lasting 1Gyr and $S/N = 50$, but with observations only in the UV. Parameters listed, in order of row/column are: stellar mass $\log_{10} M_*$, Star formation maximum age cutoff (SF Duration), metallicity Z, ionising photon escape fraction f_{esc}, exponential SFH inverse time constant λ, and dust curve shape parameters $\tau_V \& \mu$ (see section 2.2.1.3). White points on 2-D histograms show maximum likelihood of the fit, grey vertical/horizontal lines show input values.

2.5 Conclusions

This chapter detailed the development and basic testing of a new SED fitting ode INTERROGATOR. It has been designed specifically with the upcoming Webb telescope in mind, and specifically the study of EoR galaxies that it will enable.

The code has one core philosophy behind it – flexibility. INTERROGATOR utilises a range of SPS models, IMFs, star formation/metal enrichment histories, gas and dust models. Other innovations include an MCMC inference engine which efficiently samples parameter space, and a novel gas/dust reprocessing model based off of Charlot and Fall [2000].

We test the code by generating mock observations using the observation generator built in to the code, and the. test how well INTERROGATOR recovers the parameters using the same modelling assumptions as went into the observations. We find that INTERROGATOR offers good recovery of the parameters traditionally accessible to photometry such as stellar mass and dust attenuation.

We opt not to experiment with the reconstruction using other models here, as we only wish to test that the fitter worked correctly, and in the next chapter, we use INTERROGATOR to (re-)analyse photometric observations of low-redshift extreme emission line galaxies, potential analogues of high$-z$ star forming galaxies. In chapter 4 we propose a possible extension to the star formation (and metal enrichment) history parametrisation based on cosmological hydrodynamical modelling.

2.5.1 Future Development

The version of INTERROGATOR described in this chapter is *fully working* and can be turned to analysing observations (as in Chapter 3). However, INTERROGATOR is designed to be extendible with new elements and features added over time. Here we briefly describe some of these potential future developments.

Performance Perhaps the largest issue facing the current version of INTERROGATOR is performance. To complete a full analysis of a galaxy requires thousands to millions of model

SEDs to be generated resulting in a relatively slow code. While fine for a small number of objects, as we discover many more high-redshift galaxies (or apply INTERROGATOR to galaxies at lower-redshift), the need to analyse larger samples of galaxies will become important. A priority for future development must then be identifying speed bottlenecks and addressing them.

Stellar Population Synthesis Model and Initial Mass Function INTERROGATOR already includes the possibility to utilise several stellar population synthesis (SPS) model grids. As models are upgraded or new models become available these can easily be added to INTERROGATOR.

Alongside the choice of SPS model we could also, where available, add additional initial mass functions (IMFs). In addition, some code (e.g. PEGASEV2) permit the calculation of SSP spectral grids for an arbitrary IMF [Fioc and Rocca-Volmerange, 1997]. This opens the possibility of parametrising the IMF, for example the high-mass slope α, and fitting the free parameters (or at least marginalising over a range).

Star formation and metal enrichment history This version of INTERROGATOR includes a range of star formation history parameterisation but in each case the metallicity is assumed to be constant, something which will not be true in the real Universe. A first expansion of INTERROGATOR, described in Chapter 4, includes a new parameterisation of the star formation and metal enrichment history based on cosmological hydrodynamical simulations. This parameterisation is based specifically on galaxies in the early Universe and may not be applicable to mature galaxies in the later Universe. This opens the possibility of further changes.

Spectroscopy Internally INTERROGATOR generates SEDs, at the resolution of the input SPS models, including both stellar emission and reprocessing by dust and gas. In this version of INTERROGATOR however we have not yet implemented the ability to utilise spectroscopic observations. With the arrival of *Webb* however spectroscopy of high-redshift galaxies

will become much more commonplace (and useful) thanks to NIRSpec and WFSS modes on NIRISS and NIRCam. The only difficulty here is developing a routine to match the characteristics of the observed spectra (wavelength range, resolution, etc.) with that of the model spectra.

Direct comparison with spectra may also motivate a more sophisticated nebular emission model. As noted, our default model assumes values for the ionisation parameter U and hydrogen density n_H. While these have only a small effect on broadband photometry they can significantly impact individual lines.

Thermal IR emission At present Interrogator only includes attenuation by dust and not re-emission. With the advent of ALMA it is now becoming routinely possible to observe dust continuum emission even in very high-redshift galaxies. This motivates the future development of a thermal IR emission model in Interrogator. The most straightforward approach would be to adopt energy-balance, in which the energy absorbed by dust from the UV - optical - near-IR is directly re-emitted as thermal IR emission according to some model. Models here include a simple black-body, a grey-body, or more complicated models including multiple (e.g. hot and cold) dust components.

It is perhaps worth noting however that observations of galaxies alone a single line of sight do not necessarily need to be energy balanced as in, for example Battisti *et al.* [2019]. This is because the while the (re-)emission from dust is isotropic the absorption won't be. For example, a population of stars with no dust between and the observer would clearly experience no attenuation, and thus, would, if energy-balance is applied expect, no IR emission. However, if there was a dust cloud on the far side of the population some fraction of the light absorbed from that direction would be re-emitted into the line of sight of the observer. An observer would then see a stellar population with no attenuation but also an IR source.

Chapter 3

Local Analogues of Distant Star Forming Galaxies

This chapter demonstrates an application of INTERROGATOR to a sample of Extreme Emission Line Sources (EELS) in order to explore how model assumptions can affect the physical properties inferred. We obtain this sample from the Galaxy And Mass Assembly (GAMA) survey [Driver *et al.*, 2016]. The high quality of available data means that a selection can be made on the line properties directly, enforcing a cut of $EW(H\alpha) \geqslant 200$Å, rather than on colour based photometric selections which are vulnerable to both interlopers and galaxies falling outside of the narrow redshift ranges they are sensitive to. Leveraging the high quality data we have available, we design a more direct selection criteria – these galaxies are defined by strong line emission, so we look specifically for EW(Hα) $>$ 175Å in the spectra, along with a redshift cut of $0.05 < z < 0.3$ (see section 3.2 for more details. After applying these selection criteria, we obtain a sample of 136 EELS.

We then fit this sample using INTERROGATOR and a variety of models. We find that these galaxies are largely low mass,but with high specific star formation rates more consistent with galaxies of much higher redshift. They also have much lower metallicities than the typical local galaxy, however they have a much flatter distribution, and are offset higher than the relation found at high redshift. This makes them good but not complete analogues of high-z galaxies, and care should be taken when connecting between them.

We find that this sample of galaxies have large model uncertainties, with median offset of up to ~ 0.4 dex in stellar mass, and up to 0.4dex in SFR_{100} (the average SFR over the last 100Myr) as well. Due to these galaxies high sSFR's, their light is dominated by its largest stars, and any change in either the fractional representation of these stars (through the SFH) or their propeties (e.g. through SPS model choice) can have wide reaching effects on the inferred physical parameters.

Finally we obtain VLT/X-SHOOTER spectra for 12 of the 19 brightest objects based on r-band magnitudes, to use the higher order Balmer and Paschen line ratios to accurately study both the metallicity using more precise electron temperature methods, and to characterise the dust content of these galaxies in more detail. We design an EMCEE-based line fitting code to calculate the line parameters, and (re)fit both the GAMA and XSHOOTER spectra.

3.1 Introduction

Two heavily intertwined and unanswered questions concerning the Epoch of Reionisation are (a) what is the timeline along which it occurred? and (b) which sources are dominant in terms of producing necessary photons to reionise the Universe? Over time as progress has been made, it has become apparent from both simulation and observation that galaxies in the mass range $10^6 M_\odot$ - $10^8 M_\odot$ with high SFR – dwarf starburst galaxies – contribute a significant fraction of the ionising photons [Finkelstein, 2019]. Therefore to understand these low mass starburst galaxies is to understand an important piece of reionisation [e.g. Bouwens *et al.*, 2012b; Finkelstein, 2012]

Despite these galaxy's hegemony at redshifts within the EoR ($z > 6$) [Stark *et al.*, 2011], observations of them are challenging as they require competitive instrumentation, long exposure times on said instrumentation, and require observations in the near-IR which is one of the most challenging wavebands to observe from the ground [Trainor *et al.*, 2015]. With that said, the challenges are not insurmountable and some progress has been made, finding these high redshift Lyman α emitters to have low metallicity, little dust and small

radii, in addition to their low stellar mass. [Pirzkal *et al.*, 2007; Finkelstein *et al.*, 2008]

In addition, the Lyman α emission from such objects will be scattered by the remnants of the neutral HI, allowing us to observe the process of reionisation in action, and track the fraction and partial distribution of the remaining neutral gas with careful study [Jensen *et al.*, 2013; Matthee *et al.*, 2015; Zheng *et al.*, 2017].

However, until the advent of *Webb* and the ELTs what we can learn from these galaxies is somewhat limited. One alternative is to turn to low-redshift, and thus much closer/brighter, analogues of these galaxies. Populations of galaxies have been found in the local Universe with similar properties to these high-z Lyman α emitters – similar locations on the fundamental metallicity relation, compact sizes, and large [OIII]λ5007/[OII]λ3727Åvalues [e.g. Cardamone *et al.*, 2009]. By studying these analogues we gain insights into the physical conditions of the high-z galaxies responsible for reionisation [Jaskot and Oey, 2014].

Perhaps more usefully though, these galaxies serve as an ideal test-bed for techniques that will ultimately be enabled by observations - rest-frame UV - optical photometry and spectroscopy - obtained by *Webb* and the ELTs at high-z.

3.1.1 Selecting Analogues

There are a number of ways of selecting analogues, however a common technique is to select on the basis of strong (high-EW) line emission, often [OIII]λ5007 but sometimes Hα. This selection can either be done *directly*, i.e. using spectroscopy, or *in-directly* making use of the unique location of these galaxies in colour-colour space.

3.1.1.1 BCDs, Green Peas and Blueberries

There are a variety of selection criteria that have been created to find high-z analogues, and while these criteria tend to find most of the same objects, they do not return the exact same samples. As we are fortunate enough to have a large sample of galaxies with spectra in GAMA, we wish to make a selection criteria which is as fundamental as possible rather

than the more photometry based approaches as taken by others.

Blue Compact Dwarfs (BCDs) were first identified in Zwicky [1965] as a subgroup of local dwarf galaxies in the Palomar Sky Survey. They are spatially compact gas rich regions with high SFRs that can either lie in the field or within a more diffuse but less starforming galaxy. subsequent studies (e.g. Aloisi *et al.* [2007]) found that they are low metallicity (around $0.02Z_{\odot}$), gas rich and are undergoing periodic starbursts.

Green peas, as discussed in Cardamone *et al.* [2009], were one of the earliest samples of EELS to be constructed. They were originally found within the Galazy Zoo project [Lintott *et al.*, 2008], a citizen science project where members of the public described the morphology of almost 10^6 galaxies presented as composite RGB images, using the *gri* filters respectively from the Sloan Digital Sky Survey (SDSS) [York *et al.*, 2000].

Galaxy Zoo provides a space for classifiers to discuss strange objects they find, and one such class was nicknamed "Green Peas" due to their appearance in the filters used for Galaxy Zoo. Green Peas are visually compact, unresolved point source like objects which appear green in Galaxy Zoo due to their strong *r* band emission. They are mostly listed as stars in the standard SDSS catalogues because of their point-line nature, however they present distinctly galaxy like spectra. Their high *r*-band magnitude is due to the [OIII]5007Åline being incredibly strong, and on the redshift range $0.112 < z < 0.360$ this line falls into the r band filter, boosting it significantly.

Cardamone *et al.* [2009] settle on the following selection criteria to separate out the Green Peas from both more standard star forming galaxies and from Quasi-Stellar Objects (QSOs) in the same redshift range.

$$u - r \leqslant 2.5 \tag{3.1}$$

$$r - i \leqslant -0.2 \tag{3.2}$$

$$r - i + 0.5 \leqslant g - r \tag{3.3}$$

$$2.5(r - z) \leqslant u - r \tag{3.4}$$

Where u, g, r, i, z are the AB magnitudes in the respective bands from the SDSS survey. In addition, they enforce a $S/N > 3$ cut in the spectral continuum around the $H\alpha$ and $H\beta$ lines – specifically from 6350-6500Å and 5100-5250Å, along with the same $S/N > 3$ enforcement for [OIII]5007Å and [NII]6583Å. The line S/N cuts are enforced in order to construct a BPT diagram [Baldwin *et al.*, 1981; Osterbrock and Pogge, 1985] in order to select out AGN. A more full discussion of this method is found in section 3.3.

The Blueberries [Yang *et al.*, 2017] are a sample of galaxies which are selected in a similar way to the Green Peas, but by looking for a large [OIII]5007Å line at $z < 0.05$, where it resides in the g-band rather than the r-band. In SDSS composites they appear similarly to BCDs – either partially resolved or wholly unresolved blue point-like objects. Their specific selection criteria are:

$$(g - r < -0.5) \text{ and } (r - i < 1.0) \text{ and } (g - i < -0.5)$$

and

$$[(g - r < -0.7) \text{ or } (g - i < -1.0)] \text{ and } (g - u < -0.3)$$

Where g, r, u, and i are simply the apparent magnitudes in each of the SDSS bands. These criteria are more complicated as not only do they need to split out the Blueberries from starforming galaxies and AGN, but also single O/A stars and white dwarfs. Both of these types of star can exhibit very similar colours, but are revealed to be imposters by a very blue $u - g$ colour, whereas Blueberries [OIII] emission cause them to be much redder.

Yang *et al.* [2017] found these selection criteria by adding large [OIII] lines to a composite of two Simple Stellar Populations, one young and one old, and by adjusting this constructions equivalent width and redshift, while monitoring how they move through the colour space.

The criteria they rest on select galaxies at $z < 0.05$, with equivalent widths EW([OIII]5007Å) > 800Å. They find that the galaxies this criteria select are low mass – $10^{6.5} M_{\odot}$ - $10^{7.5} M_{\odot}$, sSFRs around 10^{-8}yr^{-1}, and are metal poor ($7.1 < (12 + \log_{10} O/H) < 8.0$). These galaxies also typically are isolated – either in low density environments or on the

outskirts of a galactic group.

These objects can either be considered as separate populations, or as an overarching subclass of galaxies depending on how you wish to define said category. The main difference between them is their redshift. Both blueberries and green peas are compact, low mass galaxies with very strong [OIII] lines and high specific star formation rates. What separates them is where that [OIII] line falls in the observed frame – in the lower redshift blueberies it falls into the g-band, and at higher redshift, the same rest-frame emission line contaminates a different photometric band (r-band) and thus they require different selection criteria to pick out of surveys. In short, galaxies with similar intrinsic physical properties can require different and mutually exclusive observational selections due to redshifting.

3.2 Fishing for EELS in GAMA

We wish to construct a sample of Extreme Emission Line Sources in the simplest, most direct way possible, which is also independent of redshift. Surveys such as GAMA offer us a natural way to do this. Rather than making inference from broad band surveys – which is dependent on the strong emission lines falling into specific wavelength ranges – we can take a much more direct approach and just select on the lines measured equivalent width.

3.2.1 GAMA survey

The GAMA survey [Driver *et al.*, 2011] is a large area spectroscopic survey covering some 280deg^2 of sky, delivering high completeness down to a magnitude of $r < 19.8$.

This survey area is made up of a series of fields. Firstly there are three equatorial fields – G09 ($129.0 < \mathrm{RA} < 141.0$, $-1.0 < \mathrm{DEC} < 3.0$), G12 ($174.0 < \mathrm{RA} < 186.0$, $-2.0 < \mathrm{DEC} < 2.0$), and G15 ($211.5 < \mathrm{RA} < 223.5$, $-2.0 < \mathrm{DEC} < 2.0$). These fields were designed to overlap with over surveys to maxmise data coverage such as SDSS, UKIDSS, HERCHEL-ATLAS, and GALEX. Later, two southern hemisphere regions G02 ($30.2 < \mathrm{RA} < 38.8, -10.25 < \mathrm{DEC} < 3.72$) and G23 ($339.0 < \mathrm{RA} < 351.0, -35.0 < \mathrm{DEC} < -30.0$).

These spectra have moderate resolution – between 3 and 7Å – and the final catalogues contain well over 200,000 objects. In addition, photometry ranges from the UV (GALEX) through the SDSS optical bands, to far IR data from ATLAS. Figure **??** in the previous chapter shows the photometry bands available in the UV, optical and NIR to all objects, and then in addition those in the equatorial regions may have Herschel detections in the far IR.

This makes the survey ideal for our purposes. In the low redshift universe, extreme emission line galaxies are rare objects, which means that a large area is necessary to find a statistically significant sample. The moderate resolution spectra allow selection on the large equivalent width lines directly rather than using broad band fluxes, which many of the existing samples are selected on. Broad band flux selections have the possibility of contamination and also of redshift limitation – if the high flux lines such as [OIII]λ5007 are shifted into different bands or out of the band all together, the information is lost and the EELS are not selected.

As part of the GAMA data products, they also provide a variety of physical models of the galaxies, however as we will explore in section 3.4 these models make a variety of assumptions which are inappropriate for the study of these rare objects.

3.2.2 Selecting EELS

The things that the existing populations of EELS have in common is that they are low mass, low metallicity, with small radii, and they are highly star forming, almost all having specific star formation rates (sSFR) of $<$ 1Gyr

We thus opt to leverage the spectral coverage of the GAMA survey to simply look for galaxies that meet these requirements. We thus simply impose the following initial selection criteria:

$$EW_{rest}(H\alpha) \geqslant 200\text{Å} \tag{3.5}$$

$$S/N(H\alpha) \geqslant 10.0 \tag{3.6}$$

$$0.05 \leqslant z \leqslant 0.15 \text{ or } 0.18 \leqslant z \leqslant 0.30 \tag{3.7}$$

where $S/N(H\alpha)$ is the signal-to-noise in the Hα line, $EW_{rest}(H\alpha)$ is the equivalent width of the $H\alpha$ line after blue-shifting the spectra back to the rest frame, and z is the redshift of the galaxy as quoted in the GAMA catalogues.

We opt to select on Hα equivalent width because it highly correlates with sSFR. Dense HII gas is the preferred fuel for star formation, and where ever it is present, Hα emission is also plentiful. However the longer star formation goes on, the starlight causes the continuum emission to "catch up", raising the overall luminosity but lowering the equivalent width. Thus there is a sweet spot age of stellar activity where the Hα line emission is still high, but the continuum hasn't built up enough – i.e. low mass, but highly star-forming galaxies.

We apply a signal to noise cut simply to ensure that we minimise spurious objects, however we also required a visual inspection of the spectra to remove artefacts and fringed objects.

The redshift selection ideally would simply be galaxies which extend from $0 \leqslant z \leqslant 0.30$, as this is the redshift range in which $H\alpha$ is within the coverage of the spectrograph, however a few practical issues arise. The optical fibre apertures on the AAOmega telescope correspond to 2". At $z = 0.05$, $D_A(2'') \approx 2KPc$, meaning that for redshifts less than this, we are no longer probing the whole galaxy, only some region within it. This can be problematic for galaxies that have knots of intense star formation within them, which could meet the selection criteria independently of what the rest of the galaxy is doing. Applying the minimum redshift ensures that only independent, unresolved dwarf galaxies are extracted. Finally, we also do not select galaxies in the redshift range $0.15 \leqslant z \leqslant 0.18$ as $H\alpha$ becomes contaminated with a sky line.

Applying these selection criteria yields a sample of 136 galaxies. Basic properties of

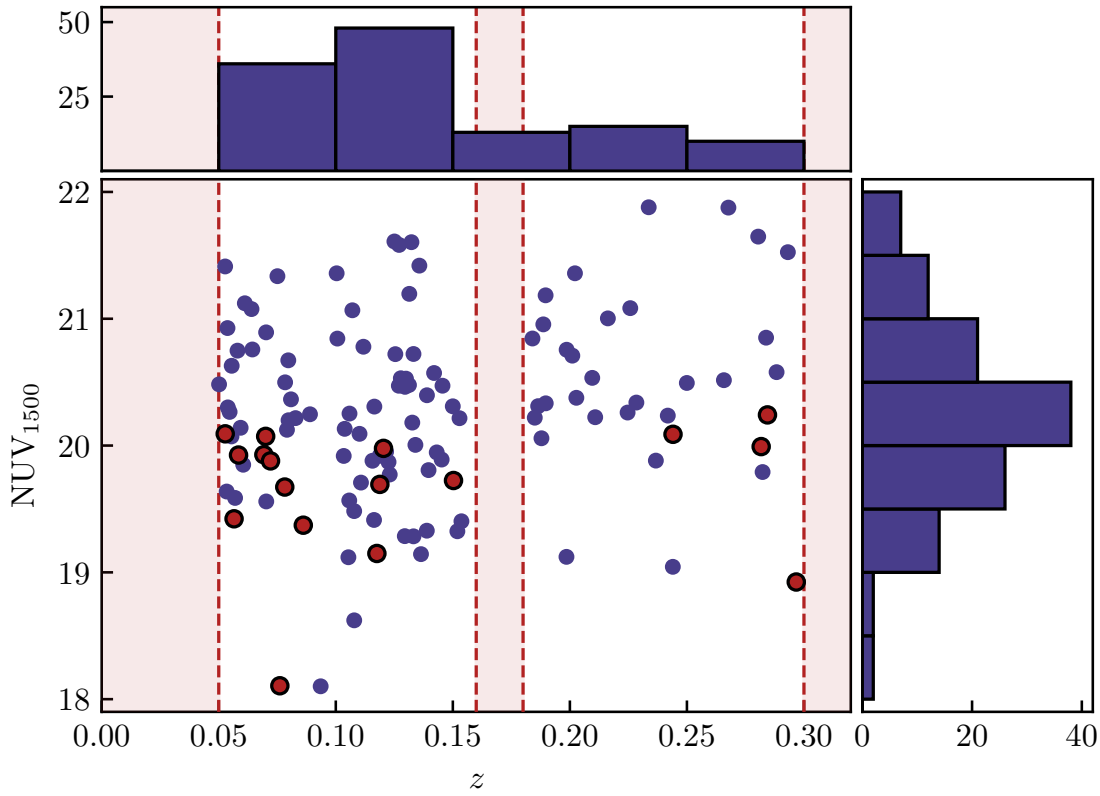

Figure 3.1: Distribution of EELS sample in redshift and UV apparent magnitude. Main panel shows the sample of 136 galaxies, top histogram shows their distribution over Δz = 0.05 bins, right histogram shows distribution in $\Delta\mathrm{NUV}_{1500}$ = 0.5 bins. Red areas are areas of redshift space excluded from selection – see main text for details. Points highlighted in red are galaxies for which spectra were obtained with VLT-XSHOOTER, see section 3.5.

these galaxies are listed at the top of appendix B. Figure 3.1 shows how these galaxies are distributed in redshift and UV magnitude. It is firstly worth noting that the sharp drop in the redshift distribution is an artefact of the fact that we exclude the band of redshift space where Hα co-incides with the skyline as discussed in the selection section. If we could correct for that the drop would be much less severe.

A visualisation of the sample is depicted in figure 3.2. Visually the galaxies fall into two categories. Firstly, galaxies that are Green Pea/Blueberry like – isolated, compact with strong g or r-band excesses. The other category is knots of star formation within larger, more diffuse galaxies. As we have selected on such a simplistic criteria – just looking for high sSFR this is perhaps unsurprising as we are agnostic to the cause of the star formation,

whether merger driven starbursts, gas rich areas of larger, diffuse galaxies or “true” low mass, low Z EELS.

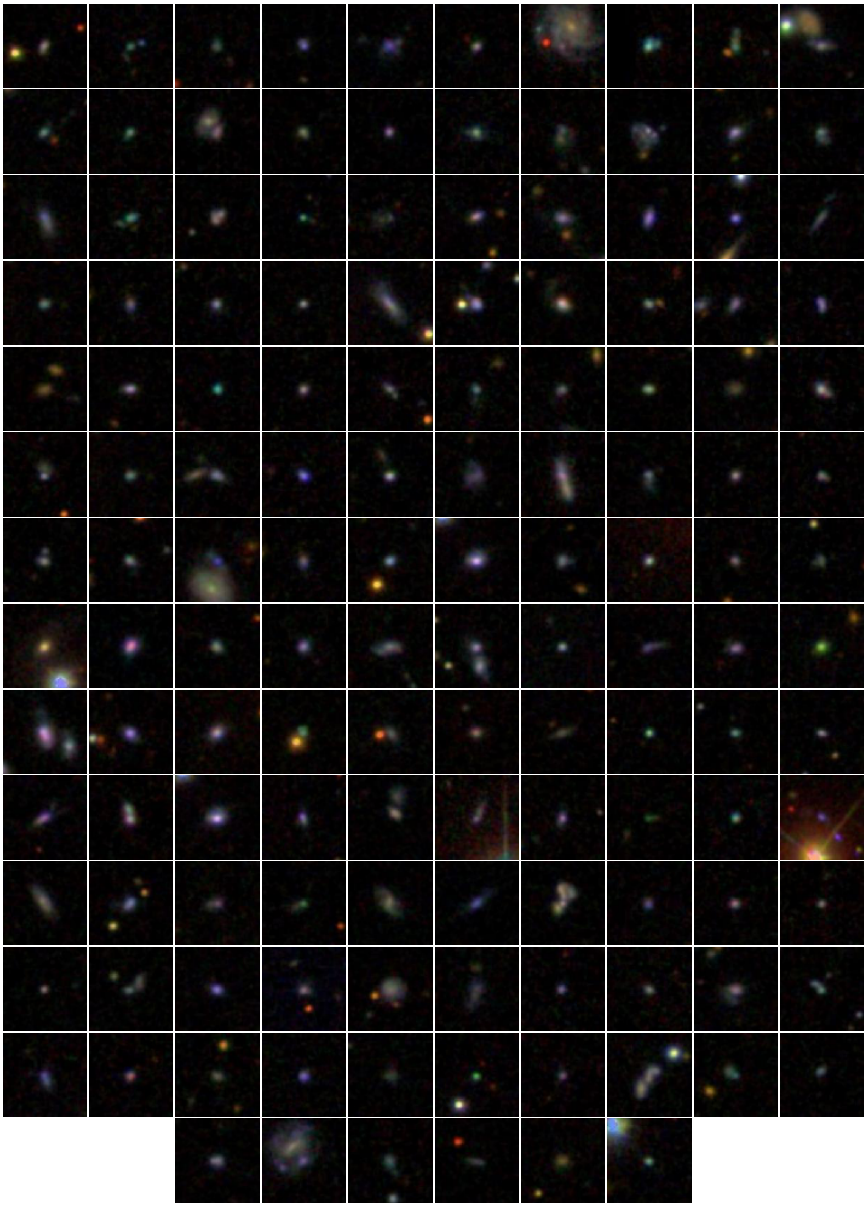

Figure 3.2: Postage stamps of the sample of galaxies, with RGB represented by the the SDSS (ug)(gr)(iz) channels. Each image is 20“×20“ on the sky.

Figures 3.4 and 3.5 show the EELS sample that has been constructed on the colour-colour planes used for the selection of Green Peas. It can be seen that there is a quite low overlap in both cuts overlap – 23% of our sample are Green Peas [Cardamone *et al.*, 2009], whereas the rest would lie within the main sequence star-forming galaxies locus. 0% of our sample coincides with the Blueberries, but this is to be expected, because although our reasoning differs (aperture considerations for this work vs. the location of the [OIII] line in the filters for green peas and blueberries) we are not probing the $z < 0.05$ range where the [OIII] line falls into the g-band filter – the defining selection criteria of the blueberries. The green peas result is also not entirely surprising for similar reasons – [OIII] only boosts the r-band at $z > 0.12$.

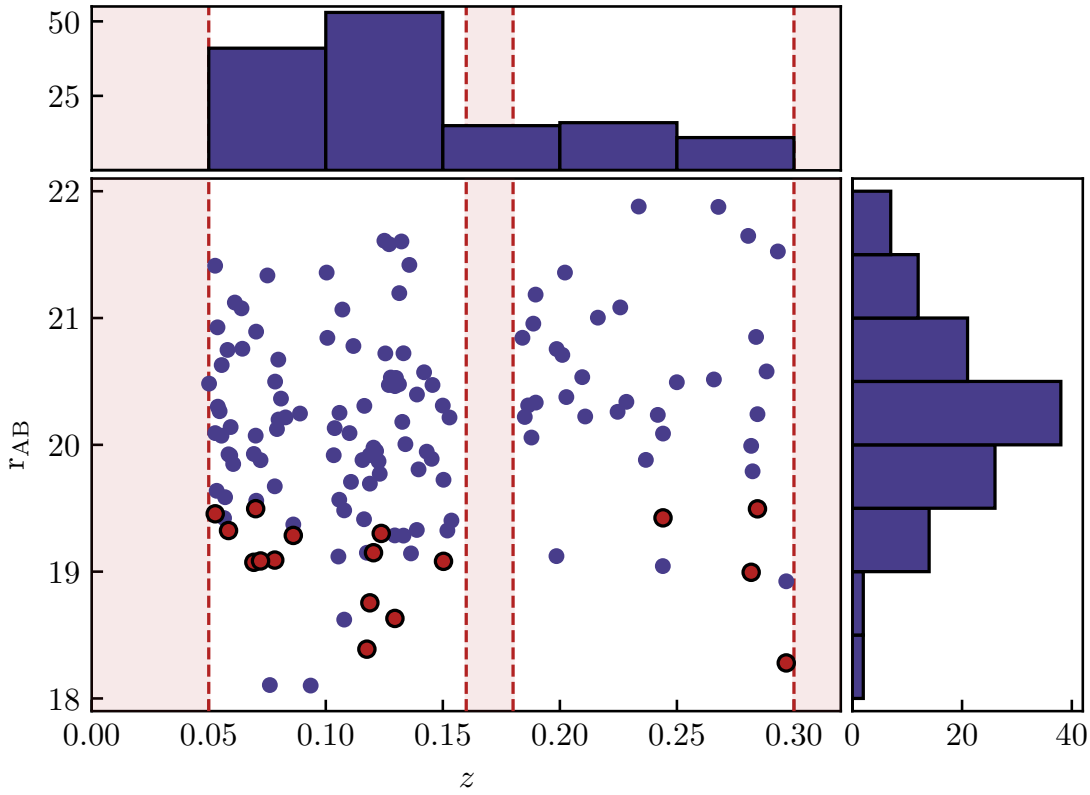

Figure 3.3: Distribution of EELS sample in redshift and r-band apparent magnitude M_r. Main panel shows the sample of 136 galaxies, top histogram shows their distribution over $\Delta z = 0.05$ bins, right histogram shows distribution in $\Delta M_r = 0.5$ bins. Red areas are areas of redshift space excluded from selection – see main text for details. Points highlighted in red are galaxies for which spectra were obtained with VLT-XSHOOTER, see section 3.5.

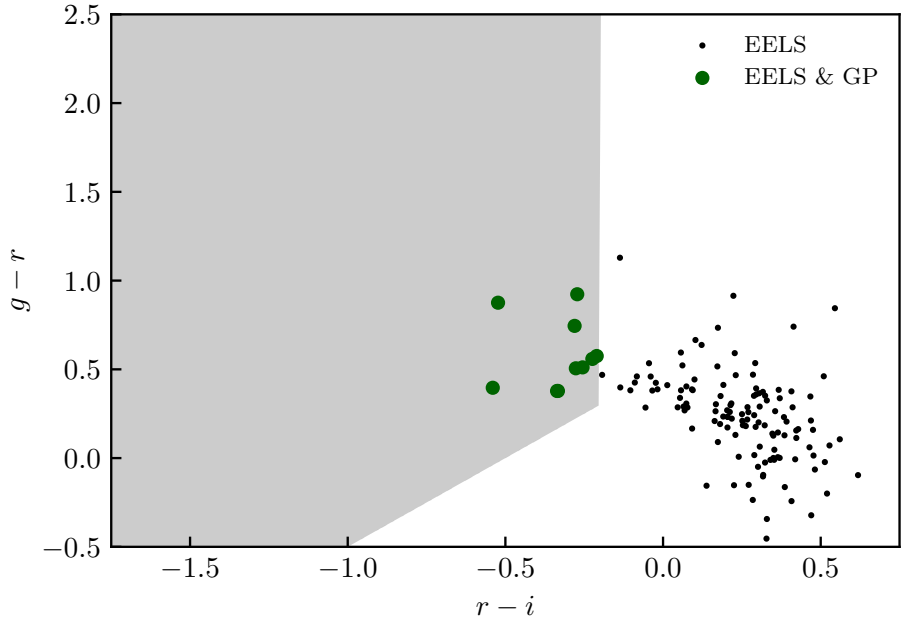

Figure 3.4: $r - i$ vs $g - r$ colour-colour diagram, as used to select for green pea galaxies in the r-i g-r colour-colour

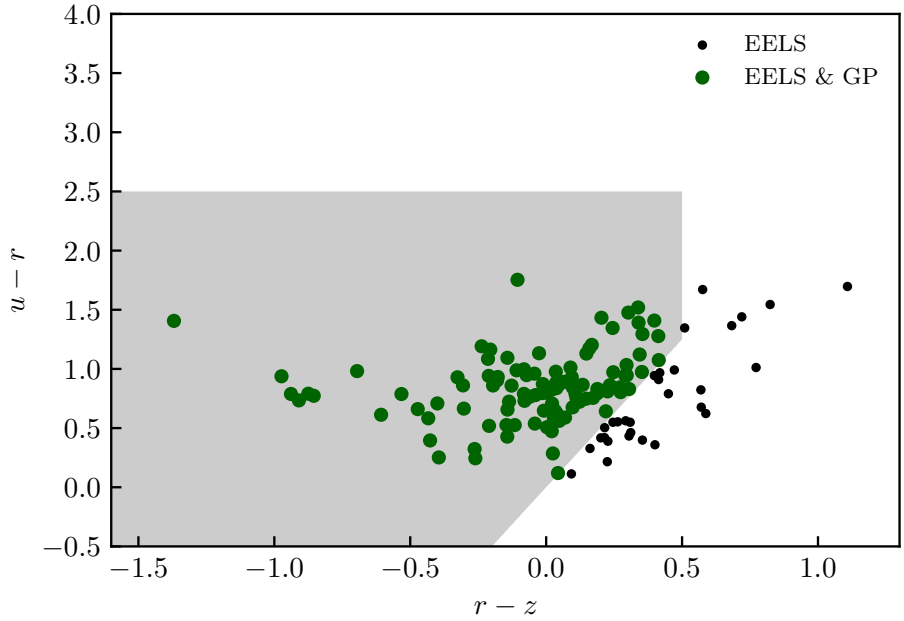

Figure 3.5: $r - z$ vs. $u - r$ colour-colour diagram.

3.3 Physical Properties

We begin by exploring the physical properties of our sample of EELS comparing them with both the wider local population of galaxies and simulated/observed high-redshift galaxies.

For reasons that will be outlined in detail in section 3.4, we ignore the existing modelling provided as in Wright *et al.* [2016]. In brief, the Wright modelling is done under two assumptions which do not hold for the specific type of galaxy we are observing here – it neglects nebular emission, under the approximation that it is a small component of the total flux, and it assumes a declining SFH with time. The first of these assumptions is untrue for these galaxies almost by definition – they were selected on their high Hα equivalent widths, and many other types of EELS are selected on large emission lines contaminating entire broad photometric bands, therefore nebular emission is patently important. The second assumption, that of declining SFH, is not so obvious, however in subsequent sections we will show that relaxing this assumption is correct for these objects – their high specific star formation rate is a product of exponentially rising star formation histories.

We therefore must construct the modelling from scratch, using INTERROGATOR with the following models & priors:

- **SPS model -** Pegase v2.0
- **IMF -** Salpeter IMF with $\alpha = -2.35$
- **SFH -** A single parameter exponential model, with the exponential time constant τ free to be both positive (dec. SFH) and negative (rising SFH)
- **Nebular Emission -** Active, provided by CLOUDY
- **Dust Modelling -** Calzetti dust curve

with exponential time constant $\tau = 1/\lambda$ free to vary on the interval $[-\infty, +\infty]$ yrs.

For data, we use the optical and near IR data from the LAMBDAR reprocessing catalogue. This data deblends many of the sources which are confused (whether by change in line

of sight or physically close sources), and reduces the outlier rate of modelled parameters significantly as compared to the original modelling [Wright *et al.*, 2016].

This set of models will be subsequently referred to throughout the rest of this chapter as the “fiducial model". It is important to note that the choice of models has a significant impact on the inferred parameters, as will be shown in later sections, but also that it is effectively a free choice.

The fiducial model was chosen as a compromise between realistic conditions (including nebular emission), previous literature (Pegase v2 is very similar to the Popular BC03 SPS model [Bruzual and Charlot, 2003] and not over-using the number of parameters (for example, using the Calzetti dust curve over the default modified Charlot & Fall model. This restriction on the number of parameters is due to the fact that these models are constructed from photometric data only, as we wish to use these galaxies as analogues to EoR galaxies, most of which do not have spectra available. We used the less-than-optimal Salpeter IMF as it is the only one supported by some of the SPS models used in the analysis in subsequent sections, and for model comparison the consistency is more important than the overall choice .

Each model was run with 500,000 iterations – 50 walkers each with 10,000 chain steps. This proved to be an excessive amount, as convergence on a parameter either happened quickly, or not at all in the case of unconstrained parameters.

3.3.1 Specific Star Formation Rates

The specific star formation rate (sSFR) is defined the amount of star formation per unit stellar mass present in a galaxy.

There are a variety of ways to measure the star formation rate of a galaxy, offering different advantages and disadvantage, and probing different timescales of star formation. For example one common way is to measure the SFR based off of the UV luminosity of the galaxy, the logic being that this light is produced by short lifespan O/B/A stars, and therefore the number of these stars tells us about the numbers of stars formed recently in

the galaxy.

This method offers the distinct disadvantage however, that the UV is the most heavily attenuated by dust, so unless the dust content of the galaxy can also be characterised in some independent way, it is impossible to know the true SFR. This is not insurmountable – far infrared measurements can probe the dust emission of the galaxy, giving tight constraints on the dust content. However without those measurements, any UV derived star formation rate will only tell the whole story in the case of a dustless galaxy. Any SFR in a galaxy with non-zero dust content is guaranteed to be an underestimate.

For our purposes then, we measure the star formation rate of the EELS using the star formation history, by simply calculating the average value of the star formation history over a 100Myr period in the following way:

$$SFR_{\text{interrogator,100Myr}} = \frac{1}{100Myr}\int_0^{100Myr} SFR(t)\text{dt} \tag{3.8}$$

whereas the GAMA SFR's follow the prescription as found in Kennicutt [1983], deriving them from the $H\alpha$ emission line as follows:

$$L_{H\alpha,int} = (EW_{H\alpha} + 2.50)10^{-0.4(M_r-34.1)}\frac{3.0\times10^{18}}{(6564(1+z))^2}\left[\frac{f(H\alpha)}{2.86f(H\beta)}\right] \tag{3.9}$$

$$SFR = \begin{cases} \frac{L_{H\alpha,int}}{1.27\times10^{34}}, & \text{for Salpeter IMF} \\ \\ \frac{L_{H\alpha,int}}{2.286\times10^{34}}, & \text{for Chabrier IMF} \end{cases} \tag{3.10}$$

where $L_{H\alpha,int}$ is the intrinsic luminosity of the $H\alpha$ line after being corrected for dust, $EW_{H\alpha}$ is the observed $H\alpha$ equivalent width, M_r is the absolute magnitude as measured in the r-band ($\lambda \sim 650$nm), z is the redshift, and $f(H\alpha), f(H\beta)$ are the observed line fluxes of the $H\alpha$ and $H\beta$ lines respectively, the ratio between these two lines is often referred to as the Balmer decrement, and can be used as a crude method of measuring dust. The 2.86 in the final term is the intrinsic (dustless) value of the Balmer decrement ($f(H\alpha)/f(H\beta)$),

and by comparing it to the measured ratio of these lines, it can correct for dust attenuation of the line and mitigate the underestimation of the SFR due to dusts presence. As will be explored in section 3.5, the Balmer decrement is sensitive to the gaseous conditions (e.g. temperature, ionisation parameter, abundances) within the galaxy, but only weakly.

The function sSFR(M∗) is often called the specific star formation main sequence. In the local Universe, it can be divided up into three distinct populations. The Main Sequence of starforming galaxies is a tight power law, which can be parameterised in a variety of ways. This work uses the following from Sargent *et al.* [2014]:

$$\mathrm{sSFR}(M_*, z)[GYr^{-1}] = 0.095 \cdot 10^{\nu \log_{10}\left[\frac{M_*}{5\times10^{10}M_\odot}\right]} \cdot \exp\left[\frac{Az}{1+Bz^C}\right] \tag{3.11}$$

where sSFR is a function of stellar mass (M_*) and has redshift (z) as a parameter. $\nu, A, B\&C$ are dimensionless constants, which are set to the best fit values from Sargent *et al.* [2014] of (-0.21, 2.05, 0.16, 1.54) respectively. In addition to this main sequence, the two other significant populations of galaxies in the local Universe. The first is the passive "red & dead" galaxies, which by a variety of mechanisms – a combination of AGN activity, past intense star formation and stripping – have lost much of their gas, leading to significantly suppressed sSFR values – around 1.5dex or more at fixed stellar mass. Between the two sequences lies a sparsely populated "green valley" of galaxies which are thought to be transitioning between the two. Finally, the main sequence has significant upward scatter – Sargent *et al.* [2014] treats this as an additional log-normal component at fixed stellar mass with peak sSFR boost ~0.4 dex above the main sequence.

From equation 3.11, we can see that the final, exponential term is simply a function of redshift. If we define $Q(z) = \exp\left[\frac{Az}{1+Bz^C}\right]$, by just plugging in numbers we can notice that e.g. $Q(0.8)/Q(0.3) \approx 0.4$. This means that standard star-forming galaxies at $z = 0.8$ can occupy a very similar position in sSFR-M_* space as $z = 0.3$ galaxies undergoing a starburst, leading to further natural motivation for these objects being good analogues to high-z galaxies.

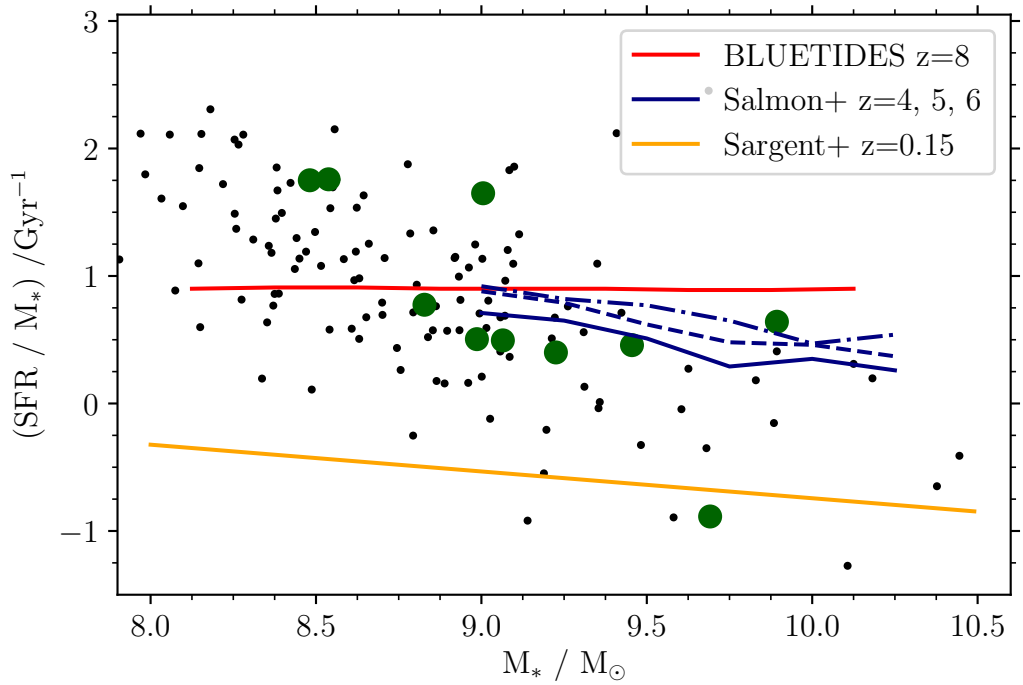

Figure 3.6: Plot of sSFR vs. Mstar for the sample of EELS, in comparison to observations at $z = 0.15$ [Sargent *et al.*, 2014], $z = 4, 5, 6$ (blue lines, from bottom to top) [Salmon *et al.*, 2015], and theoretical predictions from the BLUETIDES simulation at $z = 8$ [Feng *et al.*, 2016a].

Figure 3.6 shows the sSFRs as derived from the $H\alpha$ line strength for the EELS sample compared to the sSFR relation for all galaxies outlined in equation 3.11 with $z = 0.15$, which lies approximately in the center of the redshift cuts made during selection. Additionally, we compare to theoretical predictions from the BLUETIDES simulation, along with high redshift observations from Salmon *et al.* [2015]. The EELS largely lie significantly above the local main sequence, and much more closely match typical star-forming galaxies at much higher redshift further motivating their status as analogues.

3.3.2 Mass-metallicity relation

The second defining physical property of EELS is their low gas-phase metallicity. Gas phase metallicity is defined as the fraction of elements other than H & He in the ISM. This

is a hard quantity to measure because effectively the ISM is a sea of hydrogen with only trace amounts of all the other elements. The small quantities and complicated physics mean that it is largely impractical to measure metallicity directly, however techniques do exist to estimate it.

The most accessible method is to use measurements of emission lines produced by the interaction of ionising photons from massive stars with *nearby* gas (i.e. HII regions). Though this strictly is only a measure of the metallicity of gas illuminated by these stars and not a measure of the total gas metallicity of the galaxy, likely biasing the measurement. A further complication is that line ratios are not only dependent on the metallicity of the gas but also the ionising source (ionising spectrum and ionisation parameter) and conditions of the emitting gas including the density and temperature.

Depending on the lines available and their signal-to-noise a range of different calibrations have been explored in the literature. These techniques largely fall into two categories: *direct* methods that utilise the faint electron temperature and density (e.g. [OIIIλ4363]) lines to directly break the degeneracy of metallicity with these quantities and *strong line* methods which only use the more accessible strong lines (e.g. Hα, Hβ, [OIII]λ5007, etc.). There exist a range of strong line calibrations available in the literature.

Unfortunately the GAMA spectra *alone* (see Section 3.5) is of insufficient depth to robust measure the faint electron temperature and density lines and thus utilise the direct method. Instead we use the O3N2 diagnostic developed by Pettini and Pagel [2004]. The O3N2 quantity is:

$$O3N2 = \log_{10}\left(\frac{[OIII]\lambda5007/H\beta}{[NII]/H\alpha}\right) \tag{3.12}$$

which is related to O/H using:

$$12 + \log_{10}(O/H) = 8.73 - 0.32 \cdot O3N2 \tag{3.13}$$

where the named lines represent the line fluxes of each line, and $12 + \log_{10}(O/H)$

represents the log ratio of oxygen to hydrogen by mass present, which is a proxy for the overall metallicity of the galaxy, up to some calibration depending on the chemical abundances present. For reference, solar metallicity in this formulation is $12 + \log_{10}(\mathrm{O/H}) = 8.63$

Figure 3.7 shows the mass-metallicity relation for the EELS sample. They predominately have metallicities between $12+\log_{10}(\mathrm{O/H}) = 7.8-8.5$ (i.e. consistently sub solar), showing no significant evolution with increasing mass.

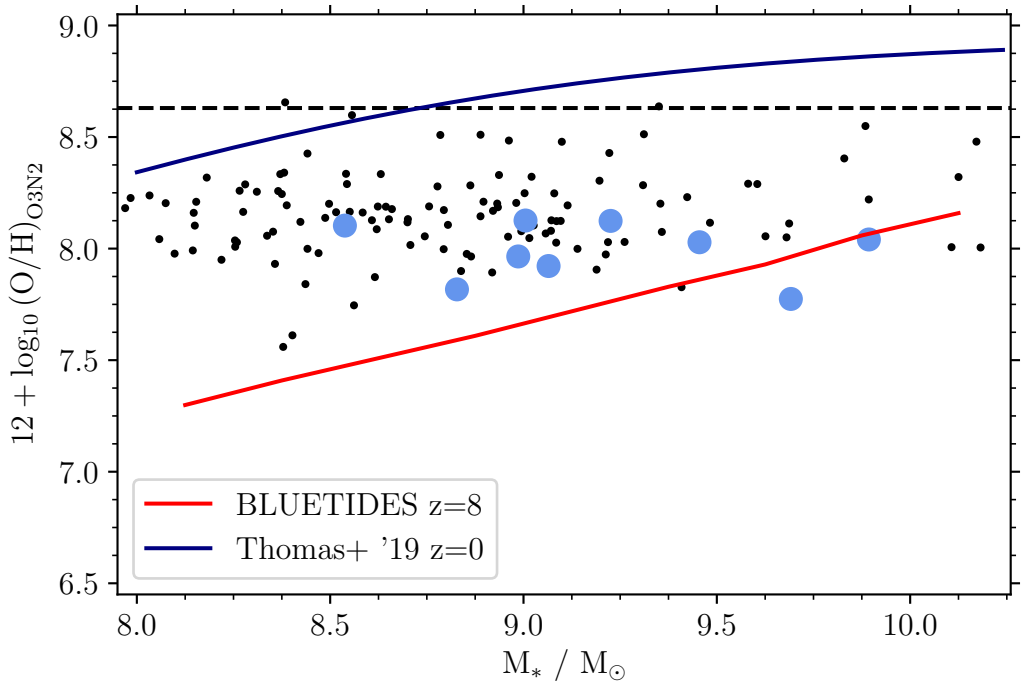

Figure 3.7: Mass-metallicity relation for the EELS sample. For comparison are lines corresponding to solar metallicity (dashed line), the BLUETIDES simulation at redshift 8 (red curve), and a local O3N2 diagnostic relation (blue curve) as measured in Thomas *et al.* [2019]. All circles are objects in the EELS sample. Larger, light blue circles are galaxies which X-SHOOTER spectra were subsequently obtained (see section 3.5.

It should be noted that in order to measure the metallicity in this way, four rest-frame optical lines must be obtained (see equation 3.13, which is a serious challenge for high redshift galaxies with current telescopic technology. Webb is ideally suited to take these measurements, obtaining deep rest-optical spectra allowing the true extent of the analogy

between EELS & EoR galaxies to be tested. Thus we simply compare the EELS to predictions from BLUETIDES, which predicts a power law with slope ~ 0.5 with increasing mass. This is in contrast to the flatter-but-higher relationship suggested by the EELS, suggesting that they have higher metallicities than all but the most massive high redshift galaxies. Finally, it is worth remarking that metallicities are both challenging to measure and simulate, exhibiting extreme sensitivities to input physics of simulations, and requiring the traversal of multiple scaling relations to obtain from spectra in this way [e.g. Sutherland and Dopita, 1993].

3.3.3 Source of ionising photons

EELS have relatively strong ionizing radiation fields, due to the large numbers of O/B/A stars active within them. However it is equally possible (especially with our selection simply on the Hα line) that the strong emission is sign of an Active Galactic Nuclei (AGN). While the existence of low-luminosity AGN is interesting the presence of the AGN will render stellar mass, star formation, and metallicity measurements invalid. Moreover, theoretical modelling suggesting the contribution of AGN to galaxies at high-z is small [Behroozi *et al.*, 2013].

Fortunately, there exist a number of nebular emission line diagnostic diagrams, so-called BPT diagrams (named after "Baldwin, Phillips & Telervich"), that can be used to distinguish the ionization mechanism of nebular gas. Several different versions of these diagrams exist, however, we focus on a single diagram, the commonly used BPT-NII diagram.

The BPT-NII diagram uses the ratios of the [OIII] & Hβ, and [NII] & Hα. The use of hydrogen lines mitigates the effect of dust: the amount of attenuation over the small wavelength ranges between [OIII] & Hβ, and between [NII] & Hα is approximately constant, therefore by normalising by these lines – whose intrinsic ratio is assumed to be approximately constant in the ISM [Osterbrock, 1974] – we can correct for dusts effect on the metal lines.

Various studies [e.g. Kewley *et al.*, 2001; Kauffmann *et al.*, 2003] have defined the

dividing line between ionisation due to star formation (massive stars) and AGN. In general galaxies with high (or strong) line ratios are associated with AGN.

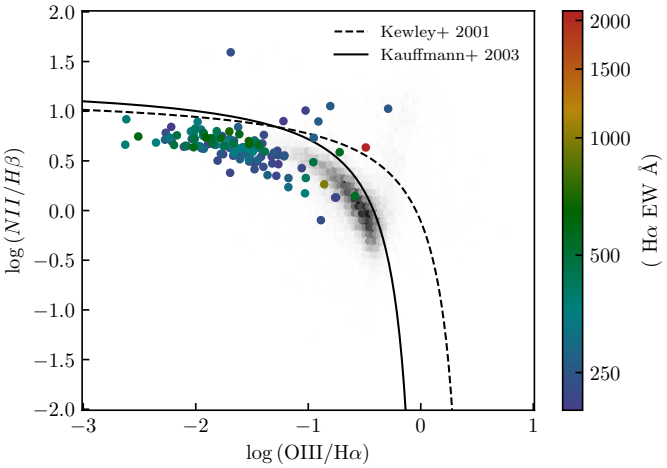

Figure 3.8: BPT-NII diagram of the EELS sample. Grey point cloud is the entire GAMA sample, while coloured points are EELS.

The BPT-NII diagram for the EELS is shown in Figure 3.8. As can be seen, most of the EELS occupy the upper left tail of the local star-forming galaxy distribution (grey point cloud is the whole GAMA sample). The location of this main cloud is in line with other studies in the literature which have found similar high-z analogues , $z \sim 2$ galaxies, and compact high-sSFR galaxies in general in this location [e.g. **??**].

However, a small number - 7 (9) - of the original EELS sources fall above the Kauffmann *et al.* [2003] (Kewley *et al.* [2001]) dividing line and are therefore likely to be contaminating AGN. Due to the difficulty in extracting the AGN and measuring the true galaxy physical properties of these sources these are omitted from subsequent analysis.

3.3.4 Star Formation History

One final physical property briefly worth noting is that of the star formation histories of these galaxies. In the standard GAMA pipeline modelling [Wright *et al.*, 2016], as almost

all of the galaxies are at low redshift, the assumption is that all of the galaxies have declining exponential star formation histories, that is:

$$SFR \propto \exp -\lambda t \tag{3.14}$$

where $\lambda = 1/\tau$ is the inverse of the e-folding time, and is strictly greater than 0.

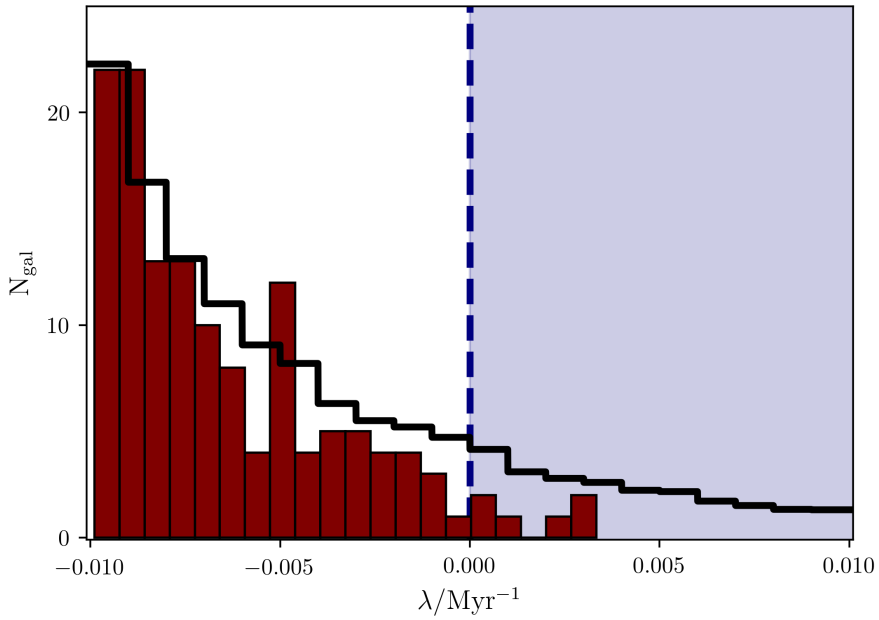

Figure 3.9: Histogram of the exponential SFH parameter λ for the 136 EELS galaxy sample. Modelling contained within GAMA catalogue restricts λ to the blue shaded area (falling exponential SFH). Red bars show histogram of median best fit parameter, whereas the black bar shows the stacked PDFs of the same objects. When parameter is allowed to move freely, all but 6 galaxies show preference for a rising SFH.

However, in our initial modelling, we opted to leave λ to vary across both positive and negative, as if these galaxies are reasonable analogues of high-z galaxies we would expect them to have rising SFH (i.e. $\lambda < 0$). Figure 3.9 vindicates this choice – almost all of the galaxies in the sample are consistent with *rising* SFHs. As will be shown explicitly later in section 4.9, this means that the standard catalogues either pathologically underestimate the number of young stars, and therefore the recent star formation activity in these galaxies,

and/or they must overestimate the stellar mass to compensate.

Summary The summary of the EELS physical properties is that they are well matched to both observations and simulations of the typical population at much higher redshift than where the EELS reside in sSFR-M_* space. However their metallicities appear, at least based on prediction from hydrodynamical models, to be too high for them to be considered true analogues of galaxies in the distant Universe, lying somewhere between the BLUETIDES predictions of $z \sim 8$ galaxies, and solar metallicity, while also exhibiting a much flatter evolution with stellar mass.

3.4 Model Comparison with INTERROGATOR

One specific question we wish to answer about these galaxies is what the model uncertainties look like – if we change some aspect of the model being used, how does that change the parameters inferred?

To do this we adopt the following methodology: each EEL sample galaxy is run through INTERROGATOR with the fiducial model as mentioned in section 3.3. To restate, this model involves the following choices & priors, and we call this model "1":

- **SPS model -** Pegase v2.0
- **SFH -** A single parameter exponential model, with time constant free to be both positive (dec. SFH) and negative (rising SFH)
- **Nebular Emission -** Active, provided by CLOUDY
- **Dust Modelling -** Calzetti dust curve

this model is then perturbed in the following ways with replacement (i.e. they are all perturbations on model 1, not on each other):

2. Swap the SPS model to BPASS v2.2.

3. Remove Nebular Emission (force $f_{esc} = 1$).

4. Change the IMF to a Salpeter IMF.

5. Restrict the SFH to be constant only.

6. Restrict the SFH to be exponentially declining only.

7. Combination of models 3 and 6, which matches the assumptions GAMA modelling make.

In addition, we include the two model fits available in the original GAMA catalogues [Wright *et al.*, 2016]:

8. Lambdar Catalogue.

9. Magphys Catalogue.

We focus on the two properties that are arguably the most important for the study of EoR galaxies – the stellar mass, and the star formation rate. Effectively these allow constraints to be placed on the star formation history (SFH) both for the individual galaxy and the cosmic SFR density as a whole.

Figure 3.10 shows the model comparisons in stellar mass. Overall, we find that the average mass undergoes significant scatter – the combinations we tested have a scatter on their medians of $\sim$ 0.2dex, and individual galaxies can have much larger changes based on model choice.

Switching the SPS model to BPASS causes the stellar mass of every galaxy in the sample to increase, with a median value of $\sim$ 0.35dex. This is mostly due to two factors – the BPASS v2.2 version only supports the Salpeter IMF, which as can be seen from model 4, increases the mass by increasing the proportion of low mass stars at fixed normalisation. In addition, BPASS is unique in that it allows stars to form binaries. High mass stars in binaries have harder spectra than those which form alone, which means less mass in the

young stellar population bins is required to reach the UV observations, and more mass is put into older, lower M/L ratio bins, increasing the overall mass.

Nebular emission contributes to stellar mass in two ways – the addition of continuum emission means that less stellar content is required to bring the continuum up to a given luminosity, as by definition the observed continuum is the sum of the stellar and nebular components. This means that if nebular emission is non-zero, there must be some reduction in the inferred stellar mass. Secondly, these fits were carried out with the broad band photometry, which is vulnerable to contamination from large nebular line fluxes, which artificially raise the observed continuum if you then neglect to include these in the model when fitting.

Switching to a Salpeter IMF over the Chabrier has the effect of increasing the proportion of low mass stars at fixed normalisation – see figure 1.3. As these low mass stars both emit weakly in the UV, and also have much higher mass-light ratios than high mass stars, the switching of IMFs will increase the mass. The two IMFs have (proportionally) the same numbers of high mass stars in, so as these are added in order to meet the UV observations, more low mass stars are added, which have little effect on the overall optical/IR flux, but add mass all the same.

As established in section 3.3, these galaxies are all consistent with exponentially increasing star formation histories. If however, we restrict the SFH to either a constant, or exponentially declining with time, the measured mass is likely to increase because the best fit SFH will often have less stars in the very youngest bins. These bins contain the stars with the lowest mass to light ratio, and "replacing" them with older stars of the same luminosity requires more mass.

These changes are highly non-linear however – model 7 is the sum of the changes of models 3 & 6, and results in almost no change in the inferred masses. It is likely that this arises because nebular continuum can be replicated with lower mass stars from a slightly more steeply declining SFH, while keeping the mass fixed, however a scenario like this is incredibly hard to test due to the complex interactions between the models.

Another result of note is that the medians are largely in 1 sigma agreement with each other, and entirely in agreement to 2 sigma, so while this effect isn't such that one model set can be "incorrect", model uncertainty is something that certainly should be taken into account when quoting the stellar mass of a galaxy measured from photometry as these are.

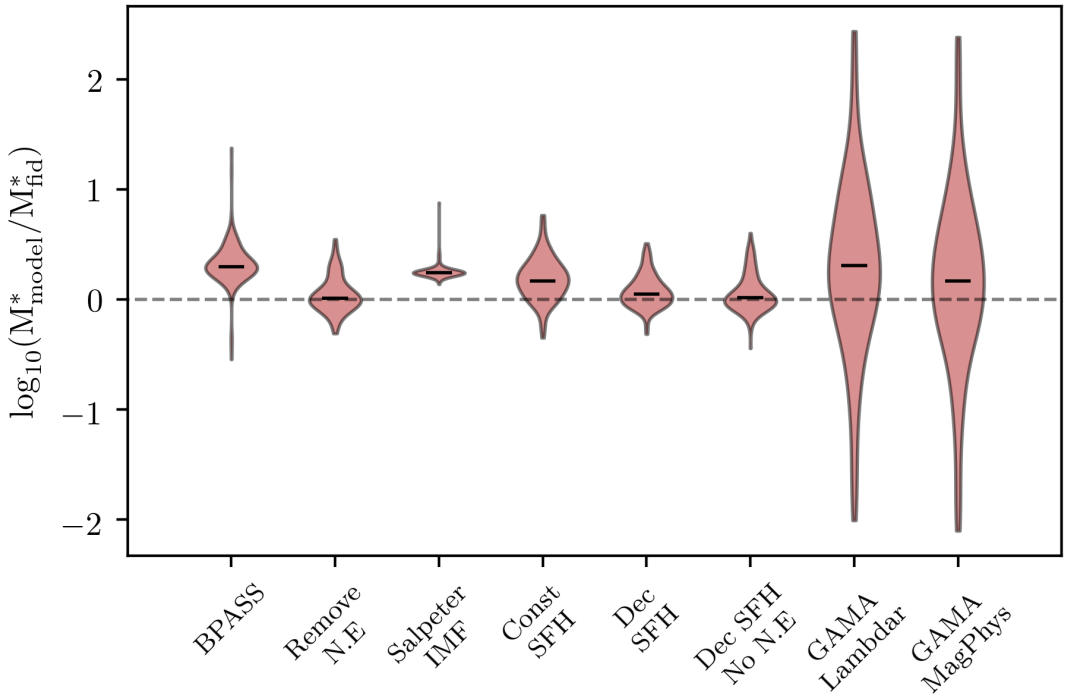

Figure 3.10: Comparison of $\log_{10}(M*/M_{\odot})$ inferred from INTERROGATOR model fits with different models. Numbered models are described in the text. Models 2-7 are perturbations on the fiducial model, and 8 & 9 are from the GAMA data products, again as described in the body text. Black points are individual galaxies, green points are the medians in each bin, with errors on the median as green errorbars.

Similarly, figure 3.11 shows the same comparison information for the SFR. It is much more difficult to make any statements on the spread of these values, as they are degenerate with other parameters such as dust content and metallicity.

There are some limited statements which can be made however. Firstly, the removal of nebular emission actually has little effect on the measured star formation rate as measured from photometry. The median is $<1\sigma$ from the fiducial model, and over 70% of individual

objects are also within 1σ of their fiducial model measurement. More curiously, even if we neglect nebular emission and enforce a declining SFH (which, as established in figure 3.9 is inaccurate for these objects) we still recover the same SFR as the fiducial model.

This is because the amount of dust is effectively unconstrained. The two GAMA models are very similar in process to the declining SFH/no nebular model, however they have one important difference – GAMA modelling includes fa infrared data from Herschel, which provides independant constraints on the dust content. This explains their significantly lower and tighter distributions – they are unable to arbitrarily add star formation & dust due to the FIR restriction, and thus cannot produce SEDs with high SFR with declining SFHs.

It is most important to note that the spread on the median represents a factor ~3 variation, but individual galaxies can have much more scatter across models than this. Individual galaaxies can see increases in SFR by a factor $\sim$ 10, and decreases in SFR by up to a factor $\sim$ 50 in extreme cases. This can be for a variety of reasons, but the underlying theme is that other parameters can "make up" for changes in modelling. If independent constraints are placed on these parameters, then the accurate reproduction of inferred parameters such as M* and SFR falls apart. It bears reiterating then, that when analysing galaxies with limited data, model uncertainties can potentially be a dominant force, and folding them into any statements on the physical properties of these types of observations important. This is especially important when looking at actual high-z galaxies, where large samples are not available, and even with Webb large samples will not be forthcoming. In addition, FIR data is likely not available for these objects either. It will therefore be of vital importance to perform this sort of test, because we ultimately don't know which set of models best represents the true Universe, and potentially the scatter in both M* and SFR can be large.

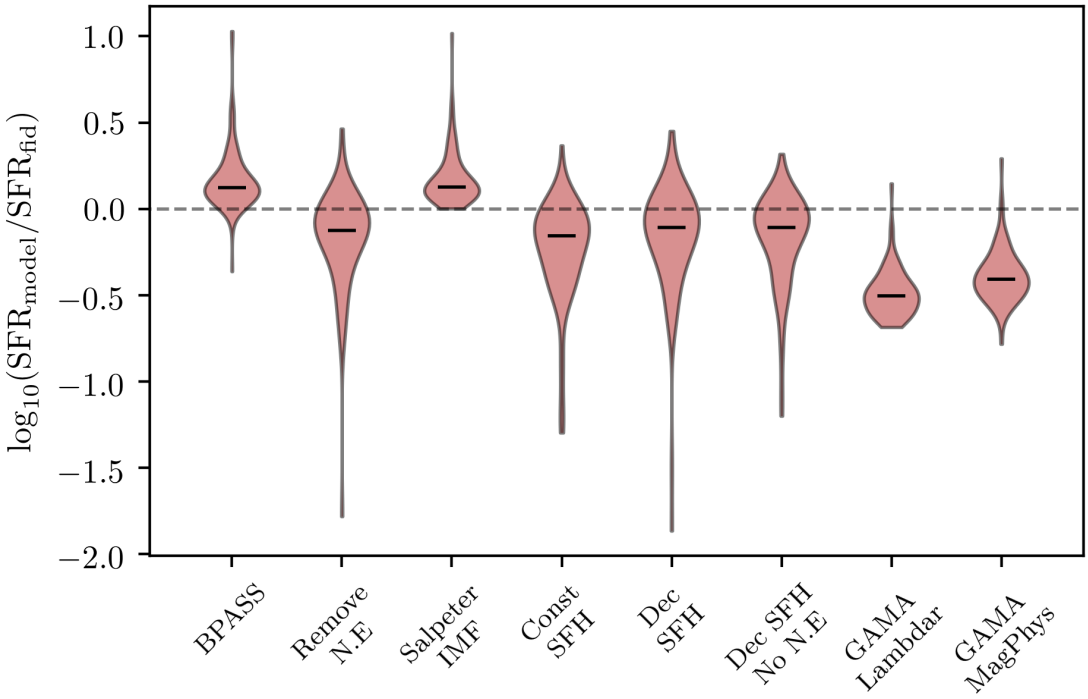

Figure 3.11: Comparison of $\log_{10}(SFR)$ inferred from INTERROGATOR model fits with different models. Numbered models are described in the text. Models 2-7 are perturbations on the fiducial model, and 8 & 9 are from the GAMA data products, again as described in the body text. Black points are individual galaxies, green points are the medians in each bin, with errors on the median as green errorbars.

3.5 Spectroscopy with VLT X-SHOOTER

The sensitivity and resolution of the GAMA spectra only allows us to measure metallicities via the imprecise strong line diagnostics.

As noted previously, the most reliable determination of elemental abundances are via relative strengths of emission lines from HII regions, including weak, temperature-sensitive transitions such as [OIII]λ436.3nm - commonly known as the *direct method* [**??**].

To provide the necessary lines, sensitivity, and resolution time was obtained on VLT/X-SHOOTER (Vernet et al. 2011) in P96B (096.B-0632, PI Wilkins) to obtain UV - NIR spectra for a sub-sample of the EELS. In addition to the measurement of the [OIII]λ436.3nm

line, the UVB arm of X-SHOOTER is sufficiently sensitive and of high enough resolution to detect and separate the [OII]$\lambda\lambda$372.7nm,372.9nm doublet, from which we can derive O+/H+ and thus remove the need for uncertain ionisation correction factors. The wavelength range accessible to X-SHOOTER also encompasses the [SII]$\lambda\lambda$671.6nm, 673.1nm doublet whose ratio is sensitive to electron density (N_e), further enabling accurate direct-method abundances [**?**]. Together, these combination of lines should provide robust metallicities of the EELS.

One unique aspect of X-SHOOTER is its ability to simultaneously obtain spectra from 300-2500nm using three arms (UVB, VIS, and NIR). This not only provides access to the lines necessary to obtaining accurate metallicities but also a host of other useful lines, enabling us to answer other science questions.

Specifically, the X-SHOOTER spectroscopy of our sub-sample of EELS will allow us to measure all the bright hydrogen Balmer and Paschen series lines, extending from 400-1900nm. Because of the intrinsic ratios of these lines are only weakly sensitive to metallicity, density, and temperature, their measurement can potentially allow us to constrain the relative attenuation across the visible and near-IR and thus allow us to constrain the dust curve.

3.5.1 VLT-XSHOOTER Observations

Observations of 19 EELS (EELS-1 $\rightarrow$ 19) were proposed with 12 ultimately observed in service mode. Each of the 12 sources were observed for $\sim$ 25 minutes. The resulting raw observations were reduced using the version 2.6.1 of the X-SHOOTER pipeline by a collaborator (J. Caruana, University of Malta) with reduced and calibrated spectra provided for analysis.

3.5.2 Line Fitting VLT-XSHOOTER spectra

With spectroscopic redshifts already established the first task was to accurately fit each target line. To acheive this we developed a simple line and continuum fitter using EMCEE (section (2.3.1) to create a simple line and continuum fitter.

We divide the spectra through by $(1 + z_S)$ where z_S is the spectroscopic redshift from the GAMA catalogue (figure 3.1) so it is in the rest frame. Then cut out a piece of the spectra at $\lambda_C \pm 50$, where λ_C is the "book" wavelength of the line, in order to isolate the line as much as possible. We treat this cut-out as a combination of a straight line (continuum) and a gaussian $\mathcal{G}$ (line emission). However, as the slope and intercept of a traditional $y = mx + c$ line are extremely unstable (as we are fitting the line very far from the pivot point at $x = 0$ we re-parameterise the continuum in terms of $\lambda_0, \lambda_1, y_0, y_1$ where λ_0, λ_1 are the wavelengths of the endpoints of the cutout, and y_0, y_1 are the fluxes at those points. This means the model function looks as follows:

$$F_{\text{model}}(\lambda) = \frac{y_1 - y_0}{\lambda_1 - \lambda_0}\lambda + 0.5(y_0 + y_1) - \frac{(\lambda_1 + \lambda_0)}{2(\lambda_1 - \lambda_0)}(y1 - y0) + A \cdot \mathcal{G}(\lambda; \lambda_C, \sigma) \tag{3.15}$$

This model therefore has 5 parameters: $A, \lambda_C, \sigma, y_0, y_1$, which represent the amplitude of the line emission, the line center, the line width, and the two endpoints of the continuum line (effectively encoding the slope and intercept of said line) respectively. Figure 3.12 shows a toy example of this fitting procedure in action, the blue line represents a model input, from which noise is added, where the peak of the line has SNR=20. This data is then fit with 50 walkers, 5000 iterations, and removal of the first 500 iterations as burn-in. The green line is then a model realisation of the median parameters, showing that the recovery is very strong in this SNR regime ($\chi^2 = 1.14$ for this example).

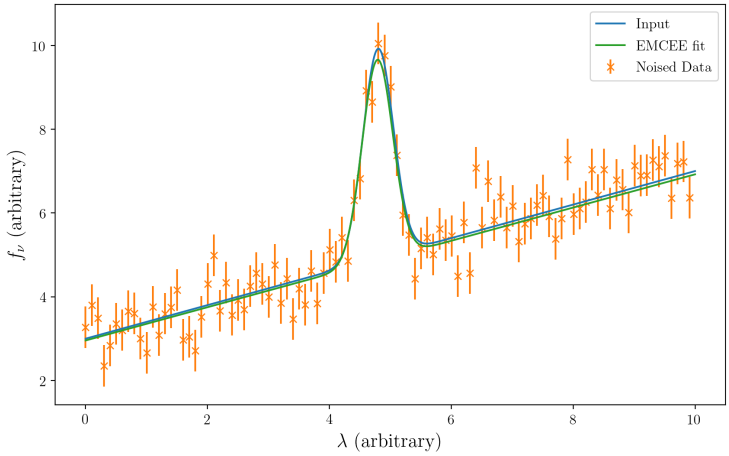

Figure 3.12: Demonstration model of EMCEE based line fitting code. Smooth input model (blue) is degraded in resolution, and noise is added (yellow) where $SNR_{peak} = 20$. Line is then refit as described in main text: green line represents the median recovered parameters.

For each line, we adopt uninformative flat priors, imposing limits of where we physically expect the parameters to lie (e.g. the model amplitude can extend from 0 to 100× the maximum data value). The one exception is the central wavelength. As we know where these lines should lie in the rest frame, but there may be some slight variation due to the sampling of the spectra, we opt for a narrow gaussian prior centered on the "book" wavelength, and with $\sigma = 5$Å.

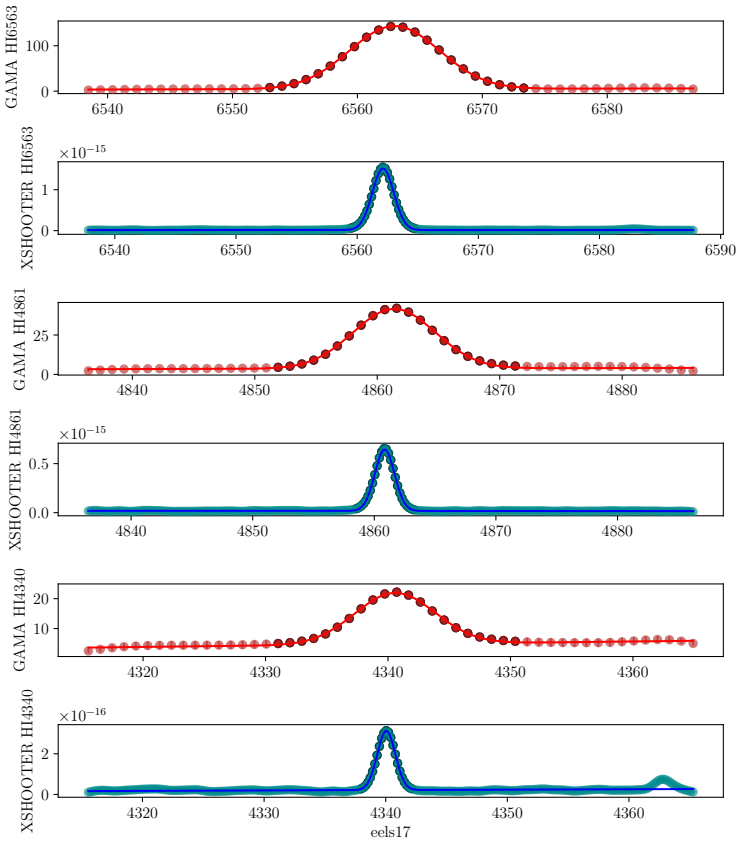

Figure 3.13: Line fit of $H\alpha$, $H\beta$, $H\gamma$ and $OIII\lambda5007$ of a galaxy from the EELS sample. Red lines are from the original GAMA spectra, and blue are from the obtained X-SHOOTER spectra. Circles represent binned data, and solid line represents the model with median parameters. Darker points are those within 3-σ of the inferred central wavelength λ_C.

We also opt to fit both the original GAMA spectra, and the X-SHOOTER spectra, both as a test case of the code and to check for consistency between the spectra. Figure 3.13 shows example fits for the GAMA (red) and XSHOOTER (blue) line emission for one of the objects. We include the other fits in appendix B, along with the full X-SHOOTER spectra of the sample.

It should be noted that during the course of this process, and following a visual examination, that the object denoted EELS-01 was fund to have a detective spectra not suitable for analysis. It is included in analysis figures for completeness, but was excluded from all calculations beyond this. The spectra can be see in appendix figure **??** for comparrison to the other sampled objects.

3.5.3 Line Ratios

Armed with the measured flux for each target line we can now explore various line ratios. To begin we explore the ratios of strong lines and compare them to the GAMA/AAT spectra derived values as an integrity check.

Balmer decrement 3.14 shows the Balmer decrement ($H\alpha/H\beta$) as calculated from the two spectra as highlighted above, and also directly from the GAMA catalogue – faded blue points represent calculations done by simply numerically integrating the continuum subtracted data, with the GAMA values taken from the catalogues [Baldry *et al.*, 2018]. The red points represent the same but calculated from a Gaussian fit, again with GAMA values taken from the catalogues and the X-SHOOTER values taken from the calculations earlier in this section. The 1:1 line represents both spectra returning consistent results for the two lines (or at the very least their ratio). The shaded blue box represents allowed values for the Balmer decrement – dust attenuates more at shorter wavelengths, so as more and more dust is added, the $H\alpha$ line is attenuated less than $H\beta$, causing their ratio to only increase. When no dust is present, we adopt the value of 2.88 as their intrinsic ratio [Osterbrock and Ferland, 2006]. While this value assumes a density $n_H = 10^{-2} cm^{-3}$ and temperature $T = 10^4 K$ for the gas, it only varies weakly in realistic ISM conditions.

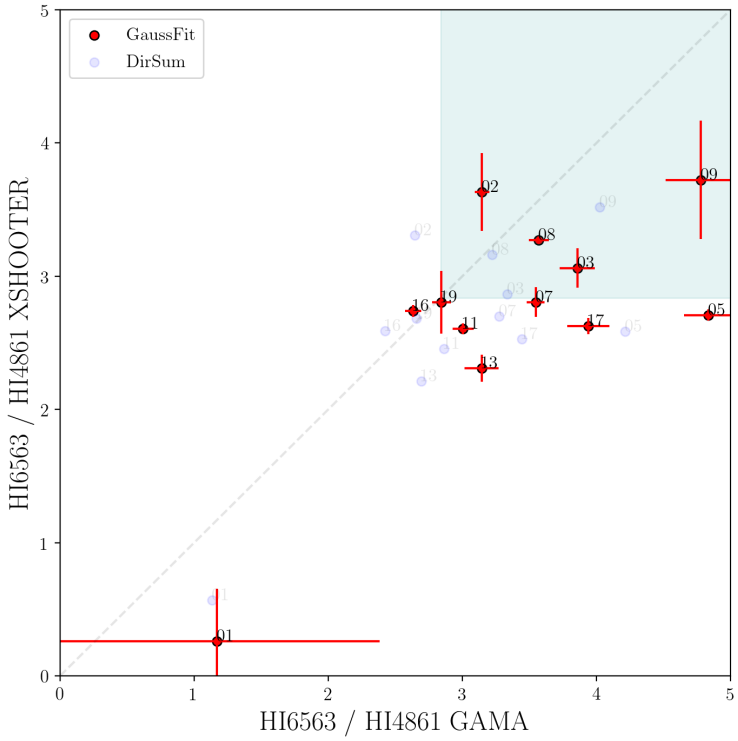

Figure 3.14: Plot of the Balmer decrement as measured in the GAMA catalogues [Wright *et al.*, 2016] vs. as measured in this work. Blue faded points represent calculations via direct summation and red points represent calculations from gaussian fits with 1-σ error bars. Marked on the plot are the 1:1 line between the two spectra, and the shaded box represents physically meaningful Balmer decrements – intrinsically the value is ≈ 2.88, and increases with increasing dust content.

As can be seen in 3.14, 8 of the 12 galaxies in the sample lie in regions of parameter space which would represent dust with a preferential attenuation of longer wavelengths. Even stranger, 3 of the 12 galaxies show this behaviour in both the GAMA and X-SHOOTER spectra. This obviously represents a problem with either the modelling or with the data acquisition. After detailed correspondence with the X-SHOOTER team, and re-reduction of the data, errors in the reduction process could not be found.

We also carried out various diagnostics to ensure that the calculations we had carried out weren't erroneous. Figures 3.15 and 3.16 show the ratio of the catalogue fluxes to the

fitted fluxes (the red fluxes shown in figure 3.13 and Appendix B) from this work for $H\alpha$ and $H\beta$, as functions of observed wavelength and of catalogue flux. These show that there is no dependence on either quantity, however we systematically underestimate $H\alpha$ slightly, and overestimate $H\beta$ as compared to the catalogues. This would increase the Balmer decrement, however it is unclear a) why this happens, or b) what an appropriate correction would be. As it still remains possible that the acquisition of these objects is also faulty (multiple GAMA catalogue measurements display un-physical Balmer decrements still) it was deemed irresponsible to attempt to apply some correction and continue the work.

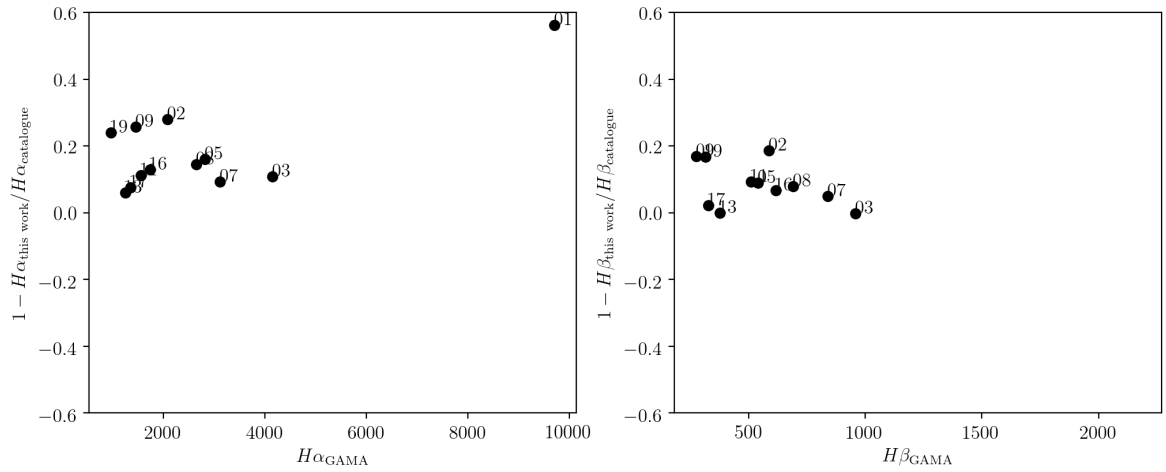

Figure 3.15: Ratio of the GAMA spectra flux for $H\alpha$ (left) and $H\beta$ (right) as measured using EMCEE (see main text) and from the GAMA catalogues [**?**] as a function of line brightness

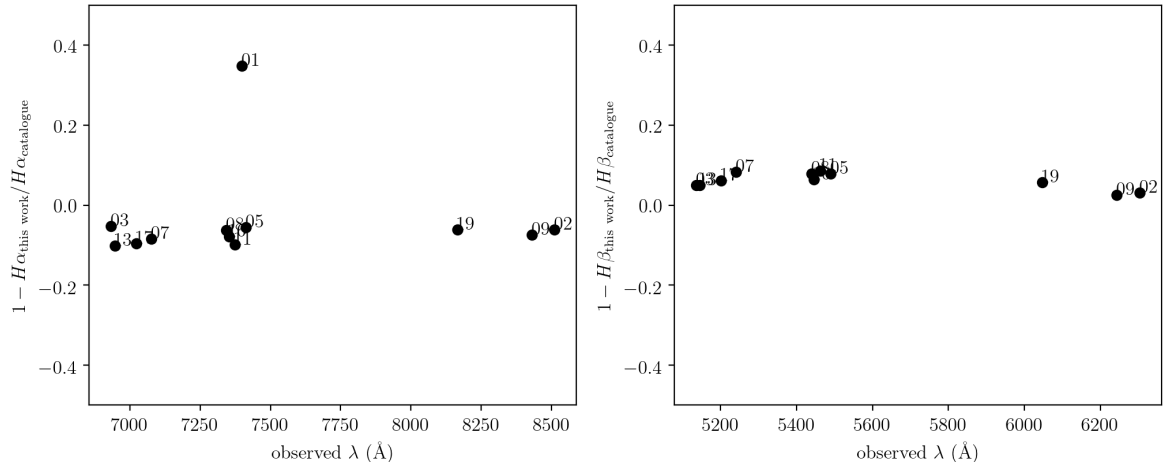

Figure 3.16: Ratio of the GAMA spectra flux for $H\alpha$ (left) and $H\beta$ (right) as measured using EMCEE (see main text) and from the GAMA catalogues [**?**] as a function of observed wavelength.

Summary VLT/X-SHOOTER observations of a sub-sample of 12 EELS were obtained, reduced, and some preliminary analysis completed. Unfortunately, early results from analysis of the Balmer decrements yielded results significantly different from the GAMA/AAT derived values and, in the majority of cases, values implying stronger attenuation at Hα than Hβ which is un-physical. With both these problems raising concerns about the integrity of the observations and/or derived quantities the decision was made to abandon this part of the project and concentrate efforts elsewhere. However, with improvements to the X-SHOOTER pipeline (the current version is 3.5 compared to 2.6 used in this study) it might be worth re-examining whether the issue still persists in the future.

3.6 Conclusions

We first, in Section 3.2, select a sample of high-z analogous galaxies from the GAMA survey. We select these galaxies on the equivalent width of their $H\alpha$ line: strong $H\alpha$ emission is produced by star formation, but if it is a high mass galaxy, the continuum will also be strong reducing the EW. Therefore we select galaxies with EW(Hα) > 200Å, and

with redshift $0.05 < z < 0.3$. We are able to make such a simple selection thanks to the high quality spectra provided in the GAMA survey, other selections have been forced to use colour based selections as they only have access to photometry. Our sample after selection consists of a sample of 136 EELS.

In Section 3.3 we then derived and analysed the physical properties of our EELS sample using using INTERROGATOR. We find that these EELS are good analogues to high redshift galaxies when considering their positions on the galaxy main sequence. They have relatively low stellar masses, and significantly enhanced specific-SFR compared to the local Universe main sequence, on average following much more closely the star forming galaxy main sequence as high as $z \sim 8$. The sample also exhibits metallicities significantly below the mass-metallicity relation, however the distribution is much flatter and much less offset than that of simulated high-z galaxies. Extreme care must be taken when trying to draw analogies between low redshift EELS or similar, and true EoR star-forming galaxies. Finally, we find in the INTERROGATOR fits, that the galaxies in our sample almost all contain rising star formation histories, which motivates our use of our physical parameters over those provided in the catalogues, as the catalogues assume a falling star formation history *a priori* and this can severely bias the measurements of other parameters.

In Section 3.4, we then moved to quantifying this difference, by carrying out a model comparison between the galaxies in our sample – i.e. how do inferred physical parameters change when we use a different model to infer them? We find scatters of $\sim 0.4dex$ in both the median stellar mass and star formation rate for the choice of models we chose, with significantly larger scatter possible on individual objects. While these galaxies are arguably the "worst case" in the local Universe, it is important to quantify these changes because the large amounts of nebular emission and unusual rising SFHs are much more common in the EoR.

Finally, as described in Section 3.5, we obtained and analysed VLT/X-SHOOTER spectroscopy of a sub-sample of 12 EELS. In principle this should permit the measurement of accurate direct method metallicities and constraints on the shape of the dust curve. We

design an EMCEE-based line fitting code to fit emission lines from these spectra, with the aim of using known intrinsic line ratios to accurately map the dust curves of these objects. Unfortunately, early analysis raised concerns of the integrity of the observations themselves or reduction prompting us to abandon this part of the project.

Chapter 4

The Star Formation and Metal Enrichment Histories of Galaxies in the Epoch of Reionisation

This chapter focuses on the star formation and metal enrichment histories and modelling of the stellar spectra of galaxies in the Epoch of Reionisation (EoR). Specifically, creating a model of how the stellar populations are distributed in age/metallicity space that is more physically representative of the populations of galaxies during this period than commonly used alternatives.

4.1 Motivation

Many SED fitting codes make the assumption that galaxy star formation histories are constant or declining (i.e. most star formation at higher ages). However, the earliest galaxies are expected to have increasing star formation histories.

Furthermore, most SED fitting techniques operate under the assumption that the stellar metallicity is constant throughout the galaxy. They make this assumption because then all that is required is a single parameter which describes the metal content for stars of all stellar ages. One notable exception is VESPA [Tojeiro *et al.*, 2007] which assigns each age bin of the SFH a different (= single) metallicity.

This model of chemical enrichment is obviously untrue – we could think about compar-

ing the very first stars – often known as population III stars, which would have almost no non-hydrogen, non-helium elements, and compare them to the next generation population II stars. These stars will have formed from gas which has been enriched by the previous generation, and are thus almost guaranteed to have higher metallicities.

In order to make any meaningful statements about these populations, it is invaluable to have a "true" distribution to compare to. We will therefore use the BLUETIDES simulation as a source of our galaxies. This offers the significant advantages that we can isolate the sources of error that arise from modelling rather than also having to contend with observational errors. We also remove any errors related to turning a population of stars into their overall light – we can ignore the effects of dust, the ISM, IGM, and any modelling errors which arise from the fact that SPS models are not a perfect representation of real stars – all of these effects of course still exist, but the models INTERROGATOR or indeed any other SED fitting code would use all ultimately take a pure stellar spectra and apply corrections to it (see 2.2.1 for how this is done).

We fist introduce the elements necessary to carry out this analysis, then model the SFHs without considering metallicity. We then introduce a way to model the metallicity distribution, and then the joint age-metallicity distribution of these galaxies, comparing to BLUETIDES in stellar population histogram space. Finally, we explore the impact this has on observables, and what modelling errors can be introduced from just the stellar spectra when detailed observations of the rest frame UV and optical are made with JWST.

The overall motivation of this approach is to offer a higher-parameter, more realistic model of the stellar populations of EoR galaxies in SFH-Z space, and to fold this model into INTERROGATOR as a sub module replacing a traditional SFH & single valued metallicity.

With the high quality data which future observatories promise, interpretation via modelling must keep pace, and this technique offers a novel approach to examining stellar populations. For lower redshift galaxies, it is not expected that this technique will be applicable as the mixing times for the galaxies gas reservoirs will be much shorter than the age of the Universe, but in the EoR where this is largely not true, the uneven distribution

of metals could be misinterpreted, leading to systematic uncertainties derived from any measurements made.

4.2 The Bluetides Simulation

As described in Section 1.4.4 a relatively recent (< 10 years) development in in numerical galaxy formation is the ability to run hydrodynamical simulations, which self-consistently follow the evolution of dark matter and baryons, in cosmological volumes (i.e. $> (50\,\mathrm{Mpc})^3$). These simulations include baryonic physics such as cooling, star formation, and feedback from stars and super-massive black holes. While these simulations still involve some sub-grid physics on small scales there is much less than used in semi-analytical models. Crucially, these simulations therefore predict star formation and metal enrichment histories by their very nature of tracking baryon physics from the outset. These are represented, in most cases, by a number of discrete (in formation epoch, metallicity, position, etc.) star particles. In cosmological simulations these star particles don't represent single stars but rather clusters of tens of thousands to tens of millions stars, depending on the resolution of the simulation.

While there are a number of prominent examples of cosmological hydrodynamical simulations such as EAGLE [Schaye *et al.*, 2015] and Illustris [**?**] one downside of these simulations is the relatively small volume simulations ($\sim (100\ \mathrm{Mpc})^3$). This is particularly problematic at high-redshift where the space density of galaxies is much less than at lower-redshift providing poor statistics. Overcoming this issue is the BLUETIDES simulations. BLUETIDES is a cosmological hydrodynamical simulation (that is, a simulation whose box is larger than the focused specifically on simulating the Epoch of Reionization (EoR), specifically at $z > 8$ (phase I) and $z > 7$ (phase II, not considered in this work). By simulating only the EoR BLUETIDES is able to simulate a much larger volume at high-resolution than other simulations.

Specifically, BLUETIDES encloses a box of $400/h$ Mpc on a side and uses $2 \times (7040)^3$

particles making it amongst the most ambitious hydrodynamical cosmological simulations ever undertaken. The simulation was performed at the National Center for Super-computing Applications, on the BlueWaters cluster, on some 650,000 cores.

Full details of the BLUETIDES hydrodynamics and sub-grid modelling are provided in Feng *et al.* [2016a]. However it is worth recording a few of the most relevant details for our purposes here:

- BLUETIDES uses a heavily modified version of the GADGET code [Springel *et al.*, 2001; Springel, 2005] described originally in Feng *et al.* [2016a]. Specifically it adopts the pressure-entropy formulation of smoothed particle hydrodynamics to solve the Euler equations [Hopkins, 2013; Read *et al.*, 2010].

- Initial conditions were generated at $z = 99$ using an initial power spectrum from Lewis and Bridle [2002]

- Star formation mechanisms were implemented according to the multi-phase star formation model outlined in Springel and Hernquist [2003], folding in additional effects from Vogelsberger *et al.* [2013]. Gas cooling is handled radiatively following Katz *et al.* [1996], and via metal cooling approximated by scaling a solar metallicity template, as used in e.g. **?**. Molecular hydrogen quantities are estimated from the column density of gas, and the precise effect of the molecular hydrogen on star formation follows Krumholz and Gnedin [2011].

- The formation of supermassive black holes (SMBHs) and their feedback are handled following Di Matteo *et al.* [2005]: halos with a mass greater then $5 \times 10^10\ h^{-1}\ M_\odot$ are identified and seeded with a black hole of mass $5 \times 10^5\ h^{-1}\ M_\odot$. This mass is consistent with models of direct collapse for the formation of SMBHs, but is ultimately a free parameter which is suggested to range between $100 M_\odot$ and $10^6 M_\odot$. Feedback energy produced from SMBHs is deposited in the gas particles surrounding the SMBH.

4.3 Star formation Histories

As discussed earlier in section 1.5.1.1, and 2.2.1.1, star formation is the most important process governing the evolution of a galaxy. The bulk properties of the stars – star formation rate, stellar age and, star formation rate – can be said to be the most fundamental properties, and measuring these accurately gives us vital insight into both the evolution of individual galaxies, and the stellar content of the Universe as a whole.

We find ourselves in the predicament that we wish for the prior on the SFH to be as uninformative as possible, because choice of a prior is ultimately a free choice. Unfortunately this is in tension with the fact that extracting SFHs from galaxy SEDs is a poorly conditioned problem [Ocvirk *et al.*, 2006], where small changes in observations results in large changes in the recovered SFH, especially for older age bins in galaxies which are continuously forming stars. This is due to the 'fact that luminosity from stars scales with their mass as anywhere from $M^{2.3}$ to M^4 depending on the mass range being considered. This means that even the black-body tails of high mass O/B/A stars can easily dominate over the peak emission of lower mass G/K/M class stars. This is the core of the problem when trying to pin down star formation histories at older ages – the remaining old stars are too dim to meaningfully contribute to any galaxy with recent star formation. We thus find ourselves in the situation whereby any measurements of key stellar galaxy properties are very sensitive to the SFH choices [e.g. McLure *et al.*, 2011; Mobasher *et al.*, 2015; Salmon *et al.*, 2015; Iyer and Gawiser, 2017].

In order to examine these choices, we begin by dividing the BLUETIDES galaxies into bins, across redshift – six bins centered at integer redshifts between 8 and 13 – and then further by stellar mass (four bins with $M_*/M_\odot < 10^8$, $10^8 < M_*/M_\odot < 10^9$, $10^9 < M_*/M_\odot < 10^{10}$ and, $M_*/M_\odot > 10^{10}$). Table 4.1 shows the numbers of galaxies contained within each of these bins.

As noted above, the stellar content of galaxies in BLUETIDES, like most cosmological hydrodynamical simulations, are represented by a discrete number of star particles with

redshift	13	12	11	10	9	8
$M_*/M_\odot < 10^8$	3	16	66	220	672	1893
$10^8 < M_*/M_\odot < 10^9$	24	122	543	2358	8589	27073
$10^9 < M_*/M_\odot < 10^{10}$	0	0	10	58	346	1650
$M_*/M_\odot > 10^{10}$	0	0	0	2	0	30

Table 4.1: Number of galaxies in the BLUETIDES sample contained within each mass and redshift bin.

formation epoch and metallicity. In the context of BLUETIDES these star particles each have an initial mass $8.47 \times 10^5 M_\odot$. While the actual mass will evolve over time as high-mass stars evolve off the main-sequence for our purposes we are only interested in the initial mass as this is what is used to define the star formation history and generate SEDs. To assemble a non-parametric star formation history for each galaxy we need only bin these particles by age.

Throughout this chapter, we opt to use SFHs normalised to the true stellar mass of the galaxy from the sum of the particle masses in BLUETIDES. This approach is so that we can examine the differences in modelling assumptions without needing to worry about effects from the best fit providing a different normalisation from the data.

A simple example of why this is necessary would be if applying our prescription kept the SED precisely the same shape, but reduced the normalisation by some amount. We could then create a degeneracy between metallicity distribution and stellar mass, which would be unbreakable. Because we are using simulation data and are able to know the true mass of stars, fixing one of the degenerate variables allows the effects of the other to be known.

As we will see later these effects are in fact degenerate, and the quantities we are largely interested in are independent of the overall normalisation – they are only dependant on the shape of the SED. This of course changes when we move from tracking the stellar population to modelling the light it produces, but having first isolated the effect provides vital insight into how to treat the SED generation process (and therefore the reverse process of SED fitting too).

4.3.1 The Average SFH by Mass and Redshift

Figure 4.1 shows these stacked SFHs, along with the two most commonly used SFHs for galaxies in the EoR. Those SFHs, as introduced in section 2.2.1.1 are referred to as constant and exponential, their explicit equations, in normalised fractional form are:

$$SFR = \frac{1}{\tau} \exp\left(-t/\tau\right) \tag{4.1}$$

and

$$SFR = \frac{1}{a_0} \begin{cases} 1 & t \leq a_0 \\ 0 & t > a_0. \end{cases} \tag{4.2}$$

Where in both cases t is the time counting backwards from the present time the galaxy is being studied. For example for the $z = 8$ sample, $t(z = 8) = 0$ and the time of the big bang is the age of the Universe at $z = 8$, i.e. $t \approx 647$ Myr. Both of these models are therefore single parameter models, for an exponential the only parameter is τ: the exponential time constant, and for a constant SFH the only parameter is a_0: how much time there is between the onset of star formation and the present epoch of the galaxy.

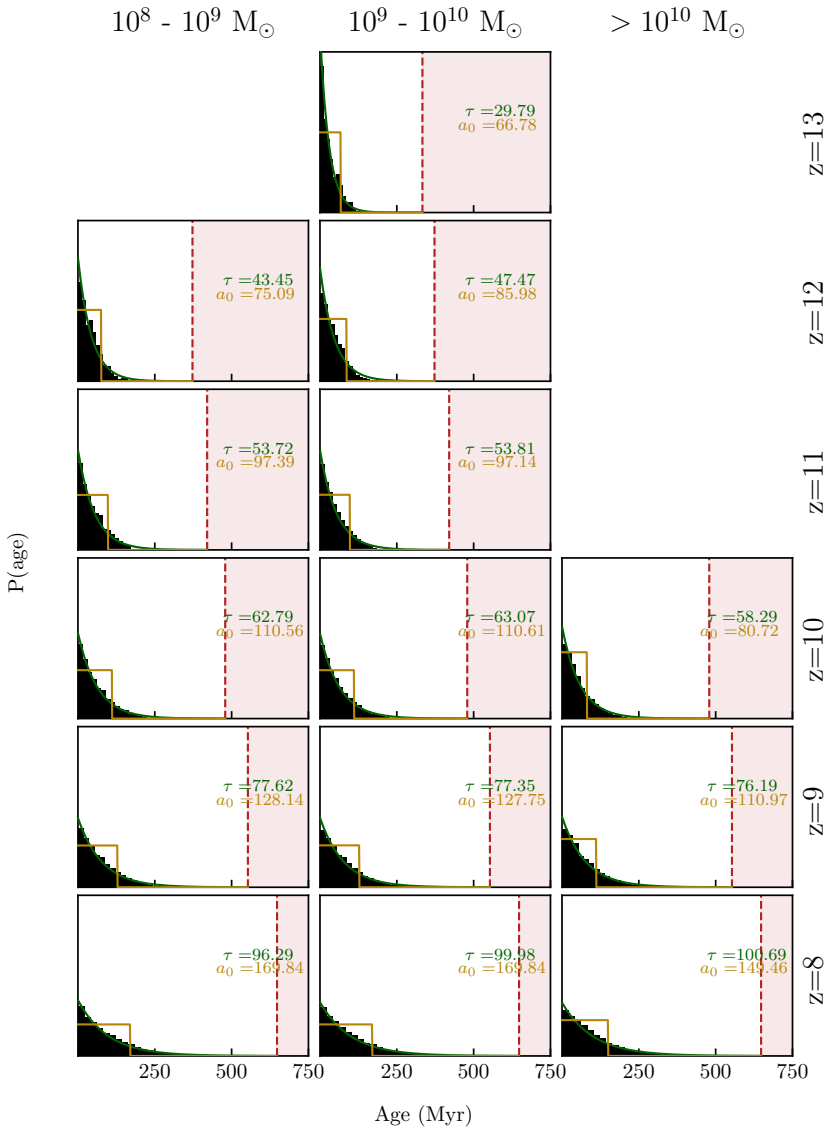

Figure 4.1: Normalised and stacked SFHs of BLUETIDES galaxies. Missing plots correspond to bins where there are less than 10 galaxies. Each plot has been given the same age scale, and the red area corresponds to the maximum age possible at this redshift (due to age of the universe considerations). The yellow line represents the best fit constant star formation history, while the geen line represents the best fit τ model – see text for details. Yellow and green inscribed numbers are the median best fit e-folding time (τ) and constant SFH cutoff parameters (a_0) respectively. Red vertical dashed line & shaded area denotes the maximum possible age of a star particle due to the age of the Universe at the given redshift.

To obtain these stacked SFHs, we separate all galaxies out into their mass/redshift bins. For each bin we then histogram all of the star particles by age. Finally we normalise each histogram to 1, resulting in the proportion of particles in each age bin. We find that the stacks of these galaxies are extremely well represented by an exponentially rising SFH (blue), over a – for example – constant SFH (yellow) across all masses and redshifts. A measure of this can be seen in figure 4.7, where the vertical lines represent the SMAPE (defined in equation 4.3) – a measure of the amount of mass placed into the wrong age bins. At higher redshift the SFH becomes steeper, with a shorter time constant for fixed mass – this is expected as these galaxies must have built up the same amount of stellar mass in a shorter time. Similarly – although it is a much weaker effect – galaxies with higher mass also have shorter e-folding times under a similar argument: they must have built up more mass in the same amount of time.

4.3.2 Individual Galaxies

While this is promising for the stacked galaxies, high redshift samples are rarely so numerous as to make statistical statements like this. It is therefore important to ensure that this SFH accurately describes individual galaxies. To do so we move away from the stacked objects, and perform the same process on each individual galaxy – histogramming the constituent star particles by age, and fitting the constant and exponentially rising SFHs to them. Finally, we calculate the performance of each fit using the following metric which is known as the Symmetric Mean Absolute Percentage Error (SMAPE).

$$\mathrm{SMAPE_{SFH}} = \frac{100\%}{\mathrm{N_{bins}}} \sum_{\mathrm{i=1}}^{\mathrm{N_{bins}}} \frac{|\mathrm{M^*_{BT,i}} - \mathrm{M^*_{model,i}}|}{0.5(\mathrm{M^*_{BT,i}} + \mathrm{M^*_{model,i}})} \tag{4.3}$$

$SMAPE_{SFH}$ represents the percentage of mass across all bins which has been "misplaced" – that is, what percentage of the total mass of the model is over or under-estimating the mass in any given bin. N_{bins} is the number of bins the BLUETIDES particles are binned into, and $M^*_{BT,i}$ and $M^*_{model,i}$ are the amounts of stellar mass in bin index i of the BLUETIDES

particles and the analytic model respectively.

This metric effectively tells us the mass of stars in each galaxy which are mis-aged, which is important because in cosmic terms all of the stars in these galaxies are young: even small changes in the ages can result in huge swings in the luminous output of these objects.

Figure 4.2 shows the histogram of $SMAPE_{SFH}$ for the galaxies in the binned samples. According to this the constant star formation (yellow) only just underperforms when compared to the exponential which was asserted to be a significantly better fit in figure 4.1.

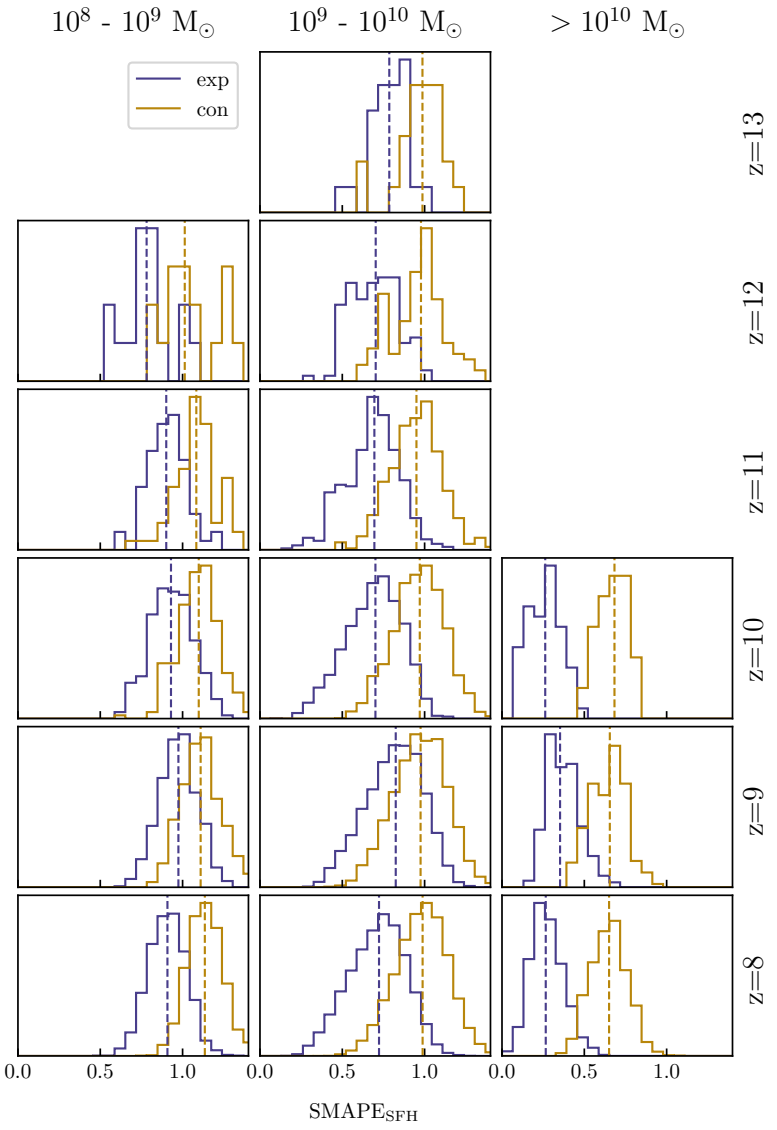

Figure 4.2: Histogram of the SMAPE (see equation 4.3) for the SFHs of the exponential model (blue) and the constant model (gold) for BLUETIDES galaxies separated by mass and redshift bins. Subplots with no histograms in represent bins containing less than 10 objects, which are at risk of producing spurious results. Dashed lines represent the medians of the histograms.

4.4 The Metallicity Distribution of Bluetides Galaxies

SED fitters tend to treat the stellar and gas phase metallicities of a galaxy as if they are constant throughout. This is a sensible approximation to make because for galaxies at most redshifts, the molecular gas which goes into producing the stars is significantly enriched, such that the supernovae produced at the end of the stellar generations life cycle won't increase the metallicity greatly above the galactic average – the galaxy as a whole will evolve together towards higher metallicity.

However, at extreme redshifts, where enrichment is lower, stars which formed at similar times can still have significantly different metallicities. This is because of the strong effect of single supernovae events, which can affect the metallicity $\log_{10} Z$ of the surrounding gas.

With this in mind, we wish to explore the effects of relaxing this assumption by answering the question: in the early EoR, where our sample of BLUETIDES galaxies reside, how much of a difference do both the star formation history and the metallicity distributions make?

4.4.1 The Average Metallicity Distribution by Mass and Redshift

We begin by examining the metallicity distributions as a whole. Figure 4.3 shows the stack distributions of the metallcities in each mass and redshift bin. Of important note is the skew or asymmetry in this distribution: there are more low-metallicity star particles than you would expect from a log normal distribution.

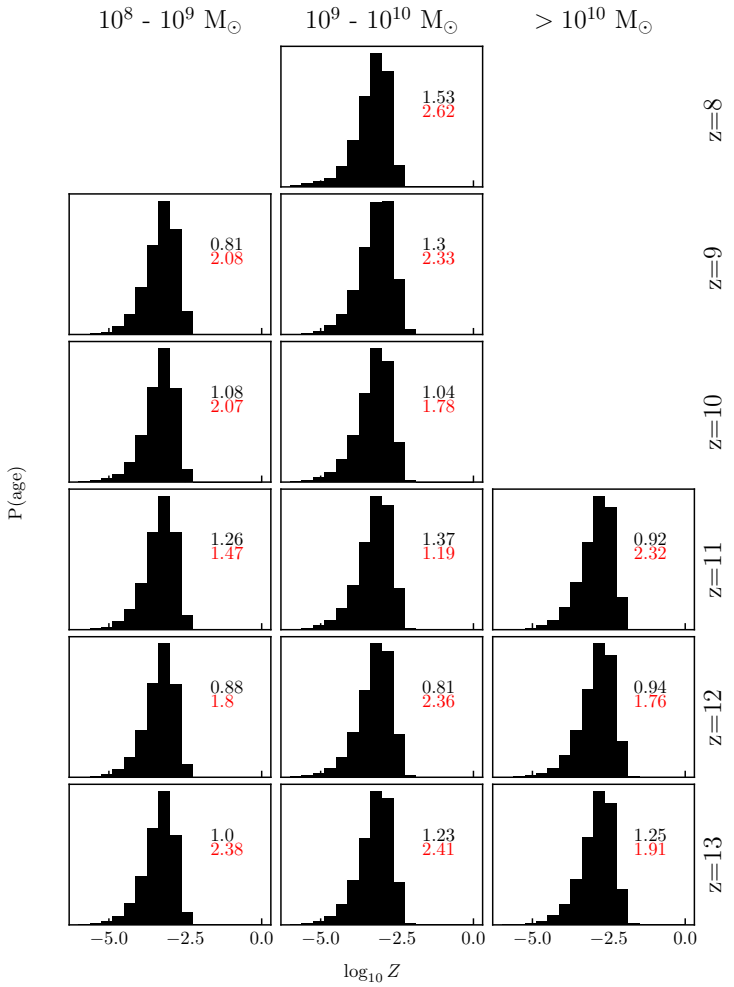

Figure 4.3: Normalised and stacked metallicity distribution of BLUETIDES galaxies. Missing plots correspond to bins where there are less than 10 galaxies. Can be seen that clearly there is a significant skew in the metallicity distribution, which would prevent us from applying some simple prescription like a log-normal to it. This is due to the age dependence of the average metallicty of a star, which we will see evolves quite strongly in time. Numbers in each panel represent the χ^2 of the distribution described in the main text (equation 4.7, and figure 4.4) in black, and a symmetric log-normal distribution in red.

We can however, build an overall distribution that well matches what is observed using a simple assumption that in each *individual* age bin, the metallicity is distributed as a normal distribution in $\log_{10} Z$, i.e.

$$N(Z) = N(t) \cdot \mathcal{G}(\log_{10} Z, \mu_Z(t), \sigma_Z) \tag{4.4}$$

where $N(t)$ is the normalisation, $\mathcal{G}$ is the normalised gaussian distribution, with shape parameters peak μ_Z, and width σ_Z. For simplicity, we are assuming that σ_Z will remain constant for all ages. Thus we have two questions that require answering – What are the functional forms of $N(t)$ and $\mu_Z(t)$?

$N(t)$ can be found by making the argument that at a fixed age, we are simply spreading all the stars in that bin into various different metallicity bins. Therefore the amount of mass in said bin should be the amount of mass that would be in the bin if we were using a single metallicity, i.e. the amount of mass as predicted by the SFH. $N(t)$ can be found by evaluating:

$$\int_{\mathrm{t0}}^{\mathrm{t1}} \mathrm{SFR(t)dt} = \int_{-}^{\infty} \infty \mathrm{N(t)} \cdot \mathcal{G}(\log_{10} \mathrm{Z}, \mu_{\mathrm{Z}}(\mathrm{t}), \sigma_{\mathrm{Z}}) \mathrm{d} \log_{10} \mathrm{Z} \tag{4.5}$$

and as the normal distribution integrates to 1, evaluating the left hand side will give $N(t)$ directly. The second question is how $\mu(t)$ should evolve in time. As far as the overall normalisation and the SFH are concerned, this can take any functional form – we could set it to be a constant value, and with a small σ_Z we would recover the uniform metallicity assumption. The next simplest thing to do is simply introduce a linear dependance between t and $\log Z$. Combined with the expression for $N(t)$, we first must show that this is able to reproduce the behaviour for the overall Z distribution, before showing how this also provides a good description of the 2-d joint distribution of t and $\log_{10} Z$ in the next section.

If we assume our linear relationship $\mu_{\mathrm{Z}} = \frac{\mathrm{dy}}{\mathrm{dt}} \mathrm{t} + \mathrm{y}_0$ where $y = \log_{10} Z$ and $y_0 = \log_{10} Z(t = 0)$, we must consider each age bin separately, and sum over these bins to reach the overall metallicity distribution, i.e.

$$N(Z) = \sum_{i}^{N_{bins}} SFR(t_i) \cdot \exp\left[-\frac{(y - \frac{dy}{dt_i} t_i - y_0)^2}{2\sigma_Z^2} \right] \tag{4.6}$$

where the index i runs over the age bins, and t_i is the age at the bin center. Inserting our preferred exponential SFH from the previous section, we arrive at the expression

$$N(Z) = \sum_{i}^{N_{bins}} \frac{1}{\tau} \cdot \exp\left[\frac{-t_i}{\tau} - \frac{(y - \frac{dy}{dt_i}t_i - y_0)^2}{2\sigma_Z^2}\right] \tag{4.7}$$

We can then ask what will happen if we shrink the age bin sizing from some width Δt to an infinitesimal dt. Doing this replaces the sum over the age bins with an (admittedly tricky) integral over t from time $t = 0$ to the age of the universe at the redshift of the galaxy t_{max}

$$N(Z) = \int_0^{t_{max}(z)} \frac{1}{\tau} \cdot \exp\left[\frac{-t}{\tau} - \frac{(y - \frac{dy}{dt}t - y_0)^2}{2\sigma_Z^2}\right] dt \tag{4.8}$$

Figure 4.4 shows the results of applying this prescription to a toy model, with parameters $\tau = 100\text{Myr}$, $y_0 = -2.4$, $\frac{\text{dy}}{\text{dt}} = -8 \times 10^{-3}\text{Myr}^{-1}$ and $\sigma_y = 0.5dex$, these parameters are within the range of parameters found to represent the metallicity distributions of these galaxies (see section 4.5) however do not represent any physical reality – they were merely chosen as an illustrative example.

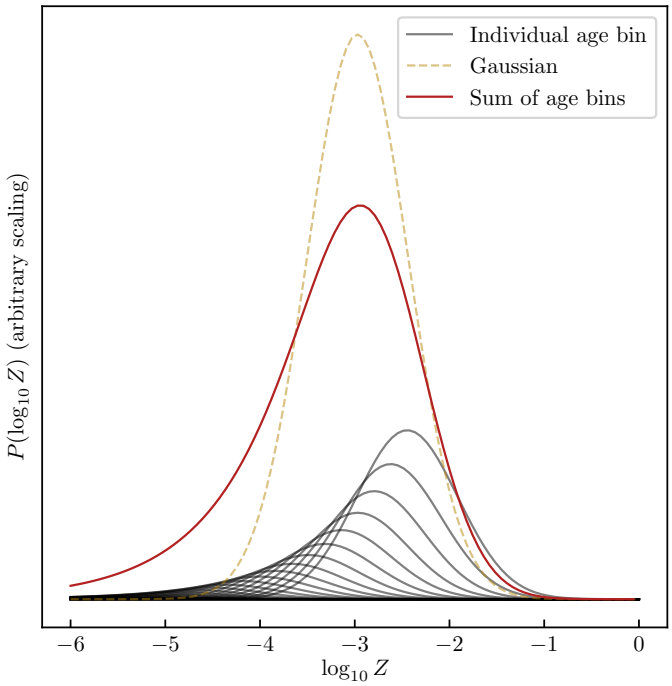

Figure 4.4: Model of how a set of age bins, each with a log-normal distribution of metallicities, with linearly evolving μ values, and exponentially decreasing amplitudes (black) can sum together to produce a skewed distribution as required to fit figure 4.3 (red). To emphasize the advantages of this formulation a log-normal distribution with the same peak location, normalisation, and σ_Z is included for reference. Y axis scale of individual bins has been increased by a factor of 10 to aid visibility.

We can see from this figure that the proposed model is capable of producing asymmetric distributions in Z. Each bin is modelled by a log-normal distribution (black) increasing in age from left to right. Their peaks begin at some metallicity Z_0, which is simply the metallicity of stars being created right now, and log-linearly move to lower metallicity with time. The summed contribution of these many high age, low-amplitude bins produces a much flatter tail towards low metallicities than the sharp cutoff which is dominated by the youngest few bins.

Now that we have a functional form of the SFH, and a way to describe the metallicity distribution of the galaxies in BLUETIDESwhich is physically motivated by the SFH and the co-evolution of metallicity with it, we can fit them simultaneously as a joint distribution.

4.5 The Joint Age-Metallicity Distribution

As outlined in sections 4.3 and 4.4.1, the joint distribution $\psi(t, Z)$ can be in general written in the form:

$$\psi_{bin}(t, Z) = A \cdot \mathrm{SFR}(t) \cdot f(t) \cdot N(Z, t) \tag{4.9}$$

where SFR(t) is the normalised SFH, $f(t)$ is the fraction of mass remaining compared to t=0, $N(Z, t)$ is the normalised metallicity distribution and A is the overall normalisation constant such that the following is true –

$$\int_0^\infty \int_{-\infty}^\infty \psi_{bin}(t, Z)\mathrm{dZdt} = M* \tag{4.10}$$

Inserting equations 4.1 and 4.4 for SFR(t) and $N(Z, t)$ respectively, the full expression for fitting galaxies in BLUETIDES will be:

$$\psi_{bin}(t, Z) = \left(\frac{M_*}{\tau\sqrt{2\pi\sigma_y^2}}\right)\exp\left(\frac{-(y - y_0 - mt)^2}{2\sigma_y} - \frac{t}{\tau}\right) \tag{4.11}$$

where as previously, $y = log_{10}Z$ the metallicity, t is the stellar age, counting backwards from the current epoch of the galaxy. That is, at redshift $z = 8$, $t(z = 8) = 0$, and t_{BB} – the time which the big bang happened – is $\approx$ 647Myr, M_* is the stellar mass of the galaxy, tau is the exponential SFH parameter, σ_y is the gaussian shape parameter for y, and $m = \frac{\mathrm{dy}}{\mathrm{dt}}$ is the slope of the age-metallicity dependance. Given this two-variable, 5-parameter model $\psi_{bin}(t, Z)$ is the mass density at a given age and metallicity, and may be integrated over the two bin dimensions to find a mass within a given range. This section will focus on examining the errors introduced by parameterising BLUETIDES galaxies in this way (as opposed to using the particle data directly).

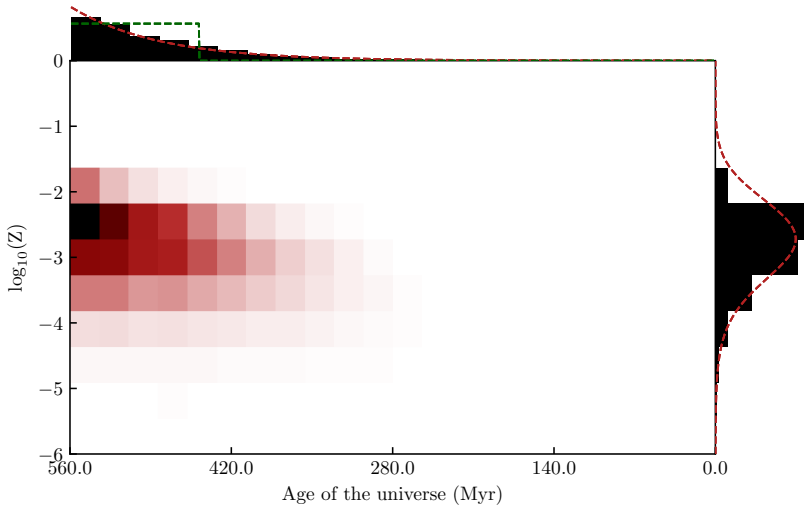

(a) Joint distribution derived by directly binning particle data

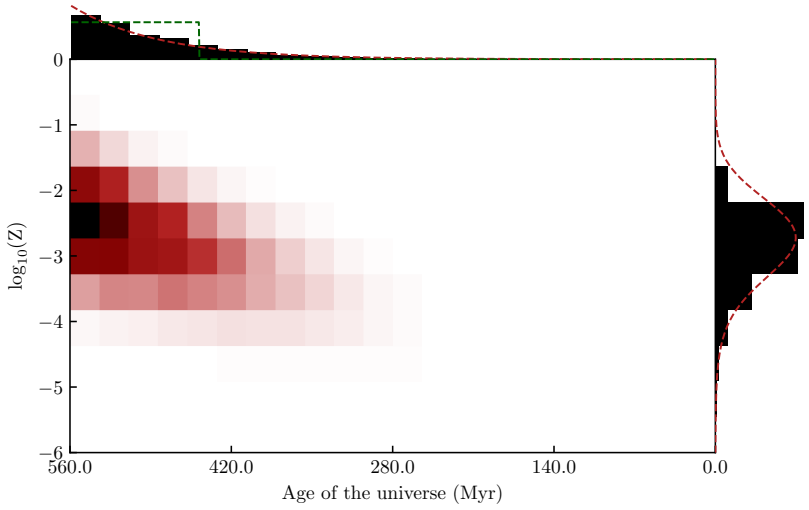

(b) Best fit joint distribution $\psi(t, Z)$ found by fitting to the particle data in (a).

Figure 4.5: Joint distributions in age and metallicity of the stack of BLUETIDESgalaxies with z=9 and $10^9 < M/M_\odot < 10^{10}$. Top histogram shows the SFH by marginalising over all metallicity bins, right histogram shows overall metallicity distribution by marginalising over age bins. Included are the best fit for these distributions using the prescription in the text (red), and the best fitting constant SFH (green) for comparison.

Figure 4.5 demonstrates the distribution in action, comparing the stack of galaxies at $z = 9$ with $10^9 < M/M_\odot < 10^{10}$. Even by eye it can be seen that the model (fig 4.5b) slightly overestimates the proportion of stellar mass at young ages and high metallicities, however it certainly reproduces the overall shape of the distribution. Similar particle and fit figures for each of the redshift and mass bins can be found in appendix C. We will therefore first assess the quality of the fits quantitatively by normalising both distributions to the same mass, and calculating the percentage error by mass in each bin individually, and for the distribution as a whole. That is:

$$\Delta f_{M_{ij}} = \frac{\left|M_{model,ij} - M_{BT,ij}\right|}{0.5(M_{model,ij} + M_{BT,ij})} \tag{4.12}$$

and

$$\mathrm{SMAPE}_{\mathrm{M_{bin}}} = \frac{100\%}{n_i n_j} \sum_{i,j}^{age,Z} \Delta f_{M_{ij}} \tag{4.13}$$

where $\Delta f_{M_{ij}}$ represents the fractional error in the age/metallicity bin with indexes i, j, $M_{model,ij}$ is the amount of mass stored in said bin according to the analytic expression, and $M_{BT,ij}$ is the mass in BLUETIDES particles. $\mathrm{SMAPE}_{\mathrm{M_{bin}}}$ is the symmetric mean absolute percentage error – this is a metric to measure the amount of mass which is incorrectly placed in the model. While this metric is not ideal – it assumes that the "true" mass that should be inside the bin is simply the mean of the two, when in reality the "truth" here is M_{BT}. However, the SMAPE avoids problems with bins that have very little mass in them. These bins typically have no star particles in from BLUETIDES and thus would be undefind for a tradiational fractional mass error. An approach would be to then neglect these bins when calculating how mass is (mis)placed but then we must contend with the fact that misplaced mass exists in all of these bins as the model is > 0 for all t, Z.

Figure 4.6 shows the joint distributions (4.6a) and the SMAPE residuals (4.6c) for using the full age and metallicity distribution – hereafter referred to as "full grid", the traditional method of using an SFH and a fixed single metallicity, and using the best fit constant SFH

along with a fixed metallicity.

The colours in the top bin represent the percentage of mass contained within each bin. The colours in the lower plot represent the percentage of mass overplaced (colour) or missing (grey) in each bin. Any bins with under 0.01% of the total mass contained within them according to the model – i.e. those with very high/low metallicites and those with large ages – are not shown, as these contribute very little ot the overall picture of the galaxy and are simply omitted here for clarity.

The binning is different to that in figure 4.5, rather than using linear bins we use bins based upon the BPASS SPS model (section 2.2.1.1) as these map more neatly into luminosity space, which will be explored in the next section.

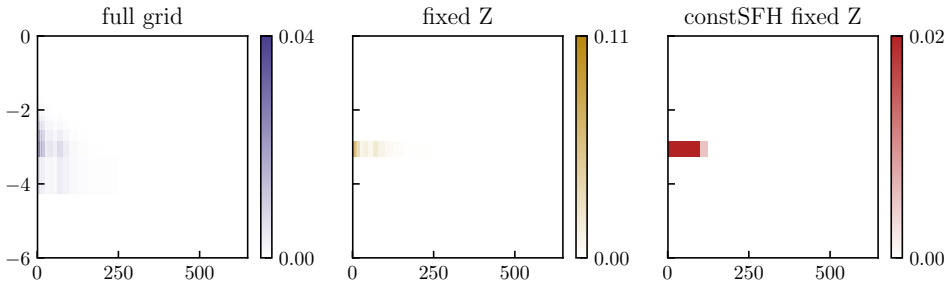

(a) Mass histogram, from $t = 0$ to $t = 750$Myr

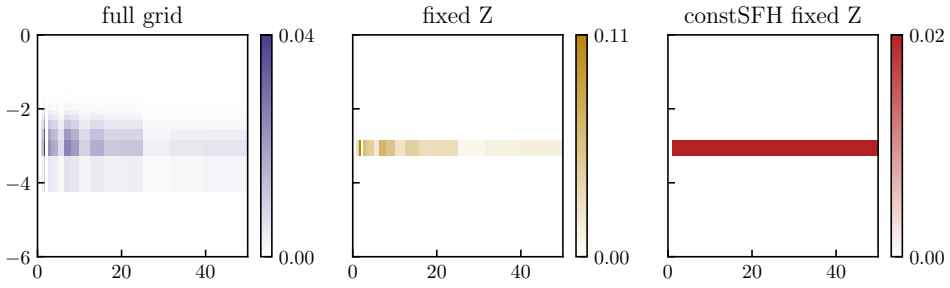

(b) Mass histogram, from $t = 0$ to $t = 50$Myr

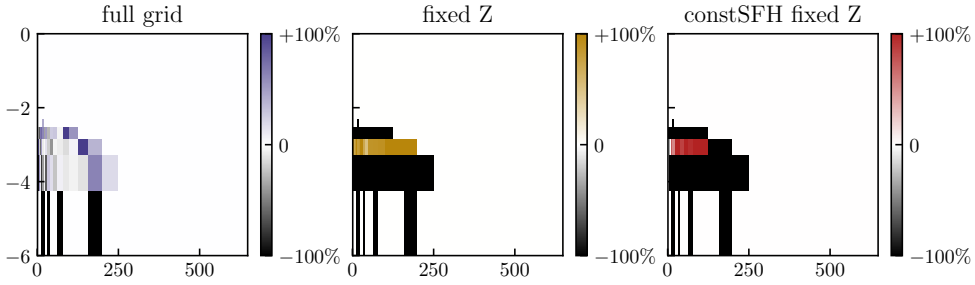

(c) SMAPE histogram, from $t = 0$ to $t = 750$Myr

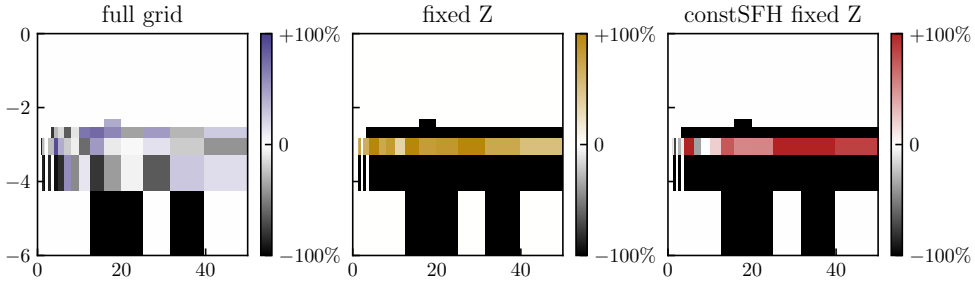

(d) SMAPE histogram, from $t = 0$ to $t = 50$Myr

Figure 4.6: Mass grids for the stack of galaxies with $z = 9$ and $10^9 < M/M_\odot < 10^{10}$. (a) and (b) show the overall fractional mass histogram of the bins, while (c) and (d) show the SMAPE (see equation 4.13) on a per-bin basis as compared to the stacked histogram of particle data. Bins containing less than 0.01% of the total mass have been set to 0 in all plots, simply as they can provide extremely large percentage errors while not contributing meaningfully to the overall picture. Subfigures (b) and (d) show the same information as (a) and (c), but simply zoom in on the first 50Myr, to aid visualisation. "Full grid" (blue) repsents the use of ψ_{bin} as in equation 4.11 as the model, "fixed Z" (gold) uses an exponential SFH, but a single metallicity value, and "constSFH fixed Z" (red) uses the same single metallicty, but a constant SFH.

It can clearly be seen in this stack that the full grid significantly outperforms both the fixed metallicity solution and the constant SFH fixed Z solution. For both of the fixed metallicity solutions, any star particle which does not fall into the single bin being used by the model is forced into that bin, resulting in all of those bins returning that they are missing 100% of the mass they "should" contain. Similarly the bins lying along the principal Z axis all contain far too much mass, because they have had all of this extra added to them from the differing metallicity bins.

The exception to this trend is the constant SFH bins at very young ages. As can be seen in e.g. figure 4.1, constant SFHs pathologically underestimate BLUETIDES star formation at young ages, and this is somewhat counteracted by adding in the mass from the other metallicity bins. These two effects conspire to counteract each other somewhat, resulting in the principal Z axis bins fitting reasonably well at young ages – however this should not be taken as a success of the model, merely a quirk, as shown by the poor performance elsewhere.

Further examples of this can be found in appendix C, they have been omitted from the main body as they show largely similar results across all masses and redshifts.

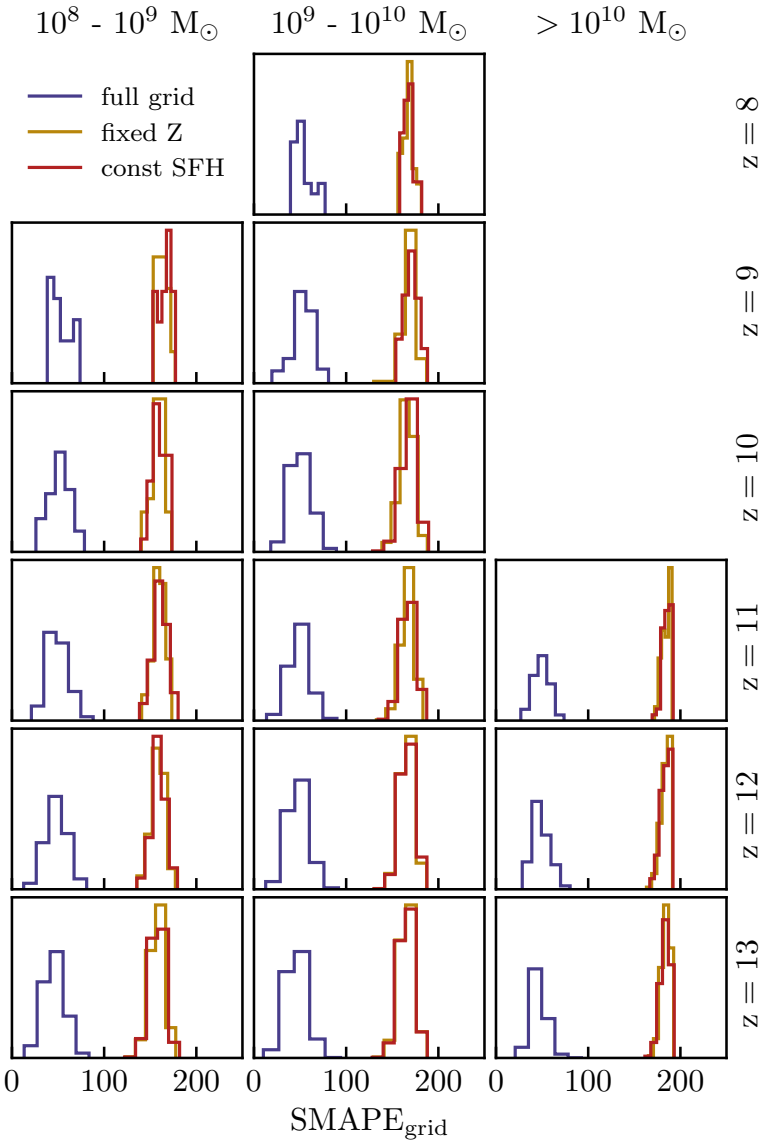

Figure 4.7: Histogram of the Symmetric Mean Average Percentage Error (SMAPE) as defined in equation 4.13 for each galaxy in the BLUETIDES sample, binned by mass and redshift. Each colour uses a different parameterisation for M_{model} – the full analytic expression as outlined in equation 4.11 (blue), an exponential SFH with single fixed metallicity (gold) and a constant SFH with fixed metallicity (red).

We now move again from stacked objects to the distributions of individual sources, in order to quantify how the analytic model performs against traditional single Z methods.

Figure 4.7 shows the overall SMAPE for the three models.

These histograms demonstrate that this approach works significantly better for replicating the stellar populations of these extreme redshift objects, across all masses and redshifts covered by BLUETIDES, and in this space on average the SFH does not have a major effect – however this is due to the effect outlined earlier whereby the constant SFH does well in young bins due to the extra mass moved in there from other metallicities mitigating the under-estimation from the SFH shape – calculation of SMAPE when the metallicity is marginalised over as in figure 4.2 is perhaps a better comparison between these models.

It should be noted that as the fixed Z and constant SFH models are not smooth and contain 0's in bins that are do not contain the single Z value, and/or are older than a_0 in the constant case. When these bins coincide with bins with no star particles inside, the SMAPE becomes undefined due to the denominator being 0. Thus the SMAPE has only been calculated across those non-zeros bins for these two models (with the normalisation $n_i n_j$ being adjusted appropriately), as that is the only way it can be satisfactorily defined. The full grid model is unaffected because, as it is at it's core the product of an exponential SFH and a Gaussian, it is strictly >0 – which as outlined earlier is the motivation for using SMAPE as our metric in the first place.

4.5.1 Evolution of the joint distribution parameters

Under the assertion that this model provides a realistic replacement for the true distribution of star particles in BLUETIDES the redshift and mass evolution of these parameters can give us significant physical insight into how these early galaxies evolve.

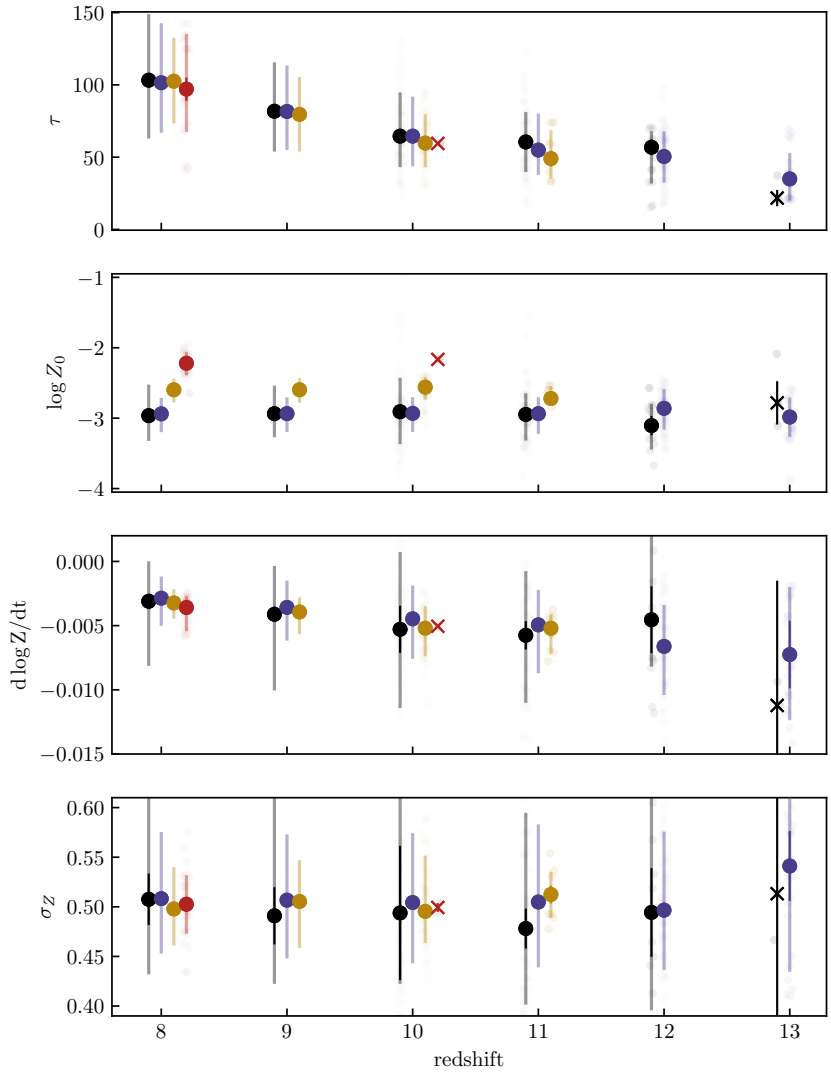

Figure 4.8: Evolution of fit parameters as described in equation 4.11. Each point represents the median of the redshift (x-coordinate) and mass (colour) bins, and the error bar represents the 16th and 84th percentiles – the true poisson errors would be $\sqrt{n}$ smaller than this, where n is the number of galaxies in the bin (see table 4.1). Groups of coloured points all co-incide with the integer redshift they are closest to, but have been scattered slightly to aid visibility. Points marked with a cross are galaxy bins with less than 10 objects and should be regarded with caution and are not used in analysis due to small number statistics. Mass bins not present at a given redshift are because no galaxies reside in that bin.

Figure 4.8 shows the evolution of these parameters by mass and redshift bins. τ governs

the shape of the star formation history. As we move to earlier and earlier cosmic times, we see that τ decreases quite sharply – by around a factor of 2 across the redshifts 8-13 at fixed mass. This is probably unsurprising, these galaxies are still forming stars at incredible rates, but every star formed is gas that is no longer available, so a decrease in this rate is inevitable. This also fits with our picture of the lower redshift universe, where most galaxies have some variant of an exponentially decreasing SFH [Wright *et al.*, 2016] – the trend merely is the very start of this transition happening. We also see a weak evolution of τ with mass. Galaxies which have assembled more mass by a given redshift have less steep SFHs. This is a similar effect – a galaxy with larger mass likely formed earlier, and thus will have begun the process of using up its available gas much more quickly.

$\log Z_0$ represents the metallicity of the stars that have just been formed. We see very little evolution with redshift, however $\log Z_0$ has a strong mass dependence, especially towards higher masses. This, similarly to the τ dependence, is because higher mass galaxies must have begun their star formation at earlier times in order to build up all the mass they contain. Thus higher mass galaxies have had more generations of stars go through their life cycle, leading to higher metallicity.

The age-metallicity slope $\frac{dZ}{dt}$ shows a weak redshift dependence, with the relationship flattening towards lower redshifts. This is consistent with the view that for most galaxies, using a single parameter metallicity is a reasonable reproduction of reality. However at the extreme redshifts observations are beginning to push to, it may be prudent to switch to an age dependant model, as over the course of $\approx$ 500Myr the metallicity can change by as much as $\Delta \log Z \sim 2$.

Finally, the scatter in the age-metallicity relationship remains relatively constant across redshift, with a weak dependence on mass. This is related to the flattening of the relationship with time. Galaxies that have assembled a larger collection of stars have likely had more generations of stars, and thus more enrichment of both the gas and the stars themselves. This increasing mixing will cause the galaxy to slowly have more uniform metallicity compared to a galaxy which has only just begun star formation, which will have a more clumpy metal

morphology.

4.6 Stellar Spectra Modelling of Galaxies in Bluetides

Showing that this model performs well at assigning star particles into the correct places is all well and good, however it is also vital to examine how each model performs in terms of observables, as the only direct data we receive from a galaxy is the light, and this is how all statements about the stellar population must be made.

Typically with observations we are solving the reverse problem – we have a set of fluxes and must create a model which is capable of producing that data. However here we are examining the forward problem – how do a fixed set of parameters correspond to fluxes when run through different models. Throughout this section we will use the BPASS v2.1 SPS model (see section 2.2.1.1 for details) to convert the histograms of star particles into stellar spectra. We also use nebular emission models recommended by the BPASS team which are created in CLOUDY v13.03 (see section 2.2.1.2) for this purpose.

Throughout this section, we fix the stellar mass of the galaxy to be the same as the BLUETIDES mass, in order to isolate the effect of moving star particles around in age/Z without the effect of the overall normalisation. We also for simplicity use the BPASS age & metallicity bins, without interpolation. While it is possible that this may have some effect on the conclusions drawn, we argue that this effect would be small due to the distinguishablity between spectra is roughly proportional to their log-separation in time [Ocvirk *et al.*, 2006].

In addition, throughout this section, we define the fiducial spectra to be the spectra constructed from the BLUETIDES particles directly by simply assigning each particle an SSP spectra from the BPASS library and summing the results. The analytical models we have constructed are then assessed based on the quality of the approximation of this "true" spectra.

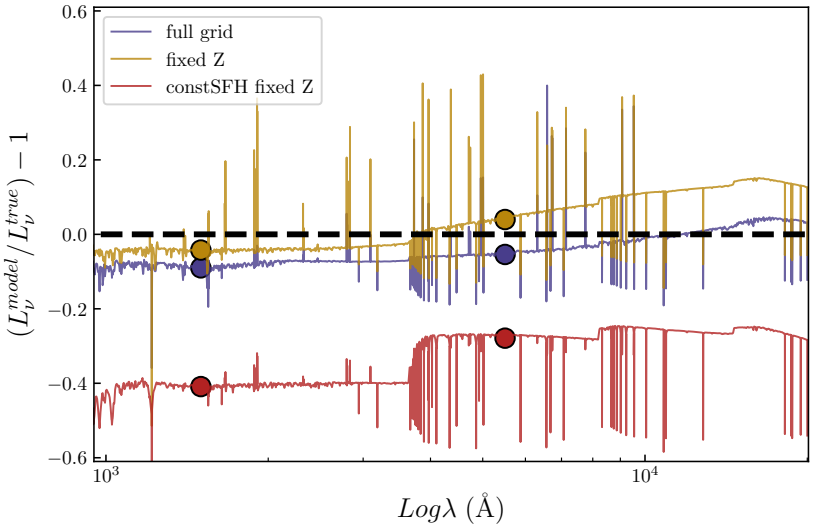

Figure 4.9: Spectra of stacked BLUETIDES galaxies with z=9 and $10^9 < M/M_\odot < 10^{10}$. As in the joint distribution section three models are used: the full analytic expression as outlined in equation 4.11 (blue), an exponential SFH with single fixed metallicity (gold) and a constant SFH with fixed metallicity (red). Circles represent the UV flux L_{UV} as measured through a top-hat filter from 1300 to 1700 , a commonly used proxy for unobscured star formation rate.

Figure 4.9 shows the stellar plus nebular emission spectra of the stack of galaxies with $z = 9$ and $10^9 < M/M_\odot < 10^{10}$ for each model used in the previous joint distribution sections. These spectra have each been divided through by the spectra derived directly from BLUETIDES , so a perfect reproduction would correspond to a horizontal line at $y = 0.0$.

As can be seen, both the full grid model and the exponential SFH & fixed Z models perform well (the median deviation from the BLUETIDES spectra is -1.4% and +1.6% respectively) while the constant SFH significantly underestimates (median deviation -27.2%) the flux. These spectra demonstrate that in terms of the continuum, or if one were using photometry, the spectra is largely insensitive to how the metallicities are distributed – whether one uses a wide distribution or a single value makes little difference to the overall normalisation of the output spectra. It is therefore obviously advantageous in these situations to use a single Z value, as that is the minimum number of parameters which encapsulate the behaviour of the spectra. This argument is reinforced when we also consider figure

4.8, specifically the evolution of $\frac{dZ}{dt}$. As the redshift decreases, the slope of the principal age-metallicity axis decreases, until at $z = 8$ it is already close to a constant metallicity anyway, leaving only the spread in Z to affect the spectra when compared to a single value.

However, this analysis reveals that it is extremely important to get the SFH correct. Switching from an exponential SFH to a constant and holding the normalisation constant means that young stars are effectively replaced with old stars. This means that per unit mass the galaxy produces much less light, as young stars are that much more efficient at producing light. Applying the reverse logic to this, if one were to fix the flux (as in an observation) applying a constant SFH to a galaxy that in reality has something much closer to an exponential can cause a significant overestimation of both the star formation rate and the stellar mass.

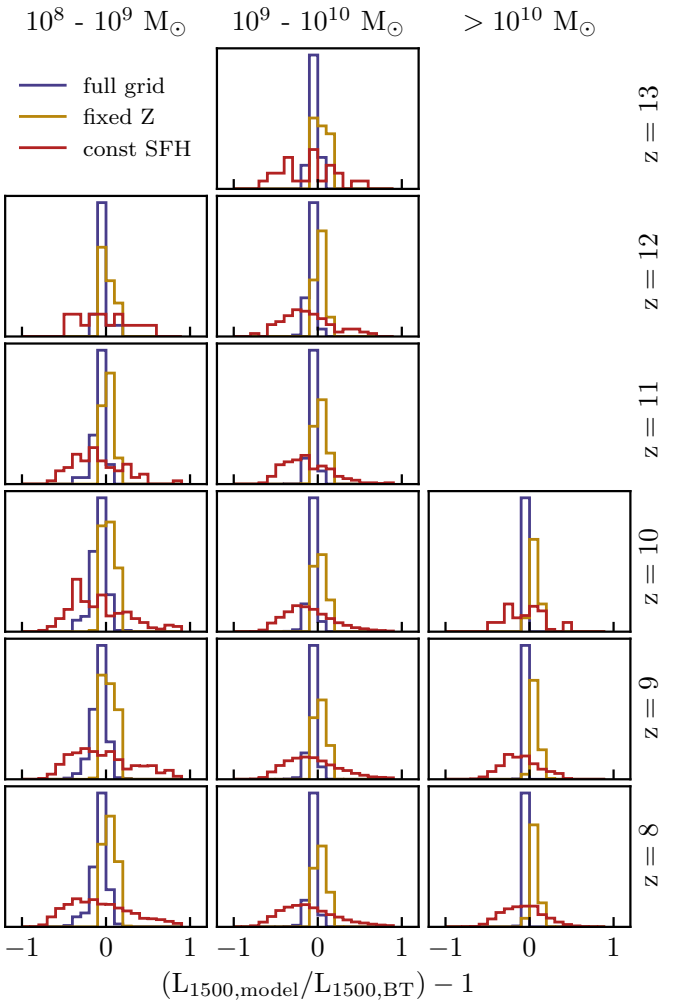

Figure 4.10: Histogram of L_{UV}, the luminosity through a perfect top-hat filter extending from 1300 to 1700 for each galaxy in the BLUETIDES sample, binned by mass and redshift, as compared to the "true" value derived from the BLUETIDES star particles directly. Each colour uses a different parameterisation for M_{model} – the full analytic expression as outlined in equation 4.11 (blue), an exponential SFH with single fixed metallicity (gold) and a constant SFH with fixed metallicity (red).

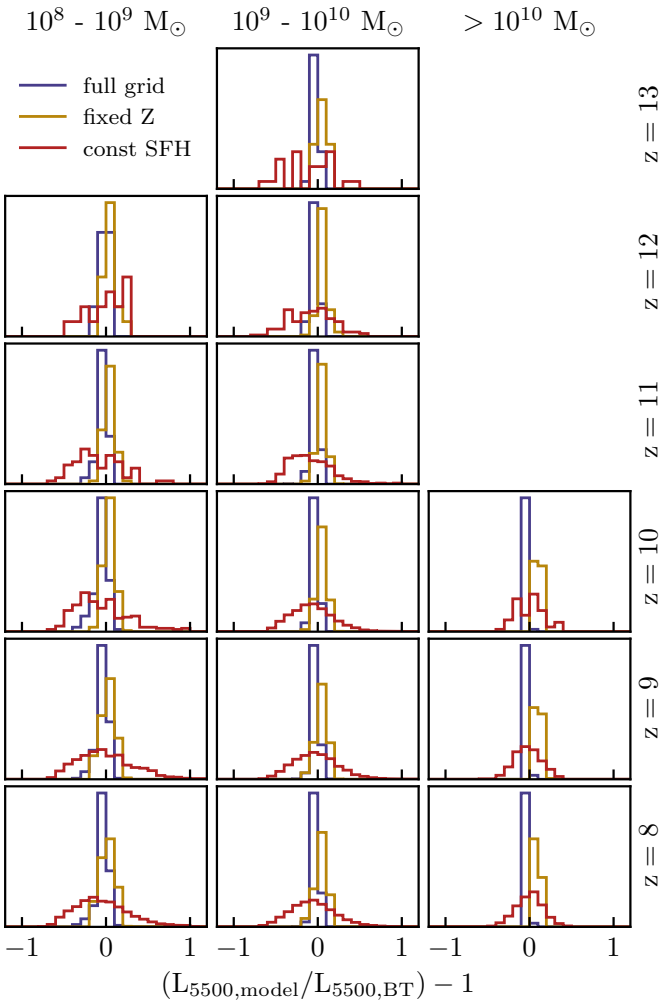

Figure 4.11: Histogram of V_{5500}, the luminosity through a perfect top-hat filter extending from 5100 – 5900 for each galaxy in the BLUETIDES sample, binned by mass and redshift, as compared to the "true" value derived from the BLUETIDES star particles directly. Each colour uses a different parameterisation for M_{model} – the full analytic expression as outlined in equation 4.11 (blue), an exponential SFH with single fixed metallicity (gold) and a constant SFH with fixed metallicity (red).

Figures 4.10 and 4.11 show the distributions of the individual galaxies with the usual mass and redshift binning for the UV luminosity (L_{1500}) and the V band luminosity (V_{5500}) respectively.

In the majority of mass and redshift bins, the full grid and fixed Z models recover the

true luminosities in both bands very well, with a small scatter around 0. The constant SFH performs less well, with a large scatter, but still remains within a factor of two (± 1) for almost all individual objects.

The only exception to this trend is the high mass galaxies. In these bins fixed metallicities habitually over-predict both the the UV and optical luminosity. This is because at these higher masses, while the age-metallicity relation flattens, the scatter in metallicities at fixed age is still relatively large, and the flux is not linear in this quantity. That is to say, if we consider a stellar population in an age bin to have some mean metallicity $< Z >$, with a symmetric distribution, SSPs with $< Z > +\epsilon$ for some positive quantity ϵ will not have a luminosity differing from that of $L_{<Z>}$ by the same factor as an SSP with metallicity $< Z > -\epsilon$. These populations do not serve to "cancel out" – the populations with higher-than-average metallicity see a faster drop in their luminosities than those that are below average: condensing to a single average metallicity model in population space does not produce the desired results in luminosity space.

4.7 Conclusions

Firstly, it is important to establish the star formation history of these galaxies, as this is ultimately the dominant aspect which is recoverable from observations. We fitted BLUETIDES galaxies both in stacks and as individual galaxies with a variety of SFHs, and found that across all mass and redshift ranges being considered they were significantly better served by an exponential SFH, with a time constant which decreased with redshift.

We then introduce an age dependant metallicity – younger stars will on average have higher metallicities. The slowly evolving galaxies of the modern Universe have plenty of time for their stars/gas to mix so the galaxy evolves as a whole, whereas the stars in high-z galaxies are evolving so fast, that this can have an appreciable effect. We recreate the skewed overall metallicity distribution by spreading the metallicity of the stars at each fixed age over all metallicities in a normal distribution. This, combined with the exponential

SFH established earlier reproduces the desired behaviour, closely matching the BLUETIDES galaxies in terms of how the stars are distributed in age and metallicity.

We note that many of these parameters possess evolution with either changes in mass or redshift. Largely, parameters controlled by the star formation history trend towards a less steep history with higher normalisation as time goes on, while parameters governing the metallicity are sensitive to the stellar mass of the galaxy – galaxies that have had time to build up significant stellar mass have also had time for the enrichment to become more uniform throughout.

Finally, we move into observable space, creating stellar & nebular SED's from these SFHZ grids in order to isolate the effect that the evolution and scatter in metallicity would have on the light being produced. We find that the imposition of a constant SFH (or indeed any SFH which largely suppresses the true stellar mass contained in the youngest bins) leads to a large reduction in the continuum flux, around 35%. This argument can also be inverted – inappropriately choosing a constant SFH when fitting one of these galaxies will result in a significant overestimation of the mass due to the underrepresented O/B/A stars. While the use of a fixed metallicity compared to the grid model largely does not impact the photometry, such a model largely provides better estimates of the line fluxes in the optical. Such a mode may therefore be useful in the era of Webb, when rest frame optical imaging and possibly spectroscopy are accessible for EoR galaxies.

Chapter 5

Conclusions

In this thesis, we have developed a novel SED fitting code INTERROGATOR, which has been designed specifically with the study of EoR galaxies using the Webb telescope in mind. In Chapter 2 I focus on a description and brief test of the code, documenting how each component of the luminous material in a galaxy is modelled, and how they are combined to infer the physical properties of a galaxy based on its broad band flux observations. Chapter 3 demonstrates an application of INTERROGATOR, selecting a sample of Extreme Emission Line Sources from the GAMA survey, and fitting them with a variety of models using INTERROGATOR in order to more appropriately measure their physical parameters, and to carry out a comparison of inferred parameters based on varying the model assumptions. Finally, Chapter 4 proposes a novel fitting technique based on galaxies from the BLUETIDES simulation, relaxing the assumption that galaxies have a single metallicity, rather a log-normal distribution about some age dependant central axis, and what effects this has.

Chapter 3, documents an application of a code such as INTERROGATOR. We first select a sample of EELS – a sub class of local galaxies which are defined by their high $H\alpha$ equivalent width – a predictor of high specific star formation rate. Specifically, we select for galaxies with EW(Hα) > 200Å, redshift $0.05 < z < 0.3$, and S/N > 5 in the OIIIλ5007, NIIλ6564, Hα and Hβ lines.

Traditionally, such selections have been made using inferred line fluxes based on photometry as getting continuum measurements (and therefore accurate EWs) was time con-

suming, and EELS are rare so building up a large sample is extremely prohibitive. However with recent advances in survey breadth and depth, we are able to turn to the GAMA survey to assemble such a sample based on spectroscopy. We find a sample of 136 galaxies which match the criteria selection criteria.

We then move on to deriving the physical properties of this sample. While GAMA provide modelling and inferred parameters for all objects in the survey, they do not include nebular emission in their fitting, and assume exponentially declining SFHs. While these are solid assumptions for most galaxies in the local Universe, the defining features of EELS mean that they are inappropriate – by definition we are selecting for galaxies with overwhelming amounts of nebular emission, and (as $H\alpha$ is correlated) high star formation rates which are unlikely to be declining. We therefore refit the galaxies using INTERROGATOR and a fiducial model similar to that used in the existing fits but with the relaxation of the SFH assumption and the addition of nebular emission. We find that these galaxies are low in stellar mass, ranging from $7.95 < \log M_*/M_\odot < 10.21$, but with median below $10^9 M_\odot$, but largely possess much higher specific star formation rates compared to the local Universe main sequence, on average following much more closely the star forming galaxy main sequence as high as $z \sim 8$. We also find the sample exhibits significantly lower metallicities than the local mass metallicity relation, however the distribution is significantly different to both the local and high redshift relation at $z = 8$ as derived from the BLUETIDESsimulation. Based on the O3N2 strong line diagnostic we find the relation to be largely flat over the whole range, lying somewhere between the local and EoR relations. Finally, we find our suspicion that these galaxies should be re-fit to be vindicated – almost all galaxies in the sample are consistent with rising star formation histories, with a small minority showing slightly declining – but consistent with constant – SFHs.

However, our choice of model was effectively arbitrary, and it is important to quantify the uncertainty associated with the model assumptions made. We fit the observations with a variety of different models used in modern SED fitting, and find scatters of $\sim 0.4dex$ in both the median stellar mass and star formation rate for the choice of models we chose,

with significantly larger scatter possible on individual objects. It can be argued that these galaxies are the "worst case" in the local Universe, as they have large amounts of recent star formation, which is much less poorly conditioned than older stellar populations – the addition of small amounts of young populations can have dire consequences for the overall emission, and while these galaxies are rare, the conditions are much more typical of the epoch of reionisation.

Finally, as described in Section 3.5, we obtained and analysed VLT/X-SHOOTER spectroscopy of a sub-sample of 12 EELS. In principle this should permit the measurement of accurate direct method metallicities and constraints on the shape of the dust curve. We design an EMCEE-based line fitting code to fit emission lines from these spectra, with the aim of using known intrinsic line ratios to accurately map the dust curves of these objects. Unfortunately, early analysis raised concerns of the integrity of the observations themselves or reduction prompting us to abandon this part of the project.

Finally, Chapter 4 proposes a novel handling of the star formation history and chemical enrichment histories within codes such as INTERROGATOR. We use the hydrodynamic code BLUETIDES, extracting all galaxies from redshifts 8-13. We divide them up by redshift, and then by mass bins in integer ranges from $8 < z < 13$ and $8 < \log M_* < 10$.

We then first establish the star formation histories of these galaxies, as this is the dominant component over the chemical enrichment history, at least for photometry. For each galaxy we bin star particles by age, and fit both a constant and an exponential SFH to them, finding that across all mass and redshift ranges being considered they are considerably better serviced by exponential SFHs, with a time constant which decreases with redshift. This tracks with results from the lower redshift Universe – as time goes on star formation cosmically slows down, and most galaxies in the local Universe have exponentially declining histories rather than rising.

We then argue that it is possible to fit the overall metallicity distribution by both introducing an age dependant metallicity, and adopting a metallicity distribution (specifically a gaussian distribution in $\log Z$) in each age bin. As for the SFH we have established the

younger, higher Z bins have much higher amplitudes than the older, lower Z bins, this produces the characteristic skewed global metallicity distribution in these galaxies.

Combining these assumptions together, we find good agreement in star particle histogram space between both the stacked galaxies in each bin and the overall fit $\psi(t, Z)$ in equation 4.11. In addition to the evolution of the SFH parameter τ, we find that the metallicity evolves strongly with stellar mass, increasing approximately 1dex at fixed redshift from galaxies $< 10^8 M_\odot$ to the largest galaxies at $<> 10^10 M_\odot$, in addition, the metallicity evolution with age weakly trends towards flat with redshift – this again tallies with our observations of the local Universe, where metals have sufficient mixing time to become approximately constant throughout a given galaxy, and evolve slowly in time as metallicity is a proportional quantity so a fixed amount of metal production results in a decreasing metallicity increase with time.

Finally, we move into observable space, creating stellar & nebular SED's from these SFHZ grids in order to isolate the effect that the evolution and scatter in metallicity would have on the light being produced. We find that the imposition of a constant SFH (or indeed any SFH which largely suppresses the true stellar mass contained in the youngest bins) leads to a large reduction in the continuum flux, around 35%. This argument can also be inverted – inappropriately choosing a constant SFH when fitting one of these galaxies will result in a significant overestimation of the mass due to the underrepresented O/B/A stars. While the use of a fixed metallicity compared to the grid model largely does not impact the photometry, such a model largely provides better estimates of the line fluxes in the optical. Such a mode may therefore be useful in the era of Webb, when rest frame optical imaging and possibly spectroscopy are accessible for EoR galaxies.

5.1 Future Work

Significant amounts of future work can be done on each of these projects.

INTERROGATOR is a project which is only as good as the models/assumptions it uses. In the concluding remarks to Chapter 2 we outline a range of potential improvements including: code optimisation (i.e. speeding up the calculation), expansion to other SFZHs (for example that described in Chapter 4), SPS models and IMFs, adding FIR modelling, and creating mock NIRCam/NIRISS WFSS and NIRSpec observations. These are all updates that can be done piecemeal, either as better tools (such as SPS models) are released, or as they become nessacery due to arguments made in the literature.

While Chapter 3 is largely complete and self contained the analysis of the X-SHOOTER spectroscopy of the EELS was left incomplete due to results which led to concerns about the data's integrity. One possible pathway would be to re-reduce the observations using the newest available pipeline, however this is far from a guarantee that future work would be possible.

Chapter 4 has significant possible expansion. Firstly, quantifying the stochasticity in these SFHZ relations would be a valuable approach if this type of fitting is to be used for galaxies observed in the EoR. In addition, if the work done here were to be combined with a realistic set of mass functions with redshift for the EoR, one can generate samples of galaxies by drawing from the 2-D mass/z function, and then drawing the other starlight parameter distributions (figure 4.8) at that stellar mass an redshift. Once these parameters have been drawn, it would be easy to then generate spectra, adding dust and nebular emission and creating realistic synthetic observations. While this can obviously be done directly with hydrodynamical simulations, this would be a rapid way to generate more galaxies with very similar properties, by drawing on the distributions of galaxies made by the direct method.

In addition, the expression at the heart of the BLUETIDES fits given in equation 4.11 is effectively a product of a SFH, and a term which describe the metallicity distribution at each fixed age. There is nothing special about the SFH we found for BLUETIDES galaxies, and a useful extension would be to see how this applies to galaxies in other simulations. The constant metallicity assumption usually used in SED fitting is much more appropriate at low redshift, where material has had more mixing time, however the quantification of

this effect would be undoubtably useful.

Appendix A

Testing interrogator with synthetic galaxies

This appendix shows the complete set of synthetic galaxy fits as outlined in section 2.4. Galaxies all have the same parameters (listed in the table below) except for their star formation histories. The galaxy spectra were then made with INTERROGATOR's model galaxy generator and convolved with the filter transmission functions. White noise was then applied to the observations with a signal to noise ratio of 50.

SPS model	BPASS v2.1
IMF	Salpeter, $\alpha = -2.35$
Nebular Emission	CLOUDY, escape frac. = 0
Dust	Modified Charlot & Fall "Pacman" model $\tau_V = 1.0$, $\mu = 0.25$, $t_{BC} = 10Myr$
Other params	$z = 0.0$, $\log_{10}(M_*) = 8.0$, $Z = Z_\odot/20$ height

Table A.1: Table of synthetic galaxy parameters

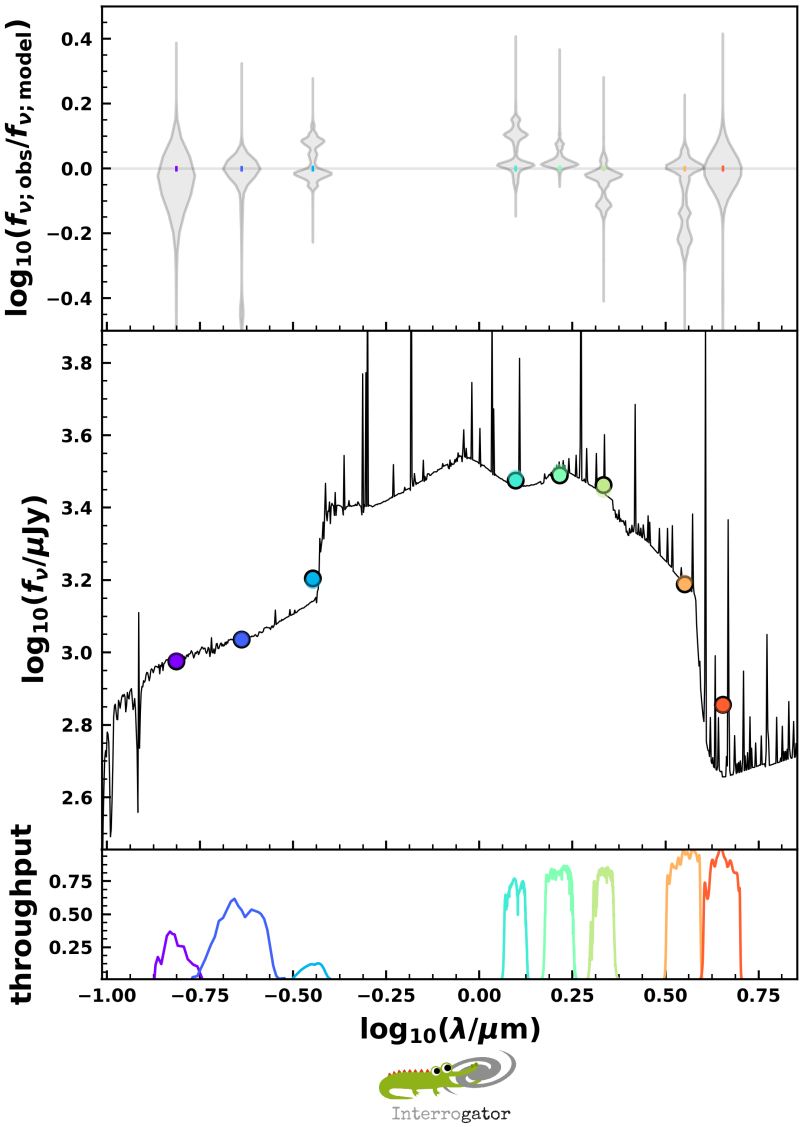

Figure A.9: INTERROGATOR SED fit of synthetic galaxy with an exponentially rising star formation history with $\lambda = 0.01\mathrm{Myr}^{-1}$. The other parameters are outlined in the table at the beginning of this appendix. Broad band filters used are those of the GAMA survey, see section 3.2

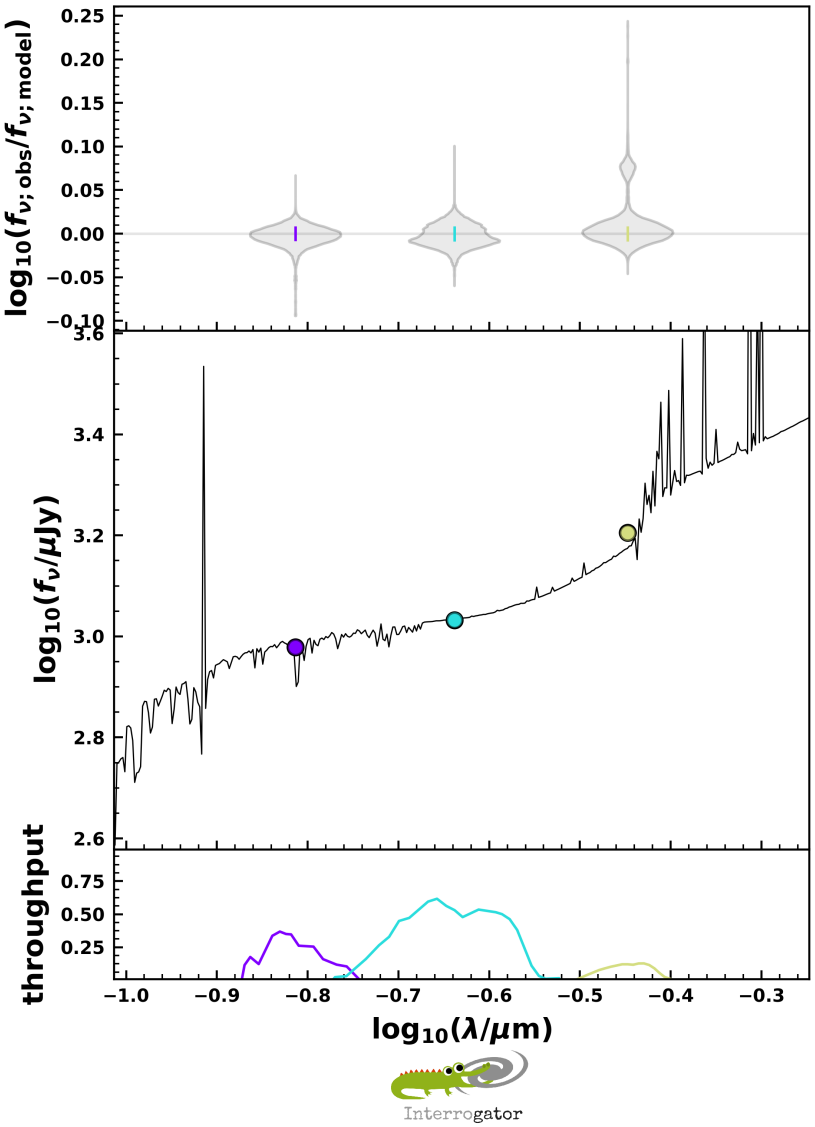

Figure A.10: Same as previous figure, except only the bluest three filters are used.

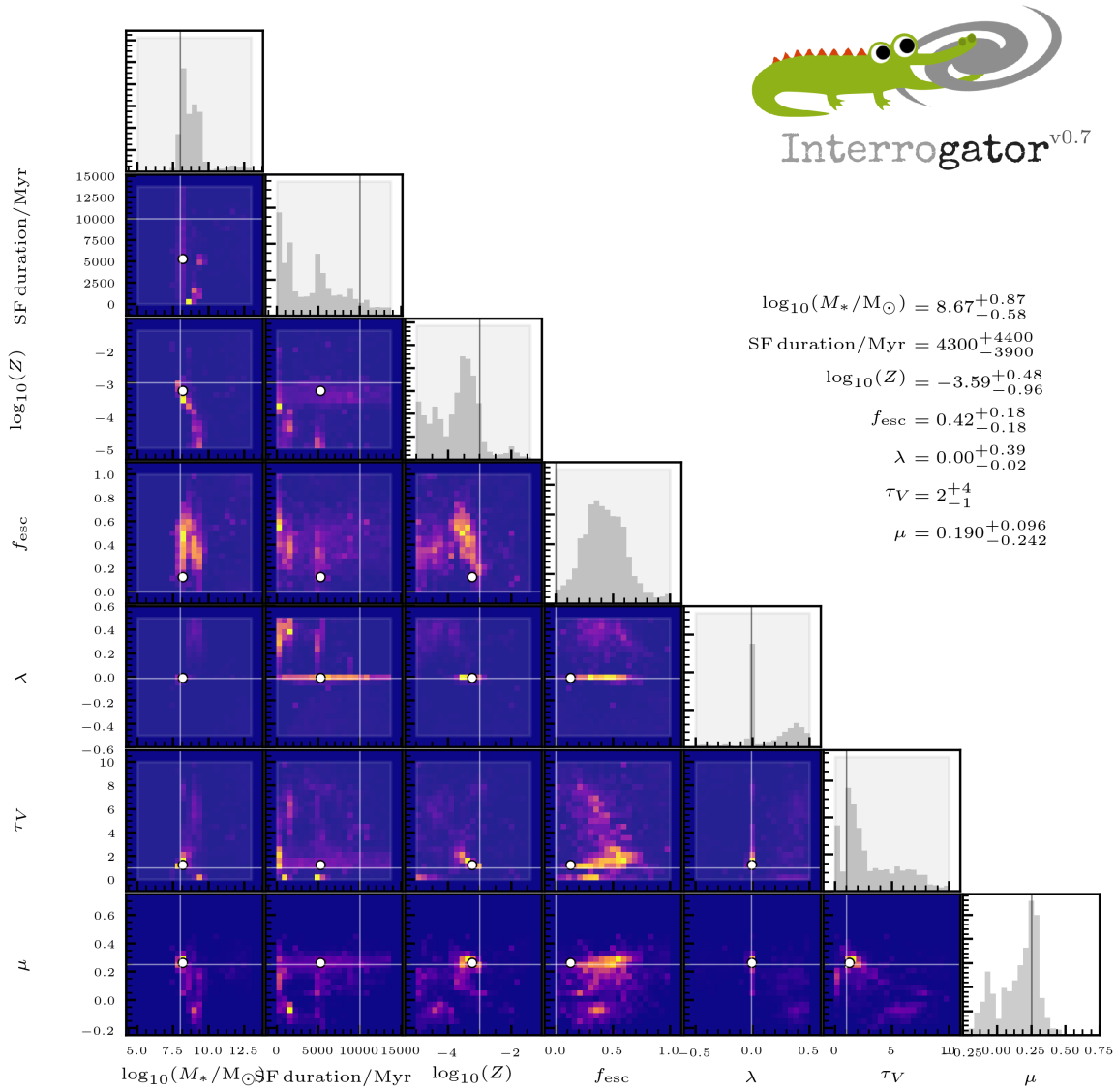

Figure A.11: Triangle plot of fit parameters for INTERROGATOR synthetic galaxy with exponentially rising star formation history with $\lambda = 0.01\mathrm{Myr}^{-1}$. Coloured panels are marginalised 2d distributions between row and column parameter, and grey histograms are the 1-D marginalised distribution of the parameter.

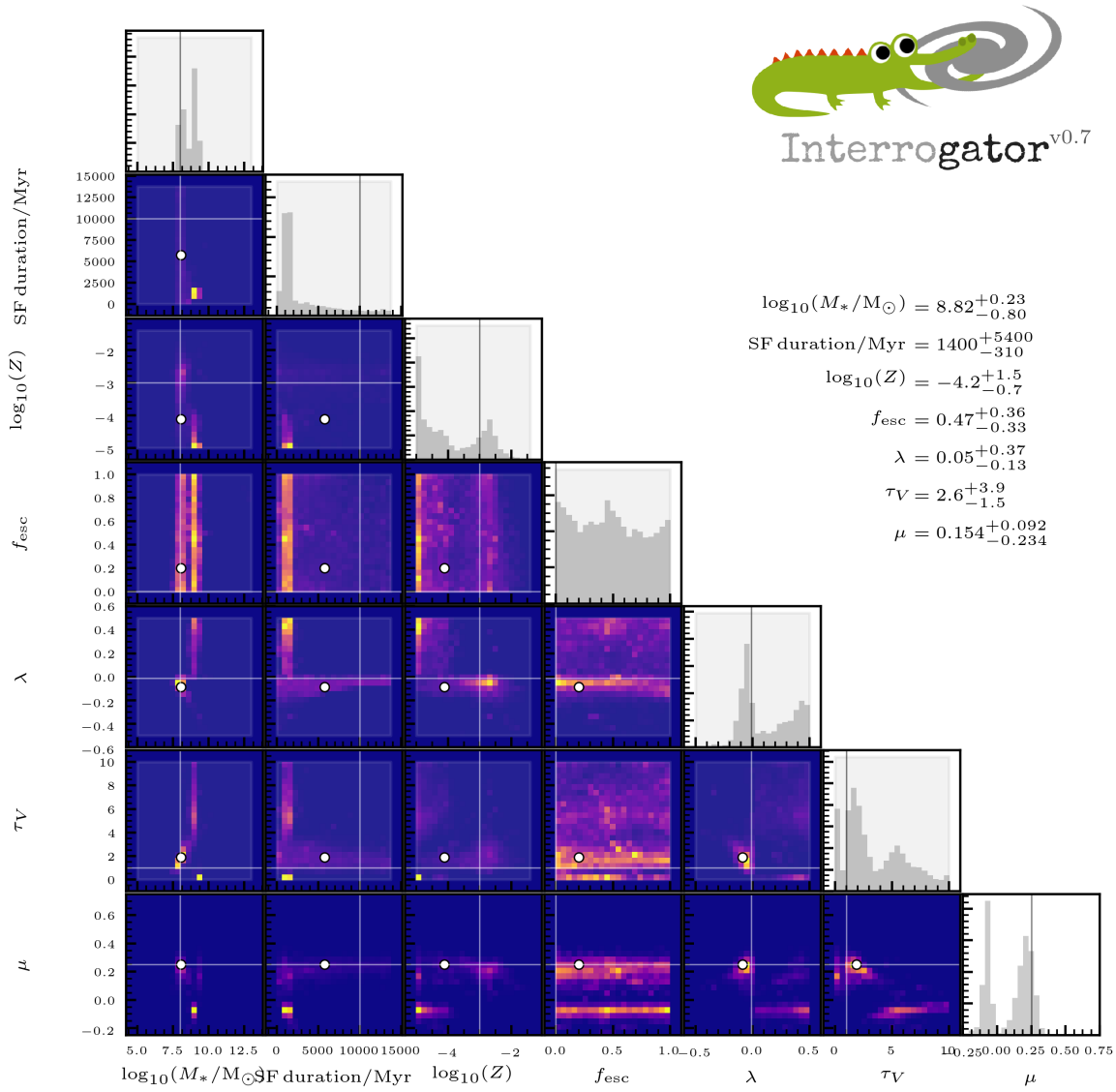

Figure A.12: Same as previous figure, except for fit to the three bluest filters.

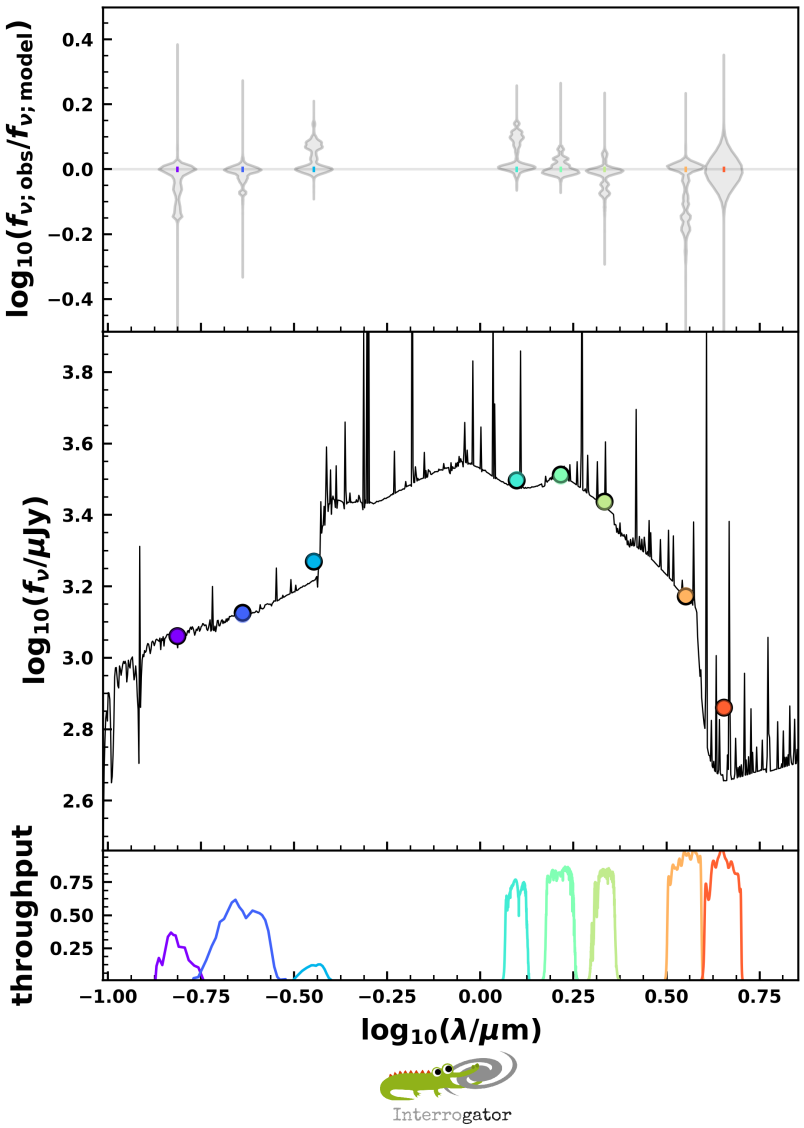

Figure A.1: INTERROGATOR SED fit of synthetic galaxy with a constant SFH 100Myr in duration. The other parameters are outlined in the table at the beginning of this appendix. Broad band filters used are those of the GAMA survey, see section 3.2

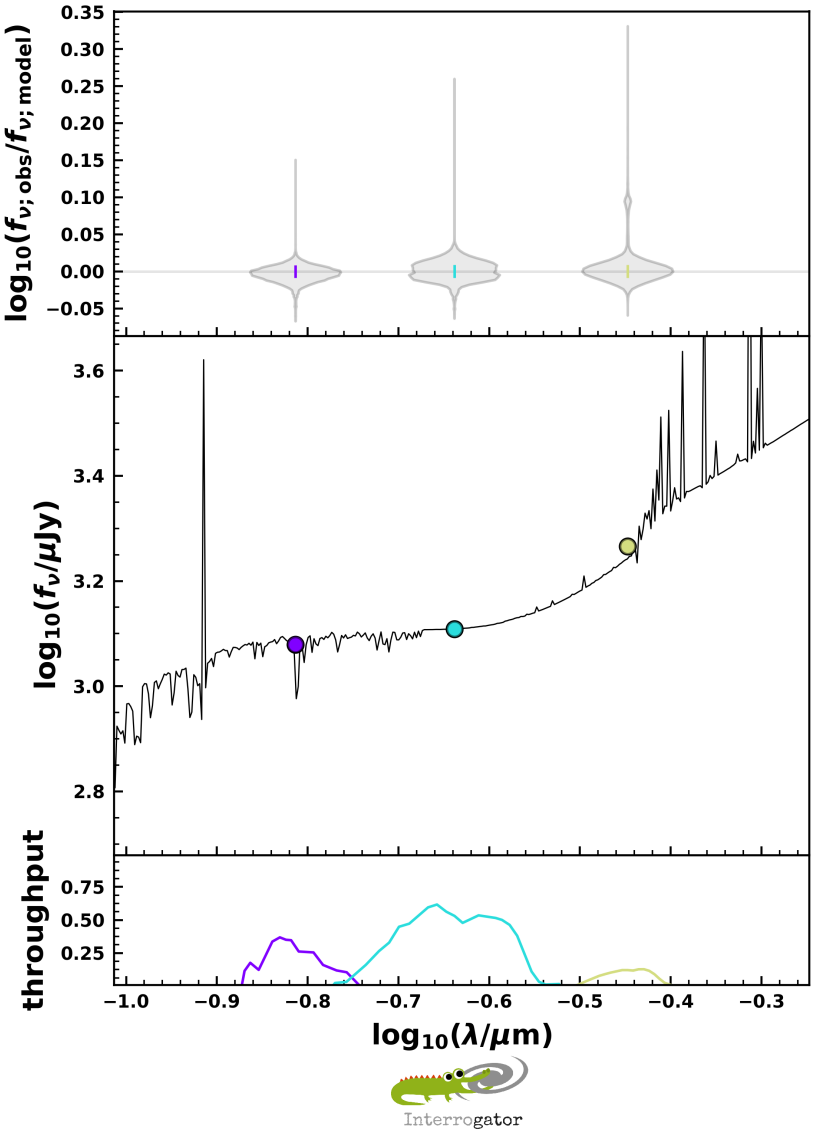

Figure A.2: Same as previous figure, except only the bluest three filters are used.

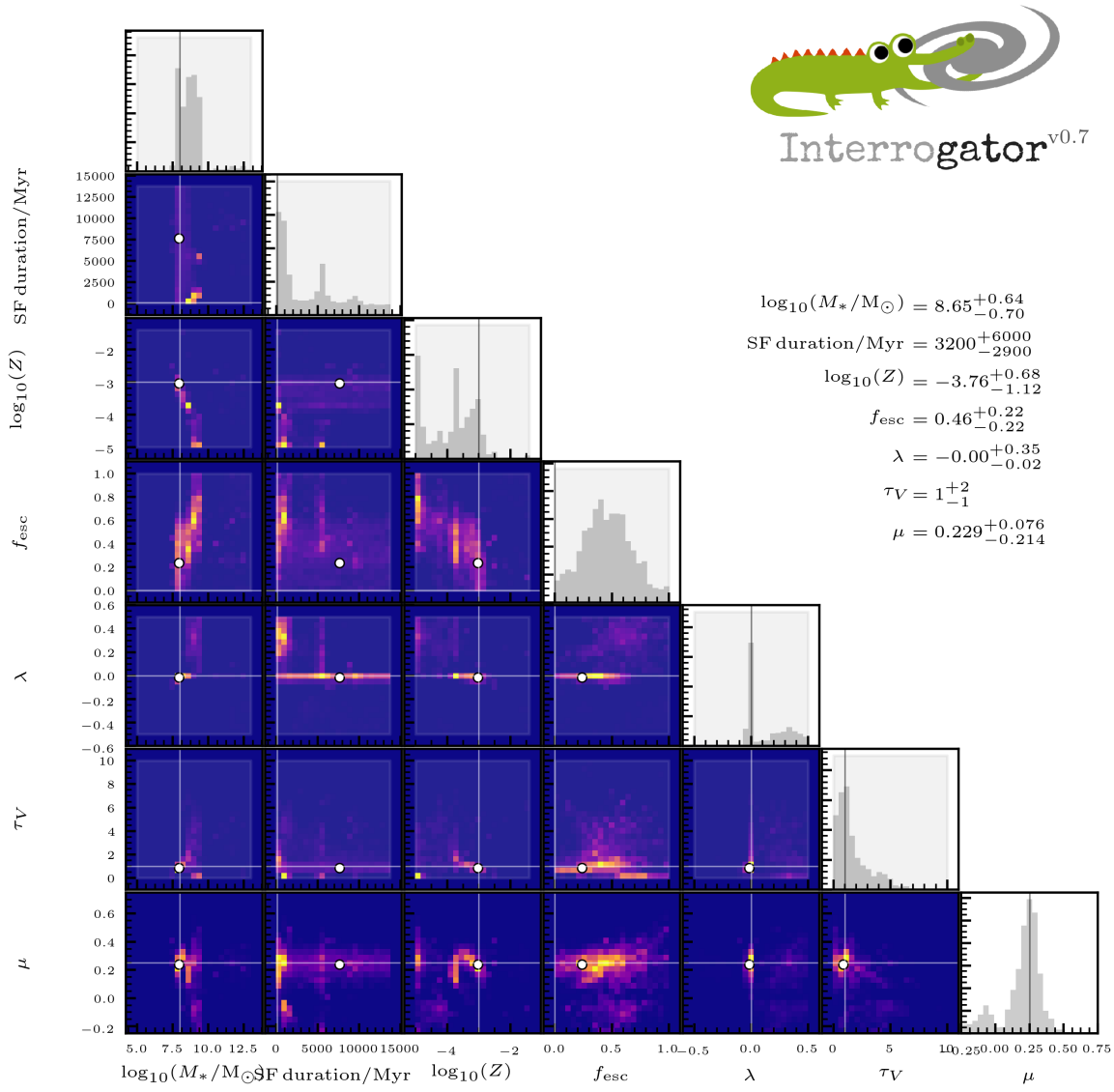

Figure A.3: Triangle plot of fit parameters for INTERROGATOR synthetic galaxy with constant SFH 100Myr in duration. Coloured panels are marginalised 2d distributions between row and column parameter, and grey histograms are the 1-D marginalised distribution of the parameter.

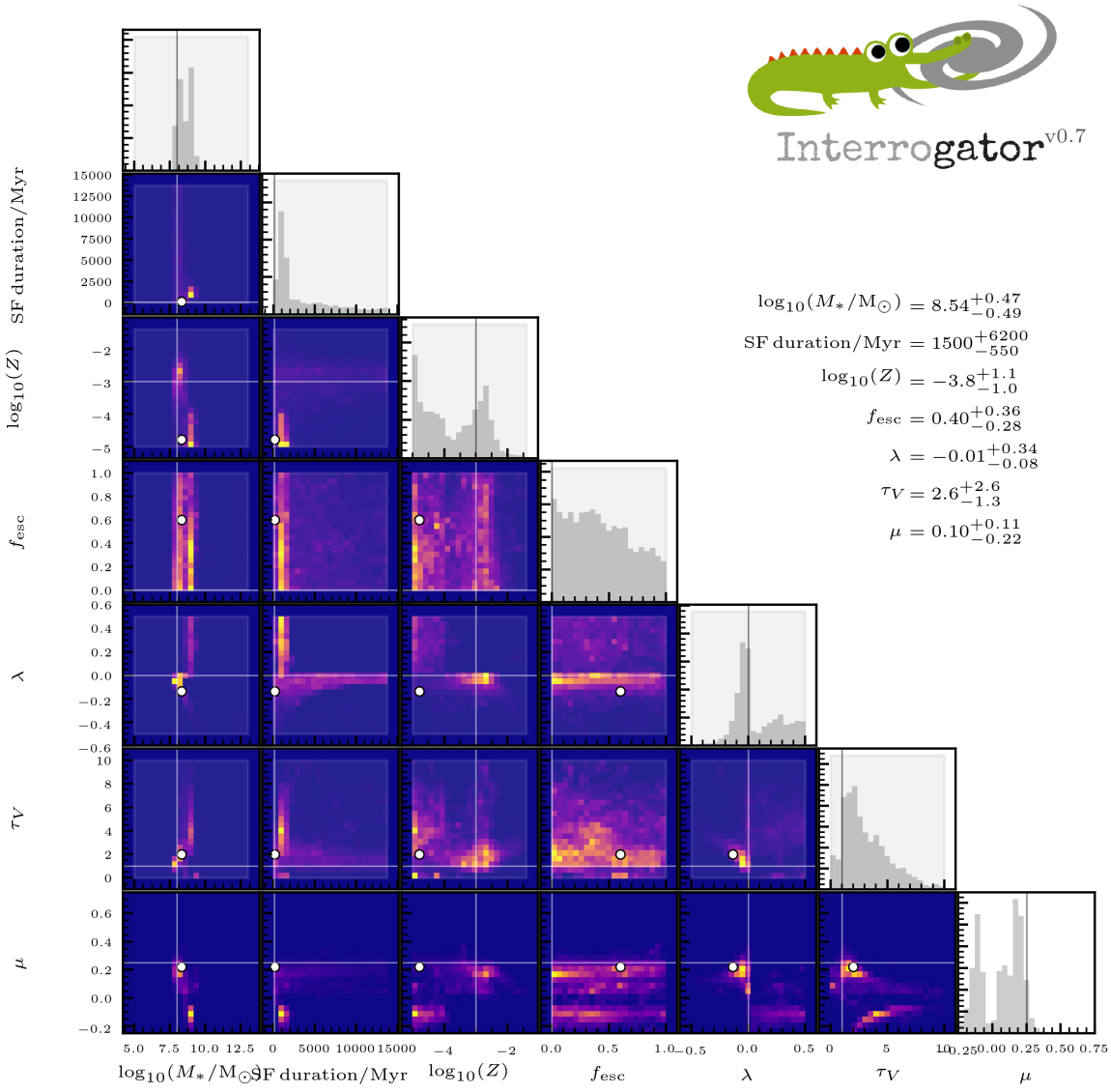

Figure A.4: Same as previous figure, except for fit to the three bluest filters.

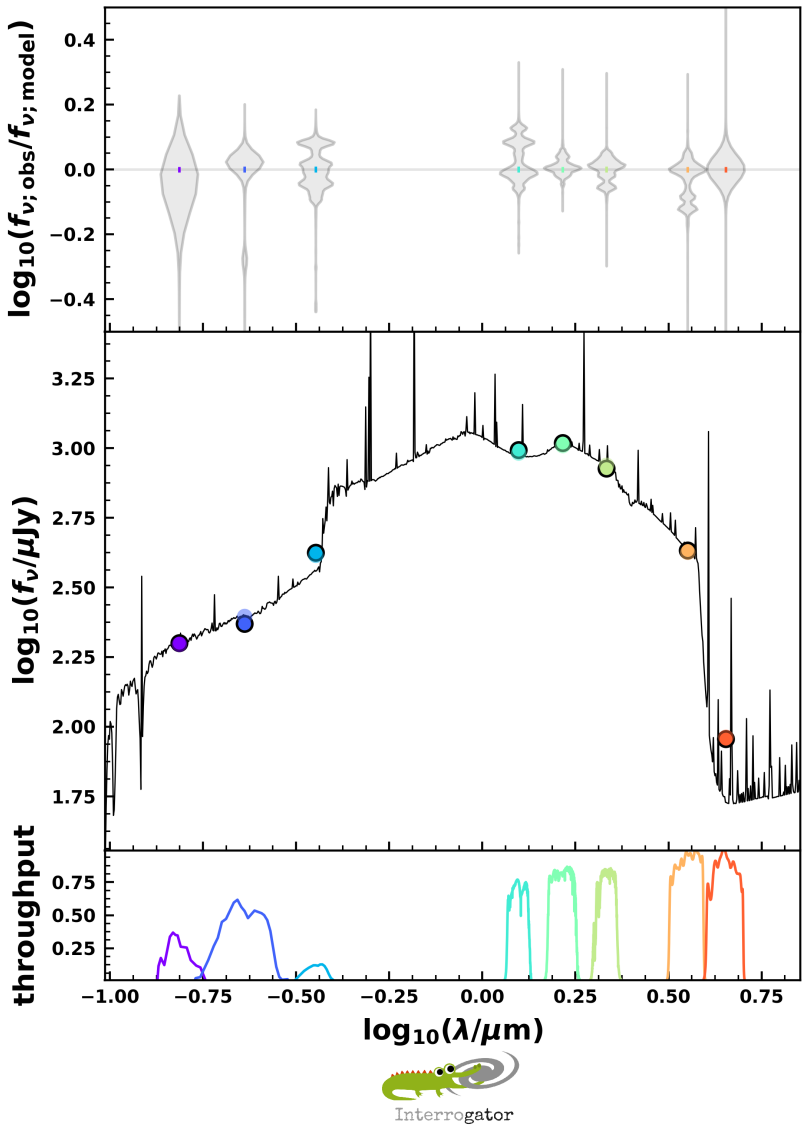

Figure A.5: INTERROGATOR SED fit of synthetic galaxy with a constant SFH 1Gyr in duration. The other parameters are outlined in the table at the beginning of this appendix. Broad band filters used are those of the GAMA survey, see section 3.2

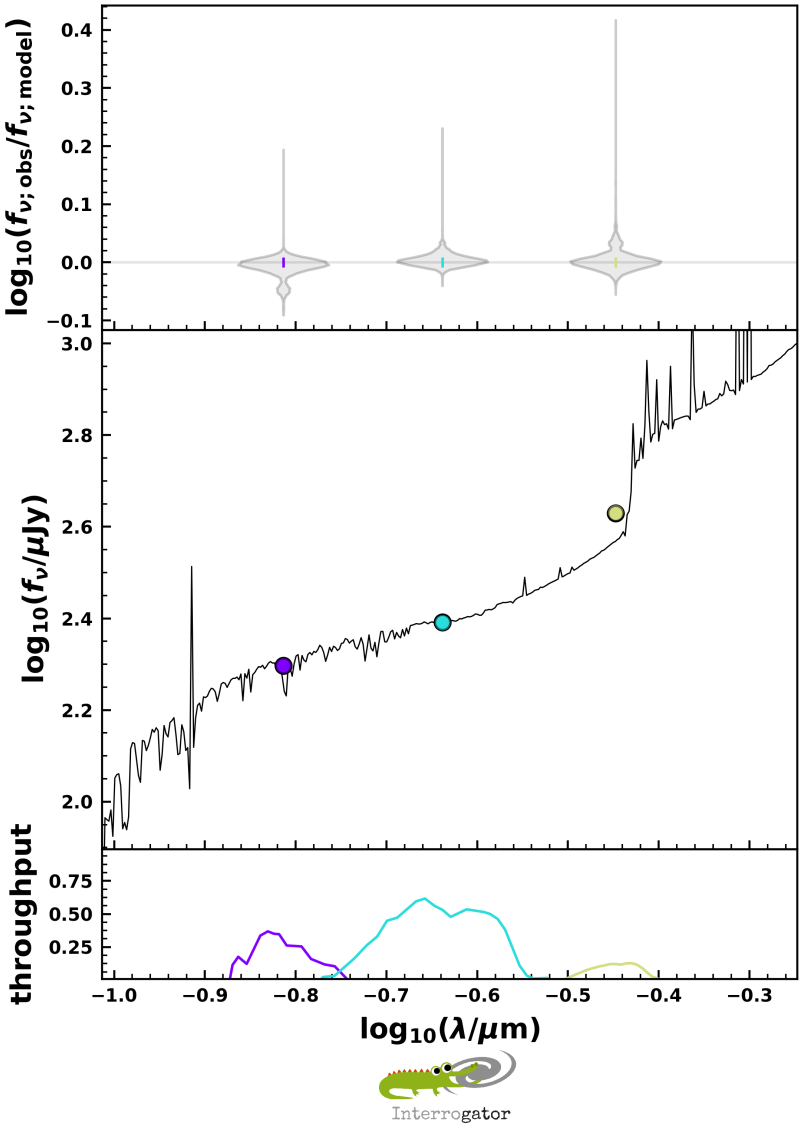

Figure A.6: Same as previous figure, except only the bluest three filters are used.

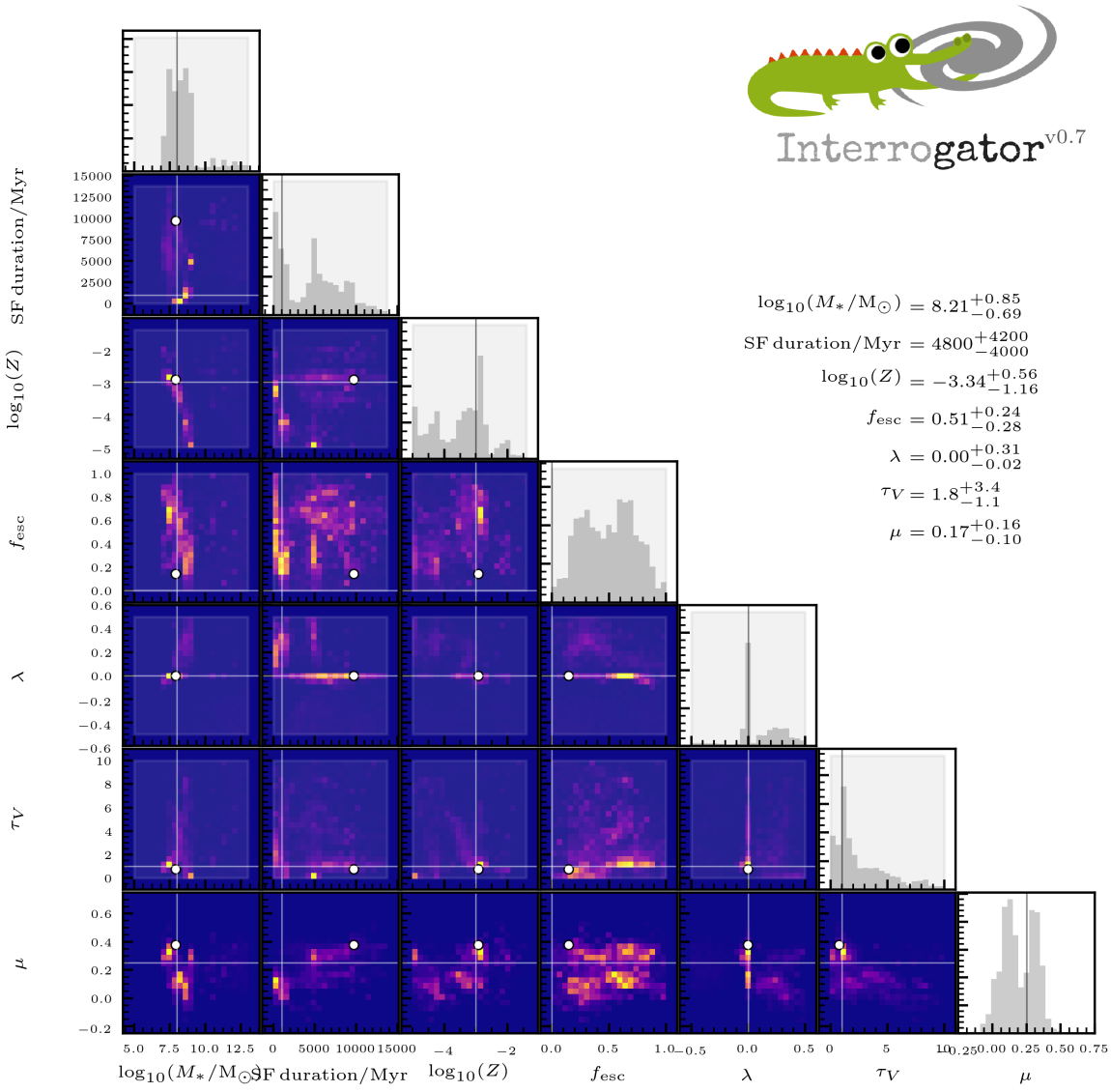

Figure A.7: Triangle plot of fit parameters for INTERROGATOR synthetic galaxy with constant SFH 1Gyr in duration. Coloured panels are marginalised 2d distributions between row and column parameter, and grey histograms are the 1-D marginalised distribution of the parameter.

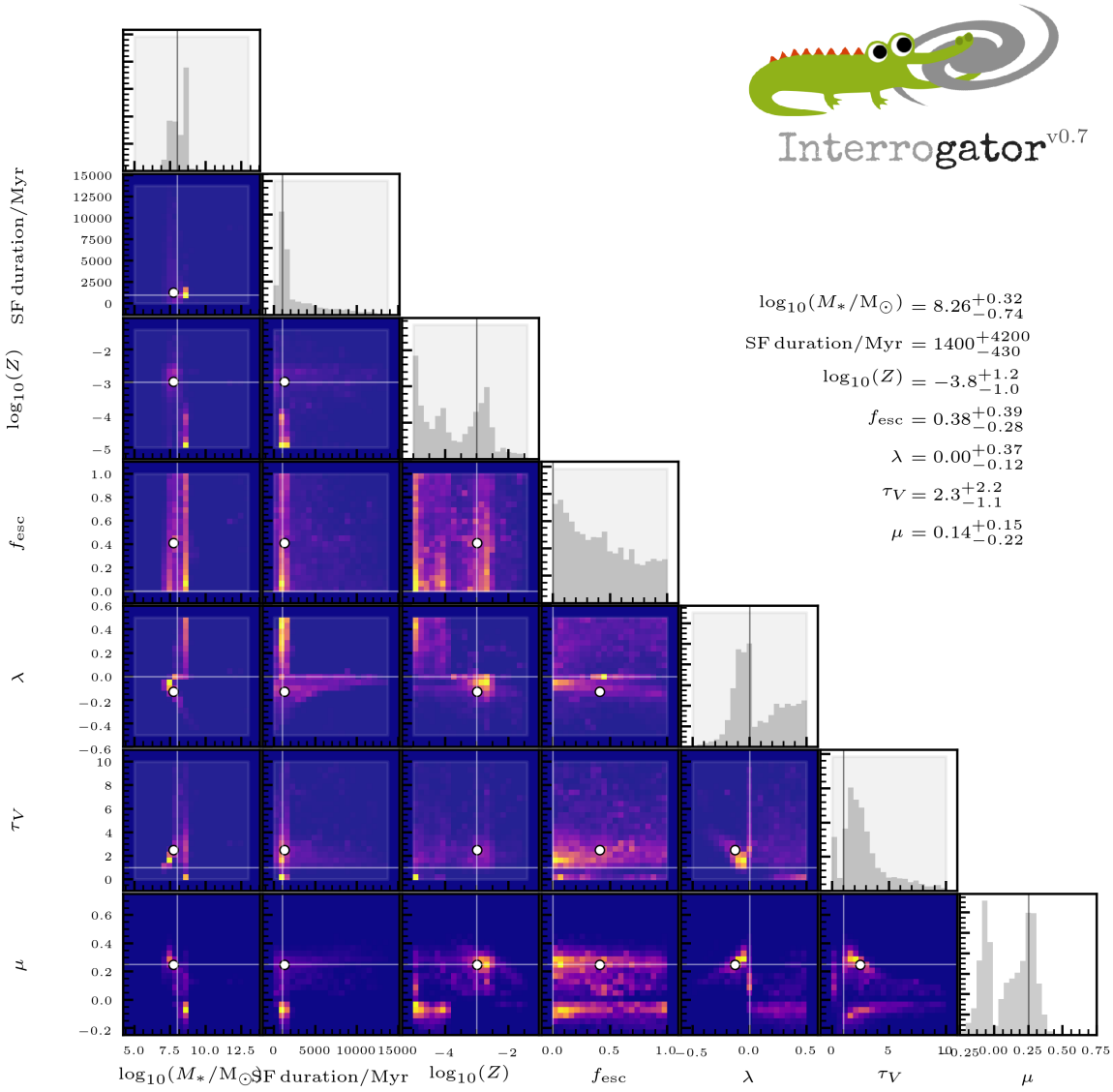

Figure A.8: Same as previous figure, except for fit to the three bluest filters.

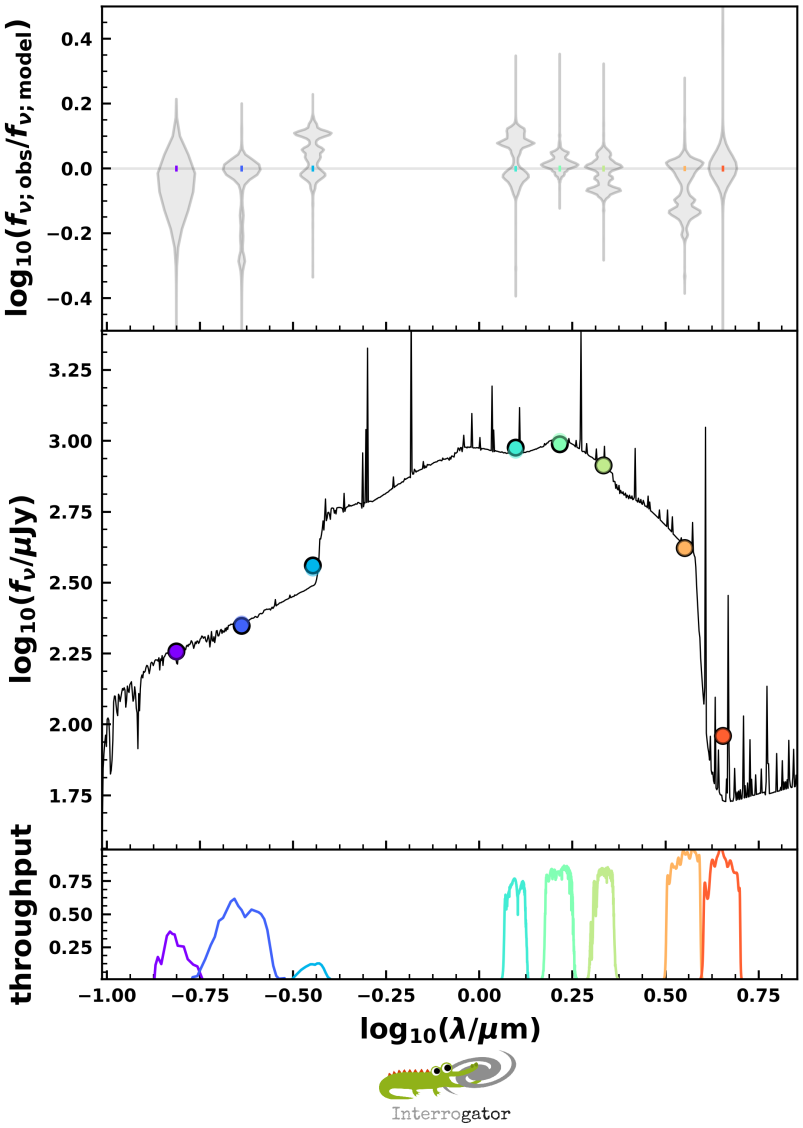

Figure A.13: INTERROGATOR SED fit of synthetic galaxy with an exponentially rising star formation history with $\lambda = 0.001 \mathrm{Myr}^{-1}$. The other parameters are outlined in the table at the beginning of this appendix. Broad band filters used are those of the GAMA survey, see section 3.2

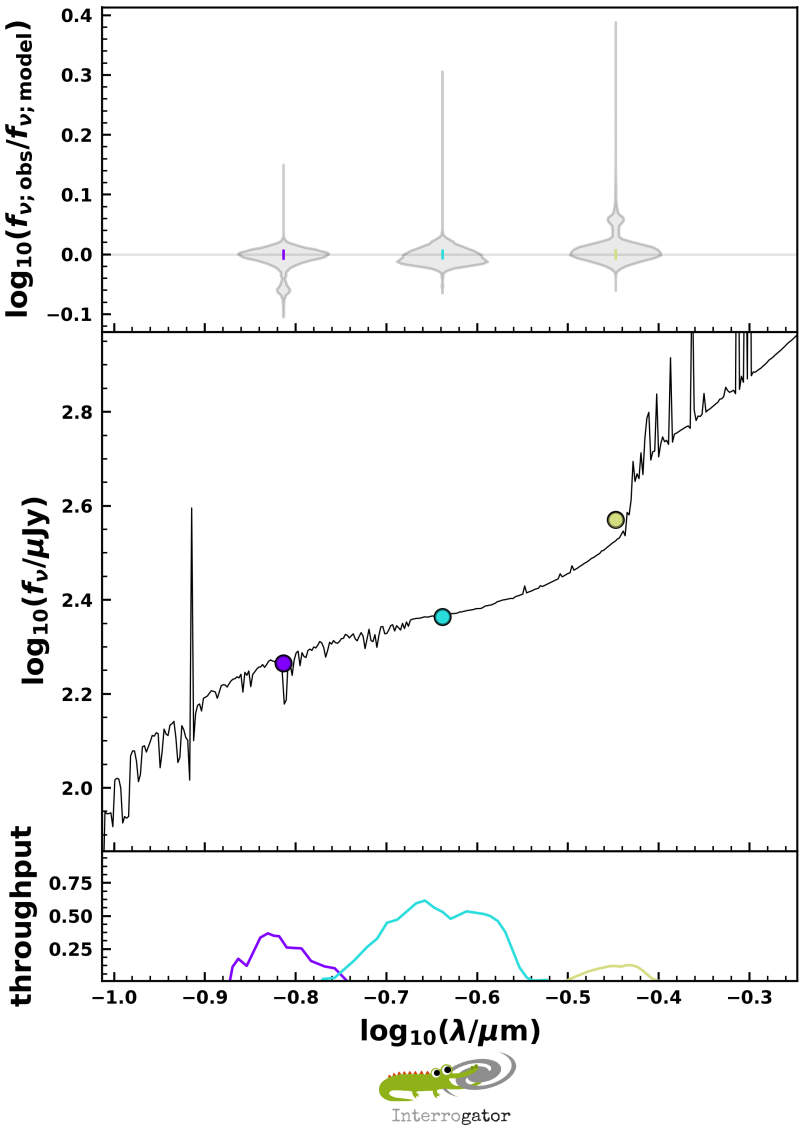

Figure A.14: Same as previous figure, except only the bluest three filters are used.

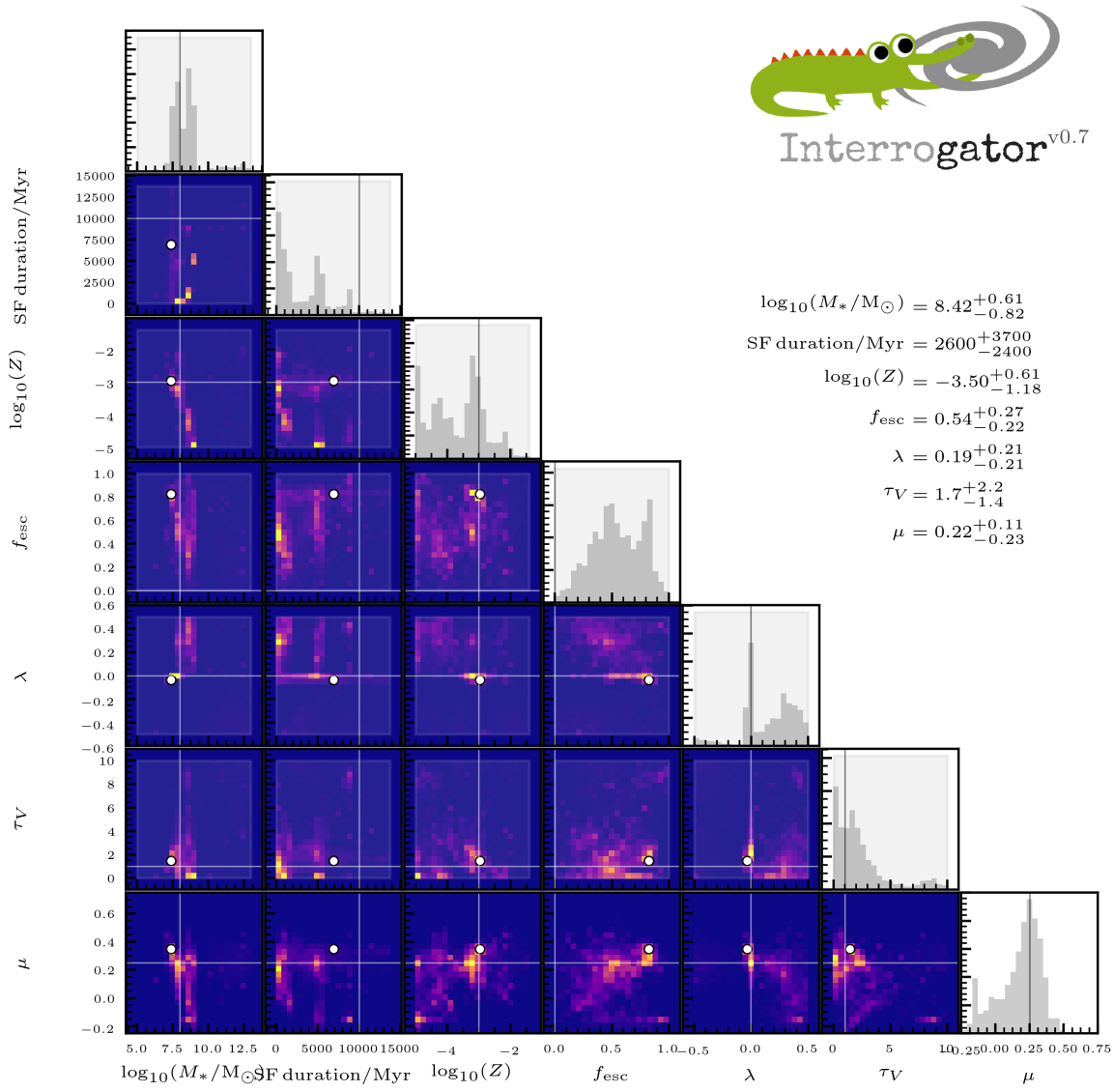

Figure A.15: Triangle plot of fit parameters for INTERROGATOR synthetic galaxy with exponentially rising star formation history with $\lambda = 0.001\mathrm{Myr}^{-1}$. Coloured panels are marginalised 2d distributions between row and column parameter, and grey histograms are the 1-D marginalised distribution of the parameter.

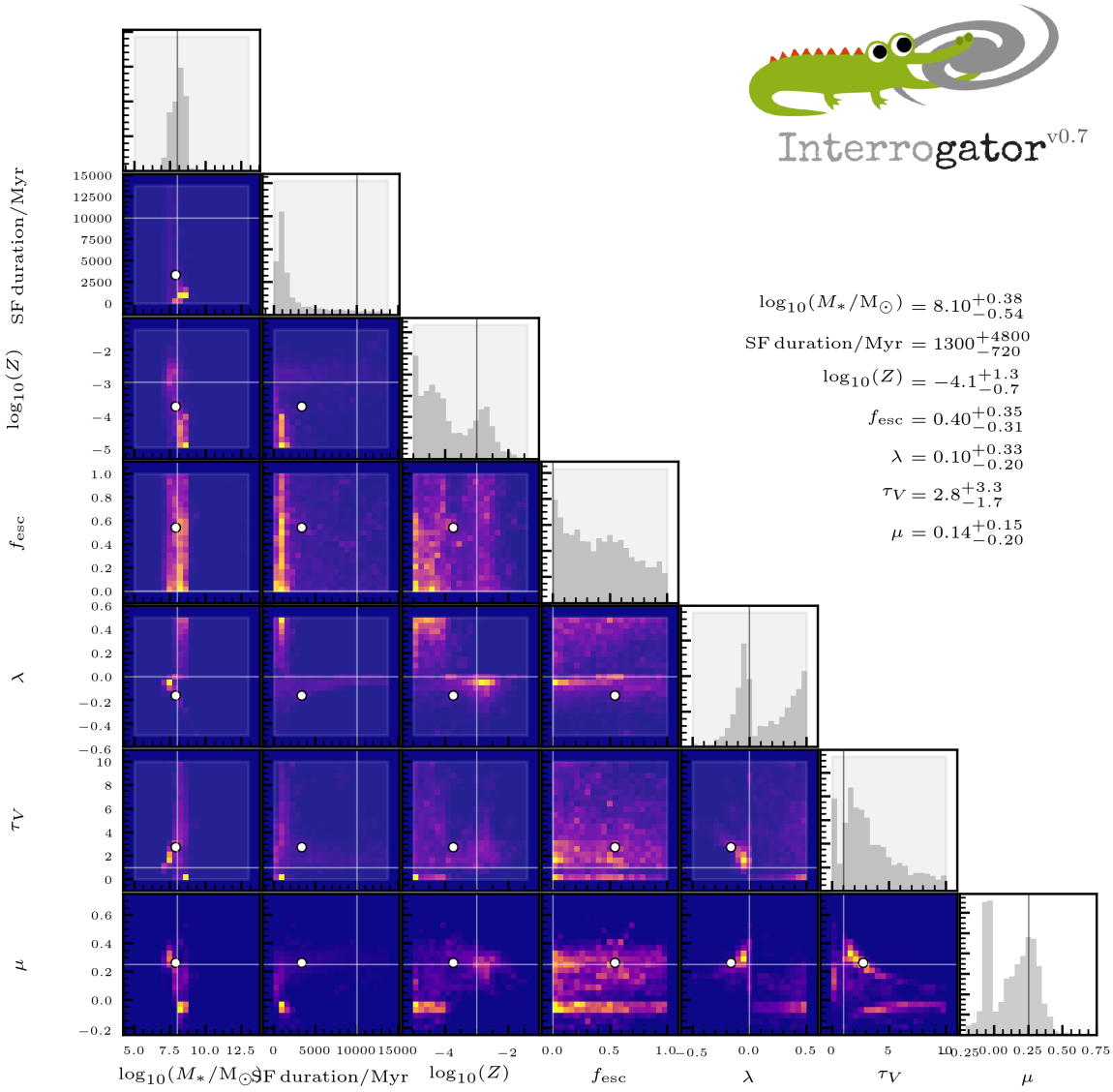

Figure A.16: Same as previous figure, except for fit to the three bluest filters.

Appendix B

X-SHOOTER spectra & Line fits of EELS subsample

This appendix contains the tabulated selection data of each galaxy in the EELS sample. As the galaxies were only selected on the Hα equivalent width, the r-band magnitude, and the galaxy redshift (see section 3.2 of the main text) we have opted to list only these quantities here. Other relevant values can be found in the full GAMA data releases [Wright *et al.*, 2016] using the catalogue IDs listed.

This appendix also contains the spectra of the EELS subsample for which VLT/X-SHOOTER spectra were obtained, and is an appendix to section 3.5. They are presented in order of their r-band brightness as measured in the GAMA survey.

The top figure on each page is the full spectra. Each spectra has been smoothed with a 3Å gaussian kernel for visibility. Black line shows the spectra, and red line shows the error spectrum.

The bottom figure is the fitting of the first three balmer series lines ($H\alpha, \beta, \gamma$) and the OIIIλ5007 line. The red fits are taken from the original GAMA survey spectra, and the blue are extracts from the spectra in the top figure. Each fit was carried out in accordance with the main text in section 3.5.

Catalogue ID	RA	DEC	r-band magnitude	redshift	HA-EW
782570	183.739	-1.859	20.0	0.13	2548.7
824670	185.304	1.391	20.2	0.06	267.7
898820	185.912	-1.029	20.3	0.14	335.2

Catalogue ID	RA	DEC	r-band magnitude	redshift	HA-EW
129830	174.645	-2.073	19.4	0.19	544.4
124480	179.702	-2.504	18.5	0.08	372.6
593480	216.766	-0.208	18.1	0.15	973.6
64900	220.611	-0.252	18.5	0.15	220.4
83810	174.266	0.471	18.6	0.11	347.3
22530	177.967	1.102	18.9	0.09	244.4
695300	181.064	0.428	18.7	0.15	218.8
106330	215.501	1.037	18.2	0.13	352.1
743280	220.523	-0.88	19.3	0.28	462.8
16970	221.244	0.772	18.9	0.21	356.2
178340	180.082	-2.019	18.6	0.11	247.6
371810	133.008	1.083	18.2	0.11	305.5
279080	135.277	0.905	18.9	0.11	513.8
372280	134.944	1.137	17.7	0.2	220.6
324450	135.949	1.669	18.3	0.24	254.7
216670	139.218	0.521	18.7	0.06	371.2
383010	139.498	1.964	17.5	0.09	217.6
219800	179.157	1.546	18.6	0.11	275.6
719040	218.042	1.431	18.9	0.14	626.4
517140	131.059	2.439	18.1	0.09	564.5
516990	130.233	2.342	18.3	0.05	278.7
419630	140.714	2.935	19.5	0.12	356.6
376180	132.313	1.488	18.4	0.21	262.6
386450	132.383	2.261	18.6	0.13	277.8
3627050	134.354	-0.805	18.8	0.07	481.2
600420	135.518	0.399	17.8	0.06	230.7
372710	137.289	1.12	19.5	0.28	233.1
210220	137.085	0.196	19.1	0.08	515.0
198500	139.822	-0.807	17.3	0.08	307.5
210610	138.874	0.152	19.1	0.07	217.3
3623140	130.892	-0.762	19.0	0.14	202.8
216900	140.315	0.581	19.4	0.14	225.2
516880	129.69	2.283	19.3	0.12	492.8
422300	130.178	2.62	19.1	0.18	210.4
518080	134.894	2.689	19.1	0.07	249.8
388660	140.821	2.624	19.7	0.2	233.0
215720	135.053	0.568	19.3	0.06	276.0
574470	135.904	-0.084	19.4	0.05	267.6
599910	133.051	0.416	19.5	0.07	343.2
381080	131.282	1.846	19.7	0.06	302.9
3603740	131.389	-1.208	18.7	0.12	313.2
3888440	137.52	-1.486	19.8	0.06	438.0

Catalogue ID	RA	DEC	r-band magnitude	redshift	HA-EW
3900000	131.824	-1.002	19.8	0.2	543.9
3862350	134.639	-1.904	19.9	0.12	225.5
3578920	130.891	-1.568	18.9	0.29	222.2
521700	130.468	2.893	19.7	0.11	220.2
845130	134.934	1.788	19.8	0.23	218.1
747580	135.525	0.267	19.8	0.18	381.4
600250	134.353	0.364	19.5	0.28	255.2
324940	137.883	1.779	19.5	0.26	575.0
322980	129.648	1.485	19.5	0.11	236.3
198800	140.898	-0.648	19.9	0.23	482.8
346490	134.037	2.006	19.8	0.12	384.8
622910	135.885	0.804	18.7	0.05	201.9
136470	175.116	-1.638	18.4	0.12	639.4
402360	174.774	1.973	20.3	0.1	360.4
396700	174.781	1.599	18.3	0.3	257.3
583780	176.603	-0.183	19.5	0.22	262.6
69960	177.704	0.0	19.4	0.13	202.1
610110	178.75	0.415	19.3	0.13	203.9
219920	179.598	1.528	18.9	0.14	445.2
560360	180.081	-0.488	19.8	0.08	236.2
610440	180.192	0.222	19.1	0.24	292.2
272920	181.257	1.399	19.8	0.13	680.1
585060	180.927	-0.134	19.9	0.13	493.9
585700	184.156	-0.049	20.2	0.2	270.9
186360	184.143	-1.658	19.1	0.19	231.3
56320	185.558	-0.26	19.5	0.13	704.9
24030	184.014	1.195	18.5	0.05	203.4
690970	176.361	-0.662	19.9	0.28	278.0
288680	179.726	1.734	17.9	0.08	305.4
138790	184.172	-1.804	19.6	0.15	401.4
143670	177.033	-1.403	19.2	0.06	363.5
85490	182.583	0.56	19.5	0.29	250.0
186070	182.909	-1.476	19.1	0.1	235.3
828180	175.005	1.719	20.2	0.08	368.5
895720	174.931	-1.0	18.3	0.06	357.4
40710	182.637	-0.744	19.5	0.08	344.1
289610	182.85	1.849	19.8	0.08	221.2
809840	183.063	1.592	20.3	0.13	216.9
143570	176.537	-1.409	19.1	0.12	465.3
946810	184.615	1.057	20.2	0.13	224.2
810220	184.305	1.63	19.9	0.1	489.5
782120	182.187	-1.762	19.7	0.06	419.0

Catalogue ID	RA	DEC	r-band magnitude	redshift	HA-EW
792370	183.216	-1.558	20.0	0.22	224.3
129980	175.328	-2.099	19.6	0.05	270.7
131420	181.256	-2.103	18.2	0.07	271.2
172040	180.727	-2.438	19.5	0.27	222.0
4194520	180.069	-2.734	19.9	0.13	227.8
583610	175.717	-0.064	19.5	0.15	397.3
4310460	181.328	1.448	19.6	0.24	290.6
3087760	175.545	1.138	20.6	0.23	623.0
792870	184.659	-1.645	20.2	0.07	258.8
958130	174.73	-0.285	20.5	0.13	410.9
107830	222.906	0.967	18.8	0.12	339.8
239920	219.636	1.47	19.0	0.28	244.5
321040	220.766	1.648	19.3	0.12	222.6
64720	219.717	-0.408	19.4	0.13	562.6
318890	212.814	1.904	19.3	0.08	262.3
238540	214.6	1.701	19.3	0.09	294.8
544280	214.711	-0.958	19.1	0.15	371.1
28740	213.328	1.089	19.5	0.05	595.4
229050	219.879	1.066	19.8	0.21	200.3
343990	223.114	1.968	19.5	0.11	200.5
569020	217.291	-0.512	19.7	0.14	221.3
714990	217.101	1.569	19.4	0.24	465.2
251670	219.818	1.932	19.8	0.19	354.5
363740	221.155	2.54	18.9	0.13	290.6
363260	218.525	2.519	19.7	0.2	205.6
265800	215.325	2.797	19.5	0.11	236.1
367100	219.251	2.932	19.7	0.06	205.7
697400	214.097	0.871	19.6	0.19	281.3
238280	213.777	1.637	19.2	0.19	298.7
91950	214.169	0.449	19.7	0.27	2115.8
739880	222.577	-1.932	19.3	0.15	299.9
63760	216.781	-0.335	19.8	0.05	1529.4
227990	215.615	1.221	19.7	0.13	205.5
92150	215.304	0.43	20.6	0.05	474.8
297340	215.428	1.519	19.9	0.19	226.9
874230	212.488	-1.292	19.9	0.05	233.6
505680	221.164	-1.961	19.9	0.12	604.3
617950	213.745	0.227	19.4	0.13	209.8
748480	212.089	0.221	19.5	0.13	546.9
594750	221.393	-0.148	19.8	0.06	236.0
740260	216.209	-1.67	19.7	0.14	310.5
720710	216.022	1.803	19.6	0.06	312.9

Catalogue ID	RA	DEC	r-band magnitude	redshift	HA-EW
746770	211.824	-0.136	19.8	0.25	361.5
47660	213.67	-0.641	19.6	0.11	222.0
583980	177.714	-0.182	19.7	0.1	227.0
610680	181.328	0.234	19.3	0.08	228.6
77480	213.444	0.169	19.3	0.13	222.0
592940	214.73	-0.188	19.3	0.19	483.4
593760	217.722	-0.155	18.2	0.12	267.4

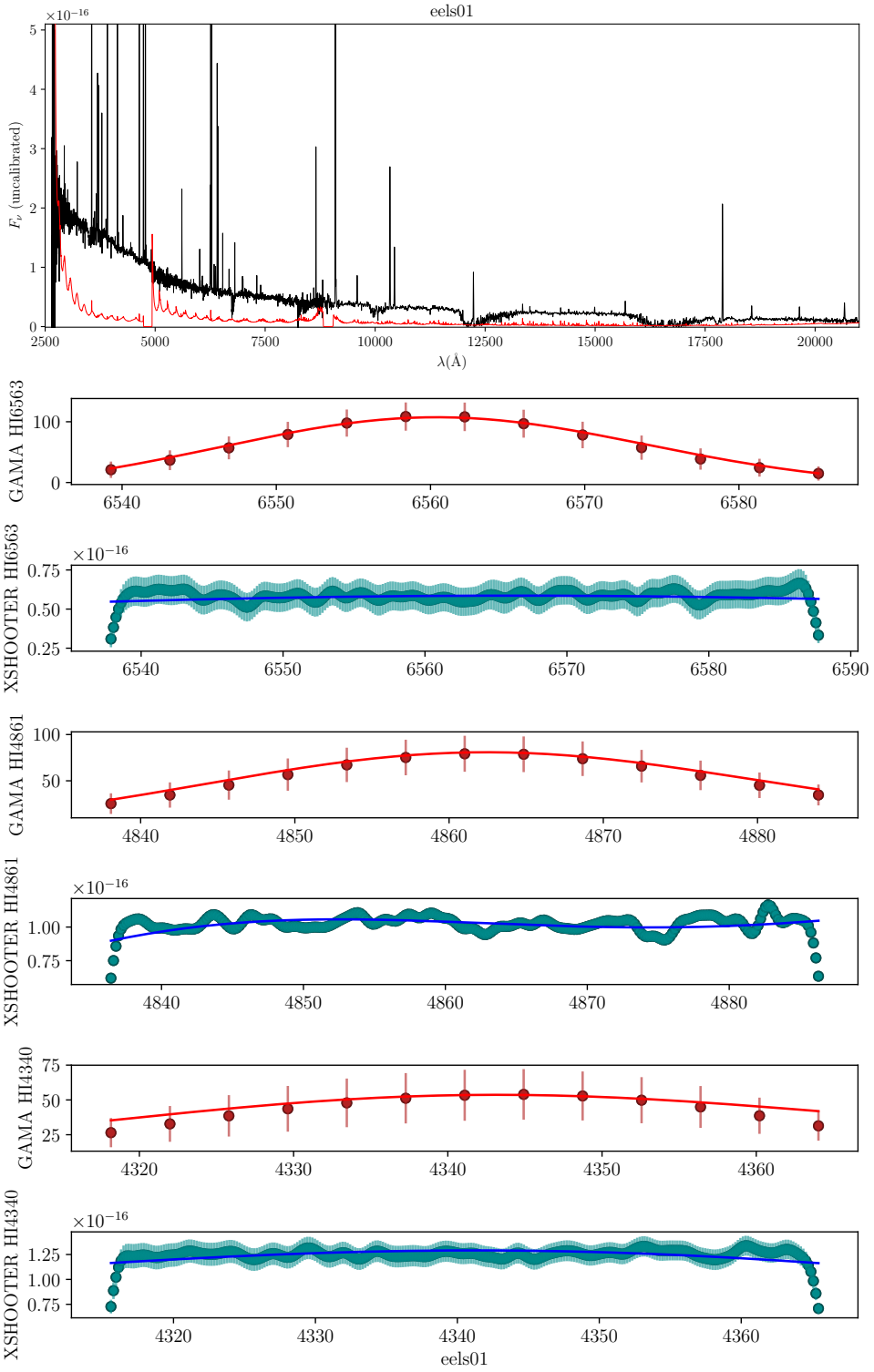
eels01
×10⁻¹⁶
F_ν (uncalibrated)
λ(Å)
GAMA HI6563
XSHOOTER HI6563
GAMA HI4861
XSHOOTER HI4861
GAMA HI4340
XSHOOTER HI4340
eels01

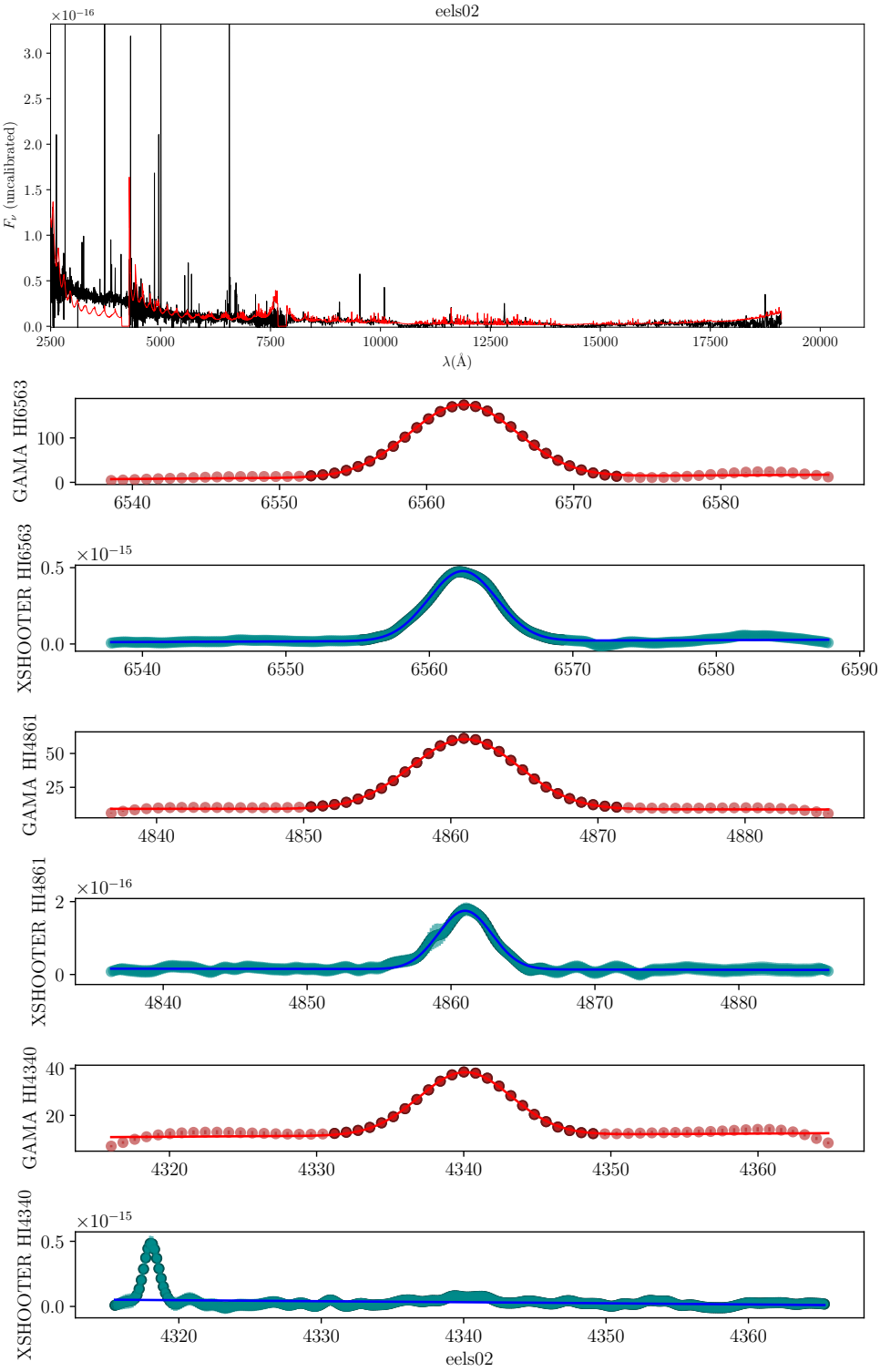
eels02
×10⁻¹⁶
F_ν (uncalibrated)
λ(Å)
GAMA HI6563
XSHOOTER HI6563
GAMA HI4861
XSHOOTER HI4861
GAMA HI4340
XSHOOTER HI4340
eels02

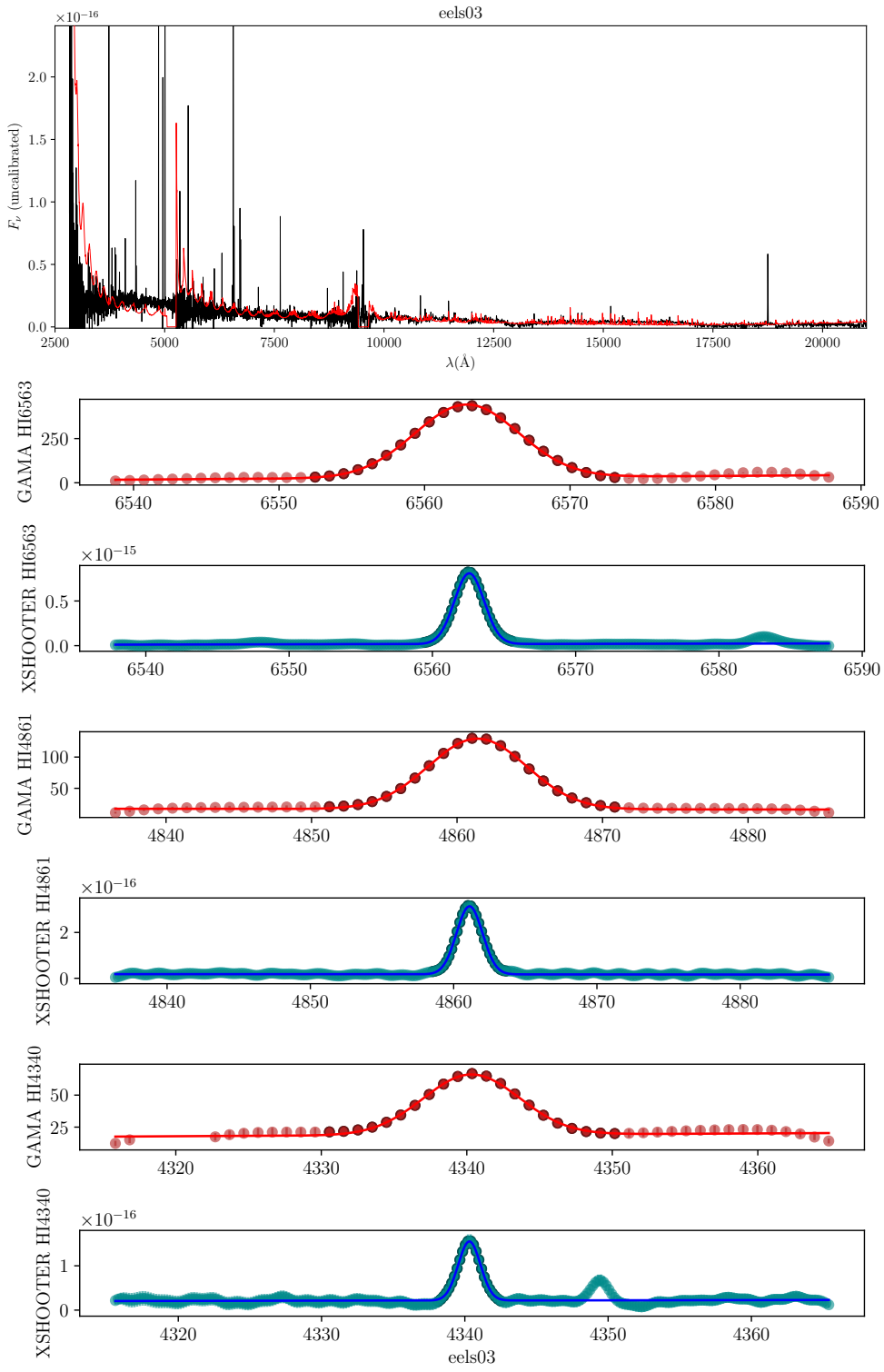
eels03
×10⁻¹⁶
F_ν (uncalibrated)
λ(Å)
GAMA HI6563
XSHOOTER HI6563
×10⁻¹⁵
GAMA HI4861
XSHOOTER HI4861
×10⁻¹⁶
GAMA HI4340
XSHOOTER HI4340
×10⁻¹⁶
eels03

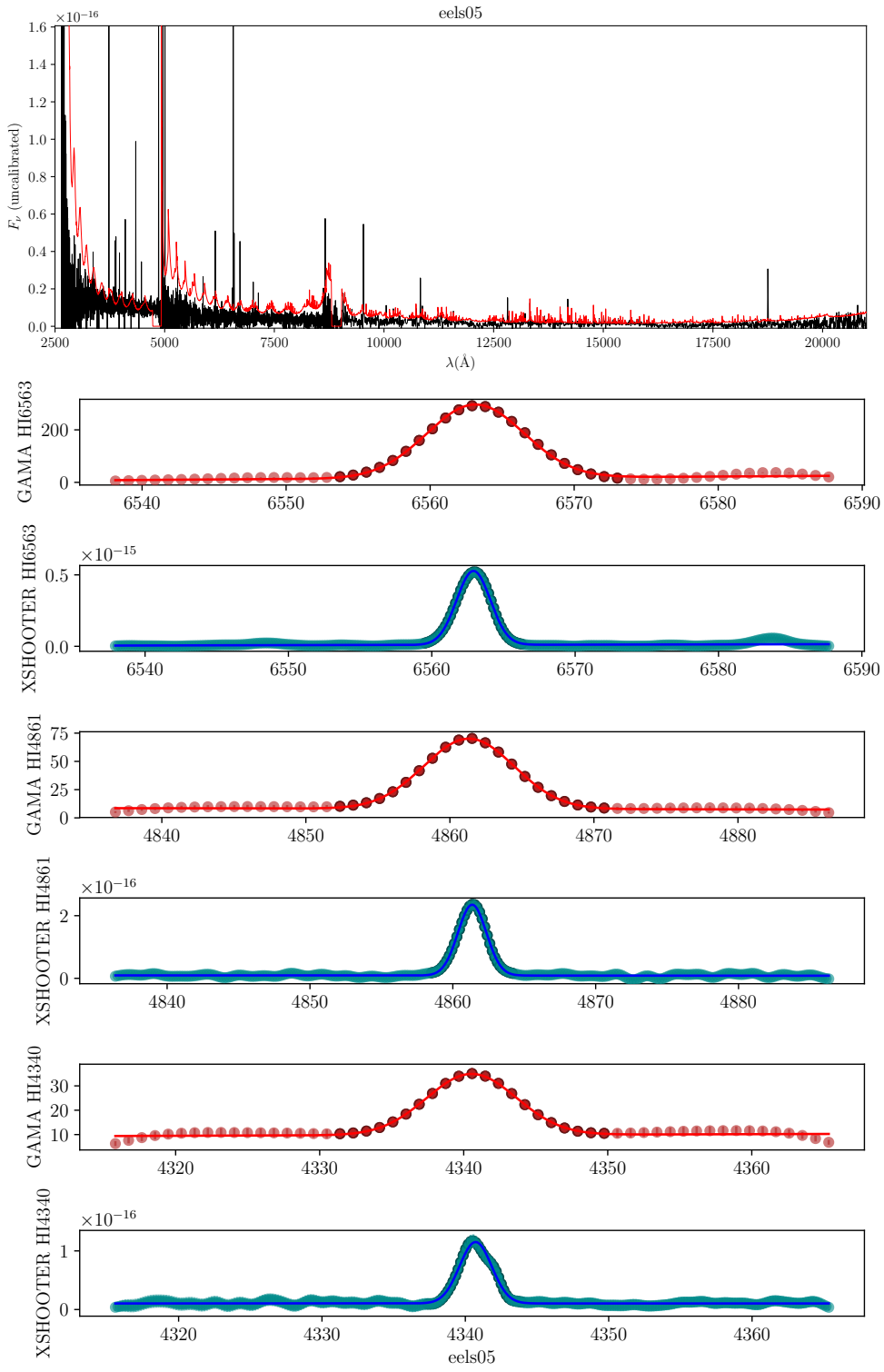
eels05
×10⁻¹⁶
F_ν (uncalibrated)
λ(Å)
GAMA HI6563
XSHOOTER HI6563
×10⁻¹⁵
GAMA HI4861
XSHOOTER HI4861
×10⁻¹⁶
GAMA HI4340
XSHOOTER HI4340
×10⁻¹⁶
eels05

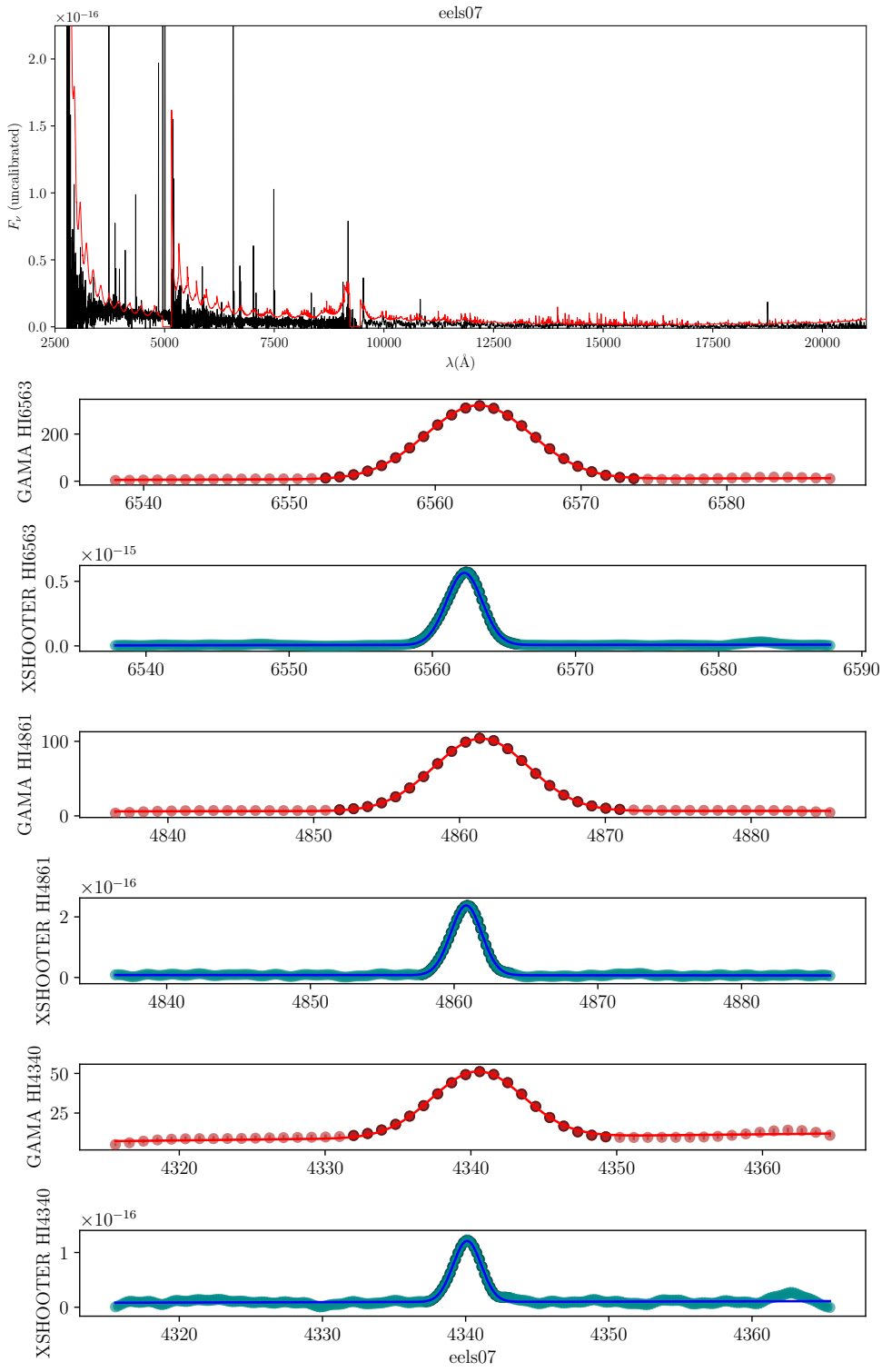
eels07
×10⁻¹⁶
F_ν (uncalibrated)
λ(Å)
GAMA HI6563
XSHOOTER HI6563
×10⁻¹⁵
GAMA HI4861
XSHOOTER HI4861
×10⁻¹⁶
GAMA HI4340
XSHOOTER HI4340
×10⁻¹⁶
eels07

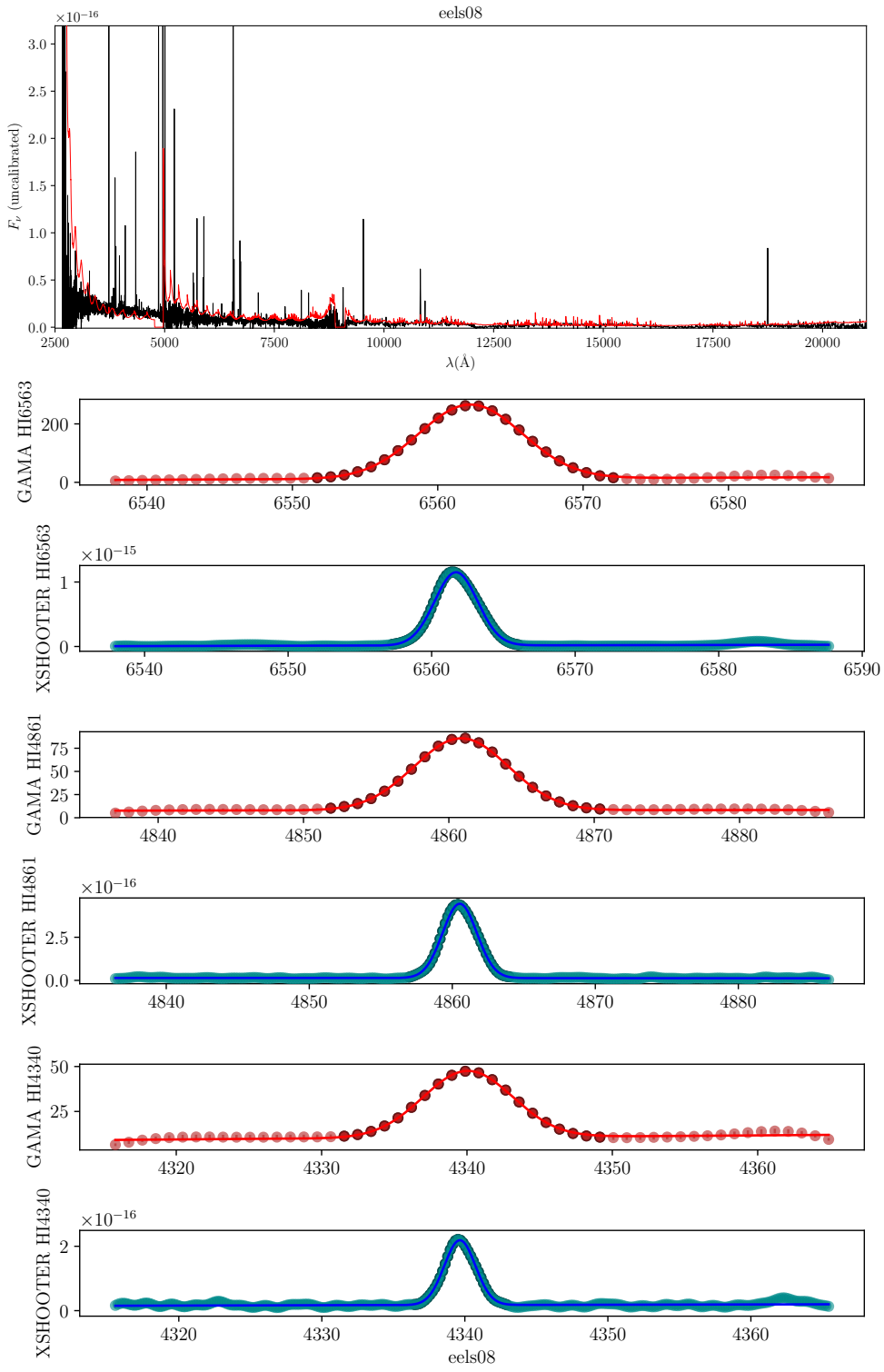
eels08
×10⁻¹⁶
F_ν (uncalibrated)
λ(Å)
GAMA HI6563
XSHOOTER HI6563
×10⁻¹⁵
GAMA HI4861
XSHOOTER HI4861
×10⁻¹⁶
GAMA HI4340
XSHOOTER HI4340
×10⁻¹⁶
eels08

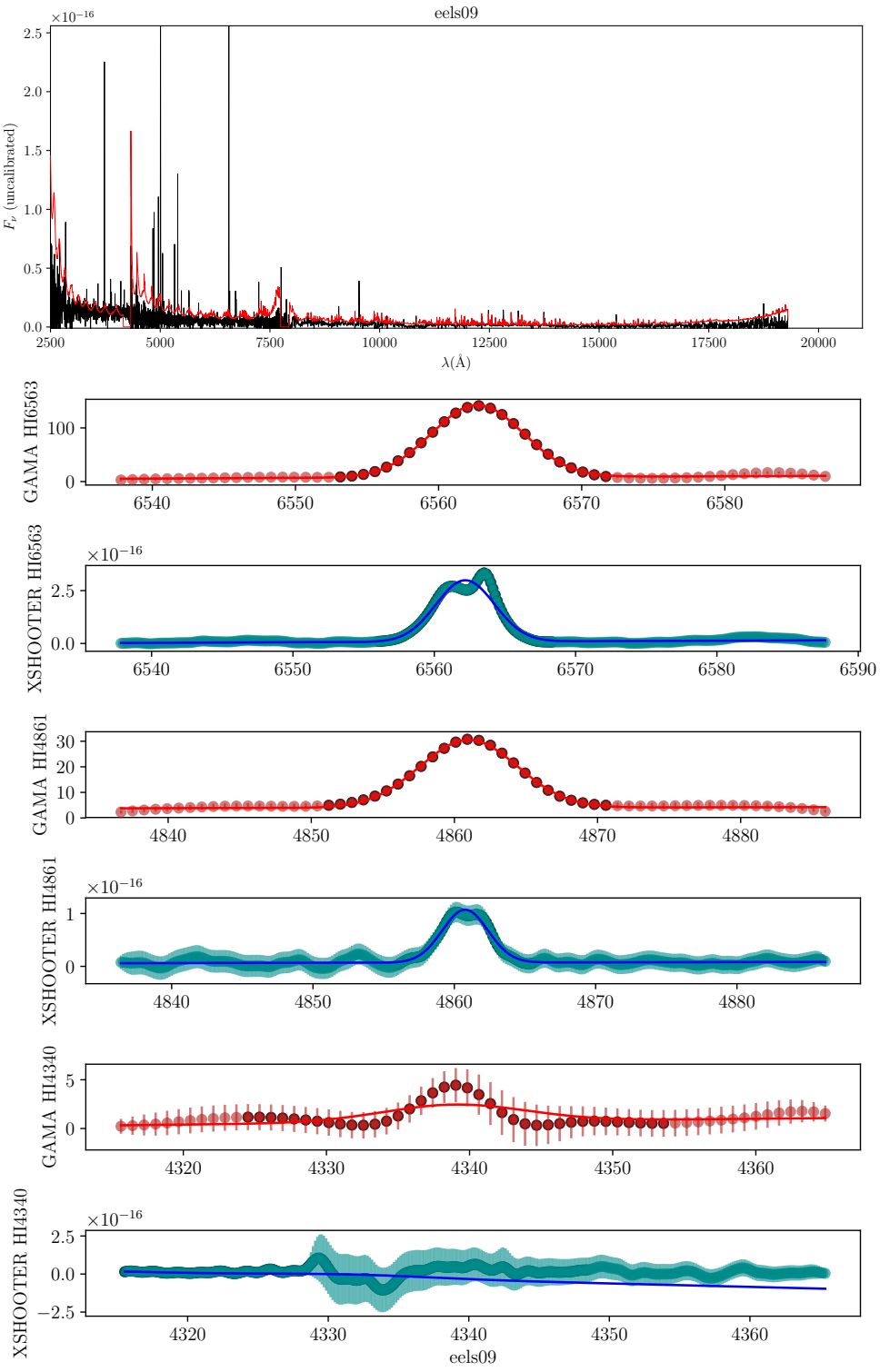
eels09
×10⁻¹⁶
F_ν (uncalibrated)
λ(Å)
GAMA HI6563
XSHOOTER HI6563
GAMA HI4861
XSHOOTER HI4861
GAMA HI4340
XSHOOTER HI4340
eels09

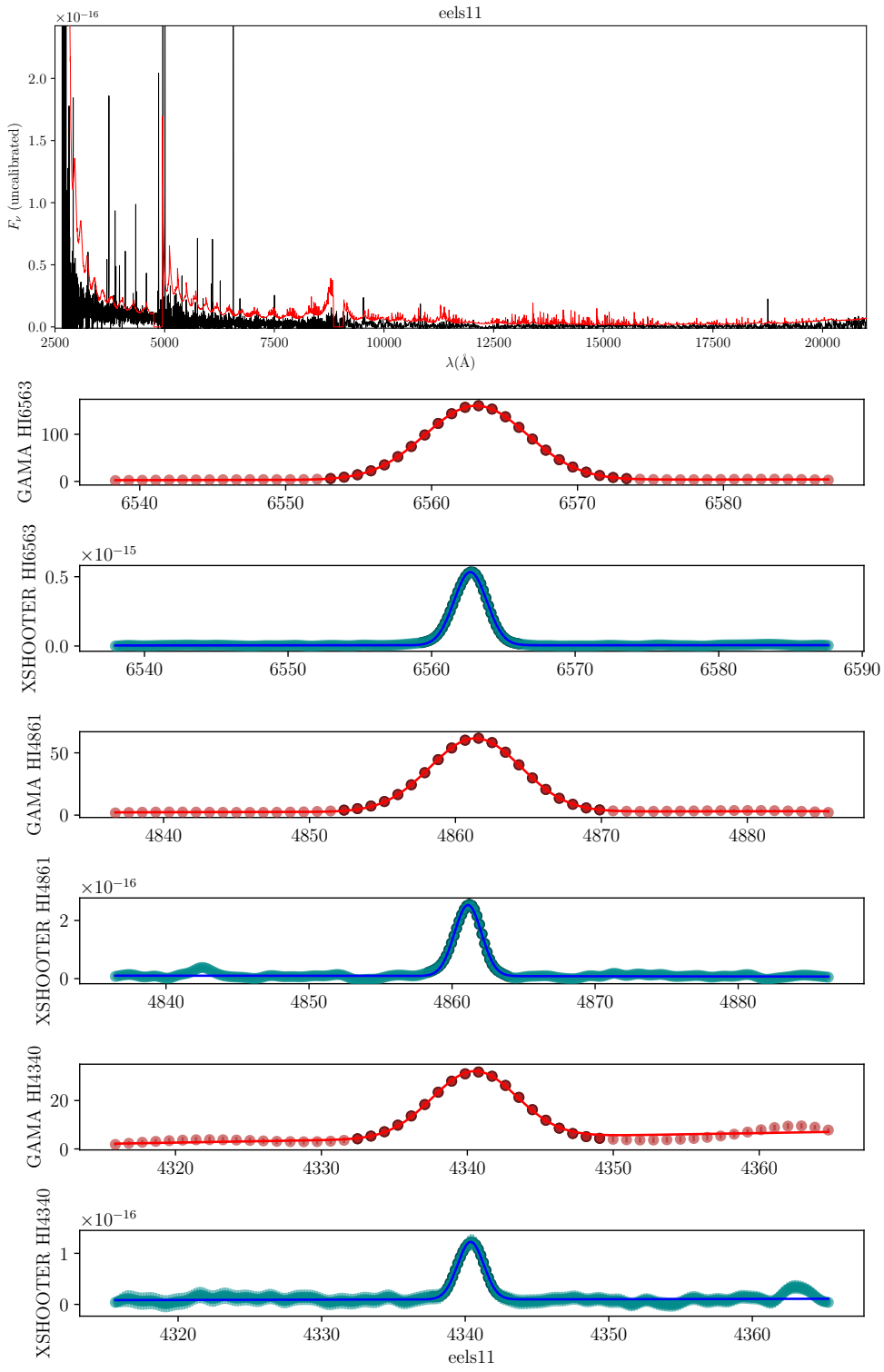
eels11
×10⁻¹⁶
F_ν (uncalibrated)
λ(Å)
GAMA HI6563
XSHOOTER HI6563
×10⁻¹⁵
GAMA HI4861
XSHOOTER HI4861
×10⁻¹⁶
GAMA HI4340
XSHOOTER HI4340
×10⁻¹⁶
eels11

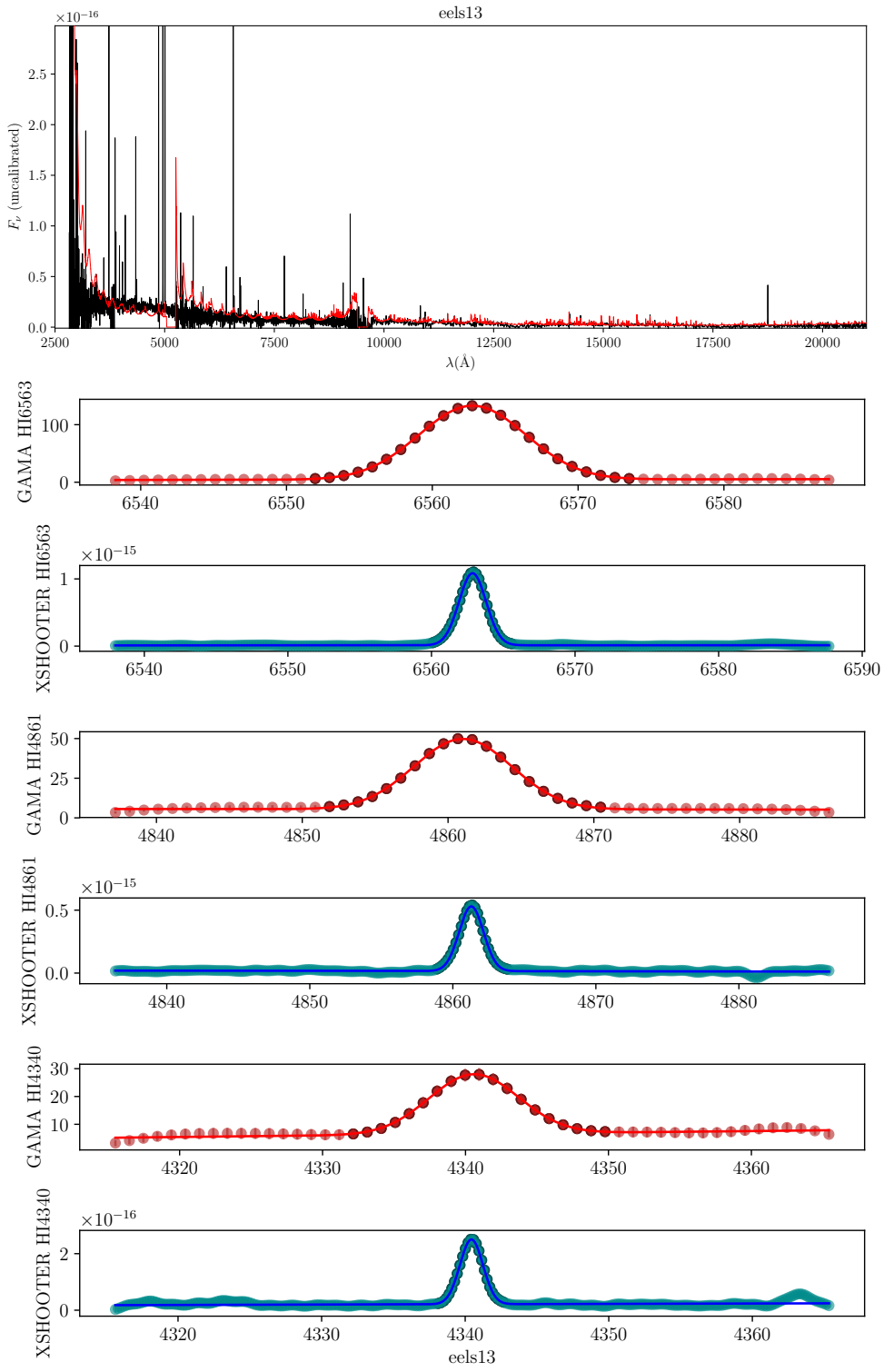
eels13
×10⁻¹⁶
F_ν (uncalibrated)
λ(Å)
GAMA HI6563
XSHOOTER HI6563
GAMA HI4861
XSHOOTER HI4861
GAMA HI4340
XSHOOTER HI4340
eels13

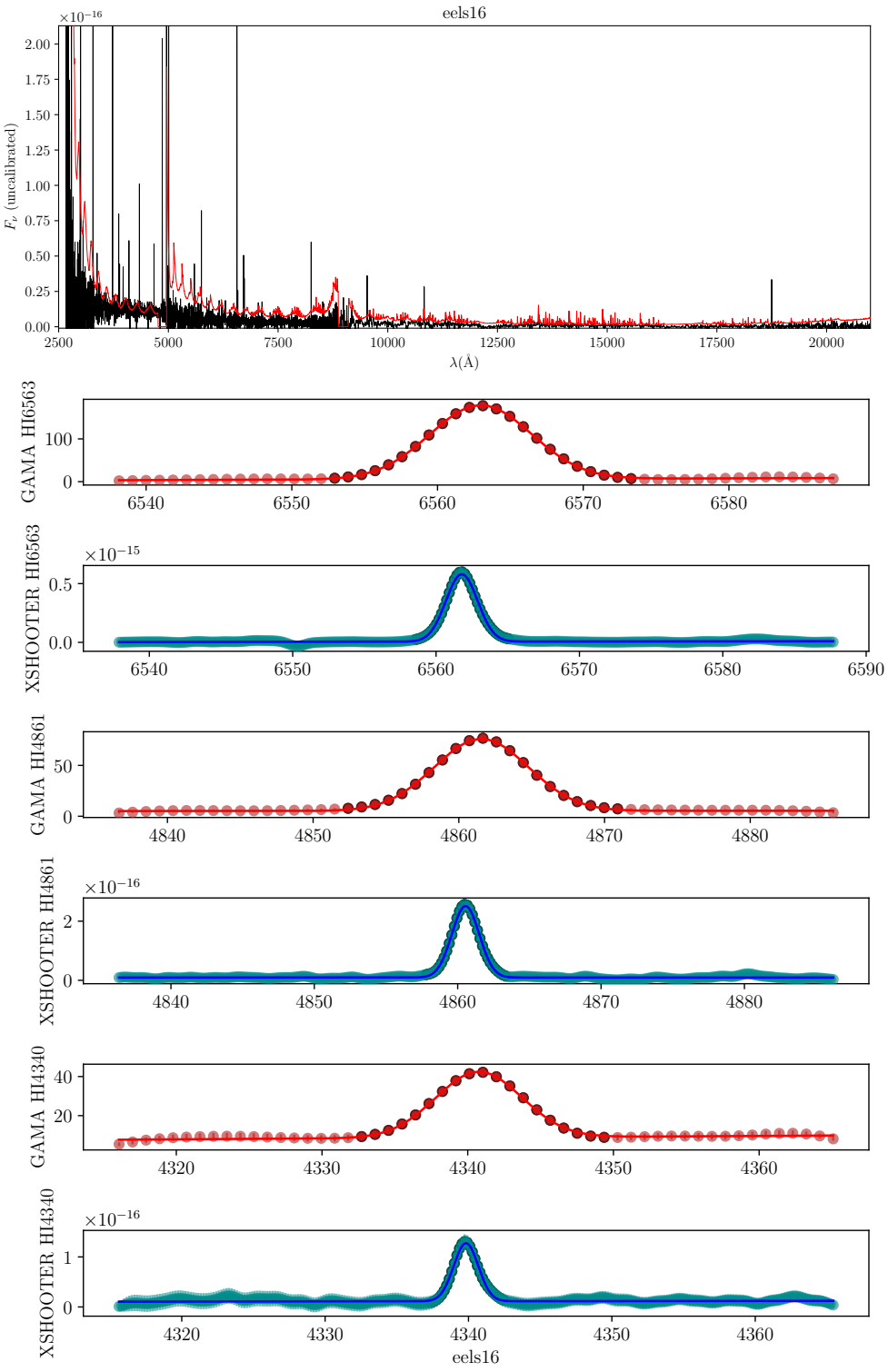
eels16
$\times 10^{-16}$
F_ν (uncalibrated)
λ(Å)
GAMA HI6563
XSHOOTER HI6563
$\times 10^{-15}$
GAMA HI4861
XSHOOTER HI4861
$\times 10^{-16}$
GAMA HI4340
XSHOOTER HI4340
$\times 10^{-16}$
eels16

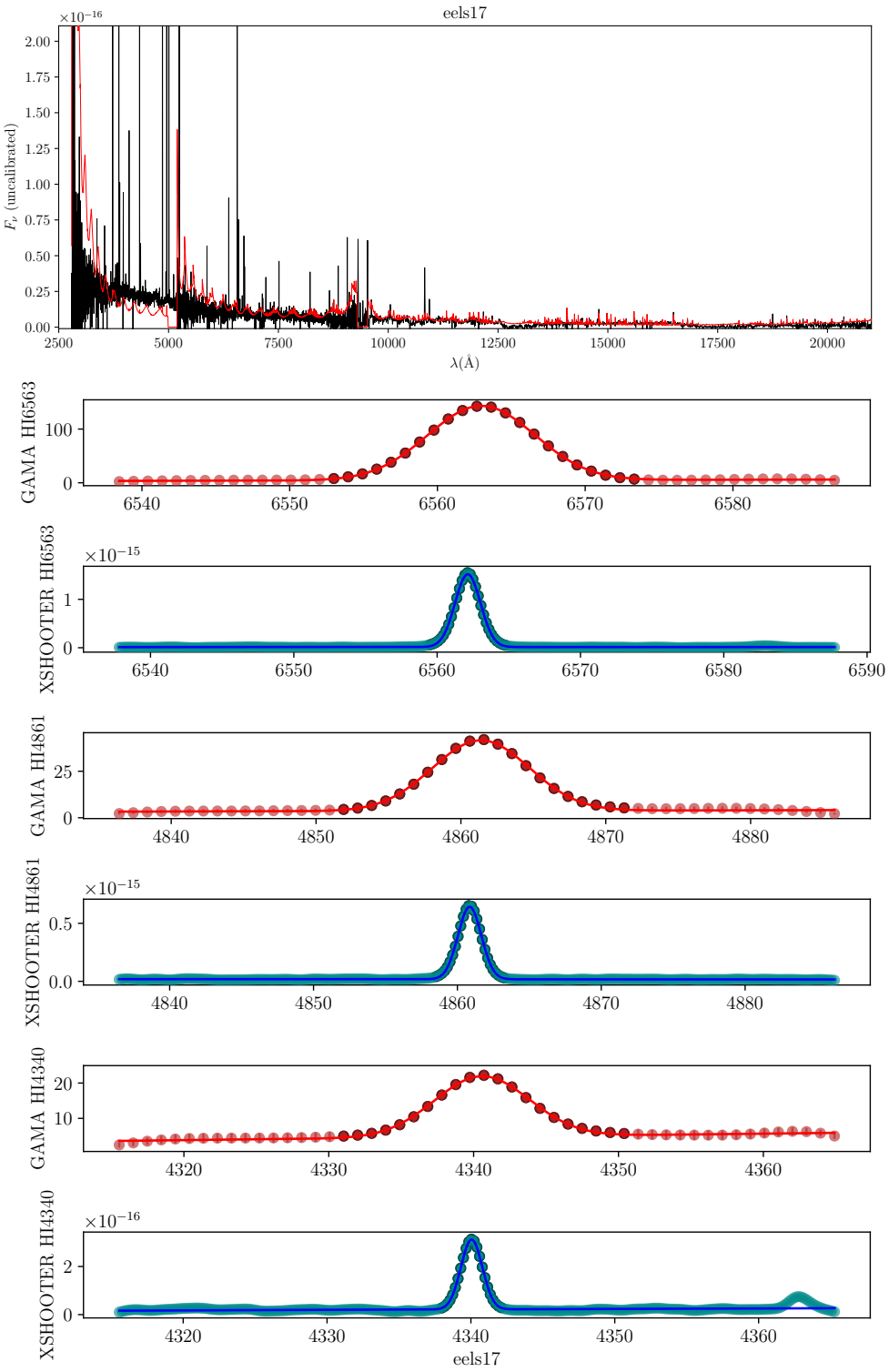
eels17
×10⁻¹⁶
F_ν (uncalibrated)
λ(Å)
GAMA HI6563
XSHOOTER HI6563
GAMA HI4861
XSHOOTER HI4861
GAMA HI4340
XSHOOTER HI4340
eels17

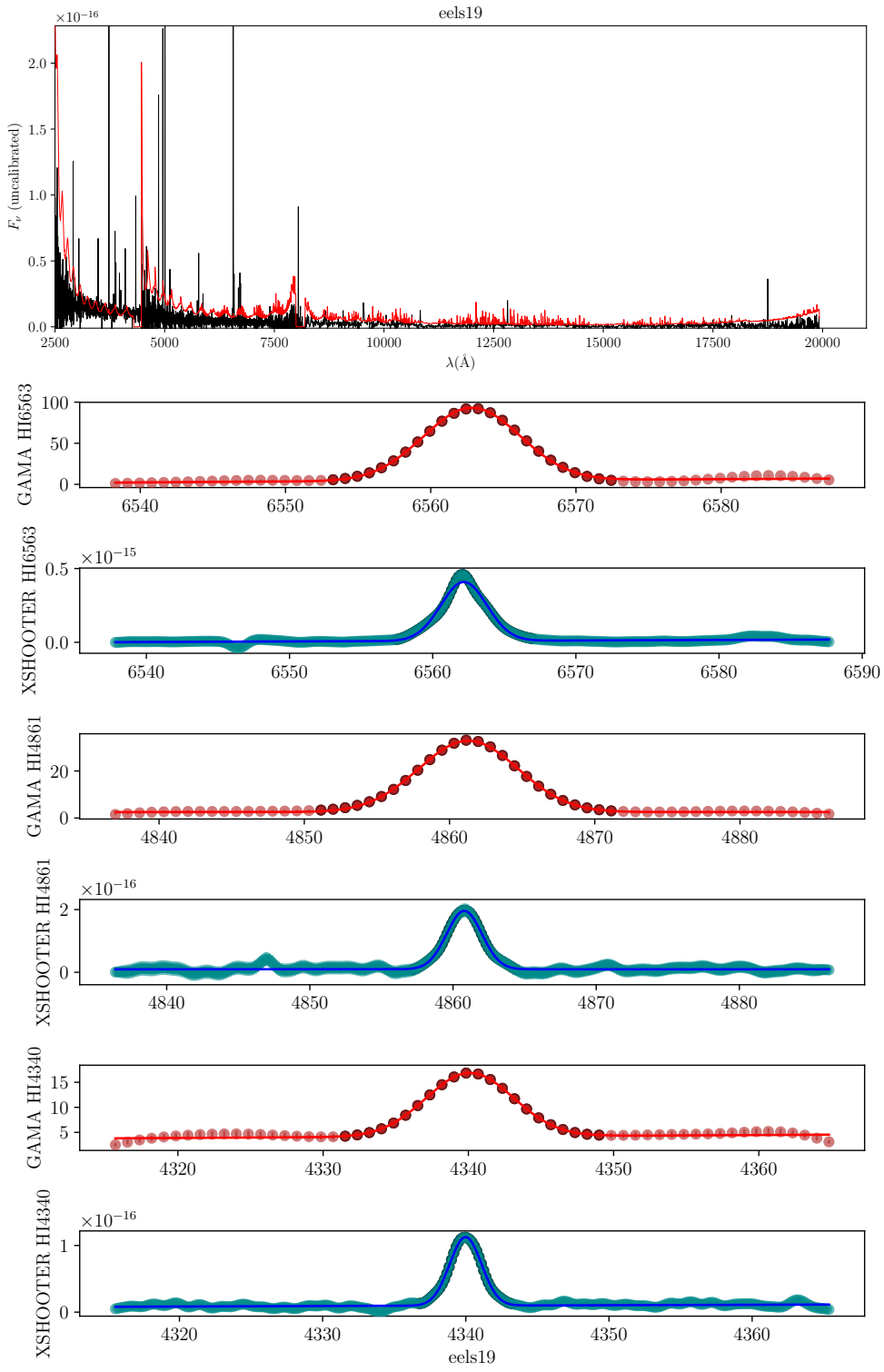
eels19
$\times 10^{-16}$
F_ν (uncalibrated)
λ(Å)
GAMA HI6563
XSHOOTER HI6563
$\times 10^{-15}$
GAMA HI4861
XSHOOTER HI4861
$\times 10^{-16}$
GAMA HI4340
XSHOOTER HI4340
$\times 10^{-16}$
eels19

Appendix C

SFH/Z Joint distribution plots

This appendix shows the joint distributions in age and metallicity of the BLUETIDES galaxies as described in section 4.5. On eac page are two figures, the top figure features the particle data binned directly, while the bottom figure is the analytic solution from equation 4.11. The central panel shows the joint 2-d distribution, while the right and top histograms show the metallicity distribution and the SFH respectively. Red dashed lines show the best fit for each marginalised distribution, and the green dashed line shows the best fir constant SFH for comparison.

Each plot is binned into 32 linearly uniform age bins stretching from $t = 0$ to $t = t_U$ where t_U is the age of the universe at the redshift of the galaxy, and 16 linearly uniform bins of metallicity stretching from $Z = -6$ to $Z = 0$.

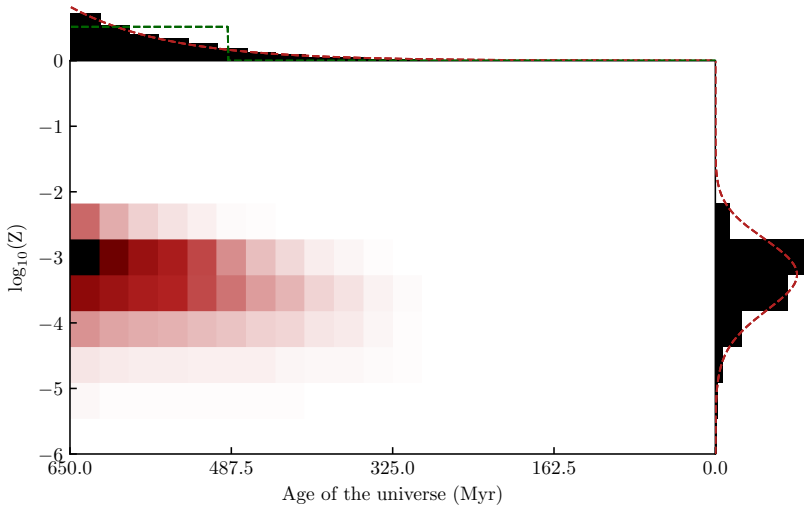

(a) Joint distribution from binned particle data

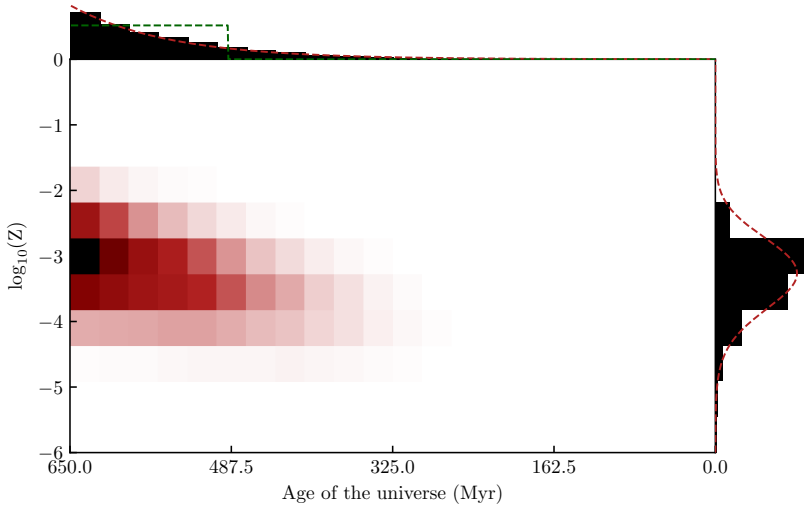

(b) Best fit joint distribution $\psi(t, Z)$

Figure C.1: Joint distributions in age and metallicity of the stack of BLUETIDESgalaxies with z=8 and $M/M_{\odot} < 10^8$.

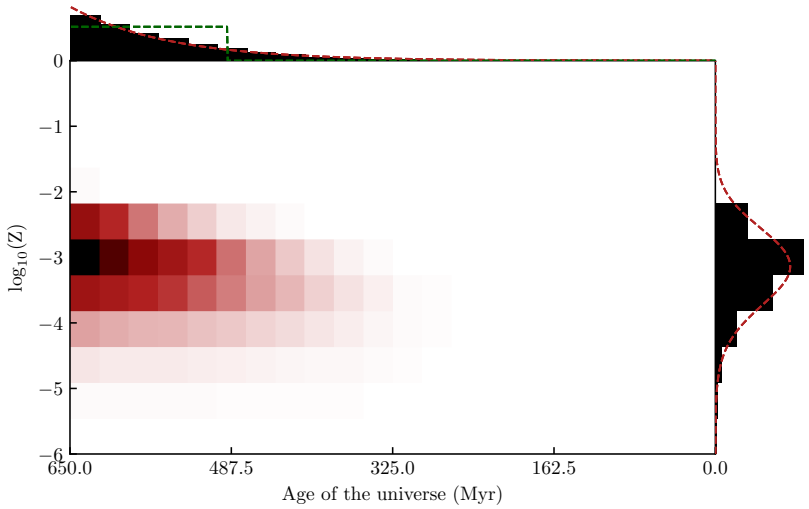

(a) Joint distribution from binned particle data

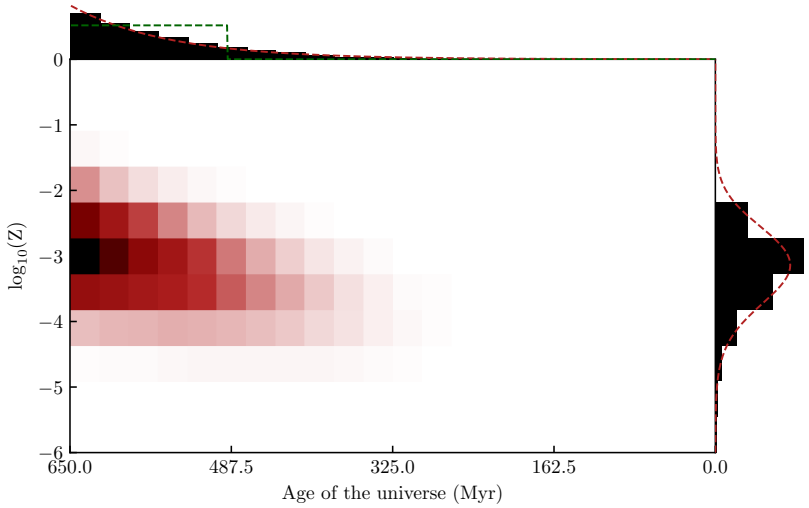

(b) Best fit joint distribution $\psi(t, Z)$

Figure C.2: Joint distributions in age and metallicity of the stack of BLUETIDESgalaxies with z=8 and $10^8 < M/M_\odot < 10^9$.

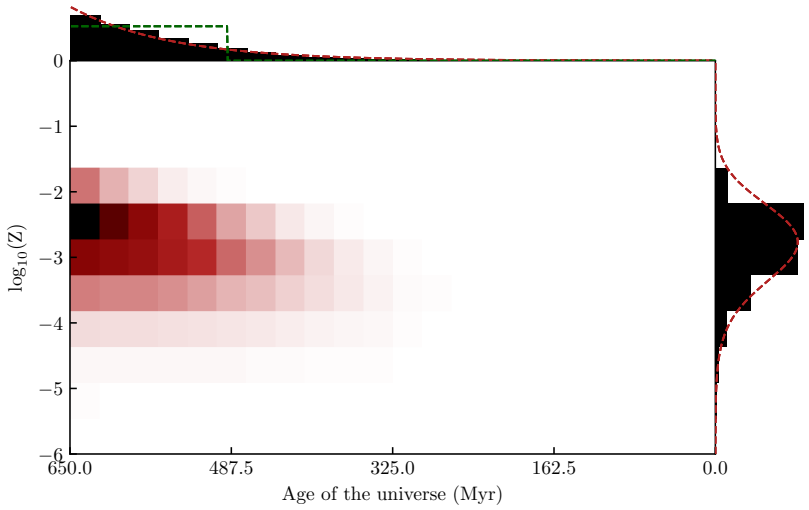

(a) Joint distribution from binned particle data

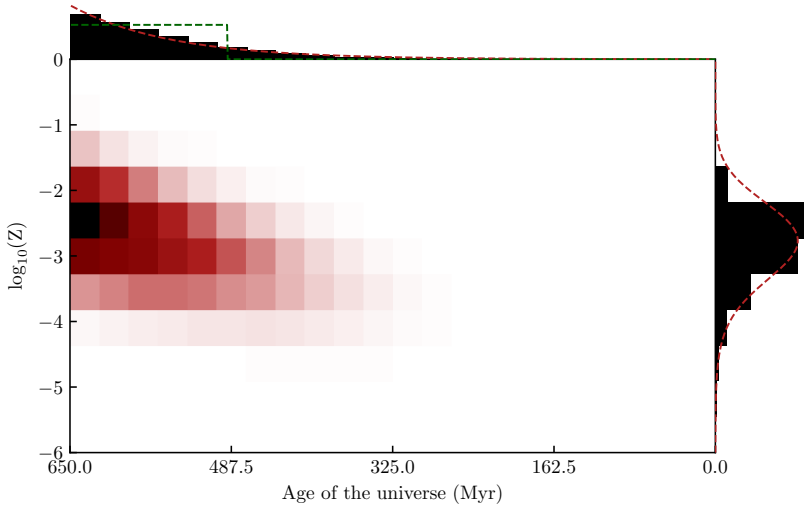

(b) Best fit joint distribution $\psi(t, Z)$

Figure C.3: Joint distributions in age and metallicity of the stack of BLUETIDESgalaxies with z=8 and $10^9 < M/M_\odot < 10^{10}$.

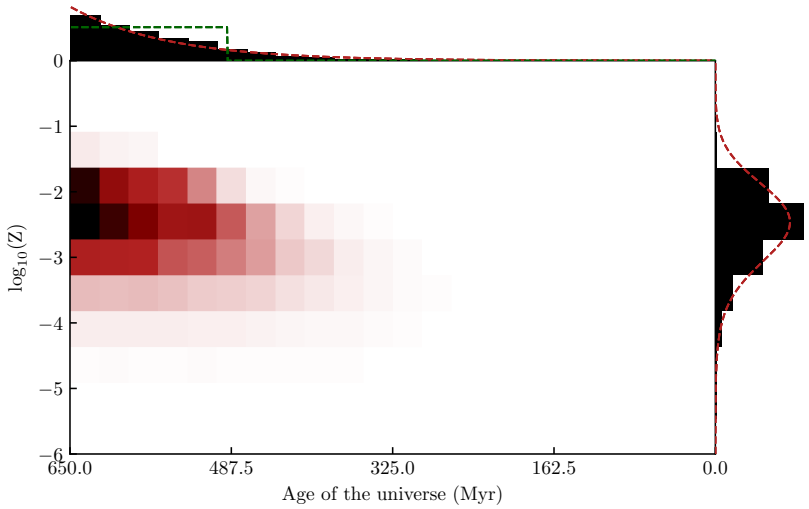

(a) Joint distribution from binned particle data

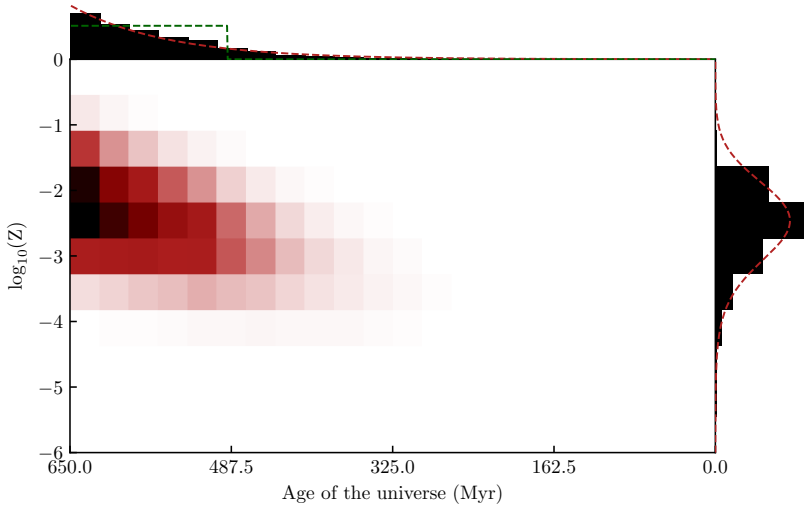

(b) Best fit joint distribution $\psi(t, Z)$

Figure C.4: Joint distributions in age and metallicity of the stack of BLUETIDESgalaxies with z=8 and $M/M_{\odot} > 10^{10}$.

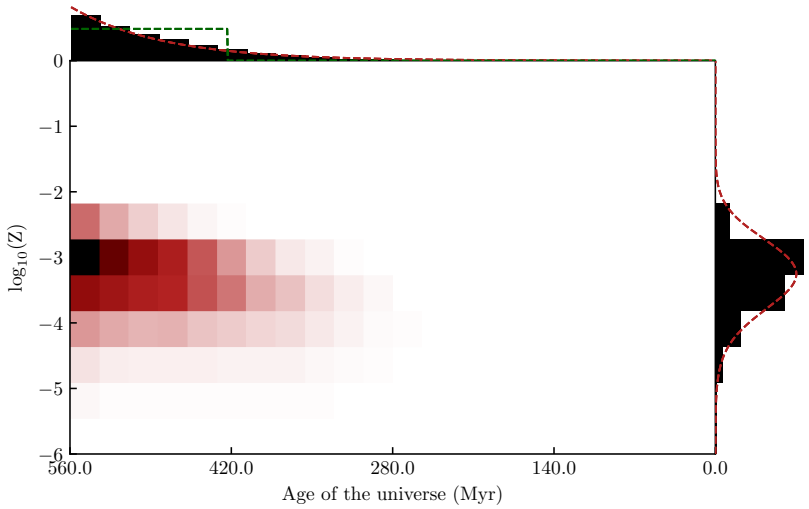

(a) Joint distribution from binned particle data

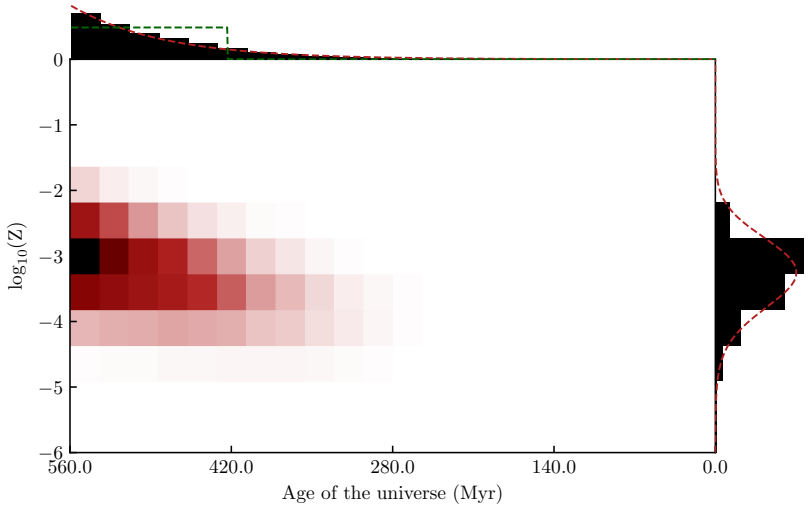

(b) Best fit joint distribution $\psi(t, Z)$

Figure C.5: Joint distributions in age and metallicity of the stack of BLUETIDESgalaxies with z=9 and $M/M_{\odot} < 10^8$.

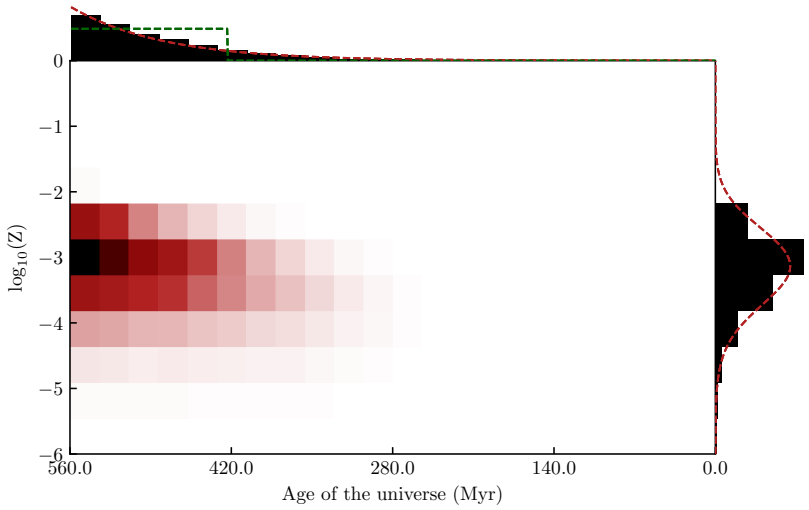

(a) Joint distribution from binned particle data

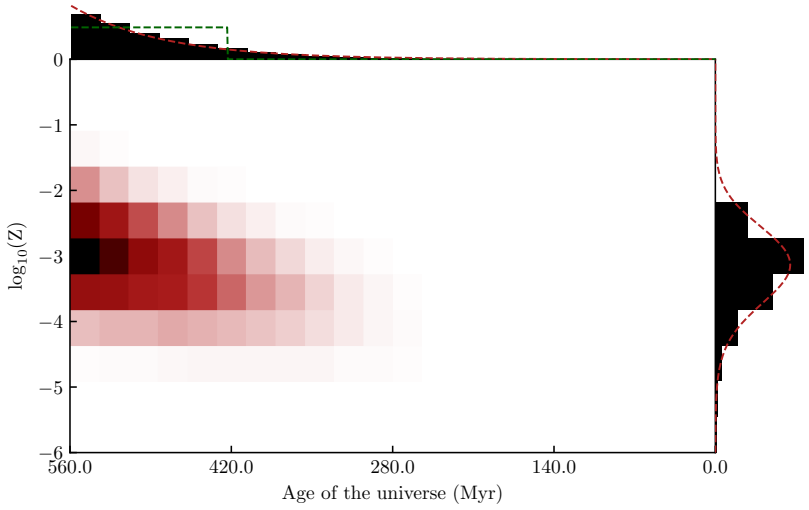

(b) Best fit joint distribution $\psi(t, Z)$

Figure C.6: Joint distributions in age and metallicity of the stack of BLUETIDESgalaxies with z=9 and $10^8 < M/M_\odot < 10^9$.

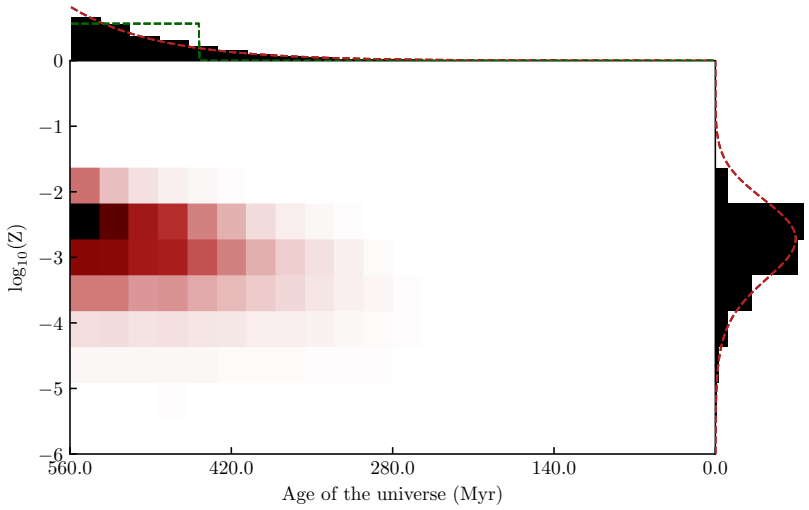

(a) Joint distribution from binned particle data

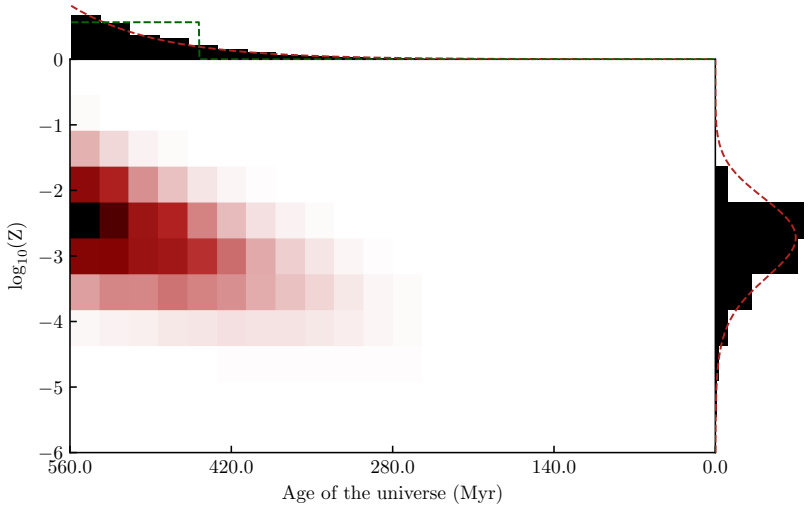

(b) Best fit joint distribution $\psi(t, Z)$

Figure C.7: Joint distributions in age and metallicity of the stack of BLUETIDESgalaxies with z=9 and $10^9 < M/M_\odot < 10^{10}$.

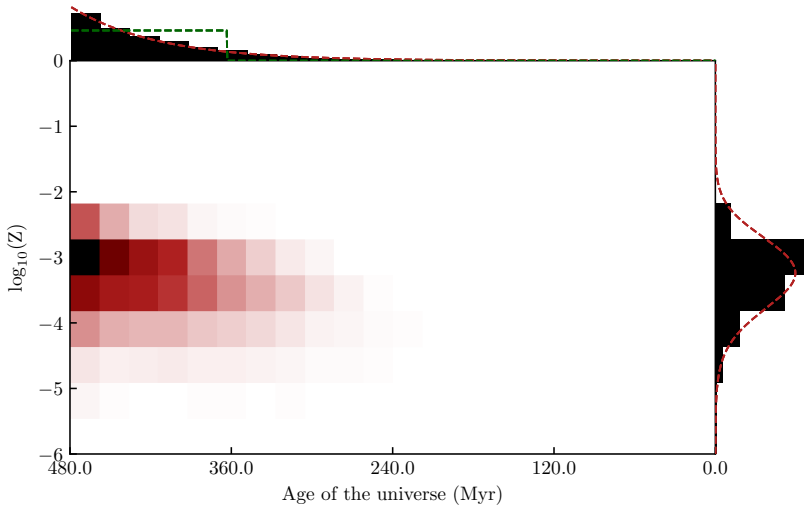

(a) Joint distribution from binned particle data

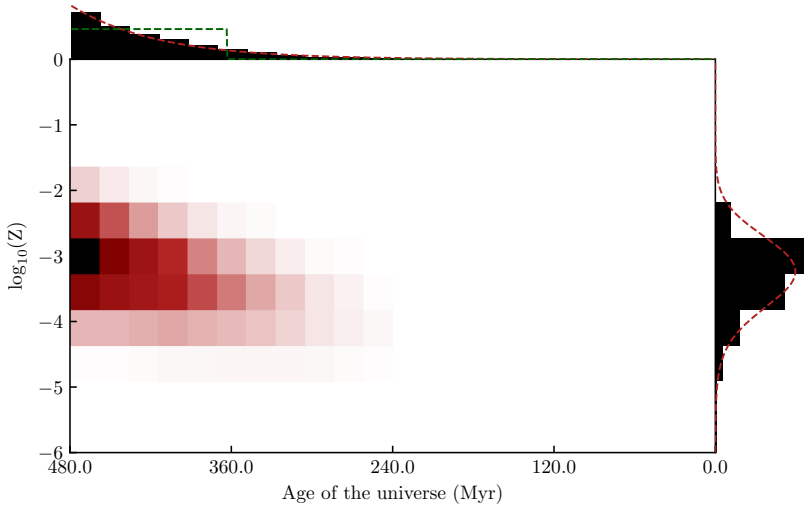

(b) Best fit joint distribution $\psi(t, Z)$

Figure C.8: Joint distributions in age and metallicity of the stack of BLUETIDESgalaxies with z=10 and $M/M_{\odot} < 10^8$.

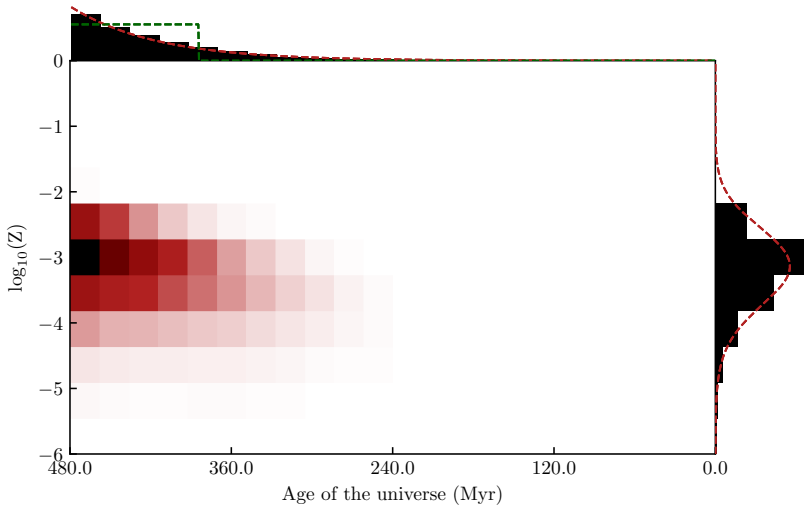

(a) Joint distribution from binned particle data

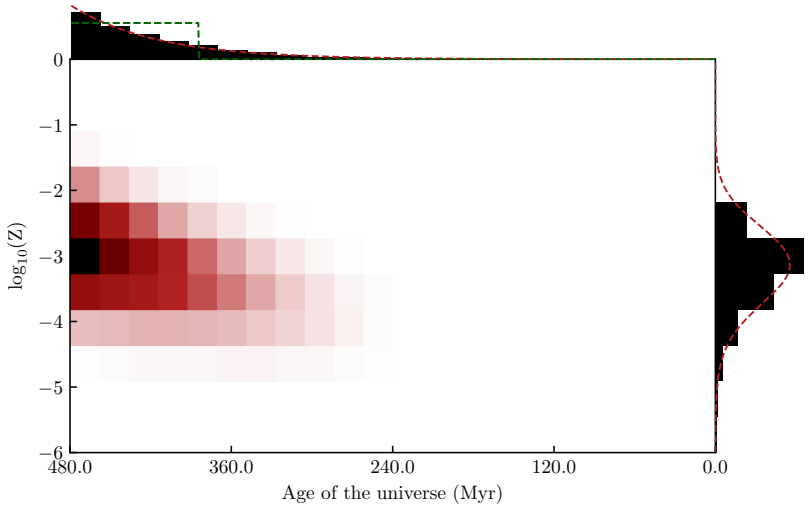

(b) Best fit joint distribution $\psi(t, Z)$

Figure C.9: Joint distributions in age and metallicity of the stack of BLUETIDESgalaxies with z=10 and $10^8 < M/M_\odot < 10^9$.

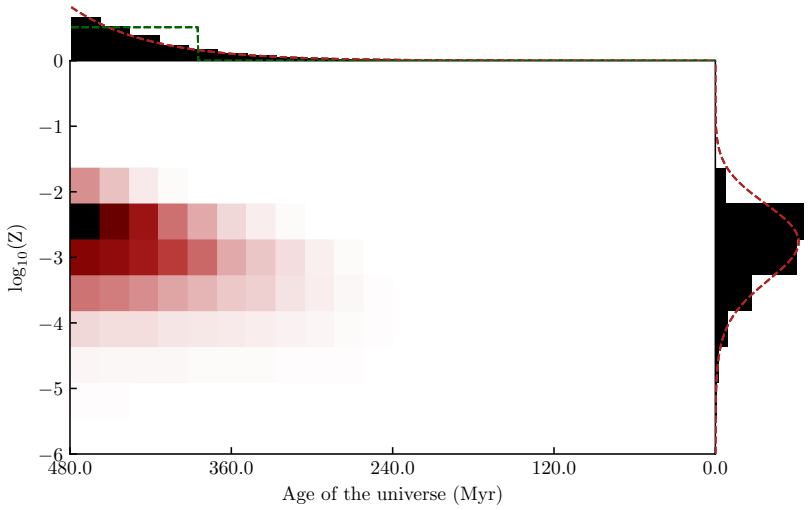

(a) Joint distribution from binned particle data

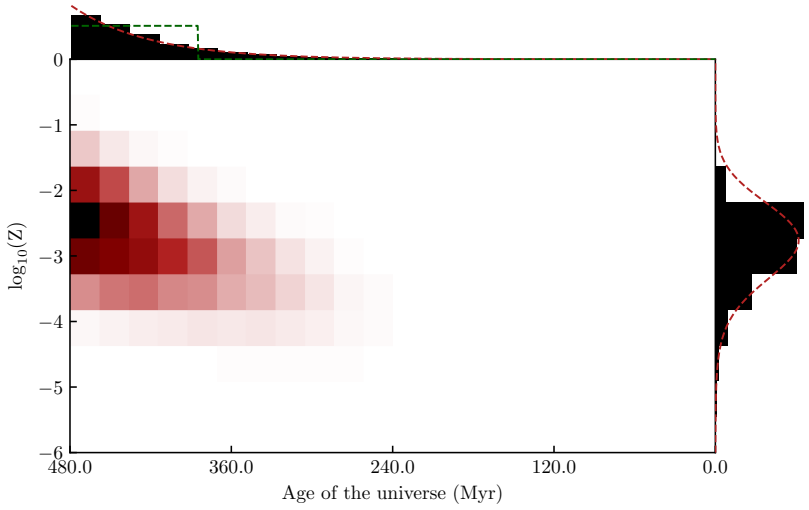

(b) Best fit joint distribution $\psi(t, Z)$

Figure C.10: Joint distributions in age and metallicity of the stack of BLUETIDESgalaxies with z=10 and $10^9 < M/M_\odot < 10^{10}$.

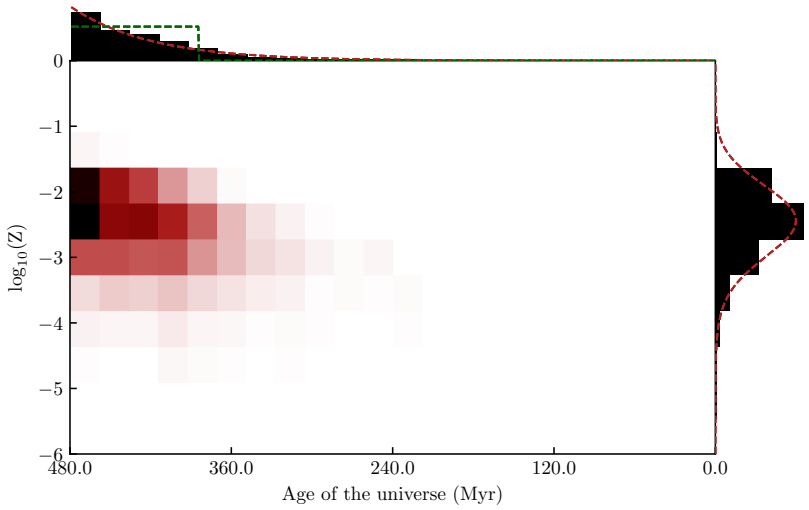

(a) Joint distribution from binned particle data

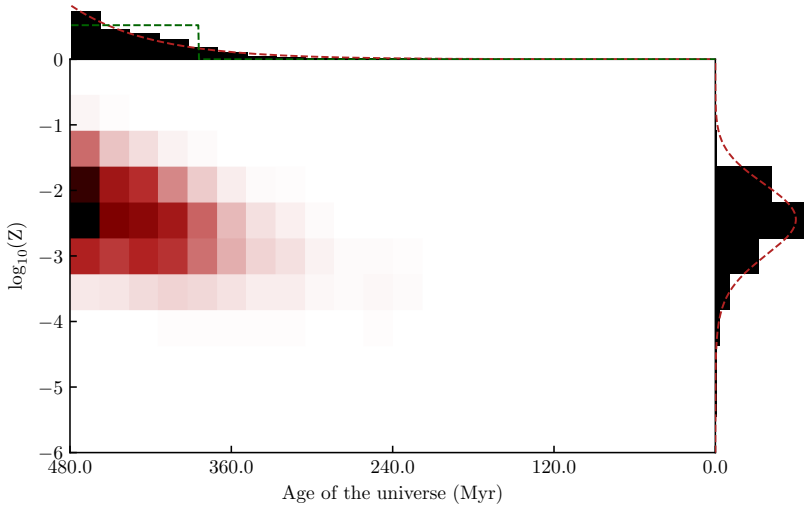

(b) Best fit joint distribution $\psi(t, Z)$

Figure C.11: Joint distributions in age and metallicity of the stack of BLUETIDESgalaxies with z=10 and $M/M_{\odot} > 10^{10}$.

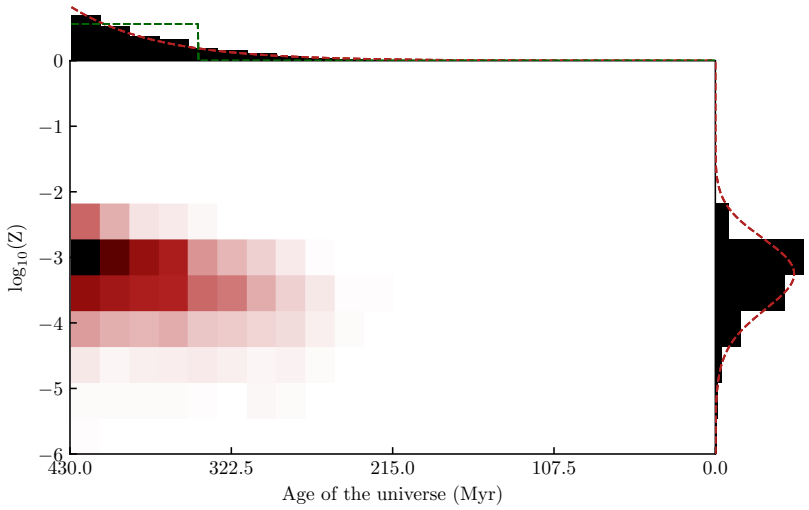

(a) Joint distribution from binned particle data

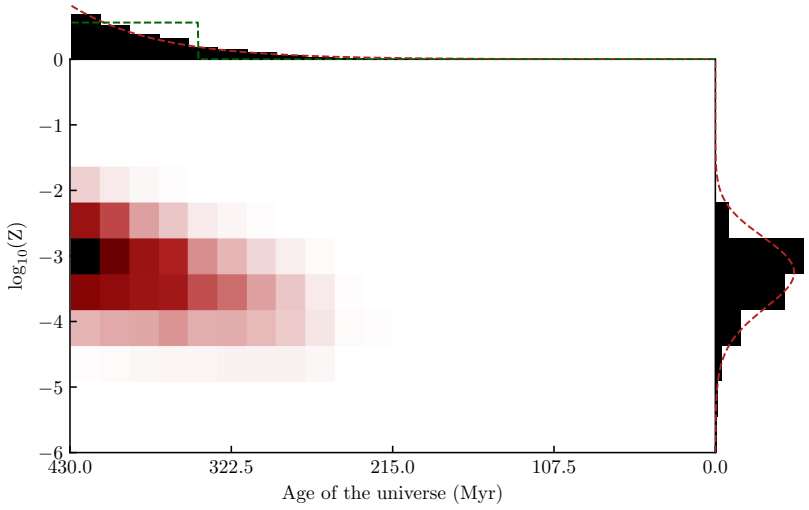

(b) Best fit joint distribution $\psi(t, Z)$

Figure C.12: Joint distributions in age and metallicity of the stack of BLUETIDESgalaxies with z=11 and $M/M_{\odot} < 10^8$.

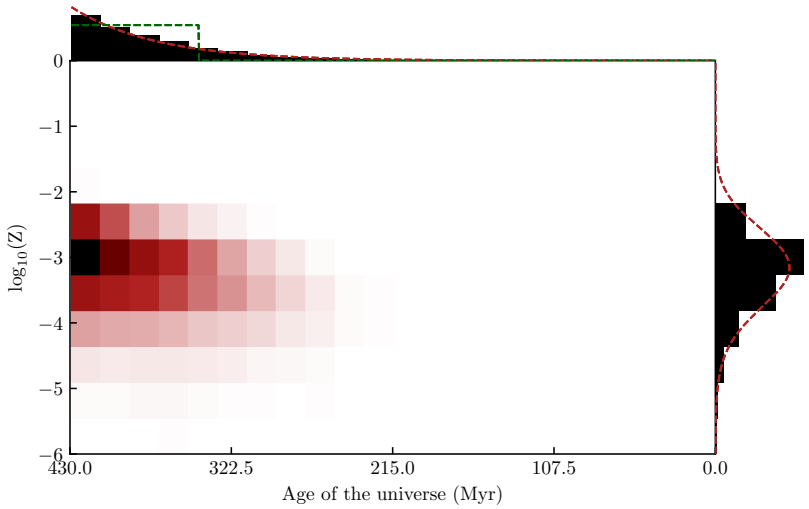

(a) Joint distribution from binned particle data

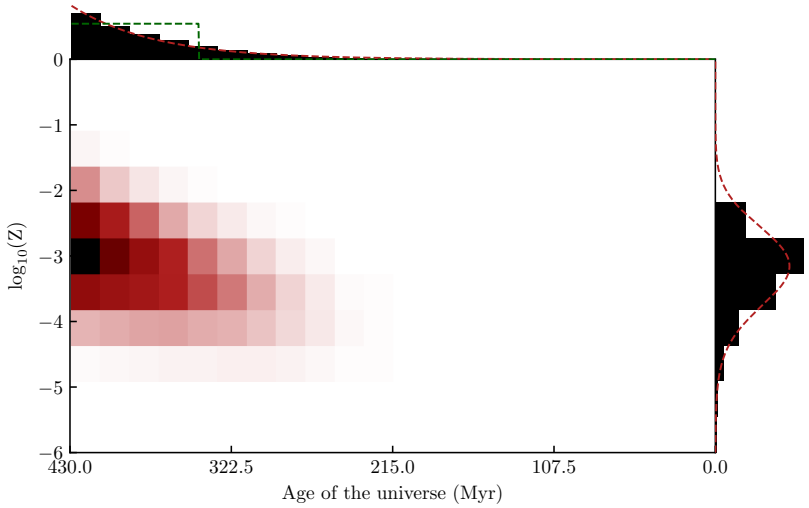

(b) Best fit joint distribution $\psi(t, Z)$

Figure C.13: Joint distributions in age and metallicity of the stack of BLUETIDESgalaxies with z=11 and $10^8 < M/M_\odot < 10^9$.

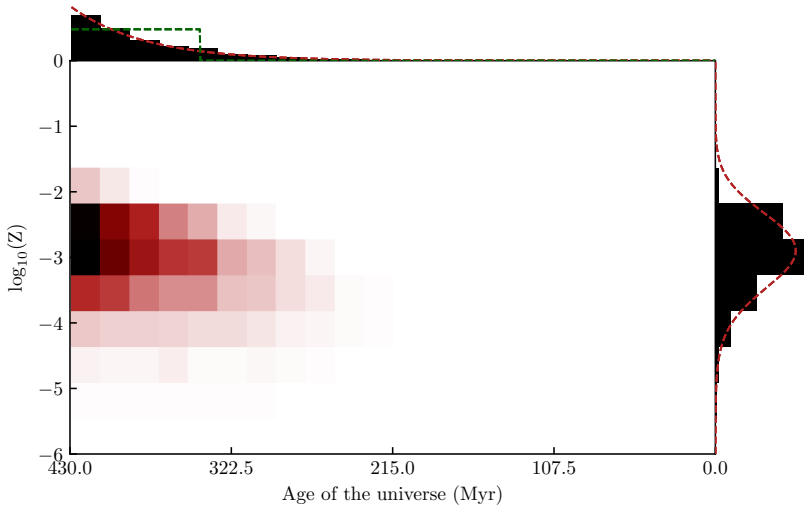

(a) Joint distribution from binned particle data

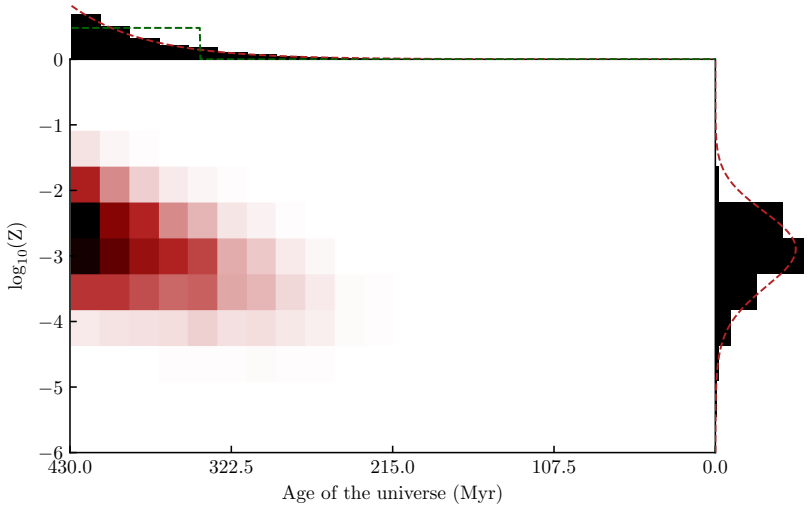

(b) Best fit joint distribution $\psi(t, Z)$

Figure C.14: Joint distributions in age and metallicity of the stack of BLUETIDESgalaxies with z=11 and $10^9 < M/M_\odot < 10^{10}$.

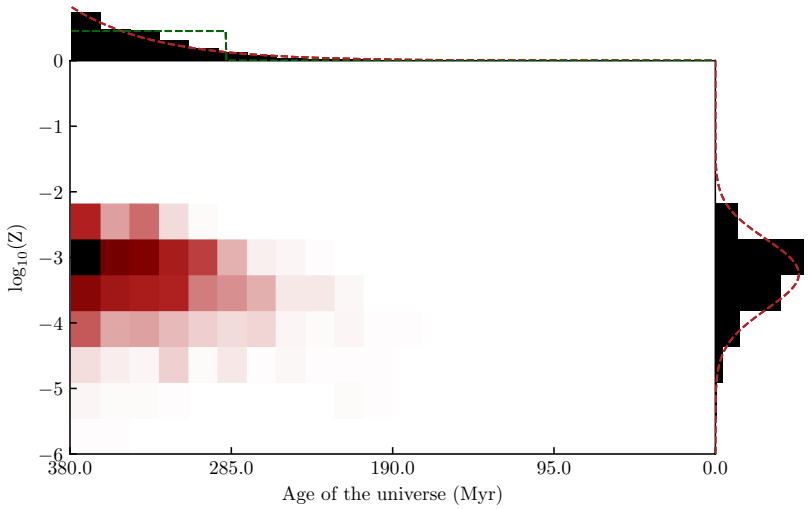

(a) Joint distribution from binned particle data

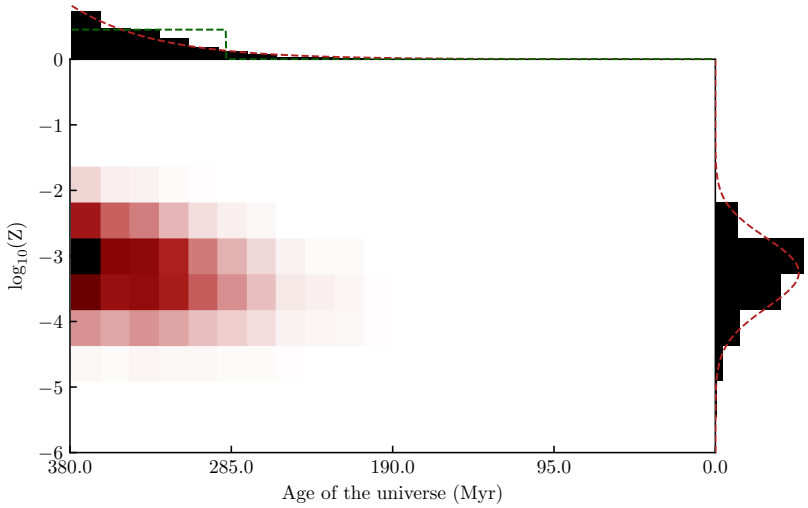

(b) Best fit joint distribution $\psi(t, Z)$

Figure C.15: Joint distributions in age and metallicity of the stack of BLUETIDESgalaxies with z=12 and $M/M_{\odot} < 10^8$.

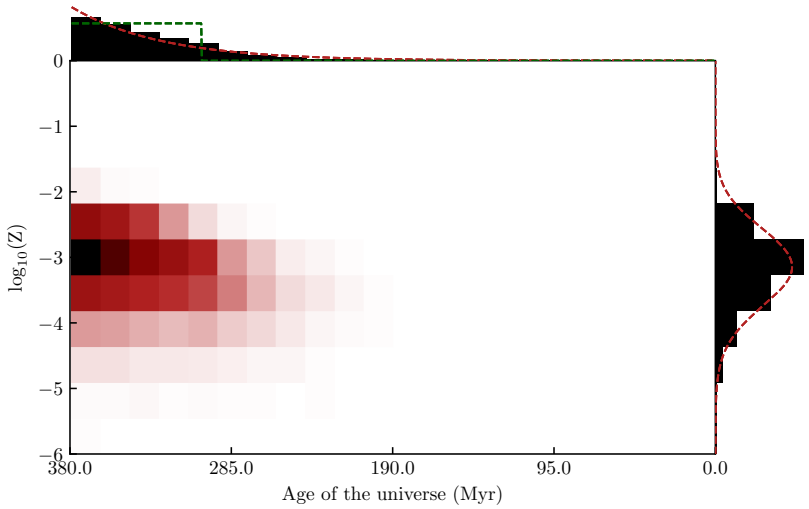

(a) Joint distribution from binned particle data

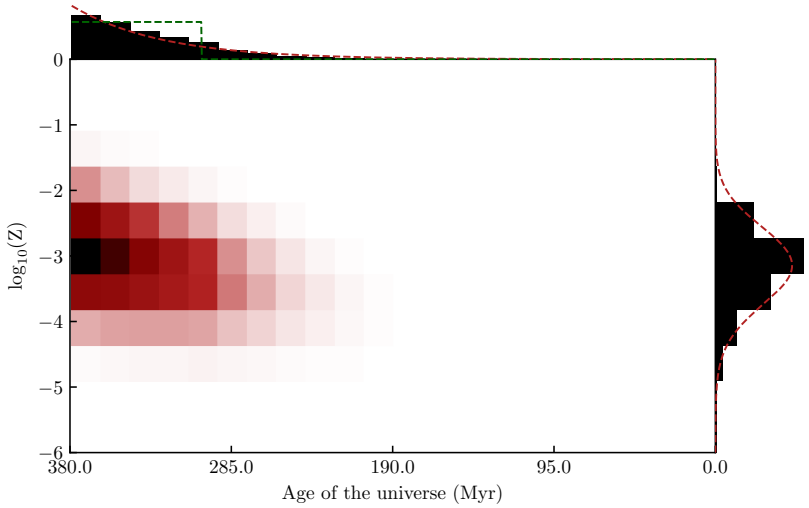

(b) Best fit joint distribution $\psi(t, Z)$

Figure C.16: Joint distributions in age and metallicity of the stack of BLUETIDESgalaxies with z=12 and $10^8 < M/M_\odot < 10^9$.

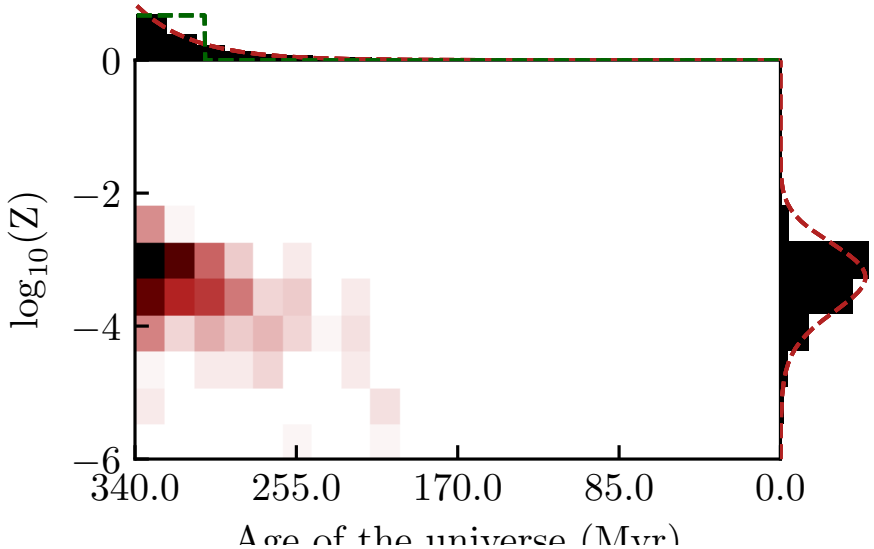

(a) Joint distribution from binned particle data

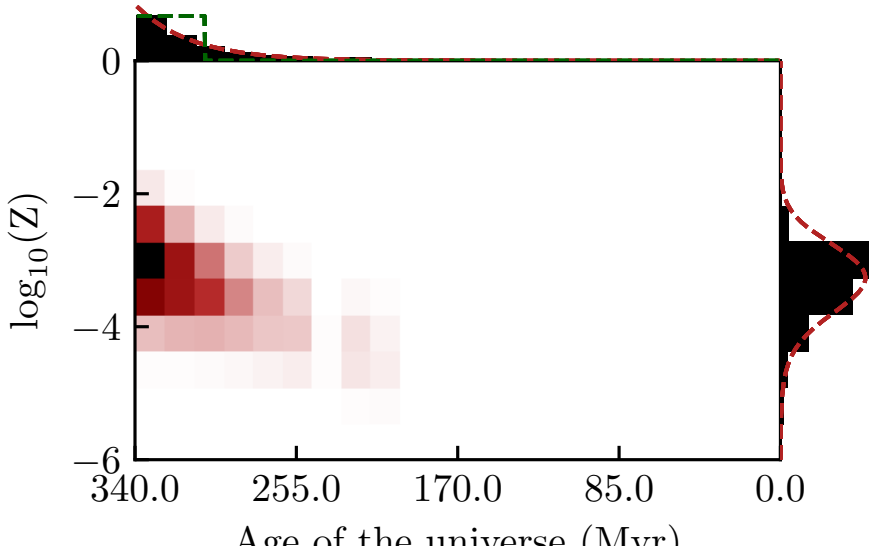

(b) Best fit joint distribution $\psi(t, Z)$

Figure C.17: Joint distributions in age and metallicity of the stack of BLUETIDESgalaxies with z=13 and $M/M_{\odot} < 10^8$.

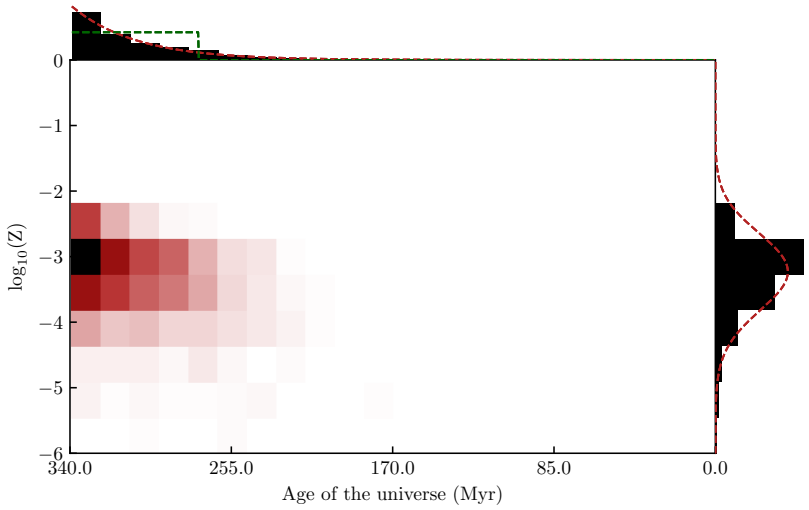

(a) Joint distribution from binned particle data

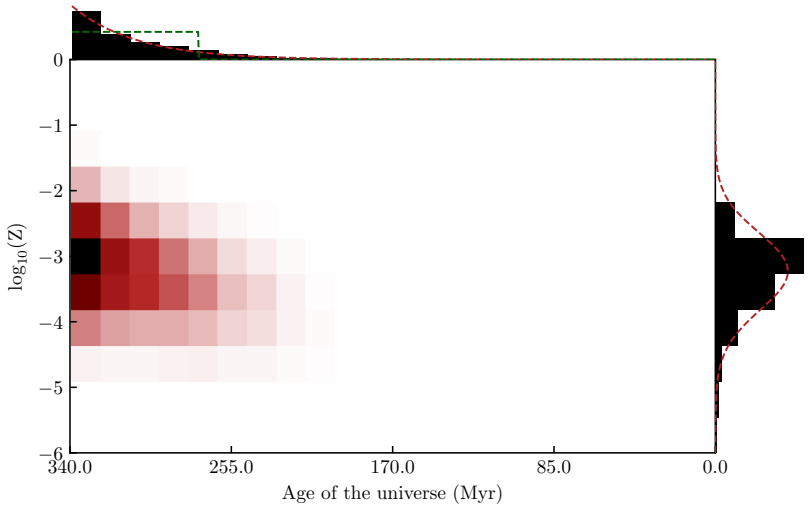

(b) Best fit joint distribution $\psi(t, Z)$

Figure C.18: Joint distributions in age and metallicity of the stack of BLUETIDESgalaxies with z=13 and $10^8 < M/M_\odot < 10^9$.

References

T. M. C. Abbott, F. B. Abdalla, S. Allam, A. Amara, J. Annis, and et al. The Dark Energy Survey: Data Release 1. *The Astrophysical Journal Supplement Series*, 239(2):18, December 2018.

C. Alcock, R. A. Allsman, D. R. Alves, T. S. Axelrod, A. C. Becker, D. P. Bennett, K. H. Cook, N. Dalal, A. J. Drake, K. C. Freeman, M. Geha, K. Griest, M. J. Lehner, S. L. Marshall, D. Minniti, C. A. Nelson, B. A. Peterson, P. Popowski, M. R. Pratt, P. J. Quinn, C. W. Stubbs, W. Sutherland, A. B. Tomaney, T. Vandehei, and D. Welch. The MACHO Project: Microlensing Results from 5.7 Years of Large Magellanic Cloud Observations. *The Astrophysical Journal*, 542(1):281–307, October 2000.

A. Aloisi, G. Clementini, M. Tosi, F. Annibali, R. Contreras, G. Fiorentino, J. Mack, M. Marconi, I. Musella, A. Saha, M. Sirianni, and R. P. van der Marel. I Zw 18 Revisited with HST ACS and Cepheids: New Distance and Age. *The Astrophysical Journal*, 667(2):L151–L154, October 2007.

E. Aprile, J. Aalbers, F. Agostini, M. Alfonsi, L. Althueser, F. D. Amaro, M. Anthony, F. Arneodo, L. Baudis, B. Bauermeister, M. L. Benabderrahmane, T. Berger, P. A. Breur, A. Brown, A. Brown, E. Brown, S. Bruenner, G. Bruno, R. Budnik, C. Capelli, J. M. R. Cardoso, D. Cichon, D. Coderre, A. P. Colijn, J. Conrad, J. P. Cussonneau, M. P. Decowski, P. de Perio, P. di Gangi, A. di Giovanni, S. Diglio, A. Elykov, G. Eurin, J. Fei, A. D. Ferella, A. Fieguth, W. Fulgione, A. Gallo Rosso, M. Galloway, F. Gao, M. Garbini, C. Geis, L. Grandi, Z. Greene, H. Qiu, C. Hasterok, E. Hogenbirk, J. Howlett, R. Itay, F. Joerg, B. Kaminsky, S. Kazama, A. Kish, G. Koltman, H. Landsman, R. F.

Lang, L. Levinson, Q. Lin, S. Lindemann, M. Lindner, F. Lombardi, J. A. M. Lopes, J. Mahlstedt, A. Manfredini, T. Marrodán Undagoitia, J. Masbou, D. Masson, M. Messina, K. Micheneau, K. Miller, A. Molinario, K. Morâ, M. Murra, J. Naganoma, K. Ni, U. Oberlack, B. Pelssers, F. Piastra, J. Pienaar, V. Pizzella, G. Plante, R. Podviianiuk, N. Priel, D. Ramírez García, L. Rauch, S. Reichard, C. Reuter, B. Riedel, A. Rizzo, A. Rocchetti, N. Rupp, J. M. F. Dos Santos, G. Sartorelli, M. Scheibelhut, S. Schindler, J. Schreiner, D. Schulte, M. Schumann, L. Scotto Lavina, M. Selvi, P. Shagin, E. Shockley, M. Silva, H. Simgen, D. Thers, F. Toschi, G. Trinchero, C. Tunnell, N. Upole, M. Vargas, O. Wack, H. Wang, Z. Wang, Y. Wei, C. Weinheimer, C. Wittweg, J. Wulf, J. Ye, Y. Zhang, T. Zhu, and Xenon Collaboration. Dark Matter Search Results from a One Ton-Year Exposure of XENON1T. *Physical Review Letters*, 121(11):111302, September 2018.

Horace W. Babcock. The rotation of the Andromeda Nebula. *Lick Observatory Bulletin*, 498:41–51, January 1939.

I. K. Baldry, J. Liske, M. J. I. Brown, A. S. G. Robotham, S. P. Driver, L. Dunne, M. Alpaslan, S. Brough, M. E. Cluver, E. Eardley, D. J. Farrow, C. Heymans, H. Hildebrandt, A. M. Hopkins, L. S. Kelvin, J. Loveday, A. J. Moffett, P. Norberg, M. S. Owers, E. N. Taylor, A. H. Wright, S. P. Bamford, J. Bland-Hawthorn, N. Bourne, M. N. Bremer, M. Colless, C. J. Conselice, S. M. Croom, L. J. M. Davies, C. Foster, M. W. Grootes, B. W. Holwerda, D. H. Jones, P. R. Kafle, K. Kuijken, M. A. Lara-Lopez, A. R. Lopez-Sanchez, M. J. Meyer, S. Phillipps, W. J. Sutherland, E. van Kampen, and S. M. Wilkins. VizieR Online Data Catalog: Galaxy And Mass Assembly (GAMA): DR3 (Baldry+, 2018). *VizieR Online Data Catalog*, page J/MNRAS/474/3875, October 2018.

J. A. Baldwin, M. M. Phillips, and R. Terlevich. Classification parameters for the emission-line spectra of extragalactic objects. *Publications of the Astronomical Society of the Pacific*, 93:5–19, February 1981.

A. J. Battisti, E. da Cunha, K. Grasha, M. Salvato, E. Daddi, L. Davies, S. Jin, D. Liu,

E. Schinnerer, M. Vaccari, and COSMOS Collaboration. MAGPHYS+photo-z: Constraining the Physical Properties of Galaxies with Unknown Redshifts. *The Astrophysical Journal*, 882(1):61, September 2019.

Robert H. Becker, Xiaohui Fan, Richard L. White, Michael A. Strauss, Vijay K. Narayanan, Robert H. Lupton, James E. Gunn, James Annis, Neta A. Bahcall, J. Brinkmann, A. J. Connolly, István Csabai, Paul C. Czarapata, Mamoru Doi, Timothy M. Heckman, G. S. Hennessy, Željko Ivezić, G. R. Knapp, Don Q. Lamb, Timothy A. McKay, Jeffrey A. Munn, Thomas Nash, Robert Nichol, Jeffrey R. Pier, Gordon T. Richards, Donald P. Schneider, Chris Stoughton, Alexander S. Szalay, Aniruddha R. Thakar, and D. G. York. Evidence for Reionization at z∼6: Detection of a Gunn-Peterson Trough in a z=6.28 Quasar. *The Astronomical Journal*, 122(6):2850–2857, December 2001.

Steven V. W. Beckwith, Massimo Stiavelli, Anton M. Koekemoer, John A. R. Caldwell, Henry C. Ferguson, Richard Hook, Ray A. Lucas, Louis E. Bergeron, Michael Corbin, Shardha Jogee, Nino Panagia, Massimo Robberto, Patricia Royle, Rachel S. Somerville, and Megan Sosey. The Hubble Ultra Deep Field. *The Astronomical Journal*, 132(5):1729–1755, November 2006.

Peter S. Behroozi, Risa H. Wechsler, and Charlie Conroy. The Average Star Formation Histories of Galaxies in Dark Matter Halos from z = 0-8. *The Astrophysical Journal*, 770(1):57, June 2013.

Edwin A. Bergin and Mario Tafalla. Cold Dark Clouds: The Initial Conditions for Star Formation. *Annual Review of Astronomy and Astrophysics*, 45(1):339–396, September 2007.

M. Betoule, R. Kessler, J. Guy, J. Mosher, D. Hardin, R. Biswas, P. Astier, P. El-Hage, M. Konig, S. Kuhlmann, J. Marriner, R. Pain, N. Regnault, C. Balland, B. A. Bassett, P. J. Brown, H. Campbell, R. G. Carlberg, F. Cellier-Holzem, D. Cinabro, A. Conley, C. B. D'Andrea, D. L. DePoy, M. Doi, R. S. Ellis, S. Fabbro, A. V. Filippenko, R. J.

Foley, J. A. Frieman, D. Fouchez, L. Galbany, A. Goobar, R. R. Gupta, G. J. Hill, R. Hlozek, C. J. Hogan, I. M. Hook, D. A. Howell, S. W. Jha, L. Le Guillou, G. Leloudas, C. Lidman, J. L. Marshall, A. Möller, A. M. Mourão, J. Neveu, R. Nichol, M. D. Olmstead, N. Palanque-Delabrouille, S. Perlmutter, J. L. Prieto, C. J. Pritchet, M. Richmond, A. G. Riess, V. Ruhlmann-Kleider, M. Sako, K. Schahmaneche, D. P. Schneider, M. Smith, J. Sollerman, M. Sullivan, N. A. Walton, and C. J. Wheeler. Improved cosmological constraints from a joint analysis of the SDSS-II and SNLS supernova samples. *Astronomy and Astrophysics*, 568:A22, August 2014.

Cynthia Blaha and Roberta M. Humphreys. A Comparison of the Luminosity Functions in U, B, and V and Their Relationship to the Initial Mass Function for the Galaxy and the Magellanic Clouds. *The Astronomical Journal*, 98:1598, November 1989.

Alberto D. Bolatto, Mark Wolfire, and Adam K. Leroy. The CO-to-H_2 Conversion Factor. *Annual Review of Astronomy and Astrophysics*, 51(1):207–268, August 2013.

R. J. Bouwens, G. D. Illingworth, P. A. Oesch, M. Franx, I. Labbé, M. Trenti, P. van Dokkum, C. M. Carollo, V. González, R. Smit, and D. Magee. UV-continuum Slopes at z ~4-7 from the HUDF09+ERS+CANDELS Observations: Discovery of a Well-defined UV Color-Magnitude Relationship for z >= 4 Star-forming Galaxies. *The Astrophysical Journal*, 754(2):83, August 2012.

R. J. Bouwens, G. D. Illingworth, P. A. Oesch, M. Trenti, I. Labbé, M. Franx, M. Stiavelli, C. M. Carollo, P. van Dokkum, and D. Magee. Lower-luminosity Galaxies Could Reionize the Universe: Very Steep Faint-end Slopes to the UV Luminosity Functions at z >= 5-8 from the HUDF09 WFC3/IR Observations. *The Astrophysical Journal*, 752(1):L5, June 2012.

Michael Boylan-Kolchin, Volker Springel, Simon D. M. White, Adrian Jenkins, and Gerard Lemson. Resolving cosmic structure formation with the Millennium-II Simulation. *Monthly Notices of the Royal Astronomical Society*, 398(3):1150–1164, September 2009.

Gabriel B. Brammer, Pieter G. van Dokkum, and Paolo Coppi. EAZY: A Fast, Public Photometric Redshift Code. *The Astrophysical Journal*, 686(2):1503–1513, October 2008.

G. Bruzual and S. Charlot. Stellar population synthesis at the resolution of 2003. *Monthly Notices of the Royal Astronomical Society*, 344(4):1000–1028, October 2003.

Gustavo Bruzual, Gladis C. Magris, and Fabiola Hernández-Pérez. Modeling low mass stellar populations. In Kristen B. W. McQuinn and Sabrina Stierwalt, editors, *Dwarf Galaxies: From the Deep Universe to the Present*, volume 344, pages 211–212, October 2019.

Kevin Bundy, Matthew A. Bershady, David R. Law, Renbin Yan, Niv Drory, Nicholas MacDonald, David A. Wake, Brian Cherinka, José R. Sánchez-Gallego, Anne-Marie Weijmans, Daniel Thomas, Christy Tremonti, Karen Masters, Lodovico Coccato, Aleksandar M. Diamond-Stanic, Alfonso Aragón-Salamanca, Vladimir Avila-Reese, Carles Badenes, Jésus Falcón-Barroso, Francesco Belfiore, Dmitry Bizyaev, Guillermo A. Blanc, Joss Bland-Hawthorn, Michael R. Blanton, Joel R. Brownstein, Nell Byler, Michele Cappellari, Charlie Conroy, Aaron A. Dutton, Eric Emsellem, James Etherington, Peter M. Frinchaboy, Hai Fu, James E. Gunn, Paul Harding, Evelyn J. Johnston, Guinevere Kauffmann, Karen Kinemuchi, Mark A. Klaene, Johan H. Knapen, Alexie Leauthaud, Cheng Li, Lihwai Lin, Roberto Maiolino, Viktor Malanushenko, Elena Malanushenko, Shude Mao, Claudia Maraston, Richard M. McDermid, Michael R. Merrifield, Robert C. Nichol, Daniel Oravetz, Kaike Pan, John K. Parejko, Sebastian F. Sanchez, David Schlegel, Audrey Simmons, Oliver Steele, Matthias Steinmetz, Karun Thanjavur, Benjamin A. Thompson, Jeremy L. Tinker, Remco C. E. van den Bosch, Kyle B. Westfall, David Wilkinson, Shelley Wright, Ting Xiao, and Kai Zhang. Overview of the SDSS-IV MaNGA Survey: Mapping nearby Galaxies at Apache Point Observatory. *The Astrophysical Journal*, 798(1):7, January 2015.

Daniela Calzetti. The Dust Opacity of Star-forming Galaxies. *Publications of the Astronomical Society of the Pacific*, 113(790):1449–1485, December 2001.

Carolin Cardamone, Kevin Schawinski, Marc Sarzi, Steven P. Bamford, Nicola Bennert, C. M. Urry, Chris Lintott, William C. Keel, John Parejko, Robert C. Nichol, Daniel Thomas, Dan Andreescu, Phil Murray, M. Jordan Raddick, Anže Slosar, Alex Szalay, and Jan Vandenberg. Galaxy Zoo Green Peas: discovery of a class of compact extremely star-forming galaxies. *Monthly Notices of the Royal Astronomical Society*, 399(3):1191–1205, November 2009.

Claude Carignan, Laurent Chemin, Walter K. Huchtmeier, and Felix J. Lockman. The Extended H I Rotation Curve and Mass Distribution of M31. *The Astrophysical Journal*, 641(2):L109–L112, April 2006.

Adam C. Carnall, Joel Leja, Benjamin D. Johnson, Ross J. McLure, James S. Dunlop, and Charlie Conroy. How to Measure Galaxy Star Formation Histories. I. Parametric Models. *The Astrophysical Journal*, 873(1):44, March 2019.

Bernard Carr, Florian Kühnel, and Marit Sandstad. Primordial black holes as dark matter. *Physical Review D*, 94(8):083504, October 2016.

Caitlin M. Casey, Desika Narayanan, and Asantha Cooray. Dusty star-forming galaxies at high redshift. *Physics Reports*, 541(2):45–161, August 2014.

Caitlin M. Casey. Far-infrared spectral energy distribution fitting for galaxies near and far. *Monthly Notices of the Royal Astronomical Society*, 425(4):3094–3103, October 2012.

Gilles Chabrier. Galactic Stellar and Substellar Initial Mass Function. , 115(809):763–795, July 2003.

Stéphane Charlot and S. Michael Fall. A Simple Model for the Absorption of Starlight by Dust in Galaxies. *The Astrophysical Journal*, 539(2):718–731, August 2000.

Alain Coc and Elisabeth Vangioni. Primordial nucleosynthesis. *International Journal of Modern Physics E*, 26(8):1741002, January 2017.

Dan Coe, Adi Zitrin, Mauricio Carrasco, Xinwen Shu, Wei Zheng, Marc Postman, Larry Bradley, Anton Koekemoer, Rychard Bouwens, Tom Broadhurst, Anna Monna, Ole Host, Leonidas A. Moustakas, Holland Ford, John Moustakas, Arjen van der Wel, Megan Donahue, Steven A. Rodney, Narciso Benítez, Stephanie Jouvel, Stella Seitz, Daniel D. Kelson, and Piero Rosati. CLASH: Three Strongly Lensed Images of a Candidate z $\approx$ 11 Galaxy. *The Astrophysical Journal*, 762(1):32, January 2013.

P. Coelho, G. Bruzual, S. Charlot, A. Weiss, B. Barbuy, and J. W. Ferguson. Spectral models for solar-scaled and α-enhanced stellar populations. *Monthly Notices of the Royal Astronomical Society*, 382(2):498–514, December 2007.

Charlie Conroy and Pieter van Dokkum. Counting Low-mass Stars in Integrated Light. *The Astrophysical Journal*, 747(1):69, March 2012.

Donald P. Cox. The Three-Phase Interstellar Medium Revisited. *Annual Review of Astronomy and Astrophysics*, 43(1):337–385, September 2005.

Elisabete da Cunha, Stéphane Charlot, and David Elbaz. A simple model to interpret the ultraviolet, optical and infrared emission from galaxies. *Monthly Notices of the Royal Astronomical Society*, 388(4):1595–1617, August 2008.

Tiziana Di Matteo, Volker Springel, and Lars Hernquist. Energy input from quasars regulates the growth and activity of black holes and their host galaxies. *Nature*, 433(7026):604–607, February 2005.

R. H. Dicke, P. J. E. Peebles, P. G. Roll, and D. T. Wilkinson. Cosmic Black-Body Radiation. *The Astrophysical Journal*, 142:414–419, July 1965.

S. P. Driver, D. T. Hill, L. S. Kelvin, A. S. G. Robotham, J. Liske, P. Norberg, I. K. Baldry, S. P. Bamford, A. M. Hopkins, J. Loveday, J. A. Peacock, E. Andrae, J. Bland-Hawthorn,

S. Brough, M. J. I. Brown, E. Cameron, J. H. Y. Ching, M. Colless, C. J. Conselice, S. M. Croom, N. J. G. Cross, R. de Propris, S. Dye, M. J. Drinkwater, S. Ellis, Alister W. Graham, M. W. Grootes, M. Gunawardhana, D. H. Jones, E. van Kampen, C. Maraston, R. C. Nichol, H. R. Parkinson, S. Phillipps, K. Pimbblet, C. C. Popescu, M. Prescott, I. G. Roseboom, E. M. Sadler, A. E. Sansom, R. G. Sharp, D. J. B. Smith, E. Taylor, D. Thomas, R. J. Tuffs, D. Wijesinghe, L. Dunne, C. S. Frenk, M. J. Jarvis, B. F. Madore, M. J. Meyer, M. Seibert, L. Staveley-Smith, W. J. Sutherland, and S. J. Warren. Galaxy and Mass Assembly (GAMA): survey diagnostics and core data release. *Monthly Notices of the Royal Astronomical Society*, 413(2):971–995, May 2011.

Simon P. Driver, Angus H. Wright, Stephen K. Andrews, Luke J. Davies, Prajwal R. Kafle, Rebecca Lange, Amanda J. Moffett, Elizabeth Mannering, Aaron S. G. Robotham, Kevin Vinsen, Mehmet Alpaslan, Ellen Andrae, Ivan K. Baldry, Amanda E. Bauer, Steven P. Bamford, Joss Bland-Hawthorn, Nathan Bourne, Sarah Brough, Michael J. I. Brown, Michelle E. Cluver, Scott Croom, Matthew Colless, Christopher J. Conselice, Elisabete da Cunha, Roberto De Propris, Michael Drinkwater, Loretta Dunne, Steve Eales, Alastair Edge, Carlos Frenk, Alister W. Graham, Meiert Grootes, Benne W. Holwerda, Andrew M. Hopkins, Edo Ibar, Eelco van Kampen, Lee S. Kelvin, Tom Jarrett, D. Heath Jones, Maritza A. Lara-Lopez, Jochen Liske, Angel R. Lopez-Sanchez, Jon Loveday, Steve J. Maddox, Barry Madore, Smriti Mahajan, Martin Meyer, Peder Norberg, Samantha J. Penny, Steven Phillipps, Cristina Popescu, Richard J. Tuffs, John A. Peacock, Kevin A. Pimbblet, Matthew Prescott, Kate Rowlands, Anne E. Sansom, Mark Seibert, Matthew W. L. Smith, Will J. Sutherland, Edward N. Taylor, Elisabetta Valiante, J. Antonio Vazquez-Mata, Lingyu Wang, Stephen M. Wilkins, and Richard Williams. Galaxy And Mass Assembly (GAMA): Panchromatic Data Release (far-UV-far-IR) and the low-z energy budget. *Monthly Notices of the Royal Astronomical Society*, 455(4):3911–3942, February 2016.

J. S. Dunlop, A. B. Rogers, R. J. McLure, R. S. Ellis, B. E. Robertson, A. Koekemoer,

P. Dayal, E. Curtis-Lake, V. Wild, S. Charlot, R. A. A. Bowler, M. A. Schenker, M. Ouchi, Y. Ono, M. Cirasuolo, S. R. Furlanetto, D. P. Stark, T. A. Targett, and E. Schneider. The UV continua and inferred stellar populations of galaxies at z 7-9 revealed by the Hubble Ultra-Deep Field 2012 campaign. *Monthly Notices of the Royal Astronomical Society*, 432(4):3520–3533, July 2013.

G. Efstathiou, M. Davis, S. D. M. White, and C. S. Frenk. Numerical techniques for large cosmological N-body simulations. *The Astrophysical Journal Supplement Series*, 57:241–260, February 1985.

John J. Eldridge and Elizabeth R. Stanway. The effect of stellar evolution uncertainties on the rest-frame ultraviolet stellar lines of C IV and He II in high-redshift Lyman-break galaxies. *Monthly Notices of the Royal Astronomical Society*, 419(1):479–489, January 2012.

J. J. Eldridge, E. R. Stanway, L. Xiao, L. A. S. McClelland, J. C. Bray, G. Taylor, and M. Ng. Binary Population and Spectral Synthesis. In J. J. Eldridge, J. C. Bray, L. A. S. McClelland, and L. Xiao, editors, *The Lives and Death-Throes of Massive Stars*, volume 329, pages 396–396, November 2017.

J. J. Eldridge, E. R. Stanway, L. Xiao, L. A. S. McClelland, G. Taylor, M. Ng, S. M. L. Greis, and J. C. Bray. Binary Population and Spectral Synthesis Version 2.1: Construction, Observational Verification, and New Results. *Publications of the Astronomical Society of Australia*, 34:e058, November 2017.

Richard S. Ellis, Ross J. McLure, James S. Dunlop, Brant E. Robertson, Yoshiaki Ono, Matthew A. Schenker, Anton Koekemoer, Rebecca A. A. Bowler, Masami Ouchi, Alexander B. Rogers, Emma Curtis-Lake, Evan Schneider, Stephane Charlot, Daniel P. Stark, Steven R. Furlanetto, and Michele Cirasuolo. The Abundance of Star-forming Galaxies in the Redshift Range 8.5-12: New Results from the 2012 Hubble Ultra Deep Field Campaign. *The Astrophysical Journal*, 763(1):L7, January 2013.

R. Farmer, M. Renzo, S. E. de Mink, P. Marchant, and S. Justham. Mind the Gap: The Location of the Lower Edge of the Pair-instability Supernova Black Hole Mass Gap. *The Astrophysical Journal*, 887(1):53, December 2019.

G. G. Fazio, J. L. Hora, L. E. Allen, M. L. N. Ashby, P. Barmby, L. K. Deutsch, J. S. Huang, S. Kleiner, M. Marengo, S. T. Megeath, G. J. Melnick, M. A. Pahre, B. M. Patten, J. Polizotti, H. A. Smith, R. S. Taylor, Z. Wang, S. P. Willner, W. F. Hoffmann, J. L. Pipher, W. J. Forrest, C. W. McMurty, C. R. McCreight, M. E. McKelvey, R. E. McMurray, D. G. Koch, S. H. Moseley, R. G. Arendt, J. E. Mentzell, C. T. Marx, P. Losch, P. Mayman, W. Eichhorn, D. Krebs, M. Jhabvala, D. Y. Gezari, D. J. Fixsen, J. Flores, K. Shakoorzadeh, R. Jungo, C. Hakun, L. Workman, G. Karpati, R. Kichak, R. Whitley, S. Mann, E. V. Tollestrup, P. Eisenhardt, D. Stern, V. Gorjian, B. Bhattacharya, S. Carey, B. O. Nelson, W. J. Glaccum, M. Lacy, P. J. Lowrance, S. Laine, W. T. Reach, J. A. Stauffer, J. A. Surace, G. Wilson, E. L. Wright, A. Hoffman, G. Domingo, and M. Cohen. The Infrared Array Camera (IRAC) for the Spitzer Space Telescope. *The Astrophysical Journal Supplement Series*, 154(1):10–17, September 2004.

Yu Feng, Tiziana Di-Matteo, Rupert A. Croft, Simeon Bird, Nicholas Battaglia, and Stephen Wilkins. The BlueTides simulation: first galaxies and reionization. *Monthly Notices of the Royal Astronomical Society*, 455(3):2778–2791, January 2016.

Yu Feng, Tiziana Di-Matteo, Rupert A. Croft, Simeon Bird, Nicholas Battaglia, and Stephen Wilkins. The BlueTides simulation: first galaxies and reionization. *Monthly Notices of the Royal Astronomical Society*, 455(3):2778–2791, January 2016.

G. J. Ferland, R. L. Porter, P. A. M. van Hoof, R. J. R. Williams, N. P. Abel, M. L. Lykins, G. Shaw, W. J. Henney, and P. C. Stancil. The 2013 Release of Cloudy. *Revista Mexicana de Astronomia y Astrofisica*, 49:137–163, April 2013.

J. R. Findlay, W. J. Sutherland, B. P. Venemans, C. Reylé, A. C. Robin, D. G. Bonfield, V. A. Bruce, and M. J. Jarvis. Selection constraints on high-redshift quasar searches in the

VISTA Kilo-degree Infrared Galaxy survey. *Monthly Notices of the Royal Astronomical Society*, 419(4):3354–3367, February 2012.

Steven L. Finkelstein, James E. Rhoads, Sangeeta Malhotra, Norman Grogin, and Junxian Wang. Effects of Dust Geometry in Lyα Galaxies at z = 4.4. *The Astrophysical Journal*, 678(2):655–668, May 2008.

Steven L. Finkelstein, Casey Papovich, Brett Salmon, Kristian Finlator, Mark Dickinson, Henry C. Ferguson, Mauro Giavalisco, Anton M. Koekemoer, Naveen A. Reddy, Robert Bassett, Christopher J. Conselice, James S. Dunlop, S. M. Faber, Norman A. Grogin, Nimish P. Hathi, Dale D. Kocevski, Kamson Lai, Kyoung-Soo Lee, Ross J. McLure, Bahram Mobasher, and Jeffrey A. Newman. Candels: The Evolution of Galaxy Rest-frame Ultraviolet Colors from z = 8 to 4. *The Astrophysical Journal*, 756(2):164, September 2012.

Steven L. Finkelstein. The colors of galaxies at 4 < z < 8 and their contribution to reionization. In Masayuki Umemura and Kazuyuki Omukai, editors, *First Stars IV - from Hayashi to the Future* -, volume 1480 of *American Institute of Physics Conference Series*, pages 261–266, September 2012.

Steven L. Finkelstein. Constraining the Evolution of Reionization with US-ELT Followup of WFIRST Deep Drilling Fields. In *American Astronomical Society Meeting Abstracts #234*, volume 234 of *American Astronomical Society Meeting Abstracts*, page 315.03, June 2019.

M. Fioc and B. Rocca-Volmerange. PEGASE: a UV to NIR spectral evolution model of galaxies. Application to the calibration of bright galaxy counts. *Astronomy and Astrophysics*, 500:507–519, October 1997.

Daniel Foreman-Mackey, David W. Hogg, Dustin Lang, and Jonathan Goodman. emcee: The MCMC Hammer. *Publications of the Astronomical Society of the Pacific*, 125(925):306, March 2013.

K. C. Freeman. On the Disks of Spiral and S0 Galaxies. *The Astrophysical Journal*, 160:811, June 1970.

A. Friedmann. Über die Krümmung des Raumes. *Zeitschrift fur Physik*, 10:377–386, January 1922.

Macarena García Marín, George Rieke, Michael Ressler, Dan Dicken, Tom Greene, Jane Morrison, Sarah Kendrew, Stacey Alberts, Michael Regan, David Law, Ori Fox, Tea Temim, Dean Hines, Pierre-Olivier Lagage, Pamela Klaassen, John Pye, Gillian Wright, and Alistair Glasse. Observing recommendations for JWST MIRI users. In *Observatory Operations: Strategies, Processes, and Systems VII*, volume 10704 of *Society of Photo-Optical Instrumentation Engineers (SPIE) Conference Series*, page 107041I, July 2018.

R. Gilmozzi and J. Spyromilio. The European Extremely Large Telescope (E-ELT). *The Messenger*, 127:11, March 2007.

Jonathan Goodman and Jonathan Weare. Ensemble samplers with affine invariance. *Communications in Applied Mathematics and Computational Science*, 5(1):65–80, January 2010.

Norman A. Grogin, Dale D. Kocevski, S. M. Faber, Henry C. Ferguson, Anton M. Koekemoer, Adam G. Riess, Viviana Acquaviva, David M. Alexander, Omar Almaini, Matthew L. N. Ashby, Marco Barden, Eric F. Bell, Frédéric Bournaud, Thomas M. Brown, Karina I. Caputi, Stefano Casertano, Paolo Cassata, Marco Castellano, Peter Challis, Ranga-Ram Chary, Edmond Cheung, Michele Cirasuolo, Christopher J. Conselice, Asantha Roshan Cooray, Darren J. Croton, Emanuele Daddi, Tomas Dahlen, Romeel Davé, Duília F. de Mello, Avishai Dekel, Mark Dickinson, Timothy Dolch, Jennifer L. Donley, James S. Dunlop, Aaron A. Dutton, David Elbaz, Giovanni G. Fazio, Alexei V. Filippenko, Steven L. Finkelstein, Adriano Fontana, Jonathan P. Gardner, Peter M. Garnavich, Eric Gawiser, Mauro Giavalisco, Andrea Grazian, Yicheng Guo, Nimish P. Hathi, Boris Häussler, Philip F. Hopkins, Jia-Sheng Huang, Kuang-Han Huang, Saurabh W. Jha, Jey-

han S. Kartaltepe, Robert P. Kirshner, David C. Koo, Kamson Lai, Kyoung-Soo Lee, Weidong Li, Jennifer M. Lotz, Ray A. Lucas, Piero Madau, Patrick J. McCarthy, Elizabeth J. McGrath, Daniel H. McIntosh, Ross J. McLure, Bahram Mobasher, Leonidas A. Moustakas, Mark Mozena, Kirpal Nandra, Jeffrey A. Newman, Sami-Matias Niemi, Kai G. Noeske, Casey J. Papovich, Laura Pentericci, Alexandra Pope, Joel R. Primack, Abhijith Rajan, Swara Ravindranath, Naveen A. Reddy, Alvio Renzini, Hans-Walter Rix, Aday R. Robaina, Steven A. Rodney, David J. Rosario, Piero Rosati, Sara Salimbeni, Claudia Scarlata, Brian Siana, Luc Simard, Joseph Smidt, Rachel S. Somerville, Hyron Spinrad, Amber N. Straughn, Louis-Gregory Strolger, Olivia Telford, Harry I. Teplitz, Jonathan R. Trump, Arjen van der Wel, Carolin Villforth, Risa H. Wechsler, Benjamin J. Weiner, Tommy Wiklind, Vivienne Wild, Grant Wilson, Stijn Wuyts, Hao-Jing Yan, and Min S. Yun. CANDELS: The Cosmic Assembly Near-infrared Deep Extragalactic Legacy Survey. *The Astrophysical Journal Supplement Series*, 197(2):35, December 2011.

M. L. P. Gunawardhana, A. M. Hopkins, R. G. Sharp, S. Brough, E. Taylor, J. Bland-Hawthorn, C. Maraston, R. J. Tuffs, C. C. Popescu, D. Wijesinghe, D. H. Jones, S. Croom, E. Sadler, S. Wilkins, S. P. Driver, J. Liske, P. Norberg, I. K. Baldry, S. P. Bamford, J. Loveday, J. A. Peacock, A. S. G. Robotham, D. B. Zucker, Q. A. Parker, C. J. Conselice, E. Cameron, C. S. Frenk, D. T. Hill, L. S. Kelvin, K. Kuijken, B. F. Madore, B. Nichol, H. R. Parkinson, K. A. Pimbblet, M. Prescott, W. J. Sutherland, D. Thomas, and E. van Kampen. Galaxy and Mass Assembly (GAMA): the star formation rate dependence of the stellar initial mass function. , 415(2):1647–1662, August 2011.

James E. Gunn and Bruce A. Peterson. On the Density of Neutral Hydrogen in Intergalactic Space. *The Astrophysical Journal*, 142:1633–1636, November 1965.

Alan H. Guth. Inflationary universe: A possible solution to the horizon and flatness problems. *Physical Review D*, 23(2):347–356, January 1981.

Michael Hauser. Search for the Cosmic Infrared Background Radiation using COBE Data. NASA STI/Recon Technical Report N, January 2001.

Bruno M. B. Henriques, Robert M. Yates, Jian Fu, Qi Guo, Guinevere Kauffmann, Chaichalit Srisawat, Peter A. Thomas, and Simon D. M. White. L-GALAXIES 2020: Spatially resolved cold gas phases, star formation, and chemical enrichment in galactic discs. *Monthly Notices of the Royal Astronomical Society*, 491(4):5795–5814, February 2020.

David W. Hogg. Distance measures in cosmology. *arXiv e-prints*, pages astro–ph/9905116, May 1999.

Philip F. Hopkins. Pressure-Entropy SPH: Pressure-entropy smooth-particle hydrodynamics, May 2013.

A. M. Hopkins. The Dawes Review 8: Measuring the Stellar Initial Mass Function. , 35:39, November 2018.

Edwin Hubble. A Relation between Distance and Radial Velocity among Extra-Galactic Nebulae. *Proceedings of the National Academy of Science*, 15(3):168–173, March 1929.

Jr. Iben, I. and A. Renzini. Asymptotic giant branch evolution and beyond. *Annual Review of Astronomy and Astrophysics*, 21:271–342, January 1983.

G. D. Illingworth, D. Magee, P. A. Oesch, R. J. Bouwens, I. Labbé, M. Stiavelli, P. G. van Dokkum, M. Franx, M. Trenti, C. M. Carollo, and V. Gonzalez. The HST eXtreme Deep Field (XDF): Combining All ACS and WFC3/IR Data on the HUDF Region into the Deepest Field Ever. *The Astrophysical Journal Supplement Series*, 209(1):6, November 2013.

Kartheik Iyer and Eric Gawiser. Reconstructing The Star Formation Histories Of Galaxies Through Sed Fitting Using The Dense Basis Method. In *Galaxy Evolution Across Time*, page 2, June 2017.

A. E. Jaskot and M. S. Oey. The Origin and Optical Depth of Ionizing Photons in the Green Pea Galaxies. In *Massive Young Star Clusters Near and Far: From the Milky Way to Reionization*, pages 171–174, September 2014.

Hannes Jensen, Peter Laursen, Garrelt Mellema, Ilian T. Iliev, Jesper Sommer-Larsen, and Paul R. Shapiro. On the use of Lyα emitters as probes of reionization. *Monthly Notices of the Royal Astronomical Society*, 428(2):1366–1381, January 2013.

T. Jeřábková, A. Hasani Zonoozi, P. Kroupa, G. Beccari, Z. Yan, A. Vazdekis, and Z. Y. Zhang. Impact of metallicity and star formation rate on the time-dependent, galaxy-wide stellar initial mass function. *Astronomy and Astrophysics*, 620:A39, November 2018.

Neal Katz, David H. Weinberg, and Lars Hernquist. Cosmological Simulations with TreeSPH. *The Astrophysical Journal Supplement Series*, 105:19, July 1996.

Guinevere Kauffmann, Timothy M. Heckman, Christy Tremonti, Jarle Brinchmann, Stéphane Charlot, Simon D. M. White, Susan E. Ridgway, Jon Brinkmann, Masataka Fukugita, Patrick B. Hall, Željko Ivezić, Gordon T. Richards, and Donald P. Schneider. The host galaxies of active galactic nuclei. *Monthly Notices of the Royal Astronomical Society*, 346(4):1055–1077, December 2003.

Masahiro Kawasaki, Kazunori Kohri, and Takeo Moroi. Big-bang nucleosynthesis and hadronic decay of long-lived massive particles. *Physical Review D*, 71(8):083502, April 2005.

Jr. Kennicutt, R. C. The rate of star formation in normal disk galaxies. *The Astrophysical Journal*, 272:54–67, September 1983.

L. J. Kewley, M. A. Dopita, R. S. Sutherland, C. A. Heisler, and J. Trevena. Theoretical Modeling of Starburst Galaxies. *The Astrophysical Journal*, 556(1):121–140, July 2001.

Pavel Kroupa. On the variation of the initial mass function. , 322(2):231–246, April 2001.

Mark R. Krumholz and Nickolay Y. Gnedin. A Comparison of Methods for Determining the Molecular Content of Model Galaxies. *The Astrophysical Journal*, 729(1):36, March 2011.

R. L. Larson, S. L. Finkelstein, T. Hutchison, C. Papovich, M. Bagley, I. Jung, N. Pirzkal, M. Dickinson, M. Song, A. Fontana, M. Giavalisco, M. Castellano, L. Pentricci, and S. Rojas Ruiz. Islands of Reionization: Evidence for an Overdensity at z=8.7 in the CANDELS EGS Field. In *American Astronomical Society Meeting Abstracts #235*, volume 235 of *American Astronomical Society Meeting Abstracts*, page 207.23, January 2020.

Tod R. Lauer, Marc Postman, Harold A. Weaver, John R. Spencer, S. Alan Stern, Marc W. Buie, Daniel D. Durda, Carey M. Lisse, A. R. Poppe, Richard P. Binzel, Daniel T. Britt, Bonnie J. Buratti, Andrew F. Cheng, W. M. Grundy, Mihaly Horanyi J. J. Kavelaars, Ivan R. Linscott, William B. McKinnon, Jeffrey M. Moore, J. I. Nuñez, Catherine B. Olkin, Joel W. Parker, Simon B. Porter, Dennis C. Reuter, Stuart J. Robbins, Paul Schenk, Mark R. Showalter, Kelsi N. Singer, Anne. J. Verbiscer, and Leslie A. Young. New Horizons Observations of the Cosmic Optical Background. *arXiv e-prints*, page arXiv:2011.03052, November 2020.

O. Le Fèvre, G. Vettolani, B. Garilli, L. Tresse, D. Bottini, V. Le Brun, D. Maccagni, J. P. Picat, R. Scaramella, M. Scodeggio, A. Zanichelli, C. Adami, M. Arnaboldi, S. Arnouts, S. Bardelli, M. Bolzonella, A. Cappi, S. Charlot, P. Ciliegi, T. Contini, S. Foucaud, P. Franzetti, I. Gavignaud, L. Guzzo, O. Ilbert, A. Iovino, H. J. McCracken, B. Marano, C. Marinoni, G. Mathez, A. Mazure, B. Meneux, R. Merighi, S. Paltani, R. Pellò, A. Pollo, L. Pozzetti, M. Radovich, G. Zamorani, E. Zucca, M. Bondi, A. Bongiorno, G. Busarello, F. Lamareille, Y. Mellier, P. Merluzzi, V. Ripepi, and D. Rizzo. The VIMOS VLT deep survey. First epoch VVDS-deep survey: 11 564 spectra with 17.5 $\leq$ IAB $\leq$ 24, and the redshift distribution over 0 $\leq$ z $\leq$ 5. *Astronomy and Astrophysics*, 439(3):845–862, September 2005.

Yueh-Ning Lee, Stella S. R. Offner, Patrick Hennebelle, Philippe André, Hans Zinnecker, Javier Ballesteros-Paredes, Shu-ichiro Inutsuka, and J. M. Diederik Kruijssen. The Origin of the Stellar Mass Distribution and Multiplicity. *Space Science Reviews*, 216(4):70, June 2020.

Joel Leja, Adam C. Carnall, Benjamin D. Johnson, Charlie Conroy, and Joshua S. Speagle. How to Measure Galaxy Star Formation Histories. II. Nonparametric Models. *The Astrophysical Journal*, 876(1):3, May 2019.

Aleksandra Leśniewska and Michał Jerzy Michałowski. Dust production scenarios in galaxies at z ~6-8.3. *Astronomy and Astrophysics*, 624:L13, April 2019.

Antony Lewis and Sarah Bridle. Cosmological parameters from CMB and other data: A Monte Carlo approach. *Physical Review D*, 66(10):103511, November 2002.

Andrew R. Liddle and David H. Lyth. *Cosmological Inflation and Large-Scale Structure*. 2000.

Chris J. Lintott, Kevin Schawinski, Anže Slosar, Kate Land, Steven Bamford, Daniel Thomas, M. Jordan Raddick, Robert C. Nichol, Alex Szalay, Dan Andreescu, Phil Murray, and Jan Vandenberg. Galaxy Zoo: morphologies derived from visual inspection of galaxies from the Sloan Digital Sky Survey. *Monthly Notices of the Royal Astronomical Society*, 389(3):1179–1189, September 2008.

J. M. Lotz, A. Koekemoer, D. Coe, N. Grogin, P. Capak, J. Mack, J. Anderson, R. Avila, E. A. Barker, D. Borncamp, G. Brammer, M. Durbin, H. Gunning, B. Hilbert, H. Jenkner, H. Khandrika, Z. Levay, R. A. Lucas, J. MacKenty, S. Ogaz, B. Porterfield, N. Reid, M. Robberto, P. Royle, L. J. Smith, L. J. Storrie-Lombardi, B. Sunnquist, J. Surace, D. C. Taylor, R. Williams, J. Bullock, M. Dickinson, S. Finkelstein, P. Natarajan, J. Richard, B. Robertson, J. Tumlinson, A. Zitrin, K. Flanagan, K. Sembach, B. T. Soifer, and M. Mountain. The Frontier Fields: Survey Design and Initial Results. *The Astrophysical Journal*, 837(1):97, March 2017.

Thierry Maciaszek, Anne Ealet, Knud Jahnke, Eric Prieto, Rémi Barbier, Yannick Mellier, Florent Beaumont, William Bon, Anne Bonnefoi, Michael Carle, Amandine Caillat, Anne Costille, Doriane Dormoy, Franck Ducret, Christophe Fabron, Aurélien Febvre, Benjamin Foulon, Jose Garcia, Jean-Luc Gimenez, Emmanuel Grassi, Philippe Laurent, David Le Mignant, Laurent Martin, Christelle Rossin, Tony Pamplona, Patrice Sanchez, Sébastien Vives, Jean Claude Clémens, William Gillard, Mathieu Niclas, Aurélia Secroun, Benoit Serra, Bogna Kubik, Sylvain Ferriol, Jérôme Amiaux, Jean Christophe Barrière, Michel Berthe, Cyrille Rosset, Juan Francisco Macias-Perez, Natalia Auricchio, Adriano De Rosa, Enrico Franceschi, Gian Paolo Guizzo, Gianluca Morgante, Francesca Sortino, Massimo Trifoglio, Luca Valenziano, Laura Patrizii, T. Chiarusi, F. Fornari, F. Giacomini, A. Margiotta, N. Mauri, L. Pasqualini, G. Sirri, M. Spurio, M. Tenti, R. Travaglini, Stefano Dusini, F. Dal Corso, F. Laudisio, C. Sirignano, L. Stanco, S. Ventura, E. Borsato, Carlotta Bonoli, Favio Bortoletto, Andrea Balestra, Maurizio D'Alessandro, Eduardo Medinaceli, Ruben Farinelli, Leonardo Corcione, Sebastiano Ligori, Frank Grupp, Carolin Wimmer, Felix Hormuth, Gregor Seidel, Stefanie Wachter, Cristóbal Padilla, Mikel Lamensans, Ricard Casas, Ivan Lloro, Rafael Toledo-Moreo, Jaime Gomez, Carlos Colodro-Conde, David Lizán, Jose Javier Diaz, Per B. Lilje, Corinne Toulouse-Aastrup, Michael I. Andersen, Anton N. Sørensen, Peter Jakobsen, Allan Hornstrup, Niels-Christian Jessen, Cédric Thizy, Warren Holmes, Ulf Israelsson, Michael Seiffert, Augustyn Waczynski, René J. Laureijs, Giuseppe Racca, Jean-Christophe Salvignol, Tobias Boenke, and Paolo Strada. Euclid Near Infrared Spectrometer and Photometer instrument concept and first test results obtained for different breadboards models at the end of phase C. In Howard A. MacEwen, Giovanni G. Fazio, Makenzie Lystrup, Natalie Batalha, Nicholas Siegler, and Edward C. Tong, editors, *Space Telescopes and Instrumentation 2016: Optical, Infrared, and Millimeter Wave*, volume 9904 of *Society of Photo-Optical Instrumentation Engineers (SPIE) Conference Series*, page 99040T, July 2016.

Piero Madau and Mark Dickinson. Cosmic Star-Formation History. *Annual Review of*

Astronomy and Astrophysics, 52:415–486, August 2014.

Piero Madau and Francesco Haardt. Cosmic Reionization after Planck: Could Quasars Do It All? *The Astrophysical Journal*, 813(1):L8, November 2015.

John Magorrian, Scott Tremaine, Douglas Richstone, Ralf Bender, Gary Bower, Alan Dressler, S. M. Faber, Karl Gebhardt, Richard Green, Carl Grillmair, John Kormendy, and Tod Lauer. The Demography of Massive Dark Objects in Galaxy Centers. *The Astronomical Journal*, 115(6):2285–2305, June 1998.

Claudia Maraston. Evolutionary population synthesis: models, analysis of the ingredients and application to high-z galaxies. *Monthly Notices of the Royal Astronomical Society*, 362(3):799–825, September 2005.

Christopher Martin, Mark Hurwitz, and Stuart Bowyer. Spectroscopic Limits to an Extragalactic Far-Ultraviolet Background. *The Astrophysical Journal*, 379:549, October 1991.

Philip Massey, Cornelia C. Lang, Kathleen Degioia-Eastwood, and Catharine D. Garmany. Massive Stars in the Field and Associations of the Magellanic Clouds: The Upper Mass Limit, the Initial Mass Function, and a Critical Test of Main-Sequence Stellar Evolutionary Theory. *The Astrophysical Journal*, 438:188, January 1995.

Jorryt Matthee, David Sobral, Sérgio Santos, Huub Röttgering, Behnam Darvish, and Bahram Mobasher. Identification of the brightest Lyα emitters at z = 6.6: implications for the evolution of the luminosity function in the reionization era. *Monthly Notices of the Royal Astronomical Society*, 451(1):400–417, July 2015.

R. J. McLure, J. S. Dunlop, L. de Ravel, M. Cirasuolo, R. S. Ellis, M. Schenker, B. E. Robertson, A. M. Koekemoer, D. P. Stark, and R. A. A. Bowler. A robust sample of galaxies at redshifts 6.0<z<8.7: stellar populations, star formation rates and stellar masses. *Monthly Notices of the Royal Astronomical Society*, 418(3):2074–2105, December 2011.

R. J. McLure, J. S. Dunlop, R. A. A. Bowler, E. Curtis-Lake, M. Schenker, R. S. Ellis, B. E. Robertson, A. M. Koekemoer, A. B. Rogers, Y. Ono, M. Ouchi, S. Charlot, V. Wild, D. P. Stark, S. R. Furlanetto, M. Cirasuolo, and T. A. Targett. A new multifield determination of the galaxy luminosity function at z = 7-9 incorporating the 2012 Hubble Ultra-Deep Field imaging. *Monthly Notices of the Royal Astronomical Society*, 432(4):2696–2716, July 2013.

Bahram Mobasher, Tomas Dahlen, Henry C. Ferguson, Viviana Acquaviva, Guillermo Barro, Steven L. Finkelstein, Adriano Fontana, Ruth Gruetzbauch, Seth Johnson, Yu Lu, Casey J. Papovich, Janine Pforr, Mara Salvato, Rachel S. Somerville, Tommy Wiklind, Stijn Wuyts, Matthew L. N. Ashby, Eric Bell, Christopher J. Conselice, Mark E. Dickinson, Sandra M. Faber, Giovanni Fazio, Kristian Finlator, Audrey Galametz, Eric Gawiser, Mauro Giavalisco, Andrea Grazian, Norman A. Grogin, Yicheng Guo, Nimish Hathi, Dale Kocevski, Anton M. Koekemoer, David C. Koo, Jeffrey A. Newman, Naveen Reddy, Paola Santini, and Risa H. Wechsler. A Critical Assessment of Stellar Mass Measurement Methods. *The Astrophysical Journal*, 808(1):101, July 2015.

C. A. Muller and J. H. Oort. Observation of a Line in the Galactic Radio Spectrum: The Interstellar Hydrogen Line at 1,420 Mc./sec., and an Estimate of Galactic Rotation. *Nature*, 168(4270):357–358, September 1951.

David Nataf. Characterization of Dust in the Era of Large Surveys: From Extinction in the Ultraviolet to Emission in the Microwave. NASA ADAP Proposal, October 2018.

Julio F. Navarro, Carlos S. Frenk, and Simon D. M. White. The Structure of Cold Dark Matter Halos. *The Astrophysical Journal*, 462:563, May 1996.

P. Ocvirk, C. Pichon, A. Lançon, and E. Thiébaut. STECMAP: STEllar Content from high-resolution galactic spectra via Maximum A Posteriori. *Monthly Notices of the Royal Astronomical Society*, 365(1):46–73, January 2006.

P. A. Oesch, G. Brammer, P. G. van Dokkum, G. D. Illingworth, R. J. Bouwens, I. Labbé, M. Franx, I. Momcheva, M. L. N. Ashby, G. G. Fazio, V. Gonzalez, B. Holden, D. Magee, R. E. Skelton, R. Smit, L. R. Spitler, M. Trenti, and S. P. Willner. A Remarkably Luminous Galaxy at z=11.1 Measured with Hubble Space Telescope Grism Spectroscopy. *The Astrophysical Journal*, 819(2):129, March 2016.

Donald E. Osterbrock and Gary J. Ferland. *Astrophysics of gaseous nebulae and active galactic nuclei*. 2006.

D. E. Osterbrock and R. W. Pogge. The spectra of narrow-line Seyfert 1 galaxies. *The Astrophysical Journal*, 297:166–176, October 1985.

Donald E. Osterbrock. *Astrophysics of gaseous nebulae*. 1974.

A. H. Patil, S. Yatawatta, L. V. E. Koopmans, A. G. de Bruyn, M. A. Brentjens, S. Zaroubi, K. M. B. Asad, M. Hatef, V. Jelić, M. Mevius, A. R. Offringa, V. N. Pandey, H. Vedantham, F. B. Abdalla, W. N. Brouw, E. Chapman, B. Ciardi, B. K. Gehlot, A. Ghosh, G. Harker, I. T. Iliev, K. Kakiichi, S. Majumdar, G. Mellema, M. B. Silva, J. Schaye, D. Vrbanec, and S. J. Wijnholds. Upper Limits on the 21 cm Epoch of Reionization Power Spectrum from One Night with LOFAR. *The Astrophysical Journal*, 838(1):65, March 2017.

Bill Paxton, Lars Bildsten, Aaron Dotter, Falk Herwig, Pierre Lesaffre, and Frank Timmes. Modules for Experiments in Stellar Astrophysics (MESA). *The Astrophysical Journal Supplement Series*, 192(1):3, January 2011.

P. J. E. Peebles. Tests of cosmological models constrained by inflation. *The Astrophysical Journal*, 284:439–444, September 1984.

Yichuan C. Pei. Interstellar Dust from the Milky Way to the Magellanic Clouds. *The Astrophysical Journal*, 395:130, August 1992.

A. A. Penzias and R. W. Wilson. A Measurement of Excess Antenna Temperature at 4080 Mc/s. *The Astrophysical Journal*, 142:419–421, July 1965.

S. Perlmutter, G. Aldering, G. Goldhaber, R. A. Knop, P. Nugent, P. G. Castro, S. Deustua, S. Fabbro, A. Goobar, D. E. Groom, I. M. Hook, A. G. Kim, M. Y. Kim, J. C. Lee, N. J. Nunes, R. Pain, C. R. Pennypacker, R. Quimby, C. Lidman, R. S. Ellis, M. Irwin, R. G. McMahon, P. Ruiz-Lapuente, N. Walton, B. Schaefer, B. J. Boyle, A. V. Filippenko, T. Matheson, A. S. Fruchter, N. Panagia, H. J. M. Newberg, W. J. Couch, and The Supernova Cosmology Project. Measurements of Ω and Λ from 42 High-Redshift Supernovae. *The Astrophysical Journal*, 517(2):565–586, June 1999.

Max Pettini and Bernard E. J. Pagel. [OIII]/[NII] as an abundance indicator at high redshift. *Monthly Notices of the Royal Astronomical Society*, 348(3):L59–L63, March 2004.

N. Pirzkal, S. Malhotra, J. E. Rhoads, and C. Xu. Optical-to-Mid-Infrared Observations of Lyα Galaxies at z$\sim$5 in the Hubble Ultra Deep Field: A Young and Low-Mass Population. *The Astrophysical Journal*, 667(1):49–59, September 2007.

Planck Collaboration, P. A. R. Ade, N. Aghanim, M. I. R. Alves, C. Armitage-Caplan, and et al. Planck 2013 results. I. Overview of products and scientific results. *Astronomy and Astrophysics*, 571:A1, November 2014.

Planck Collaboration, P. A. R. Ade, N. Aghanim, M. Arnaud, M. Ashdown, and et al. Planck 2015 results. XIII. Cosmological parameters. *Astronomy and Astrophysics*, 594:A13, September 2016.

Planck Collaboration, N. Aghanim, M. Ashdown, J. Aumont, C. Baccigalupi, M. Ballardini, A. J. Banday, R. B. Barreiro, N. Bartolo, S. Basak, R. Battye, K. Benabed, J. P. Bernard, M. Bersanelli, P. Bielewicz, J. J. Bock, A. Bonaldi, L. Bonavera, J. R. Bond, J. Borrill, F. R. Bouchet, F. Boulanger, M. Bucher, C. Burigana, R. C. Butler, E. Calabrese, J. F. Cardoso, J. Carron, A. Challinor, H. C. Chiang, L. P. L. Colombo, C. Combet, B. Comis, A. Coulais, B. P. Crill, A. Curto, F. Cuttaia, R. J. Davis, P. de Bernardis, A. de Rosa, G. de Zotti, J. Delabrouille, J. M. Delouis, E. Di Valentino, C. Dickinson, J. M. Diego, O. Doré, M. Douspis, A. Ducout, X. Dupac, G. Efstathiou, F. Elsner, T. A. Enßlin, H. K. Eriksen,

E. Falgarone, Y. Fantaye, F. Finelli, F. Forastieri, M. Frailis, A. A. Fraisse, E. Franceschi, A. Frolov, S. Galeotta, S. Galli, K. Ganga, R. T. Génova-Santos, M. Gerbino, T. Ghosh, J. González-Nuevo, K. M. Górski, S. Gratton, A. Gruppuso, J. E. Gudmundsson, F. K. Hansen, G. Helou, S. Henrot-Versillé, D. Herranz, E. Hivon, Z. Huang, S. Ilić, A. H. Jaffe, W. C. Jones, E. Keihänen, R. Keskitalo, T. S. Kisner, L. Knox, N. Krachmalnicoff, M. Kunz, H. Kurki-Suonio, G. Lagache, J. M. Lamarre, M. Langer, A. Lasenby, M. Lattanzi, C. R. Lawrence, M. Le Jeune, J. P. Leahy, F. Levrier, M. Liguori, P. B. Lilje, M. López-Caniego, Y. Z. Ma, J. F. Macías-Pérez, G. Maggio, A. Mangilli, M. Maris, P. G. Martin, E. Martínez-González, S. Matarrese, N. Mauri, J. D. McEwen, P. R. Meinhold, A. Melchiorri, A. Mennella, M. Migliaccio, M. A. Miville-Deschênes, D. Molinari, A. Moneti, L. Montier, G. Morgante, A. Moss, S. Mottet, P. Naselsky, P. Natoli, C. A. Oxborrow, L. Pagano, D. Paoletti, B. Partridge, G. Patanchon, L. Patrizii, O. Perdereau, L. Perotto, V. Pettorino, F. Piacentini, S. Plaszczynski, L. Polastri, G. Polenta, J. L. Puget, J. P. Rachen, B. Racine, M. Reinecke, M. Remazeilles, A. Renzi, G. Rocha, M. Rossetti, G. Roudier, J. A. Rubiño-Martín, B. Ruiz-Granados, L. Salvati, M. Sandri, M. Savelainen, D. Scott, G. Sirri, R. Sunyaev, A. S. Suur-Uski, J. A. Tauber, M. Tenti, L. Toffolatti, M. Tomasi, M. Tristram, T. Trombetti, J. Valiviita, F. Van Tent, L. Vibert, P. Vielva, F. Villa, N. Vittorio, B. D. Wandelt, R. Watson, I. K. Wehus, M. White, A. Zacchei, and A. Zonca. Planck intermediate results. XLVI. Reduction of large-scale systematic effects in HFI polarization maps and estimation of the reionization optical depth. *Astronomy and Astrophysics*, 596:A107, December 2016.

William H. Press and Paul Schechter. Formation of Galaxies and Clusters of Galaxies by Self-Similar Gravitational Condensation. *The Astrophysical Journal*, 187:425–438, February 1974.

J. I. Read, T. Hayfield, and O. Agertz. Resolving mixing in smoothed particle hydrodynamics. *Monthly Notices of the Royal Astronomical Society*, 405(3):1513–1530, July 2010.

Adam G. Riess, Alexei V. Filippenko, Peter Challis, Alejandro Clocchiatti, Alan Diercks, Peter M. Garnavich, Ron L. Gilliland, Craig J. Hogan, Saurabh Jha, Robert P. Kirshner, B. Leibundgut, M. M. Phillips, David Reiss, Brian P. Schmidt, Robert A. Schommer, R. Chris Smith, J. Spyromilio, Christopher Stubbs, Nicholas B. Suntzeff, and John Tonry. Observational Evidence from Supernovae for an Accelerating Universe and a Cosmological Constant. *The Astronomical Journal*, 116(3):1009–1038, September 1998.

M. S. Roberts and R. N. Whitehurst. The rotation curve and geometry of M31 at large galactocentric distances. *The Astrophysical Journal*, 201:327–346, October 1975.

V. C. Rubin and Jr. Ford, W. K. A Comparison of Dynamical Models of the Andromeda Nebula and the Galaxy. In Wilhelm Becker and Georgios Ioannou Kontopoulos, editors, *The Spiral Structure of our Galaxy*, volume 38, page 61, January 1970.

Brett Salmon, Casey Papovich, Steven L. Finkelstein, Vithal Tilvi, Kristian Finlator, Peter Behroozi, Tomas Dahlen, Romeel Davé, Avishai Dekel, Mark Dickinson, Henry C. Ferguson, Mauro Giavalisco, James Long, Yu Lu, Bahram Mobasher, Naveen Reddy, Rachel S. Somerville, and Risa H. Wechsler. The Relation between Star Formation Rate and Stellar Mass for Galaxies at 3.5 <= z <= 6.5 in CANDELS. *The Astrophysical Journal*, 799(2):183, February 2015.

Edwin E. Salpeter. The Luminosity Function and Stellar Evolution. *Astrophysical Journal* , 121:161, January 1955.

S. F. Sánchez, R. C. Kennicutt, A. Gil de Paz, G. van de Ven, J. M. Vílchez, L. Wisotzki, C. J. Walcher, D. Mast, J. A. L. Aguerri, S. Albiol-Pérez, A. Alonso-Herrero, J. Alves, J. Bakos, T. Bartáková, J. Bland-Hawthorn, A. Boselli, D. J. Bomans, A. Castillo-Morales, C. Cortijo-Ferrero, A. de Lorenzo-Cáceres, A. Del Olmo, R. J. Dettmar, A. Díaz, S. Ellis, J. Falcón-Barroso, H. Flores, A. Gallazzi, B. García-Lorenzo, R. González Delgado, N. Gruel, T. Haines, C. Hao, B. Husemann, J. Iglésias-Páramo, K. Jahnke, B. Johnson, B. Jungwiert, V. Kalinova, C. Kehrig, D. Kupko, Á. R. López-Sánchez,

M. Lyubenova, R. A. Marino, E. Mármol-Queraltó, I. Márquez, J. Masegosa, S. Meidt, J. Mendez-Abreu, A. Monreal-Ibero, C. Montijo, A. M. Mourão, G. Palacios-Navarro, P. Papaderos, A. Pasquali, R. Peletier, E. Pérez, I. Pérez, A. Quirrenbach, M. Relaño, F. F. Rosales-Ortega, M. M. Roth, T. Ruiz-Lara, P. Sánchez-Blázquez, C. Sengupta, R. Singh, V. Stanishev, S. C. Trager, A. Vazdekis, K. Viironen, V. Wild, S. Zibetti, and B. Ziegler. CALIFA, the Calar Alto Legacy Integral Field Area survey. I. Survey presentation. *Astronomy and Astrophysics*, 538:A8, February 2012.

M. T. Sargent, E. Daddi, M. Béthermin, H. Aussel, G. Magdis, H. S. Hwang, S. Juneau, D. Elbaz, and E. da Cunha. Regularity Underlying Complexity: A Redshift-independent Description of the Continuous Variation of Galaxy-scale Molecular Gas Properties in the Mass-star Formation Rate Plane. *The Astrophysical Journal*, 793(1):19, September 2014.

Joop Schaye, Robert A. Crain, Richard G. Bower, Michelle Furlong, Matthieu Schaller, Tom Theuns, Claudio Dalla Vecchia, Carlos S. Frenk, I. G. McCarthy, John C. Helly, Adrian Jenkins, Y. M. Rosas-Guevara, Simon D. M. White, Maarten Baes, C. M. Booth, Peter Camps, Julio F. Navarro, Yan Qu, Alireza Rahmati, Till Sawala, Peter A. Thomas, and James Trayford. The EAGLE project: simulating the evolution and assembly of galaxies and their environments. *Monthly Notices of the Royal Astronomical Society*, 446(1):521–554, January 2015.

Yali Shao, Ran Wang, Chris L. Carilli, Jeff Wagg, Fabian Walter, Jianan Li, Xiaohui Fan, Linhua Jiang, Dominik A. Riechers, Frank Bertoldi, Michael A. Strauss, Pierre Cox, Alain Omont, and Karl M. Menten. Star Formation and ISM Properties in the Host Galaxies of Three Far-infrared Luminous Quasars at z $\sim$ 6. *The Astrophysical Journal*, 876(2):99, May 2019.

Frank H. Shu, Fred C. Adams, and Susana Lizano. Star formation in molecular clouds: observation and theory. *Annual Review of Astronomy and Astrophysics*, 25:23–81, January 1987.

M. Sirianni, M. J. Jee, N. Benítez, J. P. Blakeslee, A. R. Martel, G. Meurer, M. Clampin, G. De Marchi, H. C. Ford, R. Gilliland, G. F. Hartig, G. D. Illingworth, J. Mack, and W. J. McCann. The Photometric Performance and Calibration of the Hubble Space Telescope Advanced Camera for Surveys. *Publications of the Astronomical Society of the Pacific*, 117(836):1049–1112, October 2005.

D. Spergel, N. Gehrels, C. Baltay, D. Bennett, J. Breckinridge, M. Donahue, A. Dressler, B. S. Gaudi, T. Greene, O. Guyon, C. Hirata, J. Kalirai, N. J. Kasdin, B. Macintosh, W. Moos, S. Perlmutter, M. Postman, B. Rauscher, J. Rhodes, Y. Wang, D. Weinberg, D. Benford, M. Hudson, W. S. Jeong, Y. Mellier, W. Traub, T. Yamada, P. Capak, J. Colbert, D. Masters, M. Penny, D. Savransky, D. Stern, N. Zimmerman, R. Barry, L. Bartusek, K. Carpenter, E. Cheng, D. Content, F. Dekens, R. Demers, K. Grady, C. Jackson, G. Kuan, J. Kruk, M. Melton, B. Nemati, B. Parvin, I. Poberezhskiy, C. Peddie, J. Ruffa, J. K. Wallace, A. Whipple, E. Wollack, and F. Zhao. Wide-Field InfrarRed Survey Telescope-Astrophysics Focused Telescope Assets WFIRST-AFTA 2015 Report. *arXiv e-prints*, page arXiv:1503.03757, March 2015.

Volker Springel and Lars Hernquist. Cosmological smoothed particle hydrodynamics simulations: a hybrid multiphase model for star formation. *Monthly Notices of the Royal Astronomical Society*, 339(2):289–311, February 2003.

Volker Springel, Naoki Yoshida, and Simon D. M. White. GADGET: a code for collisionless and gasdynamical cosmological simulations. *New Astronomy*, 6(2):79–117, April 2001.

Volker Springel. The cosmological simulation code GADGET-2. *Monthly Notices of the Royal Astronomical Society*, 364(4):1105–1134, December 2005.

Daniel P. Stark, Richard S. Ellis, and Masami Ouchi. Keck Spectroscopy of Faint 3>z>7 Lyman Break Galaxies: A High Fraction of Line Emitters at Redshift Six. *The Astrophysical Journal*, 728(1):L2, February 2011.

Daniel P. Stark, Richard S. Ellis, Stéphane Charlot, Jacopo Chevallard, Mengtao Tang, Sirio Belli, Adi Zitrin, Ramesh Mainali, Julia Gutkin, Alba Vidal-García, Rychard Bouwens, and Pascal Oesch. Lyα and C III] emission in z = 7-9 Galaxies: accelerated reionization around luminous star-forming systems? *Monthly Notices of the Royal Astronomical Society*, 464(1):469–479, January 2017.

Charles C. Steidel, Mauro Giavalisco, Max Pettini, Mark Dickinson, and Kurt L. Adelberger. Spectroscopic Confirmation of a Population of Normal Star-forming Galaxies at Redshifts Z > 3. *Astrophysical Journal Letters* , 462:L17, May 1996.

Ralph S. Sutherland and M. A. Dopita. Cooling Functions for Low-Density Astrophysical Plasmas. *The Astrophysical Journal Supplement Series*, 88:253, September 1993.

Max Tegmark, Michael A. Strauss, Michael R. Blanton, Kevork Abazajian, Scott Dodelson, Havard Sandvik, Xiaomin Wang, David H. Weinberg, Idit Zehavi, Neta A. Bahcall, Fiona Hoyle, David Schlegel, Roman Scoccimarro, Michael S. Vogeley, Andreas Berlind, Tamás Budavari, Andrew Connolly, Daniel J. Eisenstein, Douglas Finkbeiner, Joshua A. Frieman, James E. Gunn, Lam Hui, Bhuvnesh Jain, David Johnston, Stephen Kent, Huan Lin, Reiko Nakajima, Robert C. Nichol, Jeremiah P. Ostriker, Adrian Pope, Ryan Scranton, Uroš Seljak, Ravi K. Sheth, Albert Stebbins, Alexander S. Szalay, István Szapudi, Yongzhong Xu, James Annis, J. Brinkmann, Scott Burles, Francisco J. Castander, Istvan Csabai, Jon Loveday, Mamoru Doi, Masataka Fukugita, Bruce Gillespie, Greg Hennessy, David W. Hogg, Željko Ivezić, Gillian R. Knapp, Don Q. Lamb, Brian C. Lee, Robert H. Lupton, Timothy A. McKay, Peter Kunszt, Jeffrey A. Munn, Liam O'Connell, John Peoples, Jeffrey R. Pier, Michael Richmond, Constance Rockosi, Donald P. Schneider, Christopher Stoughton, Douglas L. Tucker, Daniel E. vanden Berk, Brian Yanny, and Donald G. York. Cosmological parameters from SDSS and WMAP. *Physical Review D*, 69(10):103501, May 2004.

Adam D. Thomas, Lisa J. Kewley, Michael A. Dopita, Brent A. Groves, Andrew M. Hopkins,

and Ralph S. Sutherland. The Mass-Metallicity Relation of Local Active Galaxies. *The Astrophysical Journal*, 874(1):100, March 2019.

R. Tojeiro, A. F. Heavens, R. Jimenez, and B. Panter. Recovering galaxy star formation and metallicity histories from spectra using VESPA. *Monthly Notices of the Royal Astronomical Society*, 381(3):1252–1266, November 2007.

A. T. Tokunaga and W. D. Vacca. The Mauna Kea Observatories Near-Infrared Filter Set. III. Isophotal Wavelengths and Absolute Calibration. *Publications of the Astronomical Society of the Pacific*, 117(830):421–426, April 2005.

Nozomu Tominaga, Hideyuki Umeda, and Ken'ichi Nomoto. Supernova Nucleosynthesis in Population III 13-50 M_{solar} Stars and Abundance Patterns of Extremely Metal-poor Stars. *The Astrophysical Journal*, 660(1):516–540, May 2007.

Ryan F. Trainor, Charles C. Steidel, Allison L. Strom, and Gwen C. Rudie. The Spectroscopic Properties of Lyα-Emitters at z $\sim$2.7: Escaping Gas and Photons from Faint Galaxies. *The Astrophysical Journal*, 809(1):89, August 2015.

Aswin P. Vijayan, Scott J. Clay, Peter A. Thomas, Robert M. Yates, Stephen M. Wilkins, and Bruno M. Henriques. Detailed dust modelling in the L-GALAXIES semi-analytic model of galaxy formation. *Monthly Notices of the Royal Astronomical Society*, 489(3):4072–4089, November 2019.

Mark Vogelsberger, Shy Genel, Debora Sijacki, Paul Torrey, Volker Springel, and Lars Hernquist. A model for cosmological simulations of galaxy formation physics. *Monthly Notices of the Royal Astronomical Society*, 436(4):3031–3067, December 2013.

Mark Vogelsberger, Shy Genel, Volker Springel, Paul Torrey, Debora Sijacki, Dandan Xu, Greg Snyder, Dylan Nelson, and Lars Hernquist. Introducing the Illustris Project: simulating the coevolution of dark and visible matter in the Universe. *Monthly Notices of the Royal Astronomical Society*, 444(2):1518–1547, October 2014.

Stephen M. Wilkins, Neil Trentham, and Andrew M. Hopkins. The evolution of stellar mass and the implied star formation history. *Monthly Notices of the Royal Astronomical Society*, 385(2):687–694, April 2008.

Stephen M. Wilkins, Elizabeth R. Stanway, and Malcolm N. Bremer. High-redshift galaxies and low-mass stars. , 439(1):1038–1050, March 2014.

Robert E. Williams, Brett Blacker, Mark Dickinson, W. Van Dyke Dixon, Henry C. Ferguson, Andrew S. Fruchter, Mauro Giavalisco, Ronald L. Gilliland, Inge Heyer, Rocio Katsanis, Zolt Levay, Ray A. Lucas, Douglas B. McElroy, Larry Petro, Marc Postman, Hans-Martin Adorf, and Richard Hook. The Hubble Deep Field: Observations, Data Reduction, and Galaxy Photometry. *The Astronomical Journal*, 112:1335, October 1996.

Rogier A. Windhorst, Seth H. Cohen, Nimish P. Hathi, Patrick J. McCarthy, Jr. Ryan, Russell E., Haojing Yan, Ivan K. Baldry, Simon P. Driver, Jay A. Frogel, David T. Hill, Lee S. Kelvin, Anton M. Koekemoer, Matt Mechtley, Robert W. O'Connell, Aaron S. G. Robotham, Michael J. Rutkowski, Mark Seibert, Amber N. Straughn, Richard J. Tuffs, Bruce Balick, Howard E. Bond, Howard Bushouse, Daniela Calzetti, Mark Crockett, Michael J. Disney, Michael A. Dopita, Donald N. B. Hall, Jon A. Holtzman, Sugata Kaviraj, Randy A. Kimble, John W. MacKenty, Max Mutchler, Francesco Paresce, Abihit Saha, Joseph I. Silk, John T. Trauger, Alistair R. Walker, Bradley C. Whitmore, and Erick T. Young. The Hubble Space Telescope Wide Field Camera 3 Early Release Science Data: Panchromatic Faint Object Counts for 0.2-2 μm Wavelength. *The Astrophysical Journal Supplement Series*, 193(2):27, April 2011.

L. Wisotzki, R. Bacon, J. Blaizot, J. Brinchmann, E. C. Herenz, J. Schaye, N. Bouché, S. Cantalupo, T. Contini, C. M. Carollo, J. Caruana, J. B. Courbot, E. Emsellem, S. Kamann, J. Kerutt, F. Leclercq, S. J. Lilly, V. Patrício, C. Sandin, M. Steinmetz, L. A. Straka, T. Urrutia, A. Verhamme, P. M. Weilbacher, and M. Wendt. Extended Lyman

α haloes around individual high-redshift galaxies revealed by MUSE. *Astronomy and Astrophysics*, 587:A98, March 2016.

A. H. Wright, A. S. G. Robotham, N. Bourne, S. P. Driver, L. Dunne, S. J. Maddox, M. Alpaslan, S. K. Andrews, A. E. Bauer, J. Bland-Hawthorn, S. Brough, M. J. I. Brown, C. Clarke, M. Cluver, L. J. M. Davies, M. W. Grootes, B. W. Holwerda, A. M. Hopkins, T. H. Jarrett, P. R. Kafle, R. Lange, J. Liske, J. Loveday, A. J. Moffett, P. Norberg, C. C. Popescu, M. Smith, E. N. Taylor, R. J. Tuffs, L. Wang, and S. M. Wilkins. Galaxy And Mass Assembly: accurate panchromatic photometry from optical priors using LAMBDAR. *Monthly Notices of the Royal Astronomical Society*, 460(1):765–801, July 2016.

Huan Yang, Sangeeta Malhotra, James E. Rhoads, and Junxian Wang. Blueberry Galaxies: The Lowest Mass Young Starbursts. *The Astrophysical Journal*, 847(1):38, September 2017.

Donald G. York, J. Adelman, Jr. Anderson, John E., Scott F. Anderson, James Annis, Neta A. Bahcall, J. A. Bakken, Robert Barkhouser, Steven Bastian, Eileen Berman, William N. Boroski, Steve Bracker, Charlie Briegel, John W. Briggs, J. Brinkmann, Robert Brunner, Scott Burles, Larry Carey, Michael A. Carr, Francisco J. Castander, Bing Chen, Patrick L. Colestock, A. J. Connolly, J. H. Crocker, István Csabai, Paul C. Czarapata, John Eric Davis, Mamoru Doi, Tom Dombeck, Daniel Eisenstein, Nancy Ellman, Brian R. Elms, Michael L. Evans, Xiaohui Fan, Glenn R. Federwitz, Larry Fiscelli, Scott Friedman, Joshua A. Frieman, Masataka Fukugita, Bruce Gillespie, James E. Gunn, Vijay K. Gurbani, Ernst de Haas, Merle Haldeman, Frederick H. Harris, J. Hayes, Timothy M. Heckman, G. S. Hennessy, Robert B. Hindsley, Scott Holm, Donald J. Holmgren, Chi-hao Huang, Charles Hull, Don Husby, Shin-Ichi Ichikawa, Takashi Ichikawa, Željko Ivezić, Stephen Kent, Rita S. J. Kim, E. Kinney, Mark Klaene, A. N. Kleinman, S. Kleinman, G. R. Knapp, John Korienek, Richard G. Kron, Peter Z. Kunszt, D. Q. Lamb, B. Lee, R. French Leger, Siriluk Limmongkol, Carl Lindenmeyer, Daniel C. Long, Craig Loomis,

Jon Loveday, Rich Lucinio, Robert H. Lupton, Bryan MacKinnon, Edward J. Mannery, P. M. Mantsch, Bruce Margon, Peregrine McGehee, Timothy A. McKay, Avery Meiksin, Aronne Merelli, David G. Monet, Jeffrey A. Munn, Vijay K. Narayanan, Thomas Nash, Eric Neilsen, Rich Neswold, Heidi Jo Newberg, R. C. Nichol, Tom Nicinski, Mario Nonino, Norio Okada, Sadanori Okamura, Jeremiah P. Ostriker, Russell Owen, A. George Pauls, John Peoples, R. L. Peterson, Donald Petravick, Jeffrey R. Pier, Adrian Pope, Ruth Pordes, Angela Prosapio, Ron Rechenmacher, Thomas R. Quinn, Gordon T. Richards, Michael W. Richmond, Claudio H. Rivetta, Constance M. Rockosi, Kurt Ruthmansdorfer, Dale Sandford, David J. Schlegel, Donald P. Schneider, Maki Sekiguchi, Gary Sergey, Kazuhiro Shimasaku, Walter A. Siegmund, Stephen Smee, J. Allyn Smith, S. Snedden, R. Stone, Chris Stoughton, Michael A. Strauss, Christopher Stubbs, Mark SubbaRao, Alexander S. Szalay, Istvan Szapudi, Gyula P. Szokoly, Anirudda R. Thakar, Christy Tremonti, Douglas L. Tucker, Alan Uomoto, Dan Vanden Berk, Michael S. Vogeley, Patrick Waddell, Shu-i. Wang, Masaru Watanabe, David H. Weinberg, Brian Yanny, Naoki Yasuda, and SDSS Collaboration. The Sloan Digital Sky Survey: Technical Summary. *The Astronomical Journal*, 120(3):1579–1587, September 2000.

Zhi-Yu Zhang, D. Romano, R. J. Ivison, Padelis P. Papadopoulos, and F. Matteucci. Stellar populations dominated by massive stars in dusty starburst galaxies across cosmic time. , 558(7709):260–263, June 2018.

Zhen-Ya Zheng, Junxian Wang, James Rhoads, Leopoldo Infante, Sangeeta Malhotra, Weida Hu, Alistair R. Walker, Linhua Jiang, Chunyan Jiang, Pascale Hibon, Alicia Gonzalez, Xu Kong, XianZhong Zheng, Gaspar Galaz, and L. Felipe Barrientos. First Results from the Lyman Alpha Galaxies in the Epoch of Reionization (LAGER) Survey: Cosmological Reionization at z $\sim$ 7. *The Astrophysical Journal*, 842(2):L22, June 2017.

F. Zwicky. Die Rotverschiebung von extragalaktischen Nebeln. *Helvetica Physica Acta*, 6:110–127, January 1933.

F. Zwicky. Blue Compact Galaxies. *The Astrophysical Journal*, 142:1293, October 1965.